

Simulation-driven design of bonded joints in fibre composite aircraft structures using progressive damage analyses

Oliver Völkerink

Deutsches Zentrum für Luft- und Raumfahrt
Institut für Faserverbundleichtbau und
Adaptronik
Braunschweig



DLR

Deutsches Zentrum
für Luft- und Raumfahrt

Forschungsbericht 2022-24

Simulation-driven design of bonded joints in fibre composite aircraft structures using progressive damage analyses

Oliver Völkerink

Deutsches Zentrum für Luft- und Raumfahrt
Institut für Faserverbundleichtbau und
Adaptronik
Braunschweig

308 Seiten
154 Bilder
49 Tabellen
311 Literaturstellen



Herausgeber:

Deutsches Zentrum
für Luft- und Raumfahrt e. V.
Wissenschaftliche Information
Linder Höhe
D-51147 Köln

ISSN 1434-8454
ISRN DLR-FB-2022-24
Erscheinungsjahr 2022

DOI: <https://doi.org/10.57676/hya4-2a09>

Erklärung des Herausgebers:

Als Manuskript gedruckt.
Abdruck oder sonstige Verwendung nur
nach Absprache mit dem DLR gestattet.

*Finite Elemente Methode, Kohäsivzonenmodellierung, Simulation, Versagenskriterien,
Faserverbundwerkstoffe, Klebeverbindungen, Entwurf, Flugzeugstrukturen, statische Tests
(Publiziert in Englisch)*

Oliver VÖLKERINK

DLR, Institut für Faserverbundleichtbau und Adaptronik, Braunschweig

***Simulationsgestützter Entwurf von Klebeverbindungen in Flugzeugstrukturen aus
Faserverbundwerkstoffen unter Verwendung progressiver Schädigungsanalysen***

Dissertation, Technische Universität Carolo-Wilhelmina zu Braunschweig

In Faserverbundkonstruktionen bieten Klebeverbindungen mechanische Vorteile gegenüber Nietverbindungen und können damit zu einer Erhöhung des Leichtbaugrads beitragen. Dennoch sind im Flugzeugbau bisher die meisten Verbindungen genietet. Eines der größten Hindernisse für die Verwendung von Klebeverbindungen ist die Komplexität der Konstruktionsaufgabe. Neben der Einhaltung der einfachen Festigkeitsanforderung wird bei Überlastung eine bestimmte Versagensart der Verbindung angestrebt. Der Bruch darf ausschließlich im Fügeteil auftreten.

Um Entwurf und Zertifizierung zu erleichtern, wird eine simulationsgestützte Ermittlung des Versagensverhaltens angestrebt. Zu diesem Zweck wird ein ganzheitlicher, aber pragmatischer Ansatz zur progressiven Schädigungsanalyse der gesamten Klebeverbindung erarbeitet. Dieser ganzheitliche Ansatz umfasst das Materialverhalten des Faserverbundwerkstoffs, welches das intra- und interlaminare Verhalten umfasst. Hinzu kommt das mechanische Verhalten des Klebstoffs einschließlich Plastizität und Schädigung. Für jede Komponente werden verschiedene Modellierungsansätze mit unterschiedlicher Komplexität und Genauigkeit untersucht. Um den erarbeiteten Ansatz zu erproben, erfolgt im Rahmen dieser Arbeit eine experimentelle Bestimmung der erforderlichen Materialparameter für luftfahrttypische Materialien. Das Potential des erarbeiteten Ansatzes wird anhand der Ableitung einer Konstruktionsrichtlinie für die geforderte Positioniergenauigkeit einer geklebten Rumpflängsnaht demonstriert.

*finite element method, cohesive zone modelling, simulation, failure criteria, fibre composites,
bonded joints, design, aircraft structures, experimental testing*

Oliver VÖLKERINK

German Aerospace Center (DLR), Institute of Composite Structures and Adaptive Systems,
Braunschweig

***Simulation-driven design of bonded joints in fibre composite aircraft structures using
progressive damage analyses***

Doctoral Thesis, Technische Universität Carolo-Wilhelmina zu Braunschweig

In fibre composite structures, bonded joints offer mechanical advantages over bolted joints and can thus contribute to lightweight design. Nevertheless, in aircraft constructions most joints use mechanical fastening elements. One of the major obstacles to the use of bonded joints is the complexity of the design task. In addition to the simple strength requirement, a specific failure mode of the joint is required. A so-called stock-break failure in the composite adherend is desired.

In order to facilitate design and certification, a simulation-based determination of the failure behaviour is aimed at. For this purpose, a holistic but pragmatic approach for the progressive damage analysis of the entire bonded joint is compiled. This holistic approach includes the material behaviour of the fibre composite adherends, i.e. the intra- and interlaminar behaviour, as well as the mechanical behaviour of the adhesive including plasticity and damage. For each component different modelling approaches, varying in complexity and accuracy, are under investigation. In order to test the compiled approaches, the required material parameters are determined experimentally within the scope of this work. To demonstrate the potential of the approach, it is applied to derive a design guideline for the required positioning accuracy of a bonded longitudinal fuselage joint.

TU Braunschweig – Niedersächsisches
Forschungszentrum für Luftfahrt

Berichte aus der Luft- und Raumfahrttechnik

Forschungsbericht 2022-21

**Simulation-driven design of bonded joints in
fibre composite aircraft structures using
progressive damage analyses**

Oliver Völkerink

Deutsches Zentrum für Luft- und Raumfahrt
Institut für Faserverbundleichtbau und Adaptronik
Braunschweig

Diese Veröffentlichung wird gleichzeitig in der Berichtsreihe „NFL
- Forschungsberichte“ geführt.

Diese Arbeit erscheint gleichzeitig als von der Fakultät für Maschinenbau der Technischen Universität Carolo-Wilhelmina zu Braunschweig zur Erlangung des akademischen Grades eines Doktor-Ingenieurs genehmigte Dissertation.

Simulation-driven design of bonded joints in fibre composite aircraft structures using progressive damage analyses

Von der Fakultät für Maschinenbau
der Technischen Universität Carolo-Wilhelmina zu Braunschweig
zur Erlangung der Würde
eines Doktor-Ingenieurs (Dr.-Ing.)
genehmigte Dissertation

von:	Oliver Völkerink
geboren in:	Nordhorn
eingereicht am:	17.03.2022
mündliche Prüfung am:	16.05.2022
Vorsitz:	Prof. Dr.-Ing. Carsten Schilde
Gutachter:	Prof. Dr.-Ing. Christian Hühne Prof. Dr.-Ing. Peter Middendorf

2022

Kurzfassung

Die Struktur moderner Langstrecken-Großraumflugzeuge besteht zu mehr als 50 % aus duroplastischen Faserverbundwerkstoffen, um die Masse des Flugzeugs gering zu halten und so auch wie dringend notwendig die CO₂-Emissionen zu reduzieren. In Faserverbundkonstruktionen bieten Klebeverbindungen mechanische Vorteile gegenüber Nietverbindungen und können damit zu einer weiteren Massereduzierung beitragen. Dennoch sind bisher die meisten Verbindungen genietet.

Eines der größten Hindernisse für die Verwendung von Klebeverbindungen ist die Komplexität der Konstruktionsaufgabe. Neben der Einhaltung der einfachen Festigkeitsanforderung wird bei Überlastung eine bestimmte Versagensart der Verbindung angestrebt. Während der Auslegung und für die Zertifizierung ist zu zeigen, dass das Versagen der Verbindung bei Überlastung auf den Bereich außerhalb der eigentlichen Klebung begrenzt bleibt. Der Bruch darf ausschließlich im Fügeteil auftreten. Erschwerend kommt hinzu, dass viele, während der Konstruktion zu wählende, Parameter die Festigkeit und das Versagensverhalten der Klebeverbindung beeinflussen. Aktuell dienen hauptsächlich physische Tests während der Konstruktion dazu, die erforderlichen Kenntnisse über Festigkeits- und Versagensverhalten verschiedener Varianten zu erhalten. Dies ist zeitaufwändig und mit hohen Kosten verbunden, begrenzt die Anzahl der untersuchbaren Designvarianten und führt nicht zu einem tieferen Verständnis für die Wirkmechanismen.

Das führt zu der Forschungsfrage dieser Arbeit: Lässt sich eine Finite-Elemente-Methodebasierte progressive Schädigungsanalyse verwenden, um die Einhaltung der Konstruktions- und Zertifizierungsanforderungen nachzuweisen? Ein solches Werkzeug könnte den Entwurfsprozess beschleunigen, Kosten einsparen und so Klebeverbindungen in Flugzeugstrukturen attraktiver machen.

Um diese Frage zu beantworten, wird ein ganzheitlicher, aber pragmatischer Ansatz zur progressiven Schädigungsanalyse der gesamten Klebeverbindung erarbeitet. Dieser ganzheitliche Ansatz umfasst das Materialverhalten des Faserverbundwerkstoffs, welches das intra- und interlaminare Verhalten umfasst. Hinzu kommt das mechanische Verhalten des Klebstoffs einschließlich Plastizität und Schädigung. Für jede Komponente werden verschiedene Modellierungsansätze mit unterschiedlicher Komplexität und Genauigkeit untersucht. Um den erarbeiteten Ansatz zu erproben, erfolgt im Rahmen dieser Arbeit eine experimentelle Bestimmung der erforderlichen Materialparameter für luftfahrttypische Materialien. Mit diesen Materialdaten wird der ermittelte Ansatz sowohl auf Ebene der Einzelkomponenten als auch auf der der gesamten Klebeverbindung anhand eigens durchgeführter Experimente validiert.

Auf diese Weise wird ein ganzheitlicher Ansatz für die progressive Schädigungsanalyse mit Empfehlungen für Modellierungsmöglichkeiten der einzelnen Komponenten in Abhängigkeit von der Anwendung und der benötigten Informationen bereitgestellt. Folglich lassen sich anwendungsorientierte Simulationsmodelle mit einem Kompromiss zwischen

Aufwand und geforderter Genauigkeit generieren. Sein Potential demonstriert der Ansatz bei der Ableitung einer Konstruktionsrichtlinie für die geforderte Positioniergenauigkeit einer geklebten Rumpflängsnaht. Den Abschluss bildet ein Ausblick, für welche Untersuchungen der erarbeitete Ansatz in Zukunft als fundierte Grundlage dienen kann.

Abstract

The structure of modern long-haul wide-body aircraft consists of more than 50 % thermoset fibre composites in order to keep the mass of the aircraft low and hence also reduce CO₂ emissions as urgently needed. In fibre composite structures, bonded joints offer mechanical advantages over bolted joints and can thus contribute to further mass reduction. Nevertheless, most joints use mechanical fastening elements.

One of the major obstacles to the use of bonded joints is the complexity of the design task. In addition to the simple strength requirement, a specific failure mode of the joint is desired. During design and certification, it must be shown that the failure of the joint in case of overload is limited to the area outside the actual bond. A so-called stock-break failure in the composite adherend is desired. At the same time, it should be pointed out that the strength and failure behaviour of the bonded joint is influenced by many design parameters. The necessary determination of the strength and failure behaviour of different variants during design is mainly carried out by physical tests. This is expensive and time-consuming, limits the number of design variants that can be investigated and does not lead to a deeper understanding of the mechanisms of action.

This leads to the research question of this thesis: Can Finite Element Method-based progressive damage analysis be used to show compliance with design and certification requirements? Such a tool could speed up the design process and save costs, making bonded joints in aircraft structures more attractive.

To answer this question, a holistic but pragmatic approach for the progressive damage analysis of the entire bonded joint is compiled. This holistic approach includes the material behaviour of the fibre composite adherends, i.e. the intra- and interlaminar behaviour, as well as the mechanical behaviour of the adhesive including plasticity and damage. For each component different modelling approaches, varying in complexity and accuracy, are under investigation. In order to test the compiled approaches, the required material parameters are determined experimentally within the scope of this work. With these material data, the determined approach is validated both at the level of the individual components and at the level of the entire bonded joint by means of specially conducted experiments.

In this way, a holistic approach for progressive damage analysis is provided with recommendations for modelling options regarding the individual components in dependence on required information and applications. Thus, application-oriented simulation models can be created with a trade-off between effort and required accuracy. To demonstrate the potential of the approach, it is applied to derive a design guideline for the required positioning accuracy of a bonded longitudinal fuselage joint. Furthermore, the outlook points out which investigations could be carried out in the future with the compiled approach as a sound basis.

Acknowledgments

The present thesis was written during my work at the Institute of Composite Structures and Adaptive Systems of the Deutsches Zentrum für Luft- und Raumfahrt e.V. / German Aerospace Center (DLR) in Braunschweig. The preparation of this thesis was only possible through the support of many different people.

First and foremost, I would like to thank Prof. Dr.-Ing. Christian Hühne for giving me the opportunity to carry out my research in the department of Composite Design and for the supervision of this thesis. The assignment of both supportive and challenging tasks in everyday work was always characterised by great trust and gave me a variety of opportunities to develop. Despite busy schedules, he always found the time for valuable discussions at short notice. I also like to express my gratitude to Prof. Dr.-Ing. Peter Middendorf for co-supervising this thesis and to Prof. Dr.-Ing. Carsten Schilde for taking over the chairmanship of the thesis committee.

At this point, I would also like to thank Prof. Dr.-Ing. habil. Klaus Rohwer for repeated, helpful discussions on the intralaminar material model as well as on the interpretation of the results achieved.

I wish to extend my special thanks to Dirk Holzhüter, who supported me as team leader of the joining technology working group both in technical terms as well as in administrative matters. I would like to thank Jens Kosmann for his support with destructive testing and the operation of the digital image correlation systems. I would also like to thank Martin Schollerer for providing experimental data and collaborative test campaigns.

Furthermore, I would like to thank Dr.-Ing. Enno Petersen and Josef Koord for the collaborative research on M21-T700GC with many helpful technical discussion and shared open hole tension und interlaminar test campaigns. In particular, I am grateful to Enno for introducing me to the Cuntze's Failure Mode Concept and for proofreading the present work.

To Jörg Nickel I would like to express my gratitude for the collaboration in popular science publications and for proofreading of the abstract. My special thanks are extended to all the technical staff, especially Christine König, Cordelia Koch, Mareike Stegmaier and Niklas Drews for producing numerous test specimens.

In addition, I would like to express my gratitude to my former students who have supported this work. These are: Lena Schwill, Chetan Gupta, Jan Keuntje, Marvin Ehrhardt, Patrick Makiela, Joshua Moll, Franziska Klimmeck, Alina Doberts and Alexander Nassen.

Moreover, I would like to thank my former and current office colleagues Dr.-Ing. Thomas Löbel, Dr.-Ing. Enno Petersen, Lutz Beyland and Marcel Andres for several valuable discussions, a relaxed working atmosphere and the occasional after-work activities.

Although not in direct connection to this thesis, I would like to thank Volker Kleimeier and Dr.-Ing. Jochen Schmidt for introducing me to fibre composite structures during my

membership in the Formula Student team of the TU Braunschweig. This introduction sparked the fascination for lightweight construction, shaped my further studies and ultimately led to this work.

I owe a great debt of gratitude to my parents and my sister, on whose support and understanding I was able to rely at all times. In particular, this applies to my father, who passed away in August 2017 after a serious illness and unfortunately will not be able to see me complete my doctorate.

Finally, I would like to take this opportunity to give a very special thank you to my wonderful girlfriend Joana. Thank you for words of encouragement in difficult times, for accepting long working days, even on weekends, for covering my back in the final phase, for your understanding that I pursue flying while doing my doctorate and simply for being who you are.

Contents

Notations	vii
List of abbreviations	vii
List of symbols	x
1 Introduction	1
1.1 Initial situation and problem statement	1
1.2 Thesis outline	3
2 Literature review on the design of composite bonded joints	5
2.1 Design of certifiable adhesively bonded joints	5
2.1.1 Civil certification requirements	5
2.1.2 Certification methodologies	7
2.1.3 Requirements for modelling and simulation in the context of certification	10
2.1.4 Certification of a bonded structure	13
2.1.5 Design methodology	15
2.2 Review of occurring damage phenomena	18
2.2.1 Typical bonded joint configurations in composite aircraft structures	18
2.2.2 Experimental observations in representative coupon specimens . . .	19
2.2.3 Implications for the design process	23
2.3 Methods for the design-supporting prediction of the failure behaviour . . .	23
2.3.1 Determination of stresses and strains in bonded joints	24
2.3.2 Failure modelling approaches for adhesives and fibre composites . . .	25
2.3.3 State of the art in FEM-based bonded joint failure prediction	26
2.4 Chapter summary	30
3 A simulation-driven design approach for composite bonded joints	33
3.1 Requirements for a simulation-driven design approach	33
3.2 Research and working hypotheses	34
3.3 Technical approach	37
4 Intralaminar failure analysis of UD fibre reinforced composites	41
4.1 Structure and approach	41
4.2 Representation of laminates for numerical analysis	41
4.2.1 Scales of a UD fibre-reinforced composite	42
4.2.2 Modelling approaches in FEM	43
4.2.3 Choice of element type	44
4.2.4 Pseudoplasticity	47

4.2.5	Types of failure at ply level	48
4.3	State of the art in mesoscale numerical modelling of fibre-reinforced composites	49
4.4	A 3D anisotropic damage / plasticity coupled continuum damage mechanics model	51
4.4.1	Constitutive model	51
4.4.2	Plasticity model	53
4.4.3	Damage initiation and propagation	55
4.4.4	Numerical implementation as user-defined material model into Abaqus	60
4.4.5	Verification with one to few element models	63
4.5	Determination of the material parameters	69
4.5.1	Elastic and strength properties	69
4.5.2	Characterisation of plasticity	69
4.5.3	In-situ strengths	75
4.5.4	Parameters for failure criteria	76
4.5.5	Intralaminar fracture toughness	78
4.5.6	Summary of intralaminar material properties	79
4.6	Validation of the material model using open hole tension tests	80
4.6.1	Experimental tests of open hole tension specimens	80
4.6.2	Modelling of open hole tension specimens	81
4.6.3	Element type and mesh sensitivity	82
4.6.4	Strength results of the numerical analyses	84
4.6.5	Stiffness and influence of intralaminar plasticity	86
4.6.6	Fracture patterns	87
4.6.7	Detailed comparison of progressive damage analyses with Cuntze's FMC and Puck's APSC	88
4.7	Simplified versions of the intralaminar model	91
4.7.1	Version for continuum shell elements	91
4.7.2	Implementation as (V)UMAT for Abaqus/Explicit	92
4.8	Conclusions and recommendations for the holistic approach	94
5	Numerical modelling of interlaminar damage growth	95
5.1	Structure and approach	95
5.2	Delaminations in multidirectional composite structures	95
5.2.1	Interlaminar failure mechanism	95
5.2.2	Static crack propagation experiments	96
5.2.3	R-curve behaviour	97
5.2.4	Interface-orientation-dependent fracture toughness	97
5.2.5	Experimental characterisation of multidirectional laminates	98
5.3	Mesoscale numerical modelling approach	100
5.3.1	Elastic behaviour	100
5.3.2	Interface strength and element edge length	101
5.3.3	Initiation criterion	102
5.3.4	Propagation criterion	103
5.3.5	Modelling R-curve behaviour	103

5.3.6	Simulation models	105
5.3.7	Evaluation of laminate stressing effort	106
5.4	Analytical methods	107
5.5	Experimental test campaign for parameter identification	108
5.5.1	Specimen manufacturing	108
5.5.2	Test setup and procedure	109
5.5.3	Data reduction methods	111
5.5.4	Double cantilever beam test for mode I parameters	112
5.5.5	End notched flexure test for mode II parameters	121
5.5.6	Mixed mode bending tests for mixed mode parameters	126
5.5.7	Summary of interlaminar material properties	130
5.6	Application to open hole tension specimens	130
5.6.1	Comparison of composite modelling approaches	131
5.6.2	Comparison of delamination areas with experimental results	134
5.6.3	Use of interface orientation-specific ERRs	136
5.7	Conclusions and recommendations for the holistic approach	137
6	Plasticity and damage modelling of structural epoxy film adhesives	141
6.1	Structure and approach	141
6.2	Adhesive selection	141
6.3	On the state of modelling structural adhesives	142
6.4	Cohesive zone modelling-based approaches	143
6.4.1	Cohesive elements (ACZ)	143
6.4.2	Elastoplastic solid elements combined with cohesive surface (AACZ)	143
6.4.3	eXtended Finite Element Method combined with cohesive surfaces (XFEM)	145
6.4.4	Damage initiation and propagation	146
6.5	Plasticity models with pressure dependent flow criteria	147
6.5.1	Von Mises	147
6.5.2	Linear Drucker-Prager	148
6.5.3	Exponent Drucker-Prager	148
6.5.4	Mahnken-Schlimmer	148
6.6	Experimental tests for elastoplastic properties	149
6.6.1	Thick adherend shear tests	149
6.6.2	Butt joint and inclined butt joint tests	152
6.7	Identification of elastoplastic material parameters	154
6.7.1	Elastic properties	154
6.7.2	Hardening curve	154
6.7.3	Parameters for yield criteria	155
6.7.4	Verification of plasticity models on the basis of TAST specimens	156
6.7.5	Comparison of plasticity models on the basis of butt joint tests	159
6.8	Identification of fracture mechanical properties	160
6.8.1	Surface pretreatment and fracture pattern	160
6.8.2	Double cantilever beam tests for mode I parameters	162

6.8.3	End notched flexure tests for mode II parameters	164
6.8.4	Mixed mode bending tests for mixed mode parameters	167
6.8.5	Calculation of fracture toughness for AACZ and XFEM approach . .	171
6.8.6	Summary of fracture mechanical properties	172
6.9	Comparison of damage modelling approaches on the basis of TAST specimens	173
6.9.1	Influence of cohesive strength	173
6.9.2	Influence of mesh size	175
6.9.3	Stiffness and strength comparison	175
6.9.4	Crack path	177
6.9.5	Computational aspects	178
6.10	Conclusions and recommendations for the holistic approach	179
7	Validation of the holistic progressive damage model with experimental data	181
7.1	Open questions regarding the holistic approach	181
7.2	Selection of validation tests	182
7.3	Single lap shear joint elements	182
7.3.1	Test specimen variants	182
7.3.2	Specimen manufacturing	184
7.3.3	Experimental testing	184
7.3.4	Numerical modelling	184
7.3.5	Results and discussion	186
7.4	Conclusions and guideline to compile a problem-specific holistic approach .	197
8	Design of a bonded longitudinal fuselage joint using the holistic PDA approach	201
8.1	Virtual testing of aircraft structures	201
8.2	Application example: longitudinal fuselage joints	202
8.2.1	Longitudinal joint of multifunctional fuselage demonstrator	203
8.2.2	Loads on the longitudinal joint	204
8.2.3	Design variants to be investigated	205
8.2.4	Positioning accuracy of the fuselage halves	205
8.3	Simulation model for virtual testing	206
8.3.1	Requirements	206
8.3.2	Modelling simplifications	207
8.3.3	Loads and boundary conditions	208
8.3.4	Selection of holistic modelling approach	210
8.4	Preliminary studies for modelling	210
8.4.1	Investigation of the required model width	210
8.4.2	Influence of pseudoplasticity of composite adherends	211
8.5	Results from virtual test bed and discussion	213
8.5.1	Strength and failure behaviour of the design variants	214
8.5.2	Design guideline for positioning accuracy	217
8.5.3	Outlook: proposed strategy for reduced experimental testing	217

8.6 Conclusion: decisive change in failure mode	218
9 Conclusions and outlook	221
Bibliography	227
List of figures	253
List of tables	259
 Appendices	 261
A Parameters of influence on static failure of composite adhesive joints	261
B Stiffness and strength data of M21-T700GC	263
C Analytical determination of in-situ strengths	265
D Single element tests of intralaminar material model	267
E Material data for 8552-IM7	269
F Validation of 8552-IM7 intralaminar modelling with OHT tests	271
G Experimental results of Hysol EA9695 DCB and ENF tests	276
H Additional MMB tests with Hysol EA9695	279
I Results of fibre composite single lap shear joint tests	281
J Observations regarding the use of different Abaqus versions	285
Own publications	287

Notations

List of abbreviations

AACZ	Adherend + Adhesive + Cohesive Zone
AC	Advisory Circular
ACZ	Adherend + Cohesive Zone
AMC	Approved Means of Compliance
APSC	Action Plane Strength Criterion
ASTM	American Society for Testing and Materials
BJ	Butt Joint
BK	Benzeggagh and Kenane
CBA	Crack Band Approach
CBT	Corrected Beam Theory
CC	Compliance Calibration
CDM	Continuum Damage Mechanics
cERR	critical energy release rate
CFRP	carbon-fibre-reinforced polymers
CLT	Classical Laminate Theory
CM	Continuum Mechanics
CP	cross ply
CPU	Central Processing Unit
CS	Certification Specification
CZM	Cohesive Zone Modelling
DAF	Disbond Arrest Feature
DCB	Double Cantilever Beam
DENT	double edge notch tension
DFEM	Detailed Finite Element Model
DIC	Digital Image Correlation
DLL	Design Limit Load
DLR	Deutsches Zentrum für Luft- und Raumfahrt e.V. / German Aerospace Center
DM	Damage Mechanics
DUL	Design Ultimate Load
EASA	European Aviation Safety Agency

ENF	End Notched Flexure
ERR	energy release rate
ESL	Equivalent Single-Layer Theory
EU	European Union
exp.D.-P.	exponent Drucker-Prager
FAA	Federal Aviation Administration
FEA	Finite Element Analysis
FEM	Finite Element Method
FF	fibre failure
FM	Fracture Mechanics
FMC	Failure Mode Concept
FRP	fibre-reinforced polymers
FSDT	First-Order Shear Deformation Theory
GFEM	Global Finite Element Model
GOM	Carl Zeiss GOM Metrology GmbH
IBJ	Inclined Butt Joint
IFAM	Institut für Fertigungstechnik und angewandte Materialforschung / Institute for Manufacturing Technology and Advanced Materials
IFF	interfibre failure
LDM	Local Damage Mechanics
lin.D.-P.	linear Drucker-Prager
LWT	Layer-Wise Theory
M&S	Modelling & Simulation
MBT	Modified Beam Theory
MFFD	Multifunctional Fuselage Demonstrator
MMB	Mixed Mode Bending
NASA	National Aeronautics and Space Administration
NDI	non-destructive inspection
OHT	Open Hole Tension
PDA	Progressive Damage Analysis
PTFE	polytetrafluoroethylene
PZL	Process Zone Length
QI	quasi-isotropic
QUADS	quadratic nominal stress criterion
REC	Relative Percentage Error Criterion
RMA	return mapping algorithm

SBT	Simple Beam Theory
SLS	Single Lap Shear
SUL	Structural Ultimate Load
TASJ	Thick Adherend Shear Joint
TAST	Thick Adherend Shear Test
UD	unidirectional
UMAT	user-defined material model for Abaqus/Standard
UQ	Uncertainty Quantification
v.M.	von Mises
VCCT	Virtual Crack Closure Technique
VUMAT	user-defined material model for Abaqus/Explicit
WWFE-I	World-Wide Failure Exercise I
WWFE-II	World-Wide Failure Exercise II
XFEM	eXtended Finite Element Method

List of symbols

Symbol	Description	Unit
	Latin	
a	crack length	mm
a_1	Mahnken-Schlimmer material parameter	
a_2	Mahnken-Schlimmer material parameter	
a_{66}	in-plane shear coefficient	
A_{eff}	effective area	mm ²
Δa	crack extension	mm
a_{expDP}	exp.D.-P. material parameter	
A_0	undamaged area	mm ²
A_{ip}	in-plane element area	mm ²
B	specimen width	mm
b	width	mm
b_{expDP}	D.-P. exponent	
B_t	parameter to indicate skewness of the crack profile due to bending / twisting coupling	
C	stiffness matrix	MPa
D	plate stiffness	
d	cohesion	MPa
D	compliance matrix	
d_{ij}	damage variable	
D_c	parameter to indicate curvature due to longitudinal/transverse bending coupling	
E	Young's modulus	MPa
f	plastic potential	
f_E	Puck's APSC failure effort	
G	shear modulus	MPa
g	normalised fracture energy	N
G_c	fracture toughness	N/mm
G_{ic}	fracture toughness in mode i	N/mm
G_T	total fracture toughness	N/mm
h	half beam thickness	mm
I	identity matrix	
I	bending stiffness	N/mm ²
I_1	first stress invariant	MPa
J_2	second deviatoric stress invariant	MPa ²
K	yield surface shape parameter	
K_i	cohesive stiffness in mode i	N/mm ³
L	length	mm
l	length	mm
L_c	characteristic finite element length	mm
$l_{ch,i}$	characteristic length in mode i	mm

Symbol	Description	Unit
l_{CZ}	cohesive zone length	mm
m	FMC interaction exponent	
m_{CC}	compliance calibration parameter	
$\mathbf{M}(d)$	damage operator	
n	increment	
n_{dm}	Puck's APSC orientation impact degradation measure	
n_{sp}	number of specimens	
\mathbf{P}	mapping matrix	
p	Puck's APSC inclination parameter	
p_{hyd}	hydrostatic stress	MPa
P	applied force	N
p_t	exp.D.-P. hardening parameter	MPa
\tilde{p}	accumulated plastic strain	
q	equivalent stress	MPa
R	strength	MPa
r	radius	mm
t	thickness	mm
T_i	traction in mode i	MPa
T_i^0	interface strength in mode i	MPa
u	displacement	mm
Y	yield stress	MPa
\mathbf{Z}	mapping matrix	
Greek		
α	hardening law exponent	
α_{PL}	Power law exponent	
β	hardening coefficient	
β_{comp}	compliance parameter	
β_{HT}	Hahn-Tsai non-linear shear parameter	
$\delta_{c,i}$	critical opening displacement in mode i	mm
δ_i	opening / crosshead displacement in mode i	mm
ε	strain	
$\Delta\varepsilon$	Strain increment	
$\Delta\hat{\varepsilon}$	perturbation strain	
η_{BK}	Benzeggagh and Kenane interaction parameter	
η_m	relaxation time	s
γ	shear strain	
$\Delta\lambda$	plastic multiplier	
μ	friction parameter for FMC	
ν	Poisson's ratio	
Φ	oblique angle	°
σ	nominal Cauchy stress	MPa
$\tilde{\sigma}$	effective Cauchy stress	MPa

Symbol	Description	Unit
τ	shear stress	MPa
θ	fracture angle	rad
θ_{md}	most direct impact fracture angle	rad
θ_{off}	off-axis angle	°
Indices		
1,2,3	coordinates in ply directions	
b	bondline	
c	compression	
el	elastic	
f	failure	
$hard$	hardening	
I,II,III	fracture mode	
init	initiation	
max	maximum	
\parallel	parallel to fibre	
\perp	perpendicular to fibre	
$soft$	softening	
ss	steady-state	
t	tension	
x,y,z	Cartesian coordinates	
y	yield	

CHAPTER 1

Introduction

This introductory chapter places the research question addressed in this thesis in its engineering context and the key challenges are briefly discussed. In addition, the outline of the dissertation is presented to offer an overview of the work.

1.1 Initial situation and problem statement

The extensive use of thermoset composite materials of over 50 % in the structure of modern long-haul wide body jet airliners contributes to their considerably improved fuel efficiency in large measure by mass reduction. In order to design damage-tolerant fibre composite structures under impact loads, tough-modified epoxy resins are used in aircrafts such as the Airbus A350 XWB. These resin systems increase the inherent toughness of the laminate, making it less susceptible to delamination caused by impact. However, composites with toughened epoxy materials show a non-linear mechanical behaviour for loads transverse to the fibre direction.

At the same time, joining technology is developing further and is moving away from joining with bolts towards adhesive bonding. Aircraft primary structures consist of many components which in thermoset composite or metal structures conventionally have to be joined with fasteners. It needs to be considered that mechanical fastening with bolts is expensive in terms of production and has several mechanical disadvantages.

With optimal use of adhesive bonding in aircraft fuselages mass savings of up to 15% are possible [1]. The reduction in aircraft mass has a direct effect on CO₂ emissions as well as direct operating costs. In the research programme Primary Adhesive Structure Technology, the potential of a fully bonded aircraft structure was evaluated with a possible operating cost saving of 20% [2]. This savings in operational cost can be explained by mass reduction due to various mechanical advantages of bonded compared to bolted joints.

To create a bolted joint load bearing fibres in the composite material forming the joint are cut. Thus, the cross-section of the structure is reduced and stress peaks occur in adjacence of the fastener element. In bolted metallic structures load is transferred by force fit with axial pre-stress. Due to the relaxation of the polymer matrix, this load path can only be used to a limited extent in composite materials [3]. As a result, when using bolted joints, the material thickness of the structure forming the joint has to be increased in the vicinity of the fastener element. To add, cleavage failure must be taken into account when defining the laminate stacking. Fasteners are cost intensive elements and

the manufacturing is a labour intensive hole drilling, hole inspection, and joining process. Overall, the presence of fastener elements is often a key dimensioning factor and could have a negative impact on the lightweight potential of the structure. In contrast, bonded joints allow joining thin-walled parts and load bearing fibres are not cut. Hence, the cross section is not reduced and stresses perpendicular to the loading direction are distributed evenly. Beyond this, bonded joints incorporate additional functions like damping, sealing and protection against corrosion.

Despite the various advantages of bonded joints over bolted joints, bolting is currently the preferred joining technology in aircraft construction, even in structures made of fibre composite materials [4]. This is due to the high demands on the design of a bonded joint as well as certification challenges.

In order to substantiate a design for a bonded joint, the failure behaviour as well as the strength has to be evaluated. Due to non-linear material behaviour of the composite adherends and the structural adhesive as well as the occurrence of multiple interacting failure modes, the prediction of the mechanical behaviour by analysis is a complex task and is still the subject of research. Therefore, the substantiation is mainly done by physical testing. However, testing is expensive and time consuming and there are conditions that cannot be addressed by a physical test. These can be, for example, load combinations that occur in the real component but can only be reproduced in the test with very high effort or not at all. The desire to support as well as reduce these physical tests leads to the main question of this thesis:

Can Finite Element-based progressive damage analyses be used to show compliance with design and certification requirements of bonded joints in fibre composite aircraft structures?

To answer this question, a holistic approach for the Progressive Damage Analysis (PDA) of composite bonded joints considering all relevant non-linearities and damage phenomena is compiled. This is done by combining state-of-the-art analysis approaches for the mechanical behaviour up to total failure of fibre composites and adhesives. Each component is selected with a trade-off between complexity and predictive accuracy to achieve a tool that can be used in practice.

The material parameters for each model component are determined on the basis of experiments conducted at DLR for a composite and an adhesive material. To extend the scope of the investigation, a second composite material is considered. The material data for the second composite material is derived based on experimental data from literature. With this material data a separate validation is performed for each model component.

The validation of the holistic model for the whole joint is carried out for different load cases at coupon and element level. Moreover, the experimental tests for validation are accompanied by modern data recording methods such as Digital Image Correlation (DIC).

Finally, the validated holistic model is applied to an engineering problem: the bonded longitudinal fuselage joint of an aircraft. Using the developed approach, virtual tests are performed to derive design guidelines for the longitudinal joint. As an outlook a possible way to reduce physical testing to a minimum is presented.

1.2 Thesis outline

Why can state-of-the-art progressive damage analyses not alleviate the challenges in the design of fibre composite bonded primary joints in aircraft structures? Chapter 2 covers the challenges in the design of certifiable bonded joints in aircraft composite structures, occurring damage phenomena in these joints, the state of the art of available analysis approaches and their limitations.

How can a simulation-driven design approach for composite bonded joints be achieved? Chapter 3 outlines the path towards a versatile and validated PDA approach for composite bonded joints as well as how it can be used to derive design guidelines for bonded joints. Based on this, the research and working hypotheses are proposed and discussed. The chapter concludes with the work breakdown structure of the thesis.

How should the intralaminar behaviour of the fibre composite adherends be modelled and how can the required material parameters be determined? Chapter 4 deals with the representation of the intralaminar behaviour of the composite adherends in the holistic model. Based on a literature study, different approaches are implemented and compared with focus on a pragmatic but accurate selection of model features. For example the representation of the lamina in the Finite Element Method (FEM)-model, the consideration of pseudoplasticity and the choice of a failure criterion are investigated. To do so, material parameters for two different carbon-fibre-reinforced polymers (CFRP) materials are determined. Finally, a recommendation regarding how to model intralaminar behaviour in the holistic model is given.

Which approaches are suitable to model the interlaminar behaviour of the adherends, how can the necessary parameters be determined and should different interface ply orientations be considered? Chapter 5 investigates interlaminar modelling for the holistic model. Based on a literature review, an approach is selected, material properties are experimentally determined and the approach is validated against experimental data. One aspect is the use of interface orientation specific fracture energies.

What kind of plasticity and damage models are needed to model the behaviour of the structural film adhesive and how can the adhesive be characterised for the chosen approach? Similar to chapters 4 and 5, in Chapter 6 the adhesive modelling for the holistic model is worked out. The adhesive modelling is subdivided into two aspects. The continuum mechanics model to describe the elastoplastic behaviour of the adhesive material and the damage model to describe discrete cracks in the adhesive bond. For both modelling aspects a literature review is conducted, modelling approaches are selected and material parameters are derived from experimental tests. The combined modelling with

plasticity and damage is then validated. Furthermore, it is investigated whether neglecting plasticity is a reasonable simplification or not.

Can the holistic PDA be validated with experimental data? Validation of the holistic model with its individual components developed in chapters 4 to 6 is conducted in Chapter 7. For this purpose, the material data previously determined for the individual components is used. The validation is based on data recorded with DIC during the experimental test of different specimens. With the different specimens various failure modes and to some extent varied mixed-mode loadings are covered.

How could the design process of a bonded longitudinal fuselage joint using the holistic PDA approach look like? Chapter 8 uses the example of the longitudinal fuselage joint to show how the developed method can be used to derive design guidelines. To achieve this, a simplified simulation model of the longitudinal fuselage joint is developed and used in conjunction with the developed holistic material modelling approach for virtual testing. In addition, it is shown how the physical testing can be reduced to an absolute minimum by using the holistic PDA approach.

Finally, in Chapter 9 the results are discussed using the research and working hypotheses and conclusions and an outlook for future work are given. The prospects indicate for which applications the developed holistic PDA approach can serve as a sound basis.

Partial results of the present work are published in [5], [6], [7] and [8].

CHAPTER 2

Literature review on the design of composite bonded joints

Why can state-of-the-art progressive damage analyses not alleviate the challenges in the design of fibre composite bonded primary joints in aircraft structures?

In order to understand the challenges involved in the design of bonded joints in fibre composite aircraft structures, this chapter covers the aspects of certification, a possible design methodology as well as possible and intended failure modes. Based on this overview, the limitations of available state-of-the-art analysis approaches that could support the design process are pointed out.

2.1 Design of certifiable adhesively bonded joints

Starting from the general civil airworthiness certification requirements, this section covers the state-of-the-art in design and certification of adhesively bonded joints in aircraft structures.

2.1.1 Civil certification requirements

Regulations for airworthiness certification

European Union (EU) Regulation 216/2008 defines common rules in the aviation sector and establishes the European Aviation Safety Agency (EASA). The major objective of these rules is to create and maintain a high and uniform level of safety in civil aviation in Europe. EU Regulation 748/2012 specifies the application rules for the airworthiness and environmental certification of aircraft and related products, components and equipment, together with the certification of design and manufacturing organisations. This regulation contains an annex, Part-21, which establishes the requirements and procedures for the certification of aircraft and related products, components and equipment as well as design and manufacturing organisations. In addition to this annex, there are also several Certification Specifications (CS) for different types of aircraft. These are listed in Tab. 2.1 below.

Table 2.1: EASA certification specifications

Certification Specification	Title
22	Sailplanes and Powered Sailplanes
23	Normal-Category Aeroplanes
25	Large Aeroplanes
27	Small Rotorcraft
29	Large Rotorcraft

The aforementioned airworthiness standards for aircraft (including rotorcraft) cover many aspects like General Design, Structure, Powerplant, Flight, Operating Limits and Instructions. However, none of these sections specifically refer to composites, except for one regulation in CS 27 and CS 29, which relate to fatigue and damage tolerance.

Guidance for certification of composite structures

The EASA provides guidance for certification of composite structures in the form of published circulars, policy statements, and memos to clarify the regulations and to provide one or more means, but not the exclusive means, of compliance. Applicants have the option to follow the published guidance to streamline the certification process but may suggest other methods. Although the regulations for metal or composite structures are the same, the means of compliance may vary significantly. The Approved Means of Compliance (AMC) 20-29 ‘Composite Aircraft Structure’ document [9] is a guidance for certification of composite structures published by the EASA. It is harmonised with Advisory Circular (AC) 20-107B from the Federal Aviation Administration (FAA) [10] and addresses regulatory requirements with a safety management philosophy [11]. A brief overview of composite structure certification from a regulatory perspective is given by Waite [12].

From safe-life to damage-tolerant structures

The design philosophy of aircraft structures regarding structural durability in its actual version has been developed in the last decades based on in-service experiences.

In 1954 two Comet I aircraft crashed although they only had few flight hours and about 1000 cycles with internal pressure loading. The Comet I was the first commercial jet-engined airliner and had a pressurised cabin. At that time, this technique was unusual. Analysis showed that the internal pressure loading led to a crack in the corner of a cabin window. This additional loading exposed the structure to 70 % of its ultimate strength in every flight. The consequence was the failure of the whole cabin due to fatigue. Those incidents resulted in the **safe life**-concept. With fatigue taken into account during the design of structures and full-scale tests being mandatory for certification of the airframe, fatigue damages should be kept so small that they would not become crucial in the life of an aircraft [13].

The next major change in the design philosophy was based on the fatal crash of a F-111

fighter aircraft from the United States Air Force, which had accumulated only about 100 flight hours, in 1969. Caused by a small initial defect in a steel fitting, which became critical in a 4.0g manoeuvre, a wing completely detached in flight. Although the aircraft was designed for loads up to 11.0g, the loading in the 4.0g manoeuvre was sufficient to exceed the residual strength of the precracked fitting. This circumstance resulted from the use of a material with low fracture toughness [13]. Due to this incident in 1974 the ‘Airplane Damage Tolerance Requirements’ [14] for military aircraft in the United States were published. In this document it is stated that fracture mechanical methods have to be used to evaluate the structural durability. Furthermore, existing cracks resulting from manufacturing defects or accidental damages should be considered. For civil applications the damage tolerance philosophy was introduced in 1978 with the amendment 45 of the FAR 25.571. With the so-called **fail-safe** philosophy, it is ensured that the structure will not fail immediately, if a damage occurs.

Despite further development of the design philosophies in 1988 a Boeing 737-200 lost a part of the upper fuselage shell at 24000 ft flight altitude and an emergency landing had to be performed. The aircraft built in 1969 had accumulated over 35000 flight hours. The accident investigation showed that a plurality of small cracks in the area of the riveted longitudinal joint of the fuselage existed before the incident. Corrosion and the disbond of an adhesive bondline resulted in multiple site damage—many small cracks forming one big critical crack. The incident shows that it is not sufficient to consider single cracks only in design-supporting mechanical analyses. Also the interaction of cracks has to be considered in the design phase.

Using the Eurofighter as example, Dilger et al. [15] show the importance of damage tolerance in the design of aircraft structures. The Eurofighter was designed as a safe-life aircraft and has been analysed by Dilger et al. with the current knowledge in the field of damage tolerance. It could be shown that a large number of the fatigue-critical areas of the aircraft were not recognised as such during the design process. This is attributed to inadequate stress analyses due to insufficiently detailed or incorrect FEM analyses as well as poor detail design and stresses the need for a simulation-driven detailed structural design.

2.1.2 Certification methodologies

A major part of the certification is the structural substantiation, which is a process that demonstrates that a design meets the structural requirements [16]. Structural substantiation has to be performed for static strength and damage tolerance considerations and thus, is a major consideration in certification of civil aircraft. However, many more aspects such as durability, crashworthiness, flutter, lightning protection, fire protection and flammability must also be considered. These aspects are not discussed in this present work. Detailed discussions on certification for civil aircraft can be found for example in [17]. There are three major certification approaches for structural substantiation ranging from certification by test only to mainly analysis-based certification. The three approaches are briefly described below:

Certification by test

The description of the certification by test approach is a concise summary of the description in [11]. As the name indicates this certification approach is based on substantiation by testing only. The base material properties are determined with lamina and laminate level tests. Using these tests the material behaviour, which includes the extremes of the operating envelope like minimum and maximum temperatures and maximum humidity, is characterised. In this way, design values are gained. In addition, the experimental data is also used to develop pass/fail criteria for in-process quality assurance and batch acceptance testing.

The substantiation of static strength, fatigue and damage tolerance requirements is also straight-forward. For this purpose full-scale tests, for some items like landing gear or control surfaces tests on component level, are performed with various loads under worst case conditions. However, the considerations of environmental effects and statistical variability of the composite material are challenging.

In this context Design Limit Load (DLL) is defined as the maximum expected load in service. Hence, the structures must withstand DLL without any harmful damage. The structure is only allowed to fail after exceeding Design Ultimate Load (DUL), which is defined as DLL times a factor of 1.5.

Certification considerations are based on traditional metallic structures without major scatter in material behaviour. Additional safety factors are only applied, if larger variations for instance with castings and metallic fittings are expected. For composites no safety factors are prescribed, but guidance is given for static strength substantiation in [9]. A safety or overload factor can for example be calculated by dividing the mean strength by A- or B-basis strength.

Certification by analysis supported by test

Certification by analysis supported by test is based on the building block approach and is common for composite structures. As for certification by test the following description is based on [11]. The building block approach is a mix of testing and analysis in a step-by-step procedure of tests and analyses from lamina to full-scale structural level. The intermediate complexity levels are from small to large coupon, element, detail, and subcomponent level. Issues of variability, environment, structural discontinuity, for example joints, damage, manufacturing defects and design or process-specific details are addressed at the different levels. By collecting data at each level, a sufficient test analysis correlation can be achieved and variations can be quantified at larger structural scales using analysis. In this way, early failures in complex full-scale tests can be avoided by lessons learned in initial and less complex tests.

Fig. 2.1 shows a schematic illustration of the building block approach. The statistical basis, which requires large quantities of tests, is provided by non-complex coupon and element level tests. Detail and subcomponent tests are used to validate the ability of analysis methods to predict failure modes and local strains and to further establish failure criteria. To add, impact damages of the assembled composite structures are also considered

at this level. The performance of non-generic design details, in contrast, is validated by subcomponent and component tests with smaller sample sizes compared to the lower levels. The final substantiation has to account for combined loads, complex load paths and out-of-plane effects. This is achieved through component tests, but the critical load cases and associated failure modes are identified by using the previously validated analytical methods.

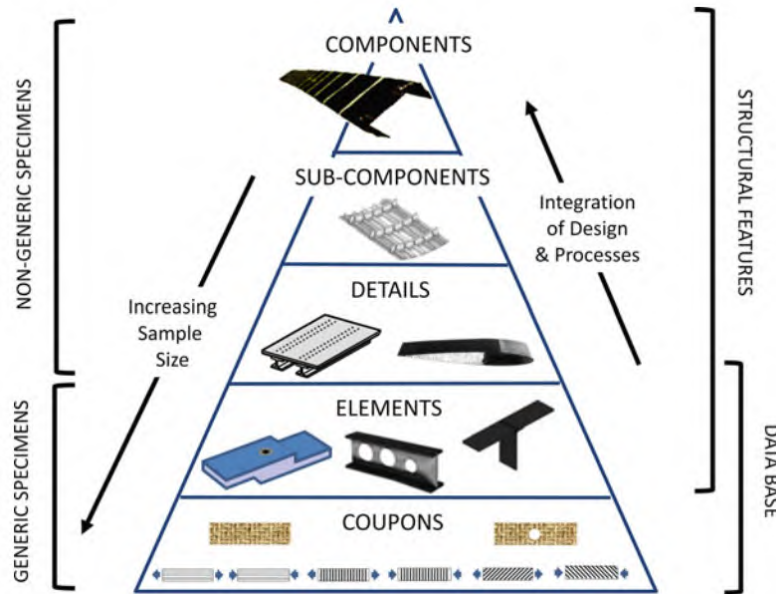


Figure 2.1: Building block approach [18]

Certification by analysis

The following section is a brief summary of the description of certification by analysis in [19]. As described above, compliance with the CS can be shown using tests only or using analysis supported by tests. Since analyses are becoming more and more widespread, there is a trend in the (aerospace) industry to rely more and more on analyses in the certification process. This trend is called certification by analysis. Nevertheless, it should be noted that this term is somewhat misleading as it implies that certification is performed without any testing at all. However, the key to acceptance of analyses in certification is that the analyses provide reliable, accurate, or at least conservative results. Thus, a complete elimination of testing would only be given if the analysis method is already fully verified and validated and is only used within its limits of validity. For this reason, the term Modelling & Simulation (M&S) is preferred in [19]:

‘Modelling and Simulation (M&S) is the use of a (conceptual, mathematical or numerical) model as a basis for simulation by computational means of physical phenomena. Modelling is the act of constructing a model; simulation is the execution of a model to obtain analytical results.’ [19]

Nonetheless, the desire for more M&S in certification is driven by several considerations.

Computational capabilities and accuracy are increasing and the commercially available M&S software packages are becoming more and more user-friendly. By using these M&S capabilities, programme risks and the amount of physical testing can be reduced. This results in a more efficient design and development process. Furthermore, more M&S can be beneficial from a safety point of view. Tests can have also their limitations and with proper M&S tools many more design variants can be examined. Finally, M&S could result not only in a better, but also safer product. Of course there are disadvantages and aspects that should be taken into account when using M&S. Modern M&S software packages are remarkably simple to use and one can easily produce erroneous results without even noticing in case of the user not having the necessary experience and / or relevant test data. Therefore, the next section introduces a framework of items which have to be addressed when using M&S in the context of certification.

2.1.3 Requirements for modelling and simulation in the context of certification

This section is a brief overview of a main items framework to be addressed by M&S activities in the context of aircraft certification published by EASA in a certification memorandum [19]. The overview focuses on the verification and validation of static strength simulations as this is the main objective of this thesis. Information on errors and uncertainties, on experience and expertise as well as on documentation and record keeping can be found in the certification memorandum. All items have to be considered, documented and shown to the authorities during a certification process.

Verification

Many publications subdivide the topic of verification into two aspects. On the one hand, during code verification confidence is established that the mathematical models and the algorithms to solve the models are working properly. On the other hand, calculation or solution verification provides confidence that the mathematical model is precisely solved. Both verification parts are performed by the collection of evidence. While code verification must only be carried out once, calculation verification has to be performed for every analyses performed. [20]

Code verification is the domain of software development. Most software used, is commercially available and no code verification is necessary by the user of the software. However, code verification also applies to scripts programmed by the user to enhance commercially available tools as well as to in-house tools not distributed by software companies. In the latter two cases, the user is also responsible for code verification. Regardless of whether the tools are commercial or in-house, the user should always be familiar with the assumptions and limitations made during analysis.

Calculation or solution verification can be structured into three parts. First, the numerical model has to be verified. Issues to be verified for static strength analyses are for example: Type of Finite Element Analysis (FEA) (linear or non-linear, Global Finite Element Model (GFEM) or Detailed Finite Element Model (DFEM)), physical properties, materials and material characteristics, units, elements (0D, 1D, 2D or 3D; beam, shell or solid), mesh,

boundary conditions, contacts and external load applications. Second, the numerical analysis error of the solution has to be estimated. Numerical errors such as round off errors, statistical sampling errors and iterative convergence errors should be small compared to errors resulting from the discretisation of the physical systems. Third, the output data generated by the analysis should be checked.

Validation

The process of determining how accurate the numerical model represents the real world with respect to its intended use, is called validation [20]. Common practice in aerospace is the application of the building block approach mentioned in Section 2.1.2 for validation. With this approach analysis results are compared with physical test data at each level of the building block pyramid. These levels could be for example coupons, elements, details, subcomponents, and components. In this context, the number of specimens decreases with increasing complexity. For this, the following issues have to be considered: The data collected during physical tests should be of high quality and as comprehensive as possible. Data should be collected for instance with strain gauges, accelerometers, load cells, high speed cameras as well as by DIC. Inherent test variability should be accounted for by multiple tests in order to ensure that validation is not based on an outlier data point. Furthermore, results of the numerical analysis should be generated before physical validation test results are available.

The test data can be compared with the analysis results in different ways, both qualitatively and quantitatively. A qualitative comparison can be used to get a first impression of the simulation's adequacy. This can be done for example by examining photos or videos taken during and after physical tests and comparing them to simulation results. In most cases, a quantitative comparison is also necessary. For scalar unities like deformations, stresses or strains the Relative Percentage Error Criterion (REC) is a simple comparison method.

Furthermore, acceptability criteria are required to determine if the difference between physical tests and simulation is acceptable or not. These criteria are called validation metrics. For deformations as well as for stresses and strains validation metrics are simple and straight forward to implement. Deviations within $\pm 5\%$ for deformations and within $\pm 10\%$ for stresses and strains are commonly accepted [21]. As an example, this strain validation metric is illustrated in Fig. 2.2.

The process of adjusting the modelling parameters in the numerical model to reduce the deviations between simulation and experimental data is known as model calibration, tuning or updating [22]. A valid way for model calibration is collecting more experimental data to enhance the understanding of the physical phenomena involved as well as reducing variability in the input data. Model calibration should not be conducted in a blind attempt by randomly adjusting parameters. Random adjustments could result in unrealistic values for some parameters and risks validating the model against only a particular set of physical test data. Consequently, the model may be invalid in other conditions.

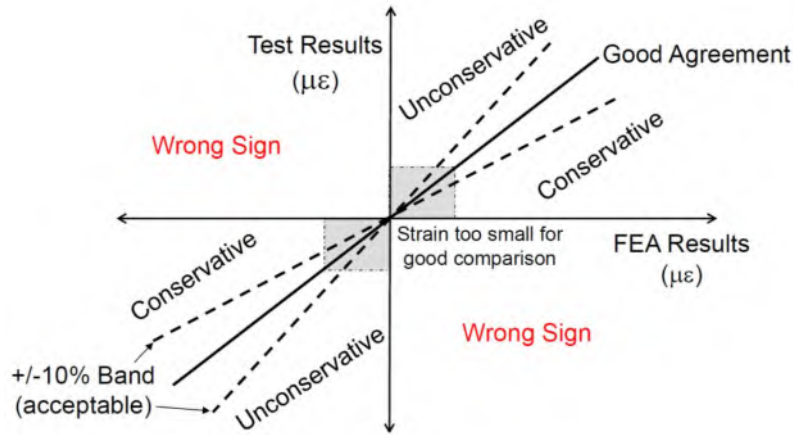


Figure 2.2: Validation metrics for strains [21]

Extrapolation and similarity

Limits of validity must be established for the satisfactorily verified and validated model with identified and addressed errors and uncertainties. Furthermore, it has to be ensured that the credible model is only used within these limits. Oberkampf et al. [23] outlined three different possible relationships between validation and application domain. These scenarios are shown in Fig. 2.3.

In Scenario (a), the validation and application domain match, which is why no extrapolation has to be performed. However, in Scenario (c) the application domain is outside of the validation domain. This means that the model would be applied beyond the limits of validity. Hence, extrapolation is needed. For this reason, the model cannot be used

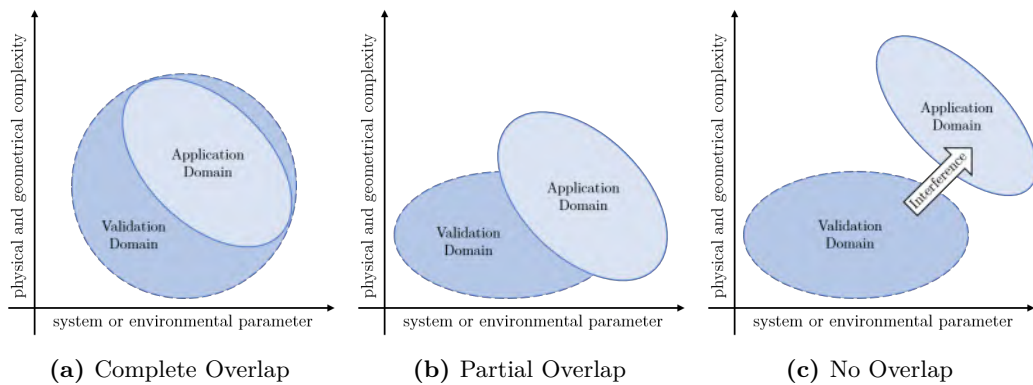


Figure 2.3: Possible relationships of the validation domain to the application domain [23]

without further validation. Even additional verification may be necessary if the model itself must be adjusted. The most challenging relationship is Scenario (b). There is a partial overlap between application domain and validation domain, but the difference, for example of the design to be investigated, is not as substantial as in Scenario (c). The computational model is still valid but some additional testing may be necessary.

Especially for cases like Scenario (b), guidance is needed on how to determine if a validated model can be used or if additional test data is needed. Such guidance for static strength substantiation can be found, for example, in AMC 25.307, which distinguishes between new structure, similar new structure and derivative structure. The question is whether an additional model is still valid or not, is subject to engineering assessment and can lead to considerable discussions between applicants and the approval authorities.

2.1.4 Certification of a bonded structure

After having clarified the framework for certification of aircraft structures in general, this section focuses on the certification of bonded composite structures.

Definition of a bonded joint

Technically there are three different types of bonded joints, which are shown in Fig. 2.4. The guidance provided by EASA only recognises bonding processes in which additional surface preparation is required for at least one interface prior to bonding. This includes co-bonding as well as secondary bonding. In the co-curing process an adhesive may be used between two laminates but the constituents are all uncured. Therefore, no surface preparation is necessary prior to bonding and cure. Since sandwich structures are considered as a specific type of composite bonded structure, they will not be further discussed in this work.

For certification considerations joints can be further classified in primary and secondary joints according to their safety relevance. Primary joints are typically single load path joints and a total failure would lead to catastrophic loss of structural integrity of the aircraft. Ordinarily, primary joints have short overlap lengths in the primary loading direction and are therefore highly loaded. An example for a primary joint would be a longitudinal fuselage joint. In contrast, secondary joints can typically be found in multiple load path structures. Thus, the failure of a single joint could lead to load redistribution to other load-carrying elements but not to a total loss of structural integrity. Bonded stringers are a common example for secondary joints. With their comparable long overlap lengths in the dominant loading direction, the stringer-skin bonded joints are low-loaded like most secondary joints.

Today's certification rules—CS 23.573(a)

The damage tolerant design philosophy of current aircraft leads to the boundary conditions for the certification of adhesive bonded joints in composite structures. According to today's

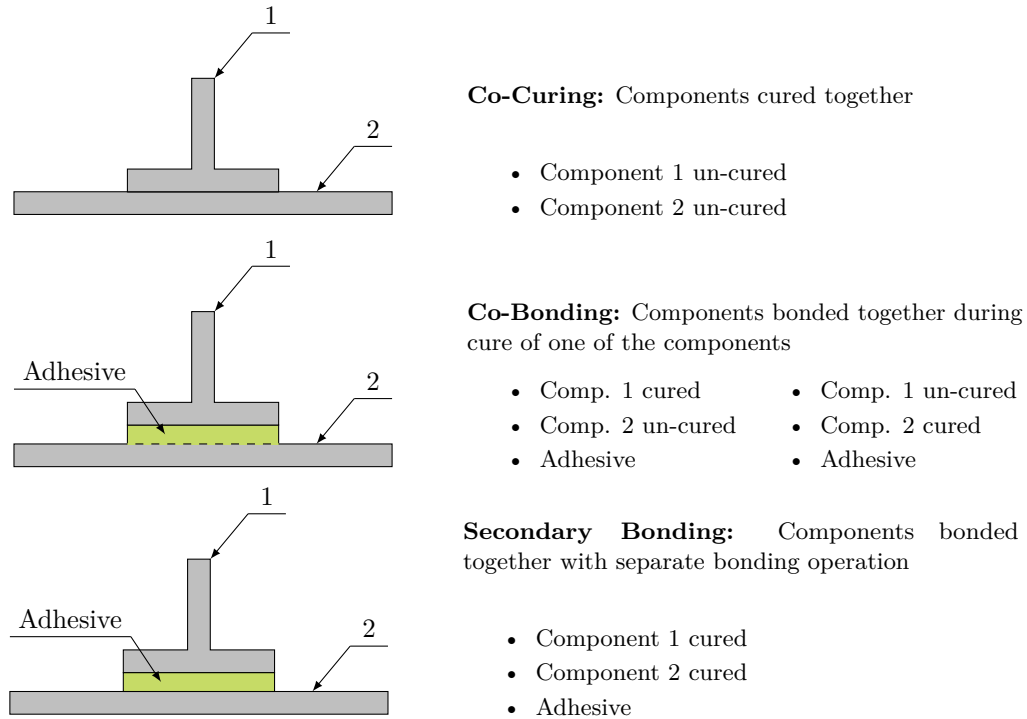


Figure 2.4: Definition of a bonded joint adopted from [24]

certification rules, cf. AMC 20-29 [9], certification of adhesively bonded primary composite joints can only be achieved in one of the following ways:

‘For any bonded joint, the failure of which would result in catastrophic loss of the airplane, the limit load capacity must be substantiated by one of the following methods—

(i) The maximum disbonds of each bonded joint consistent with the capability to withstand the loads in paragraph (a)(3) of this section must be determined by analysis, tests, or both. Disbonds of each bonded joint greater than this must be prevented by design features; or

(ii) Proof testing must be conducted on each production article that will apply the critical limit design load to each critical bonded joint; or

(iii) Repeatable and reliable non-destructive inspection techniques must be established that ensure the strength of each joint.’ [9]

Despite major research efforts, there is no robust non-destructive inspection (NDI) method available, which is able to measure the adhesive or cohesive properties of an adhesively bonded composite joint [25]. For this reason the strength of joints cannot be determined reliably by NDI and the requirement (iii) may not be fulfilled. It needs to be

noted that proof testing is not possible for each production article. It is not affordable in large commercial aircraft productions because testing, especially of large structures, is very cost-intensive and time consuming. Therefore, the requirement (ii) can also not be met. Thus, the remaining requirement (i) is the only one, which is taken into account in practice. It is one of the main reasons for the absence of adhesive bonding as standalone joining technology in primary composite joints.

State of the art is the usage of additional fasteners, called chicken rivets, which ensure the capability of the joint to carry the relevant loads even if the whole adhesive bondline has failed. These fasteners have an inherent damage tolerance capability because the required multiple load paths are represented by the individual fasteners. However, these additional fastener elements prevent the benefit from all of the advantages of bonded joints mentioned in Section 1.1. In contrast, an adhesive bond must be seen as a single fastener joint. Accordingly, a dedicated damage tolerance concept is necessary to ensure that a maximum disbond is not exceeded, for example due to fatigue loading, and a certain load can still be carried with this damage. As a consequence, adhesive bonding is currently only permitted as the sole joining technology for secondary joints.

The integration of a Disbond Arrest Feature (DAF) is currently regarded as the key element to meet the certification challenges and, by this means, open up the full potential of bonding technology [26]. In addition to the integration of DAFs, there are further requirements on the failure behaviour of the joint. This leads to a description of possible design methodologies.

2.1.5 Design methodology

According to Hart-Smith [27], the main objective of the structural design of adhesively bonded joints is that the bond itself never fails. This means that under all circumstances the adjacent structure fails before a structural failure caused by the adhesive bond can occur. This design philosophy is supported by Waite who states that ‘a correctly designed bonded joint is expected to fail in the adherend [...], although failure within the adhesive may occur’ [12].

Failure mode classification

Depending on the design, a bonded joint in a fibre composite structure can fail in different ways. In the standard American Society for Testing and Materials (ASTM) D5573 [28] a classification of the different failure modes has been published. The standard distinguishes between six different failure modes presented in Fig. 2.5.

Adhesion or adhesive failure describes a disbond at the interface between adherend and adhesive. This failure mode usually occurs due to an inadequate bonding process, especially due to insufficient surface pre-treatment. This type of failure must be avoided under all circumstances, as it is considered unacceptable by the relevant authorities [9, 10].

Cohesive failure refers to a failure purely within the bondline. In this failure mode

the cohesive strength of the adhesive is reached. Thus, the maximum strength of the bond itself is achieved.

Cracks in bonded joints with commonly seen mixed mode ratios of peel and shear stresses tend to propagate towards one adherend [29]. This cohesive failure near the interface of adhesive and adherend is referred to as **thin-layered cohesive failure**.

If failure is located in the adherends near the bond, the failure is termed **fibre-tear** or **light-fibre-tear** failure. The occurrence of these types of failure depends on the transverse properties like interlaminar composite strength and the stacking sequence in the composite adherends.

If the bond strength is greater than the laminate strength, a **stock-break failure** occurs. In this case the structure fails due to adherend breakage outside of the bond.

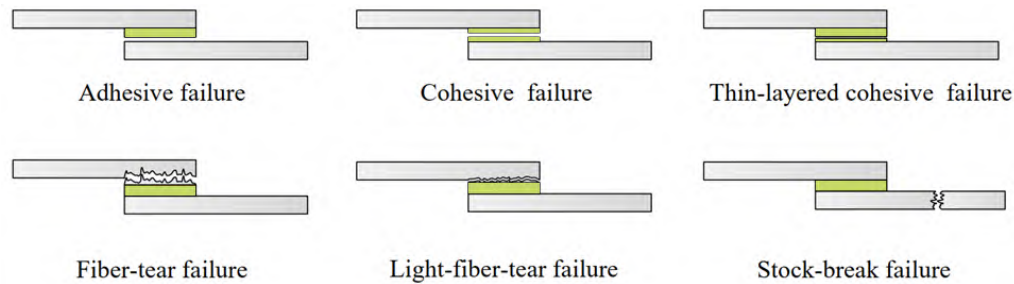


Figure 2.5: Sketches illustrating failure modes [28]

Expressed in failure modes as defined by ASTM D5573 [28], stock-break failure is the desired mode. Based on Hart-Smith's statement, Davis and Bond have proposed a certification methodology [30]. The proposed methodology is based on a comparison between the load capacity of the bonded joint (in shear) and the many different design load cases. Davis and Bond distinguish between five possible conditions:

- **Condition 1:** The adhesive load capacity is greater than the ultimate strength of the composite material which forms the joint. Thus, failure by shear through the adhesive bondline should never occur.
- **Condition 2:** The adhesive load capacity is greater than the known Structural Ultimate Load (SUL) of the surrounding structure, but less than the ultimate strength of the composite material which forms the joint. Therefore, there should never be a failure due to shear caused by the adhesive bondline itself because the structure away from the joint will fail beforehand.
- **Condition 3:** The adhesive load capacity is less than the known SUL, but greater than the DUL of the surrounding structure. Since the structural loads should never exceed DUL, failure by shear through the adhesive bondline should not occur.

Nevertheless, the adhesive bondline is the weakest element of the joint and when the structure is tested to SUL, failure occurs in the adhesive.

- **Condition 4:** The adhesive load capacity is greater than the DLL for the surrounding structure, but less than the DUL. Joints showing this strength condition are only suitable for reinforcement repairs when the structure to be repaired can sustain certification requirements also without the repair.
- **Condition 5:** The adhesive load capacity is less than the DLL for the surrounding structure. Joints showing this strength condition are only applicable when aircrafts are operated under flight restrictions, because if operating loads were not restricted, failure by shear through the adhesive bondline is possible.

Based on these considerations, the design engineers must check during the design process in which failure mode their current bonded joint design is likely to fail. The failure mode is affected by many design parameters like for example joint geometry, layup and material of the composite adherend as well as adhesive material. Fig. 2.6 provides an overview of parameters affecting the static failure strength and mode of bonded joints. A more detailed compilation of parameters and their influence on static failure is given in Tab. A.1 in the appendix.

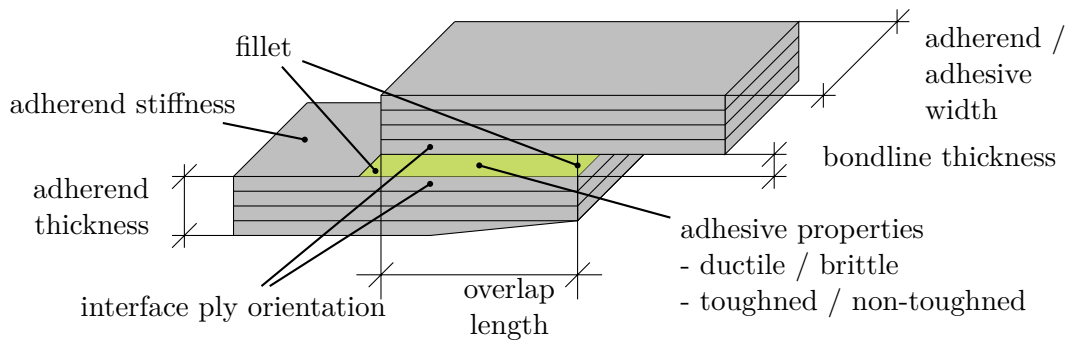


Figure 2.6: Parameters of influence on static failure of composite adhesive joints, figure based on tables from [31] and [32], cf. A.1

Apart from demonstrating that the pristine bonded primary joint can withstand relevant loads, failures in the intended mode and thus the requirements for static strength and damage tolerance must also be met. The requirement that primary joints must have design features which ensure that a maximum disbond, at which the joint can withstand at least DUL, is not exceeded, adds even more complexity to the design task. These design features can be a specific way of a design, such as scarfed joints, but also additional physical elements in the joint such as a hybrid bondline [26], with two or more materials, surface toughening [33, 34] or even rivets [35, 36]. In turn, these design features may also change the mechanical behaviour of the pristine joint and have an impact on static strength substantiation. In addition, all these aspects must be proven under different environmental conditions which makes the substantiation even more challenging.

It is therefore a complex task to predict the strength and failure mode of a joint design. If cost- and time-intensive structural testing of each design version shall be avoided, the design engineer needs capable analysis methods to predict the mechanical behaviour up to total failure during the design process.

2.2 Review of occurring damage phenomena

In order to specify the requirements for such an analysis method, the following section discusses selected publications that examine the failure of typical bonded joint configurations in composite aircraft structures in detail. In this way, the phenomena to be modelled by the method shall be derived. First, typical bonded joint configurations and their application in airframe structures are presented and then occurring damage phenomena are discussed based on representative coupon specimens from literature.

2.2.1 Typical bonded joint configurations in composite aircraft structures

In aircraft structures **single lap joints** can be found for example as longitudinal fuselage joints, see Fig. 2.7(a) or in the aft section of smaller, general aviation, aircraft, cf. Fig. 2.7(b).

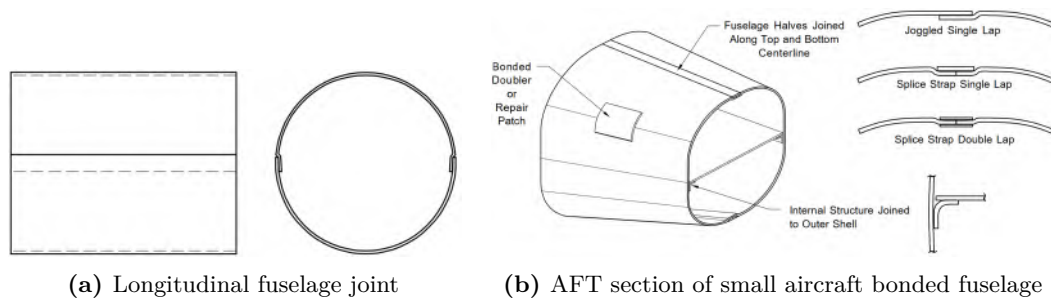


Figure 2.7: Examples of single lap joints in aircraft structures [37]

The generic bonded wing spar construction shown in Fig. 2.8 serves as an example for **double lap joints** in aircraft structures.

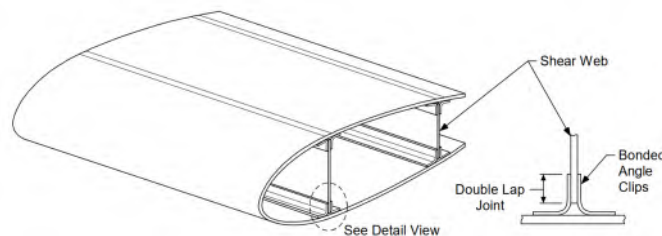


Figure 2.8: Generic bonded wing spar construction with double lap joint [37]

Extensive use of bonded joints can be found in the Cessna Citation III. The business jet provides **skin-stringer joints** as an example, cf. Fig. 2.9. In the design of the Citation III,

the stringer or longerons as well as the frames are bonded to the skin.

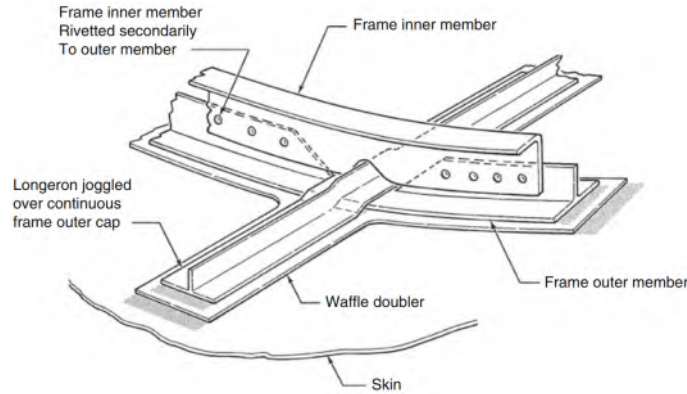


Figure 2.9: Cessna Citation III bonded frame/longeron intersection [38]

A fourth configuration of bonded joints, which can be found in aircraft in-service, are scarf or stepped joints in the repair of damaged composite parts. In Fig. 2.10 a stiffened panel repair as well as crosssections of stepped and scarf repairs are illustrated.

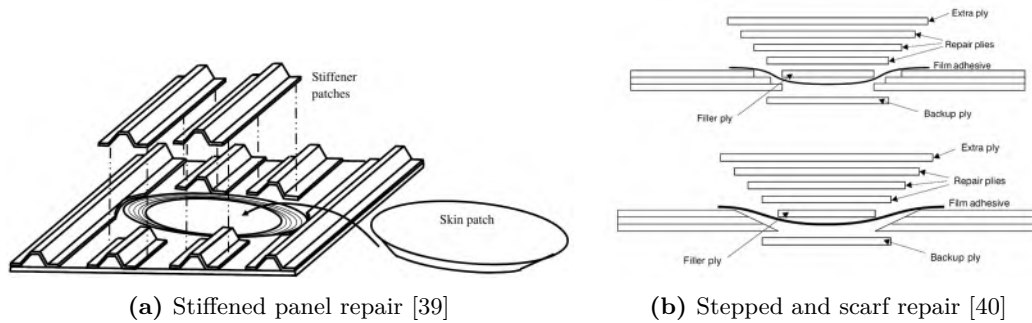


Figure 2.10: Examples of stepped and scarf repair in aircraft structures

2.2.2 Experimental observations in representative coupon specimens

Single lap joints

Purimpat et al. [41] tested single lap joints, all with the same global quasi-isotropic (QI) properties, but with different ply layups. The adherends were made from carbon fibre epoxy prepreg composite and the specimens were bonded with an epoxy paste adhesive. The observed failure patterns involve one or more of the following laminate damage phenomena: interlaminar damage (delaminations), intralaminar damage due to fibre failure (FF) and intralaminar damage due to interfibre failure (IFF) or matrix damage. Purimpat et al. reported damage initiation at the adhesive edges where the highest peel and shear stresses are located. Then the cracks followed a more or less complex path into the adherends depending on the individual stacking sequence. The further the 0° -ply was positioned away from the adhesive layer, the deeper the cracks extend into the adherends thickness direction.

The effect of the composite layup on the occurring damage mechanisms was also investigated by Kupski et al. [42]. As in the previously reviewed study, single lap joints were examined, but in this case, they were made from a thermoplastic carbon fibre composite combined with an epoxy film adhesive. The observed failure patterns are shown in Fig. 2.11.

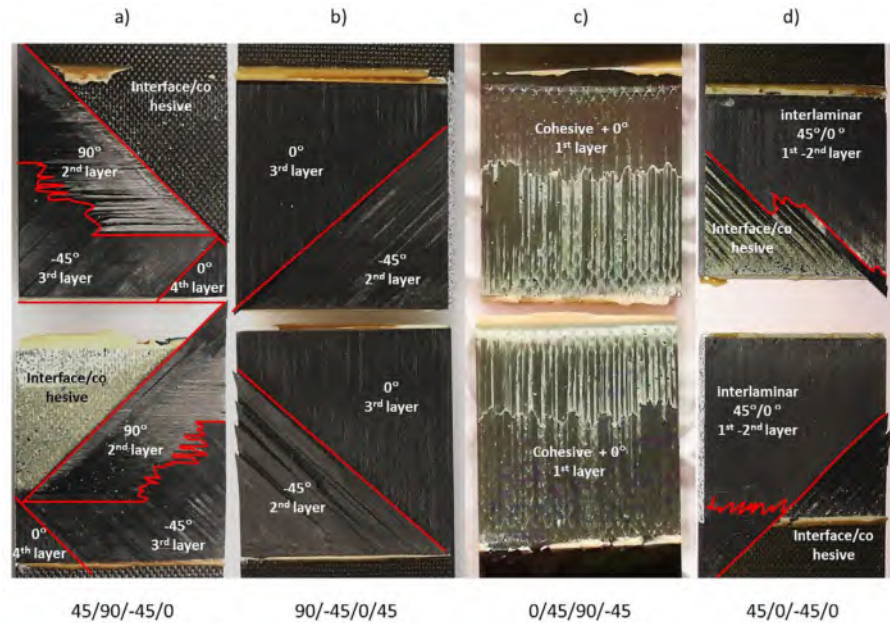


Figure 2.11: Fracture surfaces of single lap joints with different layups [42]

For specimens with 0° -plies adjacent to the bondline damage was observed predominately in the bondline accompanied with some intralaminar damage in the 0° -plies, cf. Fig. 2.11 (c). The final failure mode is cohesive. As can be seen in Fig. 2.11 (a) and (d) with a 45° -ply as the adjacent layer, a mix between damage in the bondline near the interface and damage inside the composite adherend occurred. By turning the orientation of the layer adjacent to the bond line even further away from 0° to 90° the damage leading to joint failure is entirely located inside the composite adherends, cf. Fig. 2.11 (b).

Double lap joint

Potter et al. [43] tested double lap joints made from a carbon fibre epoxy prepreg and a paste adhesive under tensile loading. The adherends had a unidirectional (UD) layup where 0° was orientated in the loading direction. A sketch of the specimens is shown in Fig. 2.12.

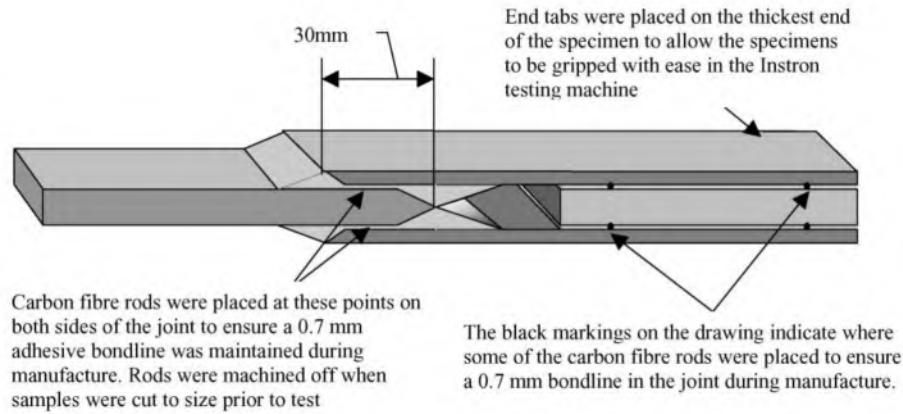


Figure 2.12: Schematic representation of double-lap joint made with UD laminate. [43]

For all specimens tested, the final failure occurred due to delamination near the adhesive/adherend-interface. Specimens with well manufactured fillets showed failure initiation by adhesive cracking. This adhesive crack then grew towards the inner adherend and initiated a delamination, as shown in Fig. 2.13(a). This delamination caused the final failure.

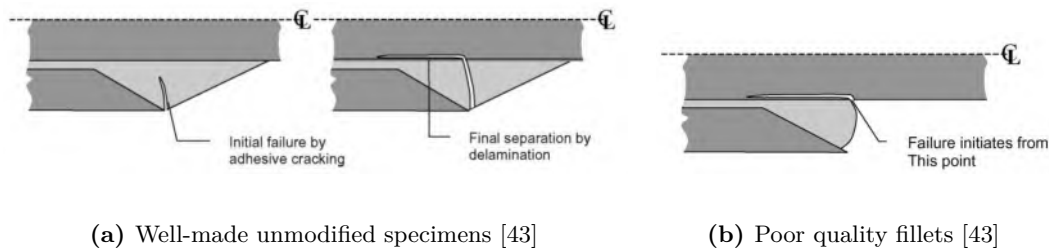


Figure 2.13: Influence of fillet on failure behaviour [43]

Specimens, where the fillet was of inferior quality, showed a different behaviour. In this case, the crack initiated at the edge between adhesive and adherend and led directly to a delamination of the inner adherend, cf. Fig. 2.13(b), which then resulted in final failure. The failure load of these specimens is only around 70% of the well-made specimens. Therefore, in this study it is shown that even a slight difference in the specimen geometry can cause a change in failure behaviour which in turn has an impact on the strength of the joint.

Skin-stringer joints

Krueger et al. [44] have tested specimens which represent stringer-to-skin bonded joints. These are shown in Fig. 2.14. For their investigations the researchers used a carbon fibre prepreg with epoxy matrix in combination with an epoxy film adhesive. The adherends had a QI layup and the specimens were tested under three different loading conditions: three-point bending, pure tension and axial tension combined with bending.

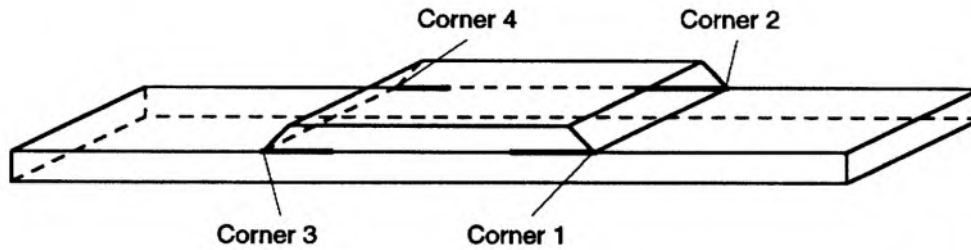


Figure 2.14: Skin-stringer bond line specimen with crack locations [44]

The reported damage patterns were observed in microsections after testing. In Fig. 2.14 the crack locations 1 to 4 are marked. Krueger et al. [44] observed a delamination in corner 1 and 4, running between 90°- and 45°-plies of the stringer part (flange), which was initiated by a matrix crack in the 90°-ply of the flange. At longer delamination length new matrix cracks branched in the 90°- and in the 45°-ply. In these locations no cracks occurred in the adhesive at all. The described damage pattern is sketched in Fig. 2.15 for illustration purposes.

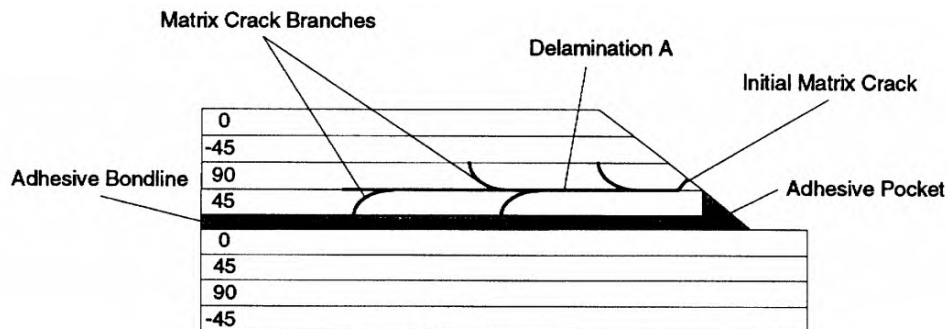


Figure 2.15: Skin-stringer bondline specimen: Typical damage patterns in corners 1 and 4 [44]

The typical damage pattern of the other two corners, 2 and 3, is shown in Fig. 2.16. At these corners a matrix crack formed in the 90°-ply of the flange and afterwards ran through the 45°-ply of the flange into the adhesive bond line. At the crack tip two delaminations formed and propagated over a long length until Delamination B1 stops and Delamination B2 still continued.

Scarf joints

Scarf joints with 0° UD carbon fibre-reinforced epoxy adherends bonded to each other with an epoxy film adhesive were investigated by Kumar et al. [45]. While shallow scarf angles predominately led to FF and fibre pull-out, specimens with steeper angles showed cohesive

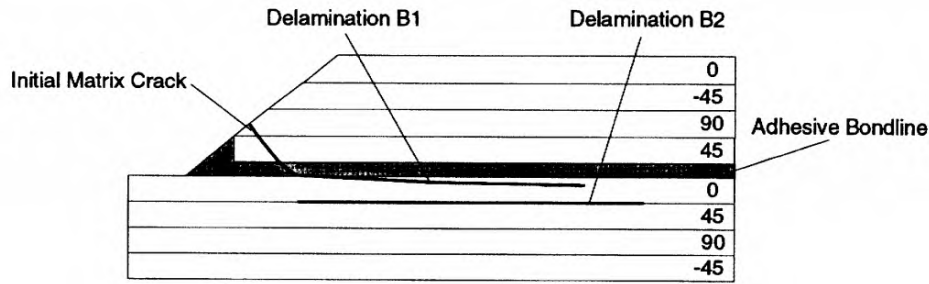


Figure 2.16: Skin-stringer bondline specimen: Typical damage patterns in corners 2 and 3 [44]

failure in the adhesive. This implicates that the damage pattern strongly depends on the scarf angle.

2.2.3 Implications for the design process

In all examples discussed above, damage in the composite adherends could be observed. Nevertheless, only some of the joint configurations developed damage in the adhesive itself. Furthermore, it can be noted that all types of composite damage phenomena (inter- and intralaminar) occurred. An introduction to the different composite damage phenomena can be found in the corresponding chapter in Section 4.2.5. In the single and double lap joints as well as in the skin-stringer-joints delaminations and matrix cracks were reported, whereas in the scarf joints also FF was noted. Only in the single lap joint study conducted by Kupski et al. [42] cracks in the adhesive led to final (cohesive) failure. Especially the study of Potter et al. [43] underlines that the occurring damage phenomena can have a large impact on the final failure mode according to ASTM D5573, cf. Fig. 2.5, and thus also on the achieved strength. Moreover, the types of damage occur in part simultaneously and may also interact with each other.

The studies illustrate that all phenomena must be considered in the design phase of bonded joints in composite structures. Furthermore, an understanding of the damage phenomena and failure mode is necessary to improve designs in this phase. The challenge is that failure mode and strength, as shown in Fig. 2.6 and Tab. A.1, depend on many design parameters.

2.3 Methods for the design-supporting prediction of the failure behaviour

In the design of aircraft structures, a distinction is made between structural sizing and detail design. Using a GFEM model with limited detail, also known as FEM loads model, in the structural sizing general design parameters such as the ply layup, the shape and the size of stiffeners as well as the stiffener spacing are defined. Sizing drivers are static strength, damage tolerance, durability as well as stiffness respectively deflection. The internal loads determined in the structural sizing are then used in the detail design to dimension structural details such as joints with regard to their load capacity and to assess

their potential failure modes. [16]

Since the design of bonded joints is part of the detail design, this work focuses on methods for detail design and the terms design and detail design are used as synonyms.

This subchapter reviews available methods that can support the engineer in the detail design process using analytical or numerical approaches. The analysis of the bonded joint can be divided into two aspects. On the one hand there are analytical-, numerical-, and respectively FEM-based approaches for predicting the stresses in the adhesive layer and the adjacent composite adherend. On the other hand there are failure models, which predict at which load the adhesive layer and/or the surrounding composite parts are overstressed and fail. The latter models use the stress and sometimes the strain fields determined with the former methods as input data.

The following overview is intended to show the capabilities as well as the limitations of the methods currently available and is not exhaustive. Extensive reviews of available methods to be used in the detail design can be found for example in [46], [47] and [48].

2.3.1 Determination of stresses and strains in bonded joints

The first analytical model for the prediction of stress distribution in the adhesive, known as shear-lag model, was developed by Volkersen in 1938 [49]. It was originally developed for riveted joints and only covers the shear stress distribution as it neglects effects due to rotation of the adherends. Furthermore, it assumes linear-elastic behaviour of the adherends as well as of the adhesive. In 1944, Goland and Reissner [50] were the first researchers to consider adherend rotation or secondary bending. Therefore, their solution also predicts the adhesive peel stress distribution. In contrast to the two aforementioned models, Hart-Smith takes into account the plasticity of the adhesive in shear in his analysis report of single and double lap joints for the National Aeronautics and Space Administration (NASA) from 1973 [51]. Five years later, Ojalvo and Eidinoff modified the model introduced by Goland and Reissner in order to predict the variation of shear stress through the bond thickness [52]. It needs to be considered that these classical analytical theories are based on beams and neglect the stresses in depth direction. Therefore, effects due to shear and normal stresses in this direction are not considered. However, these stresses can be of particular importance for fibre composites, as the stresses in depth direction, for example due to 45° plies, vary significantly.

Beyond the classical theories, there is a plethora of complex analytical theories that take into account a wide variety of effects in order to overcome the limitations mentioned above. An example of this is provided by Tsai et al. [53], who extend the classical theories by the normal and shear deformations in depth direction, thus enabling the consideration of anisotropic materials. Further theories that explicitly consider fibre composites adherends were developed by Wah [54], Yang and Pang [55] and Allmann [56] as well as Renton and Vinson [57]. The majority of theories assume linear-elastic material behaviour for both the adherends and the adhesive. In this context, the theories of Crocombe and Bigwood [58], Wang et al. [59] as well as Adams and Mallick [60], which are able to take plasticity into account, are mentioned without further explanation. In most cases, however, these models cannot be applied to fibre composites and do not have a closed-form solution. Therefore, they have to be solved numerically which diminishes the advantages of analytical solutions.

At this point, it should be emphasised that the models mentioned represent only a fraction of those available. A comprehensive overview is for example provided by da Silva et al. [61, 62].

A general limitation of the analytical solutions is that only simple geometries can be modelled. In addition to the aspect that modelling of adherends made of fibre composites and their failure is only possible to a limited extent, this leads to the fact that FEM-based approaches are preferable for the considered application.

The FEM-based evaluation of stresses and strains enables the consideration of more complex geometries as well as the use of a variety of material models for the adhesive and the composite adherend materials. Apart from the transversely isotropic properties of the fibre composites under consideration, the non-linear material behaviour of modern toughened epoxy-based composites, for example shown by Schäfer et al. [63], can also be taken into account. Similarly for adhesives, FEM-based approaches and, thus, the possibility of using more complex plasticity models make it possible to reproduce material behaviour more accurately. It is well-known that the plastic yielding of polymers in general is sensitive to hydrostatic pressure [64]. Wang et al. [65] show the pressure sensitivity in experiments for a rubber-toughened film adhesive commonly used in aerospace applications (FM73) and recommend using yield criteria which account for the influence of hydrostatic stresses.

2.3.2 Failure modelling approaches for adhesives and fibre composites

Models for evaluating the strength and failure behaviour of adhesive bonds and fibre composite structures are the subject of many scientific studies. These models can essentially be divided into three different categories: The Continuum Mechanics (CM), the Fracture Mechanics (FM) and the Damage Mechanics (DM) approach.

The CM approach is the most common approach in this context. Models based on this approach compare determined stresses or strains, sometimes also functions of the stress or strain field, with critical or allowable values. However, finding a universal strength or strain allowable is difficult due to the bi-material stress singularities inherent in composite bonded joints. When FEM is used for stress determination, the highest occurring value often depends on the choice of discretisation. [46]

To overcome these difficulties some authors suggest using stress or strain values at a certain distance from the singularities [66]. The challenge then is no longer the determination of the allowable itself, but the selection of a proper position where the stresses or strains are considered.

In CM it is assumed that structures and material are continuous. Discrete defects such as cracks are not represented. In FM, in contrast, the progression of discrete cracks is analysed. Failure is assumed when a critical energy release rate (cERR), a critical stress intensity factor or a critical crack tip opening displacement is reached [46]. With this energy-based approach, the stress singularity problem of the continuum mechanics approaches

can be overcome. Nevertheless, the assumption of an existing precrack is necessary. A common representative of the approach is the Virtual Crack Closure Technique (VCCT) [67].

In contrast to FM with the DM approach, however, it is possible to describe the complete failure behaviour of a structure including initiation and propagation by modelling the damage process in the material during damage evolution smeared over a finite region. The damage initiation is determined with stress- or strain-based criteria, whereas the propagation uses energy-based approaches. Thus, the problem of singularities is also circumvented. Unlike in FM, the assumption of an existing defect or crack is not necessary. The existing DM techniques can be divided into Local Damage Mechanics (LDM) and Continuum Damage Mechanics (CDM) approaches. [46]

In the case of the LDM approach, damage is localised to a zero-volume line or surface. It is used for interfacial failures like modelling delaminations between two composite plies [68] or debonding between adhesive and adherend [69]. With the CDM approach, the damage is smeared to a finite region, e.g. within a solid element, in order to model bulk failure [70] or cohesive fracture of an adhesive bond [71]. DM approaches can be considered as state-of-research [48]. The FEM-based approaches discussed below all use a representative of this failure modelling approach, called Cohesive Zone Modelling (CZM), without exception.

2.3.3 State of the art in FEM-based bonded joint failure prediction

This section focuses on publications about FEM-based approaches to predict the strength and failure behaviour of bonded composite joints. There are many publications in which a variety of approaches is used to predict the strength and failure behaviour solely of a fibre composite structure or only of an adhesive bond. These are not part of this overview. Only research work relating to bonded composite structures which models failure in the adhesive and in the adherends is included. A more detailed state-of-the-art review on FEM-based approaches for the representation of the composite adherends intra- and interlaminar mechanical behaviour up to failure as well as modelling of the adhesive bond is given in the corresponding chapters 4, 5 and 6.

Studies considering interlaminar and adhesive damage

The strength of specimens that fail purely cohesively can be predicted to a satisfactory standard. Yet, as soon as damage in the fibre composite adherend occurs damage models for the composite have to be incorporated in the model. Many studies consider only interlaminar damage, also called delamination, and neglect intralaminar damage such as fibre and matrix damage. Some selected examples are discussed below.

Kim et al. [72] studied the damage evolution in scarf joints under impact loading with experimental tests and numerical simulations. The specimens were made from an aerospace grade UD carbon epoxy prepreg (Cycom 970/T300) with a QI layup and a rubber-toughened epoxy film adhesive (Cytec FM300). After testing, ultrasonic C-scans of the specimens revealed intralaminar matrix cracking and delaminations as well as adhesive damage. Although matrix cracking was observed in the experiments the three-dimensional

numerical model only considered interlaminar and adhesive damage. Both using local CZM with different cohesive laws for adhesive and adherend. In general, Kim et al. [72] assess that adhesive disbonding and composite delamination predictions correlate well with the experiments. However, the numerically predicted force-time history was only accurate for the initial stiffness and the first peak force. The deviation between experimental and numerical results after the first force peak was attributed to the neglect of intralaminar damage.

Shang et al. [73] used the same modelling approach for interlaminar and adhesive damage as Kim et al. [72] but in a two-dimensional model to predict the failure loads of tension loaded single lap joints. The single lap joints made from carbon fibre epoxy prepreg were loaded in tension. Two series, one with a brittle and one with a tougher adhesive, were analysed. For both series, the predicted failure load was within the 95% confidence interval of the mean experimental failure loads. However, the specimens were not examined for intralaminar damage. In addition, stiffnesses or strains were not compared between experiments and numerical results.

In the study conducted by Campilho et al. [74] a combination of solid elements and an elasto-plastic material model with the local CZM technique was used to model plasticity and damage in the adhesive of single- and double lap joints. In addition, the models included interlaminar damage. The researchers studied the influence of major geometric parameters as well as several combinations of adherend thicknesses and stacking sequences. Furthermore, the mechanical parameters of the cohesive laws were modified in order to evaluate their impact on the failure behaviour. Nevertheless, the publication does not contain the comparison with experimental results and therefore no statement on the validity of the modelling can be made.

Overall, it cannot be deduced from the presented studies that limiting the modelling of damage in the composite to delaminations is a reasonable simplification. In the one study that examined intralaminar damage in the experimentally tested specimens, intralaminar damage occurred and deviations between experiment and simulation were attributed to the neglect of intralaminar damage in the simulation.

Studies considering intra-, interlaminar and adhesive damage

There are only a few, recently published studies in which FEM-based models were used to predict failure behaviour, which, in addition to damage in the adhesive, include both inter- and intralaminar damage models. An overview of these models can be found in Tab. 2.2. In each of the studies, only one general joint configuration was taken into account to validate the model. Leone et al. [75] considered splice joints in CFRP sandwich panels. CFRP single lap joints were analysed by Taotao et al. [76] and Sun et al. [77]. The former took Z-pins as a design feature for increasing strength into account. Goh [78] investigated scarf joints with dissimilar CFRP adherends. The aforementioned studies all applied a tensile load to the joint, while Liu et al. [79] considered stepped joints under bending. In all studies only failure loads as well as a visual failure mode assessment and no DIC data were used for validation.

Table 2.2: Comparison of publications considering intra-, interlaminar and adhesive damage

Year of publication	Leone et al. [75]	Goh [78]	Taotao et al. [76]	Sun et al. [77]	Liu et al. [79]
	2015	2015	2018	2019	2019
Analysis type	3D FEM (Solid elements)	3D FEM (Solid elements)	3D FEM (Shell elements)	3D FEM (Solid elements)	3D FEM (Solid elements)
Integration	Explicit	Explicit	Explicit	Explicit	Explicit
Intralaminar damage approach	CDM	CDM	CDM	CDM	CDM
Intralaminar damage initiation	LaRC03 (stress-based)	Hashin (stress-based)	Hashin (strain-based)	Hashin (strain-based)	Hashin (strain-based)
Intralaminar damage propagation	Energy-based stress-driven exponential softening	Energy-based stress-driven linear softening	Energy-based strain-driven exponential softening	Energy-based strain-driven linear softening	Energy-based strain-driven linear softening
Intralaminar plasticity	No	No	Non-linear shear behaviour with Soutis formula	No	No
Interlaminar damage approach	Zero-thickness cohesive elements	Cohesive elements	Finite-thickness cohesive elements	Zero-thickness cohesive elements	Zero-thickness cohesive elements
Adhesive plasticity	Superposition of two bilinear traction separation laws	No	No	No	No
Adhesive damage	Finite-thickness cohesive elements	Zero-thickness cohesive elements (only interface between adhesive and adherend)	Finite-thickness cohesive elements	Finite-thickness cohesive elements	Zero-thickness cohesive elements
Application	Splice joints in CFRP sandwich panels with honeycomb core	CFRP scarf joints with dissimilar adherends and with / without disbonds	CFRP single lap joints with varying ply stacking sequence and Z-pins	CFRP single lap joints with varying geometry and ply stacking sequence	CFRP stepped lap joint under three- and four-point bending
Validation	Failure load + visual failure mode assessment	Failure load + visual failure mode assessment	Failure load + visual failure mode assessment	Load-displacement curves + visual failure mode assessment	Failure load + visual failure mode assessment

An overview of the quality of the numerical predictions in the identified studies is shown in Tab. 2.3. The stiffnesses were only compared in two out of five publications. While the stiffness agrees well in Leone et al. [75], it can only be correctly predicted in two out of three cases in Liu et al. [79]. The range of the strength prediction is with an underestimation of about 10% to an overestimation of about 16% in an acceptable range. More inconsistent results are obtained when it comes to accurate prediction of the failure mode. The failure mode can be correctly predicted in only six out of nine cases. In one case the failure mode prediction is only possible to a very limited extent and in two cases not at all. In addition, it is not clear from the publications how much model calibration has been carried out. All in all, it can be said that some of the results are quite remarkable, but there are possibilities for improvement. This relates in particular to the chosen modelling approaches.

Table 2.3: Quality of the numerical predictions in the identified publications

Publication	Application	Variant	Consistency of numerical predictions with experiments		
			Stiffness	Strength (REC)	Failure mode
Leone et al. [75]	Splice joint	Conventional splice joint	Yes	10,6%, 14,7%	Yes
		Durable redundant joint	Yes	-0,7%, +6,9%	Yes
Goh [78]	Scarf joint	HexPly parent material	Not compared	Up to 15,7%	Yes
	Scarf joint	Cycom parent material	Not compared	Up to 10,1%	No
Taotao et al. [76]	Single lap joint	Various	Not compared	No force values given	Yes
Sun et al. [77]	Single lap joint	Various	Not compared	Up to 11%	Limited
Liu et al. [79]	Stepped lap joint	3pb, 100 mm	No	7,5%	No
	Stepped lap joint	3pb, 210 mm	Yes	-2,7%	Yes
	Stepped lap joint	4pb	Yes	-9,9%	Yes

The modelling strategies in the different publications are quite similar in the choice of approaches for the individual components of the joints. However, these approaches partly lag behind the state of research in the individual fields. This is explained in more detail in the following.

All authors use three-dimensional models combined with explicit FEM solvers to study the bonded joints. Leone et al. [75], Sun et al. [77], and Liu et al. [79] use a stacked solid approach for the composite adherends. Goh [78] models the laminate with a stacked continuum shell element approach, whereas Taotao et al. [76] use stacked conventional shell elements. In some studies, which investigate the modelling of composite laminates in FEM, authors report that consideration of the general three-dimensional stress state, thus the use of solid elements, increases the prediction accuracy [80, 81].

For modelling the intralaminar behaviour up to total failure it is deemed common sense to use CDM with a fracture toughness-based degradation. Except for Leone et al. [75], who use the LaRC03 criterion, the basic Hashin failure criterion is used to detect damage initiation. However, as shown in [82], the Hashin failure criterion is not able to model matrix damage with high accuracy. This is confirmed by the World-Wide Failure Exercise II (WWFE-II). It was shown that the failure criteria of Cuntze [83] and Puck [84] describe IFF with higher accuracy [85] than Hashin's theory.

It is noteworthy that the intralaminar plasticity has been neglected by all of the authors. Taotao et al. [77] at least model the non-linear shear behaviour using the Soutis formula [86]. This non-linear behaviour is completely reversible and does not account for plastic

deformations. In contrast, in the literature several experimental results can be found [87, 88, 89, 90], which show a distinct non-linearity prior to discrete damage like FF, IFF or delaminations. This observed non-linearity is caused by plasticity of the matrix material, fibre rotation, and microcracks. Therefore, it is often called pseudoplasticity, cf. Section 4.2.4.

In all studies the commonly accepted bilinear zero thickness element-based CZM approach with material properties from a $0^\circ/0^\circ$ interface is used to model delaminations. Yet, two effects which possibly limit the prediction accuracy are neglected. There may be an R-curve effect meaning an increase in cERR during crack growth, resulting in different values for initiation and propagation. It originates from micromechanical processes at the intersection of the fibres [91]. In addition, experimental investigations of multidirectional laminates suggest that there is an, at least moderate, effect of layup on the cERRs [92]. The values from $0^\circ/0^\circ$ interfaces appear to be conservative, but an interface dependant use of cERR values could improve the prediction.

For the adhesive modelling the CZM approach in combination with finite thickness cohesive elements is used. A true plasticity model that considers the plastic behaviour of the adhesive is not used in any of the studies. Only Leone et al. [75] use a superposition of two bilinear traction separation laws to model non-linear effects in the adhesive. In contrast, Jousset and Rachik [93] conclude in their work that the exclusive use of CZM to describe the constitutive behaviour of thin adhesive layers is only permissible if the occurring plastic flows are negligible. However, this is very difficult to predict especially if the simulation method should be capable to model very general loading conditions. Therefore, the use of a single cohesive zone for an entire adhesive layer is a strong simplification [94].

In principle, the studies show that the determination of strength and failure mode for bonded joints using PDA, even with strong simplifications, is possible. Nevertheless, almost all studies presented in this section focus on the illustration of the developed PDA method itself. A justified selection and trade-off between the advantages and disadvantages of the different aspects of the modelling strategy is not part of the studies. Furthermore, none of the studies provide guidance on how the necessary material parameters should be determined. To add, only Leone et al. [75] address the question how such PDA methods can be used in the design of bonded joints. They propose to use a sufficiently fine model, which is validated for bounding cases, to efficiently evaluate intermediate values of design parameters.

2.4 Chapter summary

The design of bonded joints in composite structures for aeronautic applications is considered a very challenging and complex task. Apart from certification requirements like the integration of design features that ensure a maximum disbond of the adhesive bond, there are also requirements from design methodologies. One possible example is the specification of a desired failure mode. As shown in this chapter, the failure mode as well as the strength of the joint depend on many parameters, which have to be specified during the design phase. The compliance with these requirements can in principle be shown by experimental tests or with the help of M&S.

In the absence of reliable M&S approaches, in practice the information on failure behaviour and type as well as residual strength required during detail design and certification are determined by physical tests [95]. As a result, only a very limited number of configurations can be investigated due to time and cost constraints. In order to reduce the number of these expensive and time-consuming tests, at least in part, there is a need for a validated M&S approach for virtual structural tests of bonded joints in composite structures. A capable analysis tool would increase the number of design variants which can be checked in the design phase, would simultaneously improve the understanding of the mechanical behaviour, would enable the virtual derivation of design guidelines and would pave the way towards more virtual testing in the context of certification. In the end, such an M&S approach could help to overcome the current challenges in adhesive bonding.

To implement an holistic M&S approach for a simulation-driven detail design and certification some specific requirements have to be met. Obviously, the approach has to be verified and thoroughly validated. The ability to reliably predict the correct failure mode as well as the stiffness and the strength of the bonded structure within specified boundaries has to be proven. In addition, the individual modelling strategy decisions for an holistic M&S approach must be justified in a comprehensible manner. This means that the selection process must be well documented, including the specification of model simplifications and assumptions as trade-offs between accuracy and numerical effort and their impact on the results. Furthermore, a M&S guideline or handbook not only containing information on modelling but also providing guidance on identification of the necessary material parameters must be provided to the staff performing M&S. Such a guideline should also contain application examples to illustrate the application of the M&S approaches.

However, as shown in this chapter, to the best knowledge of the author there is no M&S analysis approach available in literature, which meets the requirements summarised above. This is the reasons why progressive damage analyses cannot alleviate the challenges in the design of fibre composite bonded primary joints to date.

In order to help overcoming these challenges, a holistic simulation approach is developed within the scope of this thesis. The next chapter summarises the requirements for such a simulation-based design approach elaborated in this chapter, presents and discusses the related research and working hypotheses. Furthermore, the technical approach to develop the holistic simulation-based design approach and finally to test the mentioned hypotheses is presented.

CHAPTER 3

A simulation-driven design approach for composite bonded joints

How can the implementation of PDA as a tool in the design of fibre composite bonded joints be achieved?

In the following, at first the requirements for a simulation-driven design approach based on the shortcomings identified in Section ?? are summarised. Based on this information, the research as well as working hypotheses regarding the compilation of a new holistic PDA approach and its implementation in the design process are postulated. The chapter closes with a break-down of the research approach to answer the postulated hypotheses.

3.1 Requirements for a simulation-driven design approach

In the previous chapter it has been shown that besides the strength itself, the failure mode is a decisive factor in the design of fibre composite bonded joints. However, due to the lack of capable numerical analysis tools, the information regarding the failure mode is obtained by experimental testing. Since physical testing is complex and expensive, the consideration of different variants during design in particular and the use of bonded joints in aircraft structures in general is limited.

The present work is intended to help remove this obstacle by providing a tool to assess the mechanical behaviour during the design phase without the need of physical tests. Such a tool needs to capture all relevant damage phenomena, cf. Fig. 3.1, but must also be pragmatic, because otherwise it would not be suitable for regular use during design. As discussed in Chapter 2, the implementation of a holistic PDA tool is a promising approach to alleviate the challenges in the design. Furthermore, it was shown in Chapter 2, that to the best knowledge of the author none of the published methods fulfil the needs for a design-supporting prediction of the mechanical behaviour up to total failure.

The desirable major requirements for the development of a holistic PDA method in a simulation-driven design process, based on the examination of current research and identification of their shortcomings in Chapter 2, are:

- an accurate description of the mechanical behaviour of composite adherends and adhesive up to failure.
- the possibility to consider plasticity of both composite adherends and adhesive.

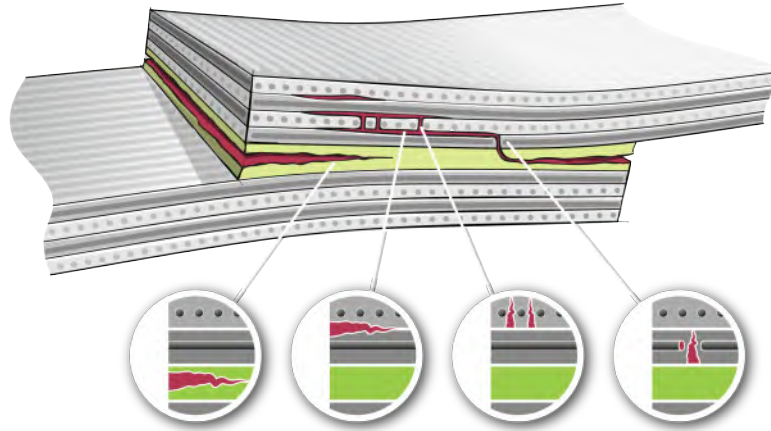


Figure 3.1: Damage phenomena in the fibre-reinforced polymers (FRP) adherends and in the adhesive layer (f. l. t. r.: crack in bondline, delamination, IFF, FF)

- the use of a three dimensional stress-based interactive phenomenological intralaminar failure criterion which is top ranked in World-Wide Failure Exercise I (WWFE-I) and WWFE-II.
- the modelling of intra- and interlaminar progressive damage.
- a possibility to use interface-orientation-specific interlaminar material data.
- the modelling of progressive damage in the adhesive.
- a demonstration of how the required material parameters can be determined and exemplary determination for one material each.
- the validation for different loadings and failure modes not only using strength and visually-assessed failure mode but also ultrasonic inspection and DIC data.
- the applicability for different (composite) materials.
- the ability to provide information regarding strength and failure mode needed during design.
- the provision of recommendations to choose individual model components for different application scenarios to ensure a well-balanced trade-off between accuracy and effort.
- the provision of an application example regarding how the holistic PDA approach can be used during design to derive design guidelines and reduce physical testing.

These requirements for the implementation of such a method in the design process lead to the following research and working hypotheses under the assumption of which this work is carried out.

3.2 Research and working hypotheses

The aim of this work is to provide a universal FEM-based PDA method that can be used to answer design questions and to develop design guidelines for bonded fibre composite

aircraft structures. Thus, it needs to be proven that:

Research hypothesis: A validated PDA approach taking into account all relevant occurring damage phenomena combined with carefully determined mechanical parameters enables the derivation of design guidelines for bonded joints in composite structures while reducing experimental tests to an absolute minimum.

The above research hypothesis is based on the assumption that besides the provision of a holistic progressive damage method itself, an idea for its use in the design process must be given and exemplified.

For a limited number of applications, previous studies have shown in principle that with PDA the determination of strength and failure mode for bonded joints is possible, cf. Subchapter 2.3. However, most of the studies presented in this section focus on the development of the PDA method itself. Only one of the studies [75] addresses the question how such methods can be used during design. Leone et al. [75] state that a sufficiently fine model, which is validated for bounding cases can be used to evaluate intermediate values of design parameters efficiently.

In this thesis, an attempt is made to go beyond a pure method for assessing intermediate design values. In addition to the development of the method itself, it will also be examined whether it can be usefully applied in the design context in order to derive guidelines answering specific question. With a specific example in the context of aircraft structural design, it is shown how the experimental testing for a design guideline can be reduced to a minimum by identifying the relevant test configurations with the holistic PDA approach. First of all, this requires a reliable and validated method for the numerical prediction of the mechanical behaviour up to total failure for the entire composite bonded joint. This leads to the first working hypothesis:

Working hypothesis I: Using a combination of selected mesoscale models for the intra- and interlaminar as well as the mechanical behaviour of the adhesive, each taking into account the progressive damage up to total failure, is a suitable approach to compile a holistic tool for analysing the strength and failure behaviour in the design process of fibre composite bonded joints.

Numerical analysis approaches can model the mechanical behaviour on different scales. The scales are referred to as micro-, meso- and macroscale. A brief introduction to the different scales applied to fibre reinforced composites can be found in Section 4.2.1. On the one hand, modelling the entire joint on the microscale is too expensive in terms of computation time since microscale models of small coupons from composite materials can only be solved with high computational effort [96]. On the other hand, models on the macroscale cannot capture all of the different damage phenomena and stress fields which are necessary to predict the correct failure mode, cf. Section 4.2.2.

This lead to a CDM- and CZM-based mesoscale modelling between the two aforementioned scales. Obviously, this type of modelling also has its disadvantages. It needs to be mentioned that the models for the different phenomena and constituents are not directly

coupled [97]. They interact only via the resulting stress and strain fields. Accordingly, there is no information exchange for example at (bi-)material interfaces to allow for crack migration. However, enhancing the approach to include such communication, or the use of approaches other than CDM- and CZM-based [97] ones, would again complicate and slow down the simulations so that they cannot be used as a pragmatic tool in design.

Therefore, two things must be shown in this thesis. Firstly, it needs to be assured that the selected model components fit together. This concerns in particular the modelling of the intra- and interlaminar behaviour of the composite adherends. Secondly, it must be proven that the combination of mesoscale models without direct coupling is sufficient and a valid approach which can be reproduced during validation and can later predict experimentally observed failure behaviour and strength. Hence, the second working hypothesis states that:

Working hypothesis II: The individual components of the holistic model, which have been verified and validated with high accuracy at the individual level, also show high accuracy for the entire composite bonded joint in the holistic PDA approach.

The majority of the studies discussed in the state-of-the-art Subchapter 2.3 only shows validation on the bonded joint level and no justification of the individual modelling choices is given. In addition, validation in the studies is performed by comparison of failure mode and strength only.

In this thesis, the verification and validation of the different PDA tools is performed isolated on the individual constituent level first. With the results for the individual components, recommendations for the different PDA tools used in the holistic approach are made. This leads to well-founded decisions for the holistic approach. After that, the modelling for each constituent is validated in the holistic model. At both levels, unlike the state of the art, DIC data is used to assess stiffness and to some extent strain fields. By doing so, validation does not only rely on strength and failure mode. This two-level selection and validation approach, first on the individual constituent level and then on the entire joint level improves the quality of the holistic method.

With this procedure, different modelling approaches are available for each individual component with an estimation of accuracy and computation time. This makes it possible to answer the third and final working hypothesis:

Working hypothesis III: The application-specific selection of the different model components in terms of accuracy, computational costs and effort for parameter identification results in a capable but pragmatic tool.

In M&S, a trade-off between accuracy and computational effort is always necessary. Yet, it needs to be considered that the most accurate tool will not be used if it is not affordable in terms of characterisation, modelling and computational effort.

To give an example, the most state-of-the-art FEM-based failure predictions, cf. Subchapter 2.3, neglect the plasticity of composite adherends and adhesive. This is a simplification in terms of characterisation effort and computational costs. However, it needs to be investigated how much the accuracy of the final method suffers from this simplification.

This kind of investigation is not performed in the aforementioned studies. Rather, the studies only show one final modelling approach.

For such simplifications it has to be shown how large the savings in terms of computational effort are and which costs in terms of accuracy will occur. To be able to assess this, different modelling approaches for the individual components have to be considered. In addition to plasticity, further examples considered in this work are the intralaminar failure criterion and the necessity of a distinct interlaminar damage model.

In this way, different holistic approaches can be compiled depending on the information required, the accuracy and the computational effort. By doing so, best practices for different applications can be provided.

3.3 Technical approach

The developed method should be as general as possible. Nevertheless, a reference material combination is needed for exemplary determination of material parameters, for verification and validation of the method and the application to an example design issue. This baseline material combination is the toughened thermoset composite material M21-T700GC from Hexcel and the Hysol EA9695 film adhesive from Henkel. Both materials are already in use in the aerospace industry.

In terms of software, the holistic PDA is developed on the basis of the commercial FEA software package Abaqus.

Chapters 4, 5 and 6 focus on the individual components of the holistic PDA.

In Chapter 4 the intralaminar behaviour is considered. Starting with an introduction to the state of the art, a modular user-defined intralaminar material model is developed and implemented. The needed material parameters are derived, and the different model variants are validated against Open Hole Tension (OHT) specimens. For the baseline material the needed tests are performed at DLR. For a second material, the procedure is followed based on literature data. Chapter 4 closes with first recommendations regarding composite modelling in the holistic approach.

Chapter 5 focuses on the interlaminar behaviour. Since most in-service structures have multidirectional layups, after a brief introduction to the state of the art, Chapter 5 puts the emphasis on characterisation of interface-orientation-specific material data. A verification is performed by simulating the characterisation experiments with the chosen approach. After that, with the help of the OHT specimens from Chapter 4 combinations of different versions of the user-defined intralaminar material model with the interlaminar modelling are under investigation. Based on the observations from the OHT simulations, recommendations for the holistic approach are made.

After a brief overview of the state of the art in adhesive modelling for strength prediction, in Chapter 6 three different CZM-based approaches are chosen to be investigated for the holistic model. The parameters needed for all three modelling approaches are identified for

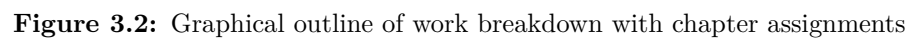
the baseline material. Then, a comparison of the models is conducted by applying them to previously experimentally-tested Thick Adherend Shear Test (TAST) specimens. With the information gained, recommendations for a fast as well as more accurate modelling approach for the holistic approach are given.

In Chapter 7 the entire holistic PDA is applied to bonded composite structures for the first time. Single Lap Shear (SLS) joint specimens are used to validate the compiled approach. For this purpose, a test series with specimens designed to fail in different failure modes is physically tested. The determined data is then used for validation under shear dominated loading. A final recommendation for two holistic approaches is made: a fast and a more accurate holistic modelling approach.

In Chapter 8 an application example for the use of the holistic PDA approach to answer a specific design question is presented. First, a brief overview of the state of the art in virtual testing as well as an introduction of the Multifunctional Fuselage Demonstrator (MFFD) as example structure is provided. This is followed by an introduction of the design questions regarding a bonded longitudinal fuselage joint of a single aisle aircraft. More specifically, the needed positioning tolerance is under investigation. The chapter closes with the results from the M&S with the holistic PDA as well as with a proposition for reduced physical testing in the context of the design issue.

Chapter 9 concludes the present work. A comparison of the achieved results with the hypotheses in this chapter is made. Finally, an outlook regarding potential future research is given.

A graphical outline of the technical approach is shown in Fig. 3.2.



CHAPTER 4

Intralaminar failure analysis of UD fibre reinforced composites

How should the intralaminar behaviour of the fibre composite adherends be modelled and how can the required material parameters be determined?

Since failure in the composite adherends is the desired failure mode for bonded joints in fibre composite aircraft structures, the numerical prediction of strength and failure behaviour is one of the most important factors for progress in the design of bonded joints. Hence, reliable numerical failure analyses of the adherends are needed to compile a holistic PDA tool for the whole joint.

Parts of this chapter have also been published in [6].

4.1 Structure and approach

This chapter focuses on the description of the mechanical behaviour up to total failure of the single plies, also referred to as intralaminar behaviour, in the FEM environment. Based on a literature study, a model to consider pseudoplasticity, a failure criterion and a degradation model are chosen. A user-defined material model for Abaqus/Standard (UMAT) and a user-defined material model for Abaqus/Explicit (VUMAT) with the previously selected components is implemented, verified, and validated. For this purpose, the required material parameters are determined experimentally. To conclude the chapter, a recommendation is made for the intralaminar modelling in the holistic model.

4.2 Representation of laminates for numerical analysis

Material models that are intended to realistically represent the behaviour of laminates, including their failure, must represent intra- and interlaminar damage mechanisms. Since the implementation of these numerous effects must bring together different theories and is thus a complex task, it is still being investigated by several researchers after decades. Numerical modelling of laminates, for example with FEM, can be done in different ways. This is explained below. Although this chapter focuses on intralaminar modelling, a modelling approach must be chosen that is compatible with interlaminar models and thus enables combination of the models in the later stages of this work.

4.2.1 Scales of a UD fibre-reinforced composite

It is noteworthy that laminates can be considered at various scales of increasing abstraction. In this work the terms micro-, meso-, and macroscale are used to describe the different scales [98, 99]. Fig. 4.1 shows the three scales which are briefly discussed in the following.

Microscale

On the microscale, the fibres and the matrix material of the composite are each described as separate materials with different mechanical behaviour. Due to the small scale, such models are only suitable for small sections of a ply, also referred to as representative volumes. These are used to investigate effects such as the propagation of cohesive matrix cracks or the debonding of fibre and matrix. Microscale analyses are suitable for determining smeared properties for the next higher scale, but not for investigating entire bonded structures, as intended in this work. An example for numerical investigations on the microscale using peridynamics, cf. Fig. 4.2, can be found in Rädcl et al. [96].

Mesoscale

One abstraction level higher, at the mesoscale, the single layer consisting of fibre and matrix is considered as a homogeneous, anisotropic material. The properties of fibre and matrix are smeared to stiffness and strength values for the entire considered volume of the single layer. These smeared properties can be determined by the aforementioned investigations on the microscale, by analytical mixture rules or by experimental tests on UD test specimens. The material behaviour on the mesoscale can be modelled three-dimensionally with an orthotropic material law. The principal material directions are in fibre direction (1), transverse to the fibre directions (2) and in through-thickness direction (3).

If transverse isotropy is applied, assuming the same properties in the transverse and thickness directions, the number of required parameters is reduced. In the case of linear-elastic material behaviour, only five independent material parameters are necessary. The modelling can be further simplified by assuming the plane stress state, as all stresses outside the 1-2 plane can then be neglected. Most of the failure criteria for fibre composites are formulated for this level of detail [99].

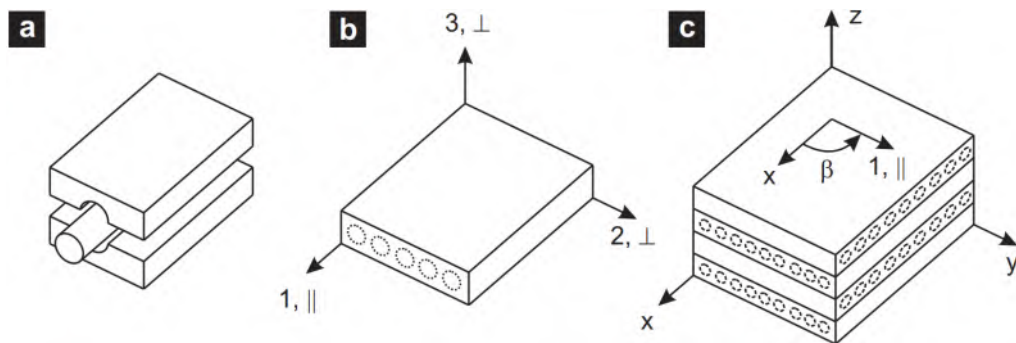


Figure 4.1: Scales of a UD fibre reinforced composite: (a) The micro-, (b) the meso-, and (c) the macroscale. [99]

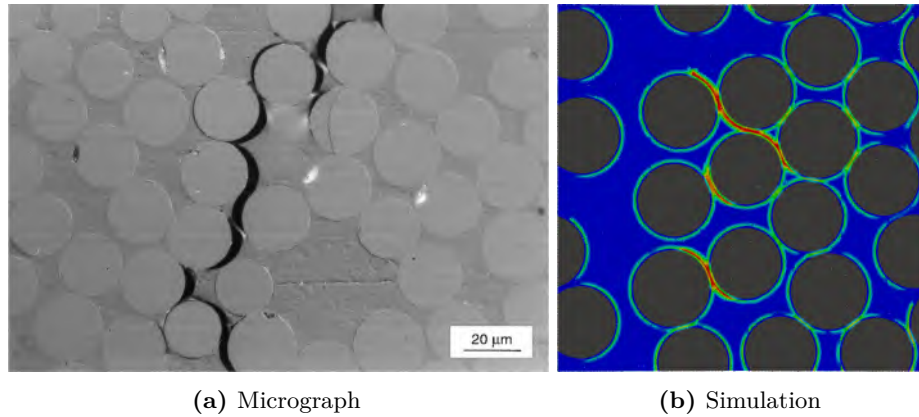


Figure 4.2: Transverse matrix cracks on microscale: Comparison of experimental investigation from Gamstedt and Sjögren [100] with peridynamic simulation from Rädcl et al. [96]

Macroscale

On the macroscale, the volume under consideration consists of a laminate of individual stacked plies with different fibre orientations. The individual quasi-homogeneous and orthotropic layers are perfectly bonded together. The global behaviour of the laminate is described by smeared properties, which can be calculated, either analytically or numerically, from the mesoscale properties of the single ply, the fibre orientations of the plies related to the laminate axes, and the geometry. Information on micro- and mesoscale are neglected. Analyses result in an average response of the whole laminate.

4.2.2 Modelling approaches in FEM

In principle, modelling at the meso- and macroscale seems suitable for the purpose in the present work. The following section gives an overview of the actual modelling approaches in FEM. Based on this overview, an approach is selected for the subsequent investigations and finally, for the holistic model.

Equivalent single-layer theories

Laminated structures typically have dimensions of small thickness in comparison to their lateral extent. This fact is the motivation for approaches that reduce the three-dimensional problem to a two-dimensional one [101].

This is achieved through assumptions regarding the deformation and stress distribution in the through-thickness direction of the laminate [102]. The thickness coordinate is eliminated by integrating along the thickness [103]. These approaches are called Equivalent Single-Layer Theories (ESLs) and allow the entire laminate to be represented with one element in thickness only. The stacking sequence as well as the thickness and orientation of the individual plies become a material property. ESLs can be classified according to their description of transverse shear stresses. In engineering applications, Classical Laminate Theory (CLT) and First-Order Shear Deformation Theory (FSDT) are the most widely used. The former theory is used for very thin laminates, while the latter is used for thicker laminates [102]. It needs to be mentioned that CLT relies on the Kirchhoff-Love hypotheses

[104]. Transverse shear and normal strains in the thickness direction are neglected. With the FSDT, based on the kinematic model of Mindlin [105] and Reissner [106], normal strains in the thickness direction are still neglected, but constant shear deformations induce interlaminar discontinuous and layer-wise constant transverse shear stresses [99].

Both of the aforementioned theories assume that plane cross sections remain perpendicular to the mean surface under deformation. This restriction is eliminated in the Higher-Order Shear Deformation Theory [107]. Some even remove the limitations of neglecting strain in the thickness direction by using fully three-dimensional constitutive laws. These models assume linear through-thickness strains [99]. However, in commercial FEM codes, composite modelling is based on CLT and FSDT [108].

All ESL approaches neglect through-thickness strains or assume them to be linear. Thus, they are not capable of fulfilling the requirements regarding the behaviour at the bi-material interface as stated by Carrera [109].

CLT requires that the displacement in through-thickness direction exhibits C_1 -continuity, the displacement as well as the derivatives must be continuous. In FSDT by contrast, transverse displacements require to be C_0 -continuous only [102]. Therefore, as Deuschle notes [99], the application of ESL models is actually strictly limited to the global structural behaviour [110, 111]. Nevertheless, stresses in the thickness direction and shear stresses can be determined with acceptable accuracy in post-processing calculations [112, 113, 114]. In this way, an evaluation of failure criteria, which are actually intended for the mesoscale, is possible with the ESL.

Layer-wise theory

The second, more detailed, approach is called Layer-Wise Theory (LWT). This theory is based on full three-dimensional anisotropic elasticity [102]. Each ply is discretised with at least one element in through-thickness direction and has its own material definition [99]. Accordingly, the orthotropic volume is modelled at the mesoscale.

Moreover, each ply has its own degrees of freedom. Therefore, unlike the ESL, only the displacement components are continuous through the thickness of a laminate. The displacement shows only C_0 -continuity in through-thickness direction [102].

The accuracy in thickness direction depends on the number of elements in this direction. Overall, this approach promises significantly more accurate results at the cost of significantly increased computation time, depending on the resolution. Furthermore, this approach allows the combination with models that can represent delaminations as discrete damages. For the aforementioned reasons, the LWT is followed in this work. In the subsequent sections, the element selection as well as the discretisation in thickness direction will be discussed.

4.2.3 Choice of element type

This section briefly discusses the advantages and disadvantages of the different element types in the context of composite modelling. A general description of the elements can be found for example in [115], or in the Abaqus manual [108].

Shell elements

General purpose shell elements (S4, S4R, S8R) are based on CLT or FSDT. Commercial FEM-solvers decide internally which theory is used depending on the thickness of the shell [108]. The thickness of the shell is given as a material property. Since z-stacking of shells is not recommended [99, 115], they are not suitable for a LWT modelling approach. For this reason, conventional shells are not further considered for the holistic modelling approach.

Continuum shell elements

Continuum shell elements (SC8R) combine the topology of solid elements with the kinematic of shells. They basically work like conventional shells but discretise an entire three-dimensional volume. The thickness is taken from the nodal coordinates and thus, the geometric representation. These elements are not only suitable for in-plane and bending problems but also for shear-dominated loadings perpendicular to the plane of the shell. Transverse shear stresses and even stresses in through-thickness direction can be calculated from the equilibrium conditions in post-processing. Unlike conventional shells, continuum shell elements have an unlimited z-stacking ability. [115]

Solid continuum elements

The accuracy of solid continuum elements (C3D8, C3D8R, C3D20, C3D20R) is based on balanced spatial dimensions. For this reason, they are usually not recommended for composite structures due to their low thicknesses compared to their lateral expansion. In addition, compared to shells they are computationally expensive [99].

However, solid continuum elements are frequently adopted in detailed analysis of composite structures. The discussion of the state of the art in FEM-based bonded joint failure prediction in the previous chapter revealed that four out of five studies use solid elements, cf. Tab. 2.2. This can be attributed to the following points:

No assumptions regarding the displacement, stress or strain fields are made. With an increasing number of elements in through-thickness direction, solutions using solid continuum elements converge to the requirements of Carrera [109]. The full three-dimensional stress state, including stresses in the through direction, can not only be calculated in post, but is part of the solution. This enables the implementation of truly three-dimensional failure and post-failure analysis of the composite plies in the holistic model [99].

In addition, stresses in the thickness direction in the laminate are expected in the case of bonded joints.

Comparison of FEM representations with Pagano's analytical solution

After selecting the LWT with continuum elements as the modelling baseline for the holistic model, the question remains which exact element type should be used and whether continuum shell elements are an alternative to solid continuum elements.

In his PhD-thesis Deuschle [99] compared different FEM laminate representations using the ESL as well as the LWT approach and also compared different element types with Pagano's analytical solution [116]. The material used in the study is 8552-IM7. Since this is one of the materials investigated in this work, the findings of Deuschle will be briefly summarised and the element choice in this work is made without further own analyses.

However, because the LWT modelling shall be used in this work, the summary of Deuschles results is focused on this.

Pagano's analytical solution is based on fully three-dimensional orthotropic material law and considers stresses and strains of the full 3D space. However, the Reissner kinematics [106] are not considered and therefore through-thickness shear stress from bending is not included. A sinusoidal load is applied to the top surface ($z = t/2$) of a simply supported rectangular plate. Along all edges, all cross-sections are supported and vertically fixed. This is shown in Fig. 4.3. The comparison between analytical solution and the different FEM representations is made based on the vertical displacement u_z .

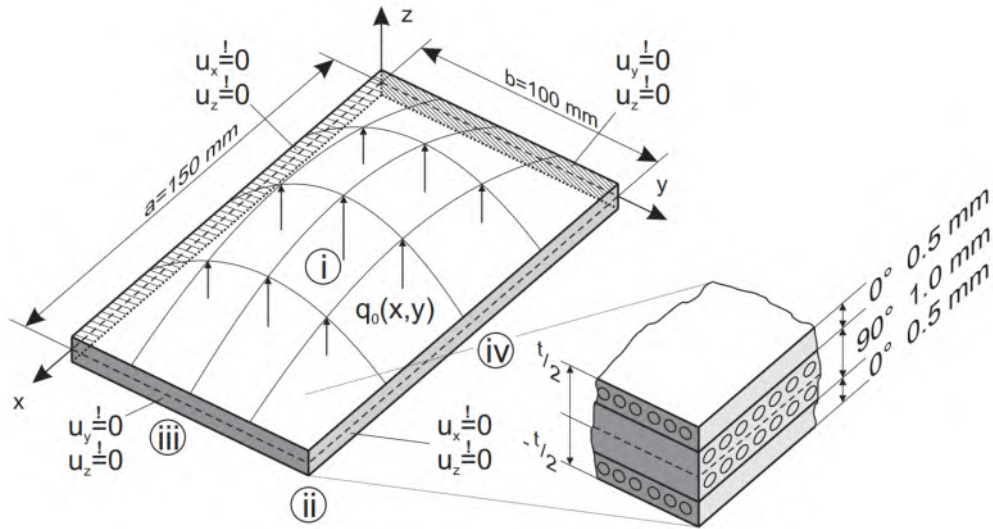


Figure 4.3: Pagano's analytical solution: Geometry, stacking sequence, load and displacement boundary conditions of the reference laminate plate. [99]

The analytical solution results in a vertical displacement of $u_z = 22.27 \text{ mm}$. Tab. 4.1 provides an overview of the results with the different element types and a lateral resolution of 20 by 30 elements. The z -discretisation is different and is described in the table. Additionally, the relative Central Processing Unit (CPU) time normalised with the CPU time of the S4R element is given.

Even though the focus in this work is on the LWT modelling, Deuschle's reference to the ESL approach and a reduced integrated shell element (S4R) as the simplest form of composite modelling is also retained as reference in this work.

Starting point of the considerations is the reduced integrated linear solid element (C3D8R) with one element across the thickness. With the lowest computational time of the LWT approaches (1.34), it yields a sufficiently accurate result of 22.61 mm. It is remarkable that the computation time only increases by 34% compared to the reference. The result of the continuum shell (SC8R) is slightly more accurate with 22.19 mm, however, with a value of 1.78, the computing time increases. The change to fully integrated solids (C3D8) brings a loss of accuracy with an increased calculation time. This results in a significant disadvantage compared to C3D8R.

The use of reduced integrated quadratic elements (C3D20R) improves the accuracy compared to C3D8 and C3D8R, but this comes with almost an eightfold increase in computing time. Fully-integrated quadratic elements are similarly accurate, but the computation time increases even further.

Increasing the discretisation to four elements per layer does not change the result with continuum shells, but increases the computation time to the level of square elements with one element across the thickness. Reduced integrated elements are unusable with four elements in the thickness direction due to the very large deviation from the Pagano solution. The same, though not quite as drastic, is the case for fully-integrated linear elements.

The solutions with the quadratic elements also show excellent accuracy with four elements across the thickness, but the computation time increases by a factor of up to 100 compared to the reference. Based on Deuschle's investigations, the C3D8R with a z-discretisation of one element is chosen as the basis in this work. In parallel, however, SC8R are also investigated in order to examine the differences between 2D and 3D representation of the stresses.

Table 4.1: FEAs of Pagano reference with different approaches, element types and through-thickness discretisations, R denotes to reduced integration, * to a quadratic ansatz. The Pagano analytical reference for the vertical displacement $u_z(a/2; b/2; -t/2)$ is 22.27 mm. [99]

material description	equivalent single layer			layer-wise			
z-discretisation	1 per laminate			1 per lamina		4 per lamina	
element family	shell	continuum shell	solid continuum	continuum shell	solid continuum	continuum shell	solid continuum
type	S4R	SC8R	C3D8R	SC8R	C3D8R	SC8R	C3D8R
	22.37	22.25	73.83	22.19	22.61	22.19	3.54
	1	1.14	2.07	1.78	1.34	8.65	7.35
	S4		C3D8		C3D8		C3D8
	22.34		30.93		18.35		15.46
	1.60		2.76		1.87		9.23
	S8R*		C3D20R*		C3D20R*		C3D20R*
	22.41		22.10		22.24		22.24
	2.01		4.94		7.32		86.37
			C3D20*		C3D20*		C3D20*
			22.19		22.23		22.24
			9.28		9.90		98.02
<i>relative CPU time</i>							

4.2.4 Pseudoplasticity

Several experimental findings reported in literature [87, 88, 89, 90], show a non-linearity prior to discrete damage such as FF and IFF or delaminations. This non-linearity originates from plasticity of the matrix material, fibre rotation, and microcracks, often described as pseudoplasticity. For example, Wang and Callus [87] observed a hyperbolic in-plane shear stress-strain relation in AS4/3501-6 $[\pm 45^\circ]_{4s}$ specimens tested under tensile loading. Van Paepegem et al. [88] tested specimens, made from Roviglas R17/475 glass fibre and Araldite LY 556 epoxy with a $[\pm 45^\circ]_{2s}$ layup, in a cyclic tensile loading process and found permanent deformations after unloading. Similar irreversible strains were observed by

Lafarie-Frenot and Touchard [89] when they tested $[\pm 45^\circ]_{2s}$ -specimens made from two different materials. One material was a thermoplastic fibre composite made from AS4/PEEK and the other material was a thermoset fibre composite made from T300/914. In addition, Vogler and Kyriakides [90] describe a non-linear stress-strain relationship in AS4/PEEK composite specimens loaded in shear, transverse compression and in an interaction of both loading cases. These findings underline that the modelling of pseudoplasticity should be investigated for the holistic PDA.

4.2.5 Types of failure at ply level

When considering the failure of FRP at the ply level, two forms of failure must be distinguished: FF and IFF.

FF refers to the tearing or breakage of fibres. In the case of quasi-static loading of the single layer, it is not only the breakage of individual elementary fibres or filaments that occurs, but rather a simultaneous failure of fibre bundles, in which tens of thousands of filaments break at the same time [117]. In an FF, a crack separates the fibres transversely to their longitudinal direction. It is noteworthy that FF occurs mainly due to tensile (FF1) and compressive (FF2) stress parallel to the fibres. The strength of a laminate against FF is very high when the load is increased rapidly until failure occurs, since the high cohesive strength of the fibre must be exceeded for an FF to occur. Macroscopically, cracked fibre bundles have the effect of a drop in stiffness [118].

IFF describes material separations in which the fibre bundles themselves do not tear, but cracks between the fibres form. These cracks usually run through the matrix material, but also along the interface between fibre and matrix. Whether the crack runs through the matrix material or along the fibre-matrix bond depends on whether the cohesive strength of the matrix or the adhesive strength between fibre and matrix is exceeded. In the case of an IFF, the UD layer is usually completely severed in thickness. The propagation of an IFF in the fibre direction depends on influencing variables such as the stress state and the homogeneity of the material. While an IFF in a UD layer can lead to total failure, in a laminate with several fibre directions an IFF does not. It damages the cohesion of the layers only locally. Nevertheless, an IFF leads to a local stress concentration, which, in turn, leads to delamination in a laminate, i.e., the separation of the individual layers, and to an increased probability of fibre breaks [117].

It needs to be mentioned that IFFs are differentiated by their causative stress. They can be caused by tensile (IFF1), compressive (IFF2) or shear load (IFF3). All failure modes mentioned above are shown in Fig. 4.4.

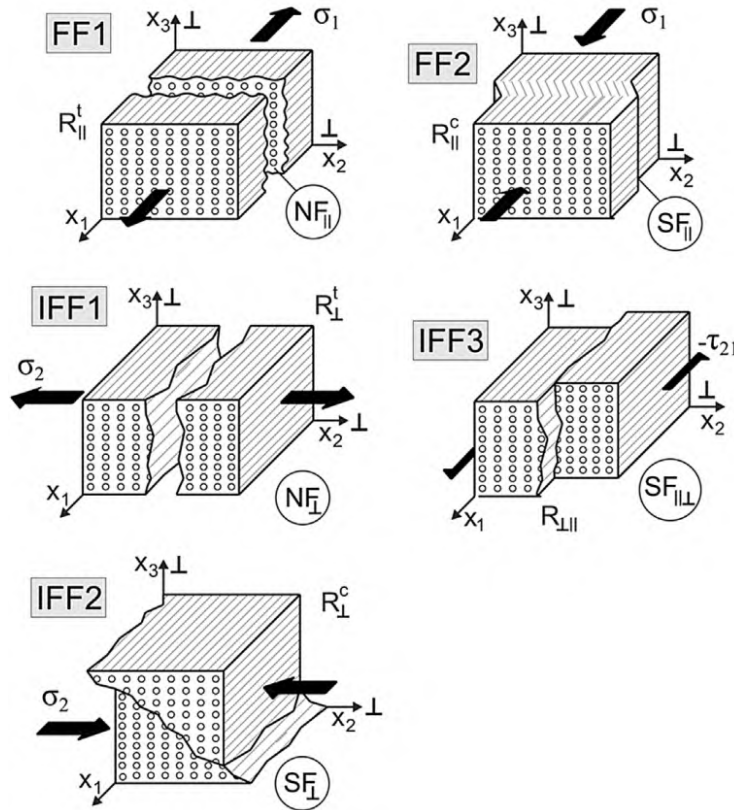


Figure 4.4: Observed failure modes for transversely-isotropic materials according to Cuntze. [119]

4.3 State of the art in mesoscale numerical modelling of fibre-reinforced composites

Analysis approaches used for mesoscale numerical modelling of fibre-reinforced composites often assume laminate failure at first ply failure. This leads to a very conservative design since fibre composite structures can carry further loads after initial damage [120]. In order to achieve an efficient and reliable design of structures, the mechanical behaviour up to total failure has to be considered in the design phase. Thus, simulation approaches for design should include damage initiation by various failure modes under complex loading as well as damage progression.

Most of the constitutive models consider composites on the mesoscale, i.e., ply by ply, and are based on CDM. The models are usually divided into three parts: A model for the mechanical behaviour prior to damage initiation, a failure criterion to be able to detect damage initiation, and a description of the mechanical behaviour in the post-failure regime [121]. Many CDM-based models for composites have been developed in the past [122]. In order to give a brief overview, a few selected models are discussed below.

Simple PDA models combine a linear-elastic constitutive formulation with a set of failure criteria for the different intralaminar failure types and a constant stiffness degradation, also called sudden degradation, after failure initiation [123, 124, 125]. A representative of

this model class, in this case with the failure criterion of Hashin [126], is used by Hühne et al. [127] to perform a PDA of composite bolted joints. However, the majority of models uses gradual degradation models [80, 128, 129]. These degradation models describe the decrease in stiffness due to damage as a linear or exponential function, which depends on the corresponding cERR. The main difference between the investigated models is the set of failure criteria used to detect failure initiation and whether they are formulated for the plane stress state or for the three-dimensional case. In the models mentioned above, for example, the failure criteria of Puck [130], Tsai-Wu [131], or the LaRC03-04 criterion [132] are used. All of the previously mentioned models assume linear-elastic mechanical behaviour prior to damage initiation.

The section on pseudoplasticity earlier in this work, cf. Section 4.2.4, shows that the assumptions of a linear-elastic behaviour prior to damage is not valid for many FRP composite materials. For this reason, a material model is required that also takes this non-linearity prior to damage initiation into account. Lüders et al. [133] developed a model for fatigue lifetime predictions using the three-dimensional failure criterion by Puck, which considers pre-failure non-linearities of the matrix. The non-linear relation between the shear stress τ and the shear strain γ is defined by an exponential function. A similar approach to describe the non-linear behaviour in shear is used by Donadon et al. [134], but instead of an exponential a polynomial cubic stress-strain relationship was applied. However, both models only consider a non-linearity prior to damage initiation for the shear components. A model with a different approach for modelling plasticity is described by Ernst et al. [135]. In their multiscale approach the plasticity is modelled on the micromechanical scale, where the behaviour of fibre and matrix is described with different material models. For the matrix, an isotropic plastic flow potential depending on the first two stress invariants is used. The non-linear stress-strain relationships are then applied in meso- and macromechanical analyses. Vogler et al. [136] use a non-associated flow rule to account for the pre-failure non-linearities. However, six yield surface parameters and three plastic potential parameters are necessary for the model to describe the material behaviour.

In contrast, a transversally isotropic plasticity model with an associative flow rule was introduced by Sun and Chen [137]. The composite material is assumed to be linear-elastic in fibre direction and only one coefficient is needed to describe the anisotropy in the plasticity. In total only three parameters are necessary. Due to its simplicity, this model was used by Chen et al. [121] and Din et al. [138] in combination with Hashin's and Puck's failure criterion respectively. Both models showed good results in the validation, but assume a plane-stress state and can therefore only be used with shell elements. Some authors report that the consideration of the general three-dimensional stress state increases the prediction accuracy [80, 81]. To add, as shown in [82], the Hashin's failure criterion does not describe the matrix damage with high accuracy. This is underlined by the WWFE-II, which showed that the failure criteria of Puck and Cuntze are able to describe those failure modes with higher accuracy [85] than the theory of Hashin. For this reason, Din et al. [138] use Puck in combination with the one parameter plasticity model of Sun and Chen. However, the Failure Mode Concept (FMC) of Cuntze [83] has the advantage over Puck [130] that no computational expensive iterative fracture angle search is needed for IFF.

The provision of a material model, unlike [121] and [138], for the general three-dimensional case with the plasticity model of Sun and Chen in combination with Cuntze's less computational-intensive failure criterion is not yet available and this can be seen as the motivation for a new material model developed specifically for the holistic PDA.

4.4 A 3D anisotropic damage / plasticity coupled continuum damage mechanics model

At the time of development of the material model, the experimental data of the baseline material M21-T700GC for testing and verification of the material model were not yet fully available. For this reason, the development is based on literature data and the thermoplastic material AS4/PEEK. From Subchapter 4.5 on, the material parameters of M21-700GC and 8552-IM7 are determined and compiled. This is followed by a validation of the material parameters on the basis of OHT test specimens.

4.4.1 Constitutive model

The proposed material model can be divided into four components: Linear-elastic behaviour (1), plastic behaviour (2), damage initiation (3), and damage progression (4). These components are illustrated in the stress-strain plot in Fig. 4.5.

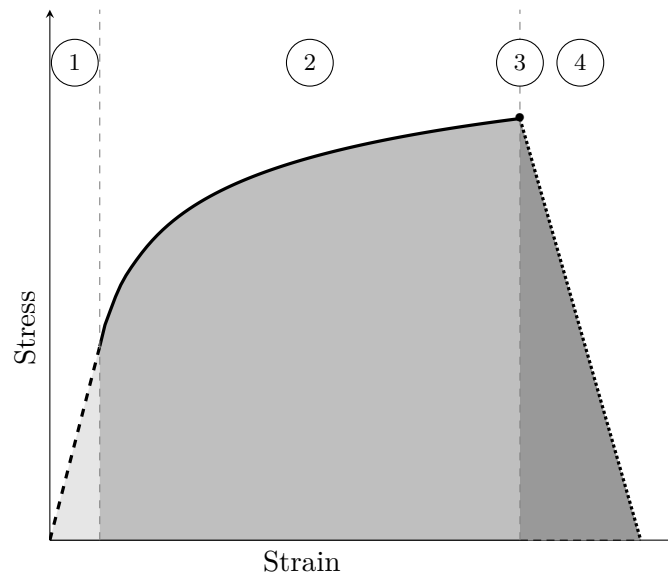


Figure 4.5: Stress-strain curve showing individual components of the proposed material model

The following section, which briefly describes the theories behind the individual components, is structured on the basis of this division.

The material model developed in this work will be used to analyse macroscopic structures. Accordingly, no discrete damage is modelled in the individual ply of the composite, but the approach of smeared damage according to Kachanov [139] is used. Under the assumption that the damage in the area under consideration is isotropic, it is assumed that the area

available for the transfer of loads A_{eff} decreases in comparison with the undamaged area A_0 . Based on this consideration an effective stress $\tilde{\sigma} = P/A_{eff}$ can now be defined to substitute the nominal stress $\sigma = P/A_0$. When damage has occurred, the effective stress $\tilde{\sigma}$ is higher than the nominal stress σ at constant load P .

In accordance with the smeared damage of Kachanov [139], Matzenmiller et al. [140] describe a damage model for an orthotropic single ply, which is used by the majority of recent CDM models for fibre composites. Therefore, it is also adopted in this work. A damage operator $\mathbf{M}(d)$ is defined, which establishes the relationship between the effective and the nominal stress:

$$\tilde{\sigma} = \mathbf{M}(d) \cdot \sigma \quad (4.1)$$

The damage operator or lamina damage tensor used in this work is constructed as follows:

$$\mathbf{M}(d) = \text{diag} \left[\frac{1}{1-d_f}; \frac{1}{1-d_m}; \frac{1}{1-d_m}; \frac{1}{1-d_s}; \frac{1}{1-d_s}; \frac{1}{1-d_m} \right] \quad (4.2)$$

In this case, d_f is the damage variable associated with FF. The damage variables d_m and d_s are associated with matrix failure under transverse respectively shear loading. These scalar damage variables take values between 0 and 1, where 0 represents the undamaged and 1 the completely damaged state. In the implementation, the values for d are limited to 0.99 in order to avoid division by zero. In addition, the damage variables d_f and d_m distinguish between damage from tensile and compressive stresses. The following relationships are used to determine a smeared damage variable from the two loading types:

$$d_f = d_{ft} + d_{fc} - d_{ft} \cdot d_{fc} \quad (4.3)$$

$$d_m = d_{mt} + d_{mc} - d_{mt} \cdot d_{mc} \quad (4.4)$$

A detailed derivation of equations 4.3 and 4.4 can be found in [80]. Due to the plasticity in the composite material, the total strain tensor ϵ results in the sum of the elastic strain tensor ϵ^e and the plastic strain tensor ϵ^p :

$$\epsilon = \epsilon^e + \epsilon^p \quad (4.5)$$

$$\tilde{\sigma} = \mathbf{C}_0 \cdot \epsilon^e; \quad \sigma = \mathbf{M}(d)^{-1} \cdot \mathbf{C}_0 \cdot \epsilon^e \quad (4.6)$$

$$\begin{bmatrix} \sigma_{11} \\ \sigma_{22} \\ \sigma_{33} \\ \tau_{12} \\ \tau_{13} \\ \tau_{23} \end{bmatrix} = \begin{bmatrix} C_{1111} & C_{1122} & C_{1133} & 0 & 0 & 0 \\ & C_{2222} & C_{2233} & 0 & 0 & 0 \\ & & C_{3333} & 0 & 0 & 0 \\ & & & C_{1212} & 0 & 0 \\ & sym. & & & C_{1313} & 0 \\ & & & & & C_{2323} \end{bmatrix} = \begin{bmatrix} \epsilon_{11}^e \\ \epsilon_{22}^e \\ \epsilon_{33}^e \\ \gamma_{12}^e \\ \gamma_{13}^e \\ \gamma_{23}^e \end{bmatrix} \quad (4.7)$$

The components of \mathbf{C}_0 are:

$$C_{1111} = E_{11}(1 - \nu_{23}\nu_{32})\Gamma \quad (4.8)$$

$$C_{2222} = E_{22}(1 - \nu_{13}\nu_{31})\Gamma \quad (4.9)$$

$$C_{3333} = E_{33}(1 - \nu_{12}\nu_{21})\Gamma \quad (4.10)$$

$$C_{1122} = E_{11}(\nu_{21} - \nu_{31}\nu_{23})\Gamma = E_{22}(\nu_{12} - \nu_{32}\nu_{13})\Gamma \quad (4.11)$$

$$C_{1133} = E_{11}(\nu_{31} - \nu_{21}\nu_{32})\Gamma = E_{33}(\nu_{13} - \nu_{12}\nu_{23})\Gamma \quad (4.12)$$

$$C_{2233} = E_{22}(\nu_{32} - \nu_{12}\nu_{31})\Gamma = E_{33}(\nu_{23} - \nu_{21}\nu_{13})\Gamma \quad (4.13)$$

$$C_{1212} = G_{12} \quad (4.14)$$

$$C_{1313} = G_{13} \quad (4.15)$$

$$C_{2323} = G_{23} \quad (4.16)$$

with

$$\Gamma = \frac{1}{1 - \nu_{12}\nu_{21} - \nu_{23}\nu_{32} - \nu_{13}\nu_{31} - 2\nu_{21}\nu_{32}\nu_{13}} \quad (4.17)$$

4.4.2 Plasticity model

Like mentioned above, the plastic strain ϵ^p represents all irreversible deformations. The portion of plastic strain in the total strain and the stress corrected for plasticity are determined using a transversally isotropic plasticity model with an associative flow rule. Sun and Chen describe a plastic potential for anisotropic fibre composite materials [137]. Under the assumption of transverse isotropy in the 2-3 plane and linear-elastic behaviour in fibre direction $d\epsilon_{11}^p = 0$, the plastic potential f for the three-dimensional case results to [141]:

$$f(\sigma_{ij}) = \frac{1}{2} [(\sigma_{22} - \sigma_{33})^2 + 4\tau_{23}^2 + 2a(\tau_{13}^2 + \tau_{12}^2)] \quad (4.18)$$

The parameter a in Eq. 4.18 weights the in-plane shear behaviour. This plastic potential was established based on Sun and Chen's observations [137] on micromechanical models, suggesting that only hydrostatic stresses cause plastic deformation. Eq. 4.19 describes the comparison between the yield limit $\bar{\sigma}_y(\tilde{p})$ and the effective stress $\bar{\sigma} = \sqrt{3f}$ in order to

distinguish between the elastic and the plastic domain:

$$f(\tilde{\sigma}, \tilde{p}) = \sqrt{3f} - \bar{\sigma}_y(\tilde{p}) \leq 0 \quad (4.19)$$

The plastic potential can also be expressed in matrix/vector notation using the mapping matrix \mathbf{P} , cf. [142], which is used in the UMAT implementation in this publication:

$$F(\tilde{\sigma}, \tilde{p}) = \frac{1}{2} \tilde{\sigma}^T : \mathbf{P} : \tilde{\sigma} - \bar{\sigma}_y^2(\tilde{p}) \quad (4.20)$$

For the plastic potential in Eq. 4.18, the mapping matrix \mathbf{P} reads:

$$\mathbf{P} = \begin{bmatrix} 0 & 0 & 0 & 0 & 0 & 0 \\ & 3 & -3 & 0 & 0 & 0 \\ & & 3 & 0 & 0 & 0 \\ & & & 6a & 0 & 0 \\ & sym. & & & 6a & 0 \\ & & & & & 12 \end{bmatrix} \quad (4.21)$$

Taking into account the associated flow rule, the incremental plastic strain components can be expressed in terms of the plastic potential f where $d\lambda$ is the plastic multiplier:

$$d\epsilon_{ij}^p = \frac{\partial f}{\partial \sigma_{ij}} d\lambda \quad (4.22)$$

From Eq. 4.18, it can be seen that plastic strains are considered in all components except for the fibre direction. As stated by Weeks and Sun [141], experiments have shown that FRP materials with a non-linear behaviour prior to damage, like thermoplastic fibre composites, do not have a defined yield point. Therefore, the yield limit $\bar{\sigma}_y(\tilde{p})$ is a function of the accumulated plastic strain \tilde{p} , which increases with load. Hence the plasticity is completely irreversible. Using a hardening law exponent α and the coefficient β , the function for the yield limit follows to:

$$\bar{\sigma}_y(\tilde{p}) = \beta \cdot (\tilde{p})^\alpha \quad (4.23)$$

By combining the models described, the plastic behaviour of a transversally isotropic material can therefore be described with only three parameters. These parameters can be determined with off-axis tensile tests as shown in [137], [141] and [143]. Due to its simplicity, the model was adopted by different authors in their elastoplastic CDM-based models [121, 138, 141] and also finds application in this work.

4.4.3 Damage initiation and propagation

In order to predict discrete damage, like FF and IFF, at the ply level, a suitable interactive, phenomenological and three-dimensional stress-based failure theory has to be incorporated in the model. Within the framework of the WWFE-II, the predictive capabilities of 3D failure criteria for FRPs were compared [85]. The WWFE-II identified the FMC by Cuntze [83] as one of the criteria with a high predictive performance. In addition to the FMC, the Action Plane Strength Criterion (APSC), originally formulated by Puck and adapted by Deuschle also shows high capabilities [84, 144]. However, the APSC requires an additional algorithm to determine the angle of fracture respectively the plane of the potential interfibre fracture. Due to this, Cuntze's FMC is the main failure theory used in this work and will be briefly discussed in the following. Puck's APSC is implemented for comparison and described in the next section.

Cuntze's Failure Mode Concept

The FMC is characterised by the basic idea of separating failure modes, which describe certain failure mechanisms. Each failure mechanism is covered by an individual failure criterion, which is associated with only one material strength. For each of the failure modes, an individual material stressing effort E_{ff} is calculated. This stressing effort is defined as the inverse of the stress-based reserve factor f_{res} [145]. The interaction of these different modes finally provides the global material stressing effort in the form of a sum equation [146]. Five different failure modes are distinguished. Similar to Hashin's criterion [126] or the APSC [144], Cuntze's FMC also differentiates FF and IFF. These modes are further distinguished according to the state of stress that causes failure. Thus, for FF, two modes, which originate from tensile (FF1) and compressive (FF2) stresses exist. Furthermore, three IFF modes are caused by tension (IFF1), compression (IFF2), and shear (IFF3) loading. The version of the FMC used in this work is published in [119]:

$$FF1 : E_{ff}^{\parallel\sigma} = \sigma_{eq}^{\parallel\sigma} / R_{\parallel}^t \text{ with } \sigma_{eq}^{\parallel\sigma} = \sigma_1 \quad (4.24)$$

$$FF2 : E_{ff}^{\parallel\tau} = \sigma_{eq}^{\parallel\tau} / R_{\parallel}^c \text{ with } \sigma_{eq}^{\parallel\tau} = \sigma_1 \quad (4.25)$$

$$IFF1 : E_{ff}^{\perp\sigma} = \sigma_{eq}^{\perp\sigma} / R_{\perp}^t \text{ with } \sigma_{eq}^{\perp\sigma} = \left[(\sigma_2 + \sigma_3) + \sqrt{(\sigma_2 + \sigma_3)^2 + 4\tau_{23}^2} \right] \quad (4.26)$$

$$IFF2 : E_{ff}^{\perp\tau} = \sigma_{eq}^{\perp\tau} / R_{\perp}^c$$

$$\text{with } \sigma_{eq}^{\perp\tau} = \left[b_{\perp\perp} \cdot \sqrt{(\sigma_2 + \sigma_3)^2 + 4\tau_{23}^2} + (b_{\perp\perp} - 1) \cdot (\sigma_2 + \sigma_3) \right] \quad (4.27)$$

$$\begin{aligned}
IFF3 : Eff^{\perp\parallel} &= \sigma_{eq}^{\perp\parallel} / R_{\perp\parallel} \\
\text{with } \sigma_{eq}^{\perp\parallel} / R_{\perp\parallel} &= \left(\left[\sqrt{b_{\perp\parallel}^2 \cdot I_{23-5}^2 + 4 \cdot R_{\perp\parallel}^2 \cdot (\tau_{13}^2 + \tau_{12}^2)^2} + b_{\perp\parallel} \cdot I_{23-5} \right] / (2 \cdot R_{\perp\parallel}^3) \right)^{\frac{1}{2}} \\
\text{and } I_{23-5} &= 2\sigma_2 \cdot \tau_{12}^2 + 2\sigma_3 \cdot \tau_{13}^2 + 4\tau_{23}\tau_{13}\tau_{12}
\end{aligned} \tag{4.28}$$

The various failure modes can be combined to form a global criterion for failure in laminates. The interaction of the individual failure modes to a global material stressing effort Eff^m is described with the interaction exponent m . This parameter m interacts with the single failure modes based on probabilistics. The global material effort Eff^m results in:

$$Eff^m = \sum_1^5 Eff^{mode} = \left(\frac{\sigma_{eq}^{\parallel\sigma}}{R_{\parallel}^t} \right)^m + \left(\frac{\sigma_{eq}^{\parallel\tau}}{R_{\parallel}^c} \right)^m + \left(\frac{\sigma_{eq}^{\perp\sigma}}{R_{\perp}^t} \right)^m + \left(\frac{\sigma_{eq}^{\perp\tau}}{R_{\perp}^c} \right)^m + \left(\frac{\sigma_{eq}^{\perp\parallel}}{R_{\perp\parallel}} \right)^m \tag{4.29}$$

As can be seen from the equations of the individual failure modes, no fracture angle is included because the stress invariants do not change with rotation or other transformation of the coordinate system. For this reason, the iterative search for the fracture angle, which is necessary in the APSC, is not required. This increases the computational efficiency of the FMC compared to the APSC.

It needs to be mentioned that if the global material stressing effort determined with the FMC reaches 1 at an integration point, further loading will cause a degradation of the material stiffnesses. Hence, a gradual damage development is activated at the integration point under consideration. First, the stiffnesses associated with the failure mode, which has the highest single effort, are degraded. As soon as further individual efforts reach 1, the corresponding stiffnesses are also degraded. The assignment of the failure modes to the stiffnesses can be found in Tab. 4.2.

Table 4.2: Assignment of failure modes to damage variables

Failure mode	$FF1$	$FF2$	$IFF1$	$IFF2$	$IFF3$
Damage variable	d_{ft}	d_{fc}	d_{mt}	d_{mc}	d_s

In the relevant literature, many degradation models control the damage progression with the evolution of the failure indices of the damage initiation criteria [80, 121, 128, 129, 138]. Since most failure criteria are stress-based, as suggested by Rohwer [147], the development of damage is also indirectly stress-based. If, as in this work, the plasticity of the material is taken into account, the maximum effective stresses, apart from $\tilde{\sigma}_{11}$, are limited by the yielding of the material. In turn, this also limits the damage variables. On this account the evolution of the damage variables is controlled by displacement in this work.

As soon as damage occurs in the fibre composite, the strain is no longer distributed

smoothly, but varies in local areas. Characteristically, the strain increment is then localised in a small zone due to local damage, while the strain in a major part of the structure is diminishing [148]. As a result, numerical models to describe failure behaviour must correctly reflect the energy dissipated in the fracture process zone. This is not the case in standard FE theory. As shown by Jirásek [149], the dissipated energy decreases with a refinement of the mesh to very small values. This results in a strong mesh dependency of the solution. In particular, smaller element sizes do not necessarily lead to a better converged solution. To remedy this, the Crack Band Approach (CBA) by Bažant and Oh [150] is used. With this approach, the computed dissipated energy is regularised using a characteristic length of the finite element L_c :

$$g_M = \frac{G_M}{L_c} \text{ with } M \in \{ft, fc, mt, mc, s\} \quad (4.30)$$

In this equation, G_M is the fracture toughness in the mode M and g_M is the dissipated energy per unit volume. As can be seen in Section 4.4.5 this approach cannot completely resolve the mesh dependency, but significantly mitigates it and is also straightforward to implement. Therefore, it is used in several other damage descriptions proposed for composites [82, 121] and also in this work. To this end, the strain-controlled degradation model with CBA from Lapczyk and Hurtado [82] is adapted for use with the FMC. Each damage variable is calculated with the following equation:

$$d_M = \frac{\delta_{M,eq}^f (\delta_{M,eq} - \delta_{M,eq}^0)}{\delta_{M,eq} (\delta_{M,eq}^f - \delta_{M,eq}^0)} \text{ with } \delta_{M,eq}^0 \leq \delta_{M,eq} \leq \delta_{M,eq}^f \quad (4.31)$$

The equivalent strain $\delta_{M,eq}^0$ describes the initiation of damage with the relationship

$$\delta_{M,eq}^0 = \frac{\epsilon_M^0}{L_c} \quad (4.32)$$

where L_c is the characteristic element length of the element under consideration. The equivalent strain at total failure $\delta_{M,eq}^f$ which corresponds to $d_M = 1$ is calculated with:

$$\delta_{M,eq}^f = \frac{2G_M}{\sigma_M^0 L_c} \quad (4.33)$$

The stresses and strains at damage initiation (σ_M^0 and ϵ_M^0) are not known a priori in Cuntze's FMC. Therefore, these measures are saved in the material routine during runtime when damage is initiated. In the IFF modes damage can be caused by multiple stress components. In this case, the component with the highest stress is used to control the degradation.

Puck's Action Plane Strength Criterion

A version of the proposed material model with Puck's failure theory is used to compare it to Cuntze's FMC. At this point, Puck's theory will only be discussed briefly. For detailed information see [130] and [99]. In this work the theory described in VDI 2230 [151] is adopted. In Puck's APSC two stressing efforts are calculated. One effort for FF $f_{E(FF)}$ and one for IFF $f_{E(IFF)}$. Taking into account the strength in fibre direction in tension R_{\parallel}^t and compression R_{\parallel}^c , the former is calculated with the following equations:

$$f_{E(FF)} = \frac{\tilde{\sigma}_{11}}{R_{\parallel}^t} \quad (4.34)$$

$$f_{E(FF)} = \frac{\tilde{\sigma}_{11}}{-R_{\parallel}^c} \quad (4.35)$$

The equations providing the stressing effort for IFF $f_{E(IFF)}$ require stresses transformed to the action plane as an input. The orientation of the action plane, in other words the fracture angle Θ , is not known a priori. For this reason, fracture angles from -90° to $+90^\circ$ are iterated in 1° steps in the present implementation. The actual fracture plane is characterised by the highest stressing effort. For further calculations, the angle Θ that results in the highest stressing effort as well as the corresponding effort $f_{E(IFF)}(\Theta)$ is used.

The equations for $f_{E(IFF)}$ are the following:

$$f_{E(IFF)}(\Theta) = \sqrt{\left[\left(\frac{1}{R_{\perp}^t} - \frac{p_{\perp\psi}^t}{R_{\perp\psi}^A}\right)\sigma_n\right]^2 + \left(\frac{\tau_{nt}}{R_{\perp\perp}^A}\right)^2 + \left(\frac{\tau_{n1}}{R_{\perp\parallel}}\right)^2} + \frac{p_{\perp\psi}^t}{R_{\perp\psi}^A}\sigma_n \quad (4.36)$$

$$f_{E(IFF)}(\Theta) = \sqrt{\left(\frac{\tau_{nt}}{R_{\perp\perp}^A}\right)^2 + \left(\frac{\tau_{n1}}{R_{\perp\parallel}}\right)^2 + \left(\frac{p_{\perp\psi}^c}{R_{\perp\psi}^A}\sigma_n\right)^2} + \frac{p_{\perp\psi}^c}{R_{\perp\psi}^A}\sigma_n \quad (4.37)$$

For tensile stresses normal to the action plane, the former equation is evaluated and otherwise it is the latter. The variables used are defined as follows:

$$\frac{p_{\perp\psi}^t}{R_{\perp\psi}^A} = \frac{p_{\perp\perp}^t}{R_{\perp\perp}^A}\cos^2\psi + \frac{p_{\perp\parallel}^t}{R_{\perp\parallel}}\sin^2\psi \quad (4.38)$$

$$\frac{p_{\perp\psi}^c}{R_{\perp\psi}^A} = \frac{p_{\perp\perp}^c}{R_{\perp\perp}^A}\cos^2\psi + \frac{p_{\perp\parallel}^c}{R_{\perp\parallel}}\sin^2\psi \quad (4.39)$$

$$\cos^2\Psi = 1 - \sin^2\Psi = \frac{\tau_{nt}^2}{\tau_{nt}^2 + \tau_{n1}^2} \quad (4.40)$$

$$R_{\perp\perp}^A = \frac{R_{\perp}^c}{2(1 + p_{\perp\perp}^c)} \quad (4.41)$$

The variables $p_{\perp\parallel}^t$, $p_{\perp\parallel}^c$, $p_{\perp\perp}^t$ and $p_{\perp\perp}^c$ contained in these equations are inclination parameters of the master fracture body in the $(\sigma_n, \tau_{nt}, \tau_{n1})$ -space and the variable $R_{\perp\perp}^A$ is parallel to fibre strength on the action plane against fracture due to $\tau_{\perp\perp}$ stresses. In this way, the fracture angle and the stresses transformed to the fracture plane are obtained in addition to the material stressing effort. Unlike Cuntze's FMC, Puck's APSC does not directly differentiate between IFFs due to tensile, compressive and shear loads. For this reason, a methodology is required to define the portion of the IFF modes. Deuschle [142] formulated an orientation impact degradation measure n_{dm} considering the computed fracture angle Θ and an angle of a most direct impact Θ_{md} for the mode under consideration:

$$n_{dm} = \left[\frac{1 - n_{min}}{2} \cdot \cos[2(\Theta - \Theta_{md})] \right] + \frac{1}{2} + \frac{1}{2}n_{min} \quad (4.42)$$

In this equation n can take values between 0 and 1, while the parameter n_{min} controls the least impact. Since no experimental results are available, the value is set to zero as proposed in the work of Deuschle [99]. Tab. 4.3 shows the values for Θ_{md} for the different components:

Table 4.3: Angles of most direct impact on the stiffness components

Θ_{md}	E_{22}	E_{33}	G_{12}	G_{13}	G_{23}
$n_{dm,i}$	0°	90°			
$n_{dm,ij}^+$			0°	90°	$+45^\circ$
$n_{dm,ij}^-$			0°	90°	-45°

In the first step, a general damage variable for IFF d_{IFF} controlled by the largest strain component is calculated. This general damage variable is then used to calculate the individual damage variables taking into account the orientation impact degradation measure:

$$d_i = n_{dm,i} \cdot d_{IFF} \quad (4.43)$$

$$d_{ij} = n_{dm,ij}^+ \cdot d_{IFF} + n_{dm,ij}^- \cdot d_{IFF} - n_{dm,ij}^+ \cdot d_{IFF} \cdot n_{dm,ij}^- \cdot d_{IFF} \quad (4.44)$$

The other parts of the degradation model work as described for the FMC in Section 4.4.3.

4.4.4 Numerical implementation as user-defined material model into Abaqus

The suggested elastoplastic material model has been implemented in Abaqus/Standard as UMAT. The following section describes the implementation of the algorithms for updating the Cauchy nominal stresses and, the state variables as well as the consistent tangent stiffness matrix. Both, the implementation and the verification are shown considering the version of the material model with Cuntze's FMC.

Computational procedure

At the beginning of each increment the values ϵ_n^e , ϵ_n^p , $\Delta\epsilon$, \tilde{p}_n , σ_n of the previous increment n are retrieved. Then the effective stress $\tilde{\sigma}$ at the time increment n is calculated with Eq. 4.1. With this information, an elastic predictor consisting of a trial strain ϵ_{n+1}^{trial} and a trial stress σ_{n+1}^{trial} is determined. The trial stress is then used to check the yield criterion F , cf. Eq. 4.19. If the increment is elastic, the stresses and strains at time $n + 1$ will be updated with the quantities of the elastic predictor. Otherwise, the actual effective stress vector $\tilde{\sigma}_{n+1}$ and the scalar valued accumulated plastic strain have to be found for the current increment. For this purpose, the effective stress vector $\tilde{\sigma}_{n+1}$ is expressed as a function of the trial stress vector $\tilde{\sigma}_{n+1}^{trial}$:

$$\tilde{\sigma}_{n+1} = (\mathbf{I} + \Delta\lambda \mathbf{D}^e \cdot \mathbf{M} \cdot \mathbf{P})^{-1} \cdot \tilde{\sigma}_{n+1}^{trial} \quad (4.45)$$

In this equation, \mathbf{I} is the identity matrix, $\Delta\lambda$ is the plastic multiplier, and \mathbf{D}^e is the elastic compliance matrix. The equivalent plastic strain of the increment $n + 1$ can be determined with the following equation

$$\tilde{p}_{n+1} = \tilde{p}_n + \Delta\lambda \sqrt{(\mathbf{P} \cdot \tilde{\sigma}_{n+1})^T : \mathbf{Z} : (\mathbf{P} \cdot \tilde{\sigma}_{n+1})} \quad (4.46)$$

where \mathbf{Z} is the mapping matrix:

$$\mathbf{Z} = \begin{bmatrix} 0 & 0 & 0 & 0 & 0 & 0 \\ & \frac{2}{3} & -\frac{1}{6} & 0 & 0 & 0 \\ & & \frac{2}{3} & 0 & 0 & 0 \\ & & & \frac{1}{3a} & 0 & 0 \\ & sym. & & & \frac{1}{3a} & 0 \\ & & & & & \frac{1}{6} \end{bmatrix} \quad (4.47)$$

A return mapping algorithm (RMA) is utilised to determine the only unknown variable in these equations $\Delta\lambda$. The RMA used in this work is described in [142] and was adapted by Din et al. [138] for the plastic potential as used by Sun and Chen [137]. The plastic multiplier determined with the RMA is used to correct the elastic predictor for the plastic effects. Regardless of whether the current increment is elastic or plastic, in the next step

of the procedure, the failure criterion, in this case Cuntze's FMC, is evaluated. If the total material stressing effort Eff^m is greater than or equal to 1, the damage variables d_{ft} , d_{fc} , d_{mt} , d_{mc} and d_s are updated. After this step, the elastic and plastic strain components are calculated and the nominal stress vector σ_{n+1} is updated considering the updated damage variables. At the end of the routine, the state variables are returned and the consistent tangent stiffness matrix is determined with the procedure described in the next section. The calculation procedure for each increment at each integration point is shown in Fig. 4.6.

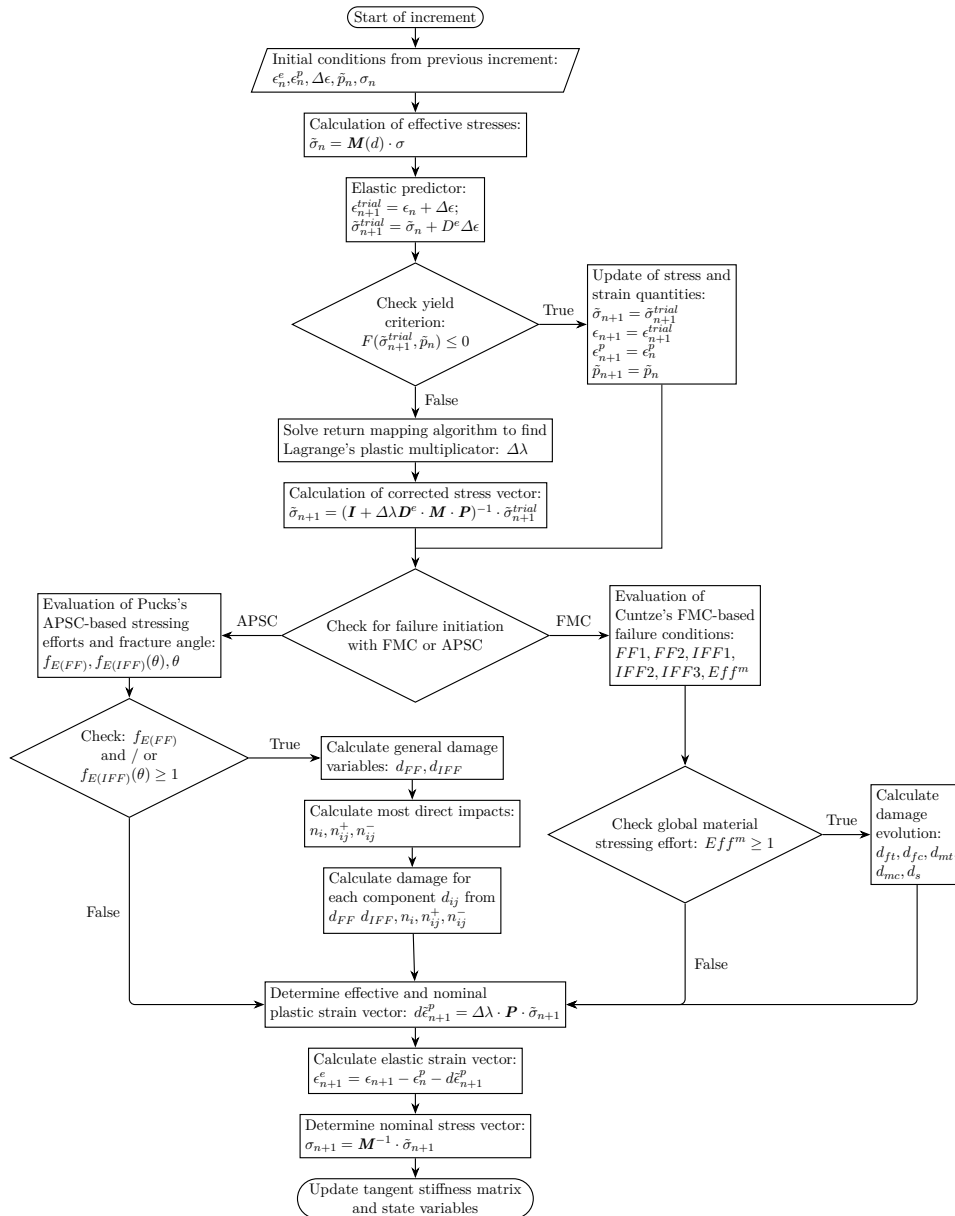


Figure 4.6: Algorithm flow chart of UMAT subroutine

Tangent stiffness matrix

Since the described material model is implemented for the implicit solver Abaqus/Standard, a tangent stiffness matrix, which is consistent with the stress-update algorithm, is required. Din et al. [138] have derived the following operator to calculate the consistent tangent stiffness for the plasticity model of Sun and Chen [137] in combination with damage:

$$C^{ep} = \frac{\partial \Delta \tilde{\sigma}_{n+1}}{\partial \Delta \epsilon_{n+1}^{trial}} = \left[(C_0)^{-1} + \Delta \lambda \mathbf{P} + \frac{1}{2\bar{\sigma}_y \tilde{H} \tilde{\zeta}} \mathbf{M} n_F n_F^T - \frac{\Delta \lambda}{\tilde{\zeta}^2} \mathbf{M} n_F n_F^T \mathbf{Z} \mathbf{P} \right]^{-1} \quad (4.48)$$

In this case $n_F = \mathbf{P} \cdot \tilde{\sigma}_{n+1}$, $\zeta = \sqrt{n_F^T \mathbf{Z} n_F}$, $\tilde{H} = \alpha \beta \tilde{p}_{n+1}^{\alpha-1}$ and $(C_0)^{-1}$ is the compliance matrix of the transversely isotropic material. In the present work, this operator was transferred to the three-dimensional stress state using the matrices \mathbf{P} and \mathbf{Z} specified in the sections 4.4.2 and 4.4.4. Tests of the implementation showed poor convergence at the beginning of damage. Therefore, the Operator 4.48 is only used as long as all damage variables d_I are equal to zero. In this case the matrix \mathbf{M} is always the same as the identity matrix \mathbf{I} and the operator becomes:

$$C^{ep} = \frac{\partial \Delta \tilde{\sigma}_{n+1}}{\partial \Delta \epsilon_{n+1}^{trial}} = \left[(C_0)^{-1} + \Delta \lambda \mathbf{P} + \frac{1}{2\bar{\sigma}_y \tilde{H} \tilde{\zeta}} \mathbf{I} n_F n_F^T - \frac{\Delta \lambda}{\tilde{\zeta}^2} \mathbf{I} n_F n_F^T \mathbf{Z} \mathbf{P} \right]^{-1} \quad (4.49)$$

From the beginning of damage, the tangent stiffness matrix is numerically determined using the perturbation technique, which is based on forward difference approximation. The components of C^{ep} are calculated as [152]:

$$C_{ijkl}^{ep} = \frac{d\sigma_{ij}}{d\epsilon_{kl}} \approx \frac{\sigma_{ij}(\hat{\epsilon}^{kl}) - \sigma_{ij}(\epsilon)}{\Delta \epsilon}, \text{ with } \hat{\epsilon}^{kl} = \epsilon + \Delta \epsilon^{kl} \quad (4.50)$$

Here, $\Delta \epsilon^{kl}$ is the perturbation strain for the kl -component and $\hat{\epsilon}^{kl}$ is the corresponding perturbed strain vector.

Viscous regularisation

With implicit solvers, the degradation of stiffness sometimes leads to convergence problems. The reason for this is that the tangent stiffness matrix is no longer positive definite. To mitigate this problem, Lapczyk and Hurtado [82] proposed the introduction of an artificial viscosity based on the regularisation model of Duvaut and Lions [153] according to the following equation:

$$\dot{d}_M^v = \frac{1}{\eta_M} (d_M - d_M^v) \quad (4.51)$$

In this equation, η_M describes the relaxation time of the viscous system and d_M^v is the regularised damage variable associated with mode M . The regularised damage variable for

the increment $n + 1$ is derived according to Chen et al. [121] as:

$$d_{M,n+1}^v = \frac{\Delta t}{\eta + \Delta t} d_{M,n+1} + \frac{\Delta t}{\eta + \Delta t} d_{M,n}^v \quad (4.52)$$

Characteristic and critical finite element size

For the CBA, described in Section 4.4.3, the in-plane characteristic element length L_c is needed in order to scale the linear degradation behaviour to the element size. This length L_c for square elements is determined by Bažant and Oh [150] with the following relationship, where A_{IP} is the in-plane area of the element:

$$L_c = \frac{\sqrt{A_{IP}}}{\cos(\gamma)} \quad (4.53)$$

Here, $|\gamma| \leq 45^\circ$ is the angle of the mesh line at which the crack band propagates. Maimí et al. [154] showed that the average of Eq. 4.54 $\bar{L}_c = 1.12\sqrt{A_{IP}}$ can be used for an unknown crack propagation direction. The solver provides the characteristic element length $L_{c,ABQ}$ in the UMAT interface for solid elements as the cube root of the element volume. For hexahedral elements, which are used in the present work, this value must be corrected with the following formula in order to obtain the in-plane element length, taking into account the ply- respective element thickness t and the unknown crack direction:

$$L_c = 1.12 \cdot \sqrt{\frac{L_{c,ABQ}^3}{t}} \quad (4.54)$$

The CBA assumes an element-wide crack band and adjusts the degraded modulus to ensure that the correct fracture energy is preserved for different element sizes. With this approach, the element size has an upper bound L^* . This is also called critical element size and is calculated using the pristine modulus E_M , the critical strain energy G_M , and the strength R_M for each mode M [150]:

$$L^* = \frac{2E_M G_M}{R_M^2} \quad (4.55)$$

If larger elements are used, a softening modulus of $-\infty$ would be determined with the CBA. This would lead to a sudden stiffness drop. In practice Bažant and Oh [150] recommend an element size of approximately half of the value determined for L^* .

4.4.5 Verification with one to few element models

To illustrate the applicability and effectiveness of the proposed combined elastoplastic damage model several numerical simulations of the progressive failure behaviour are performed. This section presents the results of three benchmark examples to verify the model. In addition, a $[\pm 45]_{2s}$ laminate under tensile loading was analysed.

Material and model parameters

Unless otherwise stated, all of the simulations have been performed with the thermoplastic fibre composite material AS4/PEEK, using the material and model parameters listed in Tab. 4.4. The elastic as well as the plastic properties are adopted from Sun and Yoon [143]. The values for tensile and shear strengths are taken from Kawai [155], whereas the compressive strengths are obtained from Sun and Rui [156]. The values for the critical strain energies are adopted from Carlile et al. [157] and Chen et al. [121].

Table 4.4: Material properties and model parameters for AS4/PEEK

Elasticity	E_{11} 126.7 GPa	$E_{22} = E_{33}$ 10.3 GPa	$G_{12} = G_{13}$ 6.0 GPa	G_{23} 3.45 GPa	$\nu_{12} = \nu_{13}$ 0.32	ν_{23} 0.49
Plasticity	a 1.5	α 0.142857	β 295.0274			
Strength	R_{\parallel}^t 2023.0 MPa	R_{\parallel}^c 1234.0 MPa	R_{\perp}^t 92.7 MPa	R_{\perp}^c 176.0 MPa	$R_{\perp\parallel}$ 82.6 MPa	
Fracture Toughness	$G_{ft} = G_{fc}$ 128.0 N/mm	$G_{mt} = G_{mc}$ 5.6 N/mm	G_s 4.93 N/mm			

Since the required parameters for Cuntze's FMC were not available for AS4/PEEK, the values determined by Petersen et al. [119] for M21/T700GC, a material with a tough epoxy matrix, were used. A brief introduction to the parameter determination as well as a table with the parameters is given in Section 4.5.4.

Verification with representative volume elements and periodic boundary conditions

This subsection is concerned with the verification of the proposed anisotropic elastoplastic damage model. The benchmark examples are calculated with cubic single element models with side lengths of 1 mm, using reduced integrated solid elements (C3D8R). The time step in the simulations is determined automatically with the restriction that the maximum time step is set to 0.005. The support and the load application are realised with periodic boundary conditions to be able to apply a load in one specific direction. These periodicity conditions are achieved by linking the degrees of freedom of the cubic model node-to-node as well as to reference points. This is done by using a plug-in for Abaqus CAE called EasyPBC by Omairey et al. [158]. As an example in Fig. 4.10 a single element model with a pure loading in the 12-direction is shown. In this case, the element nodes C1, C4, C5 and C8 are coupled with the reference point RP-1.

The first benchmark assesses the material model under cyclic tensile-compressive loading in fibre direction. The resulting stress-strain curve is shown in Fig. 4.8. In this verification, the cube is discretised with one element. First, the model is loaded in tension beyond initial failure (1). After that, the cube is unloaded (2) and then loaded in compression beyond initial compression failure (3). Once unloaded again (4), the cube is subjected to tensile loads of up to 3 % strain and significant damage (5). Following this procedure, it can be seen that the damage accumulated in the tensile part is accounted for in the compressive part of the cycle. In contrast, the compressive damage is considered in the

second tensile loading cycle. This behaviour verifies the damage variable calculation since the damage variables d_{ft} and d_{fc} are combined with Eq. 4.4 to a total damage variable in fibre direction d_f .

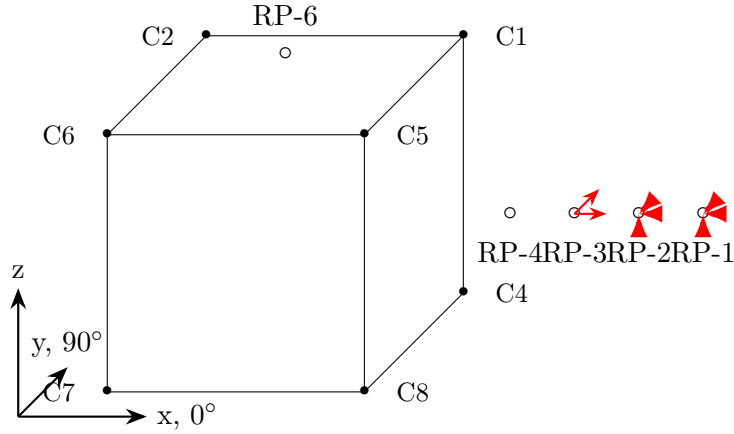


Figure 4.7: Single element model with periodic boundary conditions with loading in 12-direction

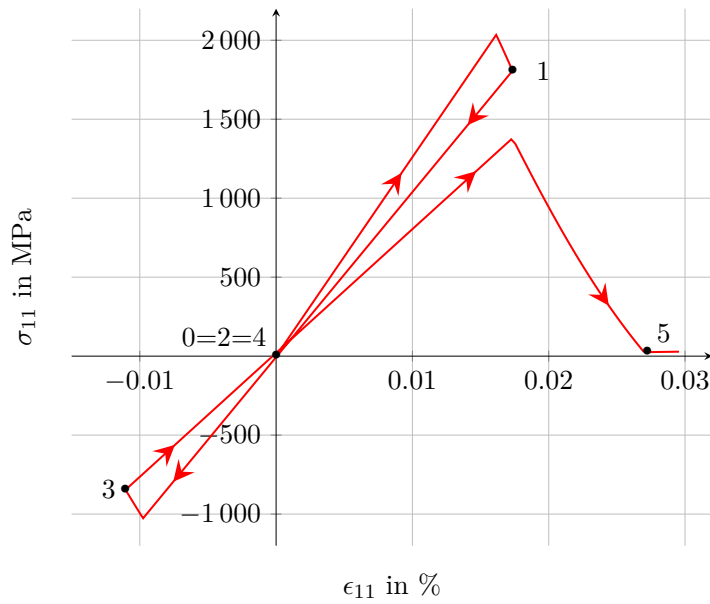


Figure 4.8: Load-displacement curves under uniaxial tensile-compressive cycling load in fibre direction

In the second benchmark example, cf. stress-strain curves in Fig. 4.9, a cube is subjected to a tensile load transverse to the fibre direction. Four different meshes were tested to assess the mesh dependency. Three models have a regular mesh with one, 27, and 125 elements, while the fourth model is also discretised with 27 elements, but with an irregular

mesh. In addition, Fig. 4.9 shows the transverse matrix damage variable d_m occurring in the cube models discretised with more than one element. In the irregular meshed model the four planes which subdivide the cube into 27 elements are inclined. In this way, a discretisation of the cube with slightly different sized and shaped elements is induced. As can be seen from the contour plot the damage always occurs in the midplane of the discretised cubes. The models with the regular meshes were also calculated with the CBA switched off. It can be observed that the stress-strain curves from the different models with the CBA switched on show some deviations, but compared to the models without the approach, a significant improvement is achieved. It can therefore be concluded that the CBA fulfils its purpose. In addition, it can be seen that the material shows some plasticity over 0.5 % strain in the transverse direction.

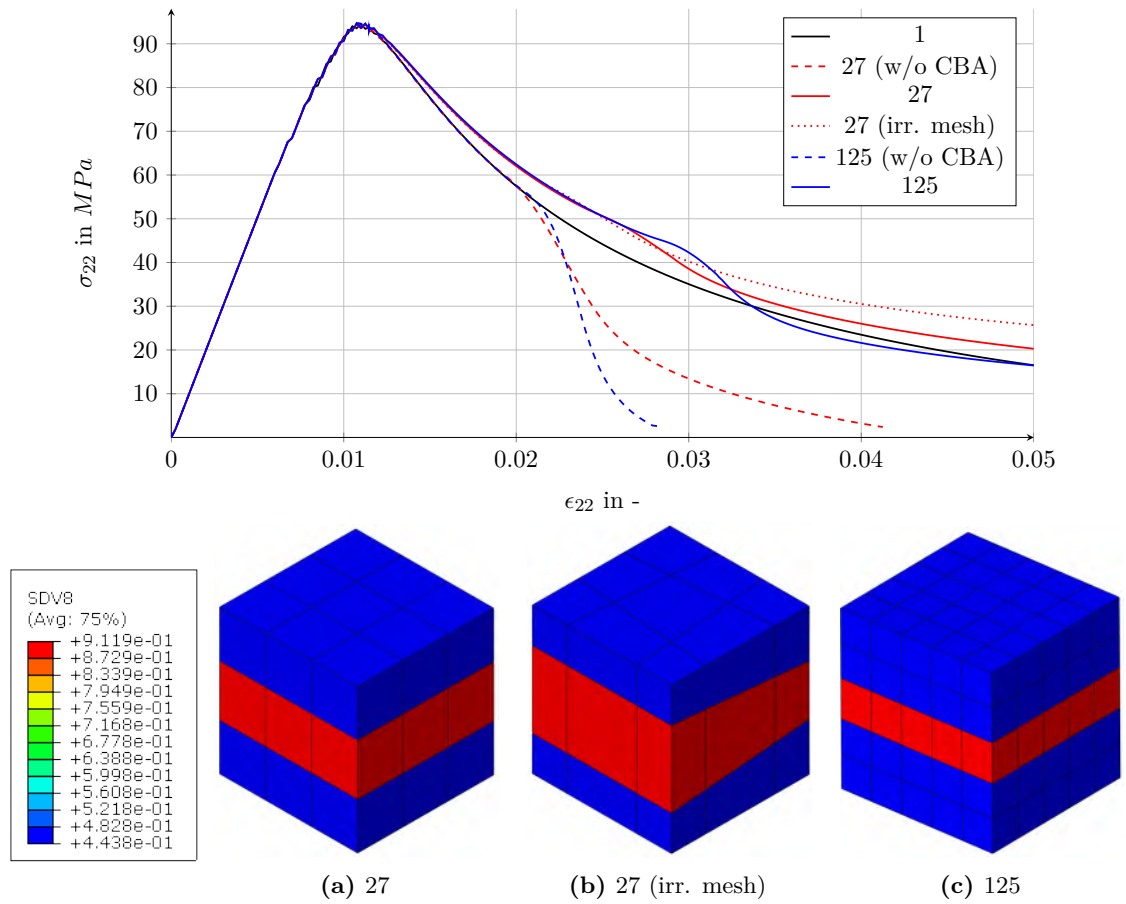


Figure 4.9: Stress-strain curve of a cubic model subjected to transverse tension loading and discretised with different meshes

The third benchmark example considers a cubic model, shown in Fig. 4.10, again, with periodic boundary conditions, subjected to pure shear loading in the 12-direction. The cube is loaded up to a certain point and unloaded again until it is stress-free. This cycle is repeated up to total failure at 8 % shear strain. The resulting stress-strain curve is plotted in Fig. 4.10. It can be seen that the plastic strain is taken into account when the load is

relieved. Moreover, the point of the previous loading is reached again when the element is reloaded. After the strength has been exceeded, the loading and unloading takes place with the degraded shear modulus.

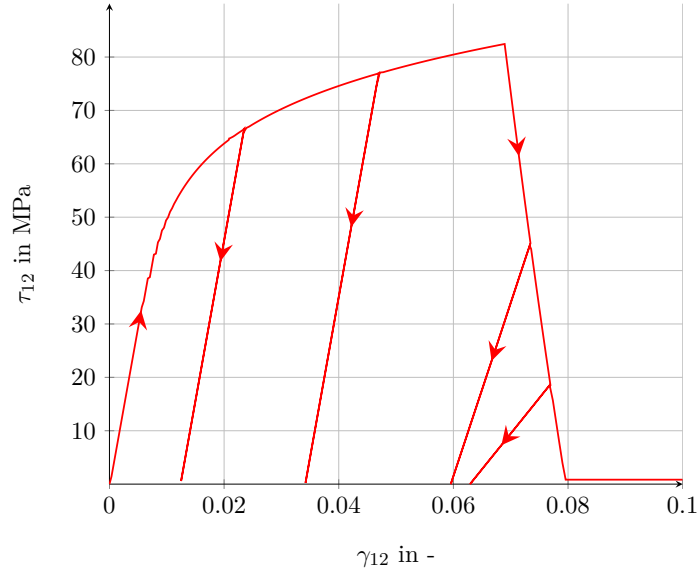


Figure 4.10: Stress-strain curve of a cubic model subjected to cyclic in-plane shear loading

For all three benchmark examples, it can be stated that the maximum stress, before the begin of degradation, corresponds to the specified strengths. In order to assess the interaction of stresses, Test Case 2 of the WWFE-II was adopted. First, the cubic model discretised with one element was loaded with different magnitudes of hydrostatic pressure p_{hyd} and then, in a second step, it was subjected to a shear loading until failure. The resulting stresses at failure are illustrated in Fig. 4.11.

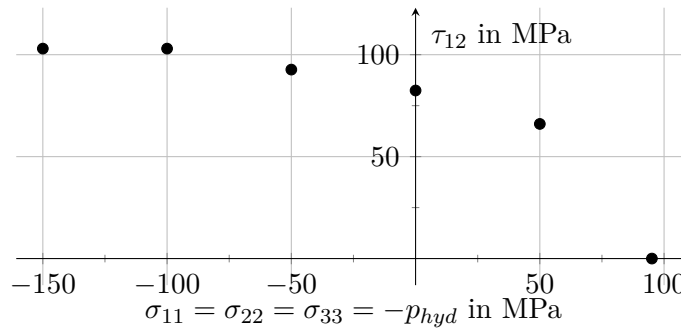


Figure 4.11: Fracture stress τ_{12} vs. stress $-p_{hyd}(= \sigma_{11} = \sigma_{22} = \sigma_{33})$ following WWFE-II Test Case 2

Since no experimental data is available for the material used in this work, only a qualitative comparison with results from WWFE-II can be made. Nevertheless, the calculations in this work are consistent with the observations in WWFE-II. The developed model is able to predict the effect of hydrostatic stresses having an impact on the shear

stress at failure. As the hydrostatic stress decreases, the shear stress at failure increases.

Numerical results of AS4/PEEK $[\pm 45^\circ]_{2s}$ laminates

To demonstrate the capabilities of the model in terms of plasticity and damage modelling, a tensile test, reported in literature, of a AS4/PEEK $[\pm 45^\circ]_{2s}$ laminate is numerically analysed. The test coupon of Lafarie-Frenot and Touchard's [89] experiment has the dimensions 230 mm x 20 mm x 1 mm. In the numerical analysis, the laminate is modelled with eight stacked elements, where each ply consists of one C3D8R element. With 1 mm, the thickness of the model is equal to the experiment. The other two dimensions are also 1 mm. Using periodic boundary conditions, the model behaves like a representative volume of the test specimen. The model is shown in Fig. 4.12.

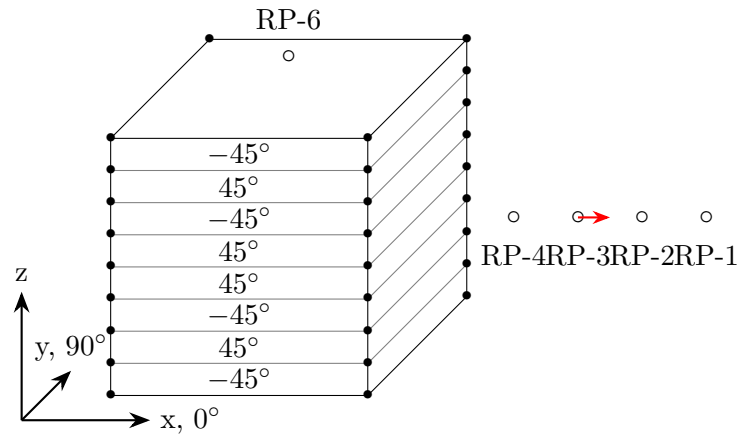


Figure 4.12: Finite element model of AS4/PEEK $[\pm 45^\circ]_{2s}$ tensile test with periodic boundary conditions

In Fig. 4.13, the stress-strain curves of the experimental test as well as the curve generated by the presented model are plotted. It can be observed that the elastoplastic material model is able to reproduce the experimental behaviour considerably well. In comparison, the same model was calculated with a variant of the presented material model without plasticity. While the predicted strength is comparable, without considering plasticity the elongation at failure is evidently too low. The slight kinks in the curve representing the numerical model with plasticity originate from the evolving yield limit, cf. Section 4.4.2. As the yield limit is initialised with 0 MPa a small first increment is always plastic. After this first increment, the yield limit increases and the following increments are elastic until the yield limit is reached again. This behaviour recurs at decreasing stress intervals.

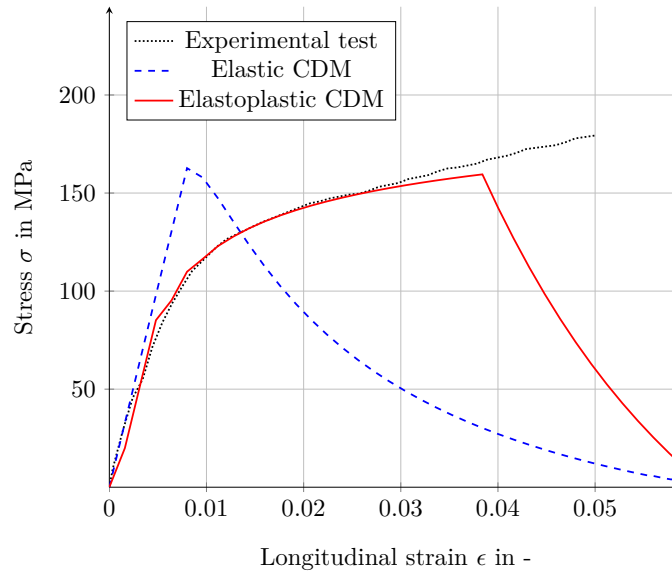


Figure 4.13: Experimentally [89] and numerically determined stress-strain curves of an AS4/PEEK $[\pm 45^\circ]_{2s}$ tensile test

4.5 Determination of the material parameters

This subchapter describes the determination of the material parameters for the main material of this work, namely M21-T700GC. At the end of this section, a summary of the determined parameters is given. The data for the second material 8552-IM7, can be found in Appendix E.

4.5.1 Elastic and strength properties

Two material batches, tested at DLR, are taken into account for the elastic as well as the strength properties. Results from the first batch as well as a detailed description of the tests and parameter derivation for M21-T700GC are published in Petersen et al. [119]. A second test batch is unpublished up to now. In this work, the mean values of the two batches are used for all elastic and strength properties. The relevant data can be found in Appendix B with Tab. B.1 relating to elastic properties and strength properties being addressed in Tab. B.2.

4.5.2 Characterisation of plasticity

The characterisation of the plasticity of the material M21-T700GC based on off-axis tension tests is described below. This is done in extension to the diploma thesis of Moll [159] supervised by the author.

Two different methods exist for the determination of the plasticity parameter a_{66} . Since the explicit solution method according to Winn and Srisharan [160] is not common in literature and the quality of the results is therefore difficult to evaluate, the iterative trial-and-error method is used in this work. According to Sun and Chen [137], the stress-strain curves of four to five different fibre angles are needed for an iterative parameter determination.

Off-axis tension tests

Off-axis tension tests were carried out on the basis of the DIN 527-2 guidelines on a Zwick 1484 servomechanical testing machine. The test speed was 2 mm/min at room temperature ($23 \pm 2^\circ\text{C}$). Strain gauges in the middle of the specimen were used to record the strains in load directions as well as perpendicular to the load direction. Seven test specimens each with seven different fibre angles θ_{off} with 10° , 15° , 20° , 30° , 45° , 60° , and 75° were tested.

A specific problem in off-axis tensile tests is the load introduction. If no or normal straight tabs are used, unintended shear loads and bending moments are induced in the test specimen due to the rigidity of the clamping in the testing machine. This leads to an early failure, i.e. at low strains, of the test specimens in the clamped area of the specimens. Such behaviour was observed in preliminary tests. However, for the determination of the plasticity parameter, the non-linear region of plastic deformation at high strains is of particular importance. Therefore, the early failure due to the not optimal load introduction severely restricts the determination of the parameters.

This can be improved by deformable [161] or rotating [162] tabs, which allow the desired stress state to be achieved.

An easier method to perform is available by using oblique tabs [163] that are designed to the fibre angle of the specimen. The geometry of the test specimens with oblique tabs is shown schematically in Fig. 4.14. The specimens have a thickness of $t = 1.5$ mm, a width of $b = 20.0$ mm and a free length of $l = 200.0$ mm. The oblique angle of the tabs is not equal to the off-axis angle of the fibres and is different for each fibre orientation. Accordingly, the angles were determined with the procedure described in [163]. The described modification of the tabs resulted in the specimens failing not only at higher strains but also in the middle of the specimens between the two clamps.

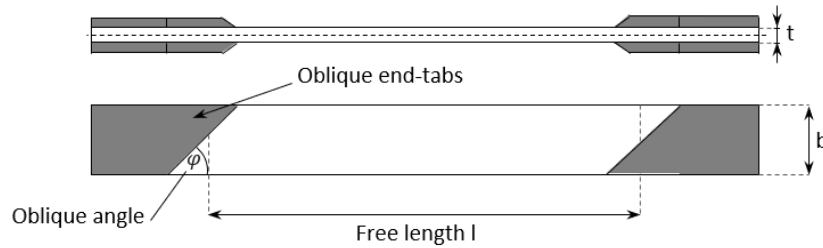


Figure 4.14: Geometry of off-axis tension test specimens with oblique tabs adopted from [159]

Results and parameter estimation

At first, mean curves for each off-axis angle are determined from the recorded stress-strain curves of the individual tests. These mean curves are shown in Fig. 4.16. The averaged curves represent the input for the iterative parameter determination. In the following, it is shown how the plastic strain values for different values of a_{66} can be determined by means of the plasticity model of Sun and Chen [137] assuming the plane stress state. The results generated with the sets of parameters obtained in this way can then be compared to the test data to determine the best fit. With the off-axis angle θ_{off} , the stresses on the

material principal axes can be related to the stress σ_x in the load direction of the machine by:

$$\sigma_{11} = \cos^2(\Theta_{off})\sigma_x \quad \sigma_{22} = \sin^2(\Theta_{off})\sigma_x \quad \sigma_{12} = -\sin(\Theta_{off})\cos(\Theta_{off})\sigma_x \quad (4.56)$$

These relationships are used in the formula for the effective stress according to Sun and Chen [137]. In fibre direction, only elastic states are assumed, which according to the plasticity model results in:

$$\tilde{\sigma} = \sqrt{\frac{3}{2}(\sigma_{22}^2 + 2a_{66}\sigma_{12}^2)} \quad (4.57)$$

Substituting Eq. 4.56 into Eq. 4.57 gives:

$$\tilde{\sigma} = h(\Theta_{off}, a_{66})\sigma_x \quad (4.58)$$

with:

$$h(\Theta_{off}, a_{66}) = \sqrt{\frac{3}{2}(\sin^4(\Theta_{off}) + 2a_{66}\sin^2(\Theta_{off})\cos^2(\Theta_{off}))} \quad (4.59)$$

With Eq. 4.58, the stress and strain values of the averaged curves can be transformed into the material coordinate system. From the strain values ε_x , the plastic strain in the major axis direction can be calculated using the already known assumption $\varepsilon = \varepsilon_e + \varepsilon_p$:

$$\varepsilon_x^p = \varepsilon_x - \frac{\sigma_x}{E_x} \quad (4.60)$$

In this context, E_x denotes the modulus of elasticity in the load direction. The plastic strain is then transformed into the material coordinate system:

$$\tilde{\varepsilon}^p = \frac{\varepsilon_x^p}{h(\Theta_{off}, a_{66})} \quad (4.61)$$

This results in seven curves, one for each fibre orientation, of the form $\tilde{\sigma}(\tilde{\varepsilon}^p)$, which are angle-independent and, when considered ideal, all converge into a master curve. To determine the master curve from the given data points, a power law is used which calculates the non-linear relationship of effective stress to effective plastic strain. The isotropic strain

hardening is thus expressed by:

$$\tilde{\varepsilon}^p = A\tilde{\sigma}^n \quad (4.62)$$

The two coefficients A_{SC} and n_{SC} are determined with the help of a Python script using the method of least squares. Using the coefficient of determination R^2 , the quality of this regression can be evaluated. This determination coefficient serves as a comparison factor to find out the best combination of the different a_{66} - A_{SC} - n_{SC} -combinations.

$$a_{66,opt.} \rightarrow R^2(a_{66}, \Theta, A_{SC}, n_{SC})_{max} \quad a_{66} \in [a_{66,min} \dots a_{66,max}] \quad (4.63)$$

The goodness of fit of parameter R^2 is shown as a function of the tested a_{66} in Fig. 4.15. In the present case, a R^2 of about 90 % is achieved in the calculation from all seven mean value curves. The maximum occurs for an a_{66} of 0.8. However, the differences in the R^2 value for a_{66} between 0.7 and 1.2 are not considerably large.

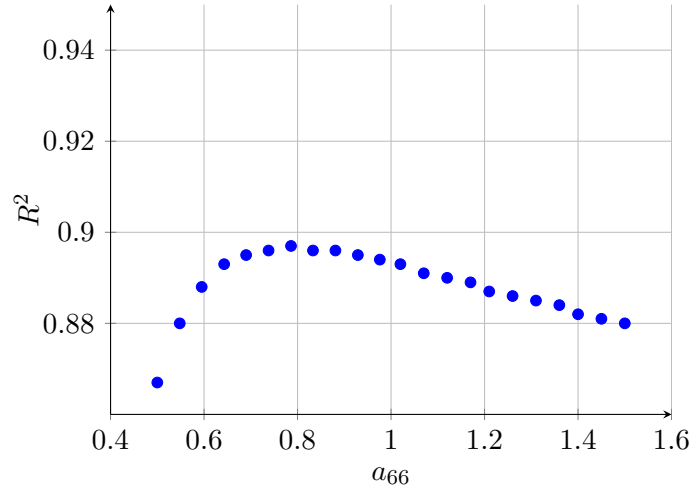


Figure 4.15: Goodness of fit for different values of a_{66}

The effective stress as a function of the effective plastic strain can be expressed with the following relationship:

$$\tilde{\sigma}(\tilde{\varepsilon}^p) = A_{SC}^{-1/n_{SC}} (\tilde{\varepsilon}^p)^{1/n} = \beta (\tilde{\varepsilon}^p)^\alpha \quad (4.64)$$

This results in the parameters $\alpha = 0.218$ and $\beta = 336.4$, which are required for the material model. The off-axis tensile tests were simulated using these values and a cubic model with periodic boundary conditions similar to the one shown in Fig. 4.12. The resulting stress-strain curves are shown alongside the experimental mean curves in Fig. 4.16. Even though there is a slightly larger deviation at an off-axis angle of 10° , it can be said

that the experimental results are in general well reproduced.

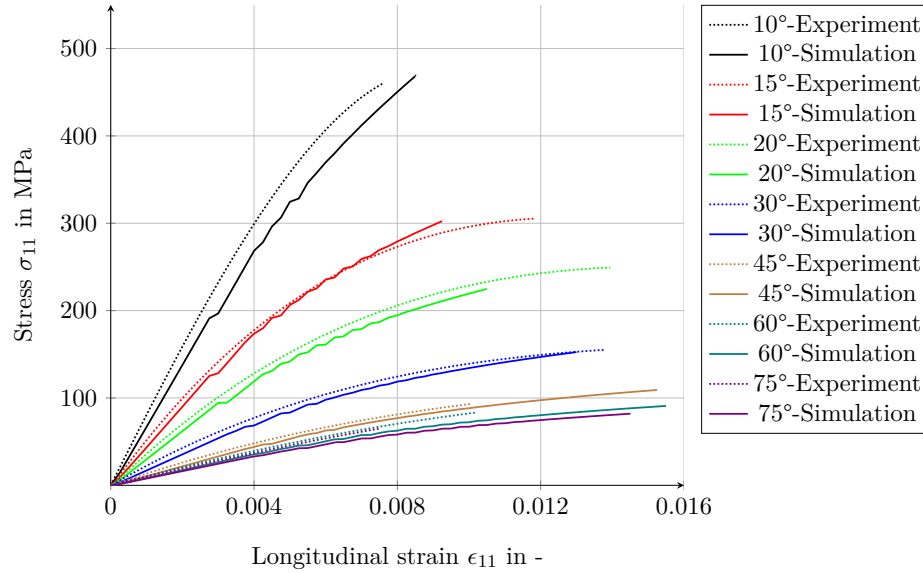


Figure 4.16: Experimental and numerical results of UD composites made from M21-T700GC under off-axial tensile loads ($a_{66} = 0.8$, $\alpha = 0.218$, $\beta = 336.4$)

Calibration of the plasticity model using $\pm 45^\circ$ -tension tests

According to studies by Winn et al. [160], the one parameter plasticity model is well suited to predict the behaviour of laminates with only one fibre orientation. The off-axis tests represent such a case. These laminates are characterised by the fact that as soon as a macroscopic crack forms, the complete laminate fails. It is noteworthy that laminates with more than one fibre orientation usually do not show this failure behaviour. Failure does not occur directly with the first macroscopic cracks, as the different layers hinder the intralaminar propagation of matrix cracks across the entire laminate thickness. The laminates non-linear region after the initial damage of a single layer which still carries load can therefore not be captured in the off-axis tests and thus has no influence on the calculation of the plasticity parameters. Furthermore, the influence of micro-cracks on the non-linearity changes the stress-strain response of multi-layer laminates [160].

In the case of using the plasticity model with multilayer composites, Winn et al. [160] recommend to calibrating the parameters phenomenologically to the application to incorporate these influences. It must be noted, that as a calibrated phenomenological model, its suitability for multi-layer laminates is increased, but the accuracy for simpler cases such as off-axis tensile tests is reduced. However, in the subsequent part of this work, mainly multidirectional laminates will be considered. For this reason, a calibration of the plasticity parameter is carried out in this work in order to adjust the influence of the shear stress more precisely. The calibration process is described in the following.

Since the aircraft laminates under investigation are often QI, involving only ply angles in

45° increments, a $\pm 45^\circ$ layup is used for this purpose. The calibration is based on $[\pm 45^\circ]$ experiments carried out at DLR. The model used for calibration is similar to the model described in Section 4.4.5 and illustrated in Fig. 4.12. In the previous section, it was shown that the plasticity parameter $a_{66} = 0.8$ is the best fit for the off-axis tests. As can be seen in Fig. 4.17, this value underestimates the plastic behaviour and thus the elongation at break.

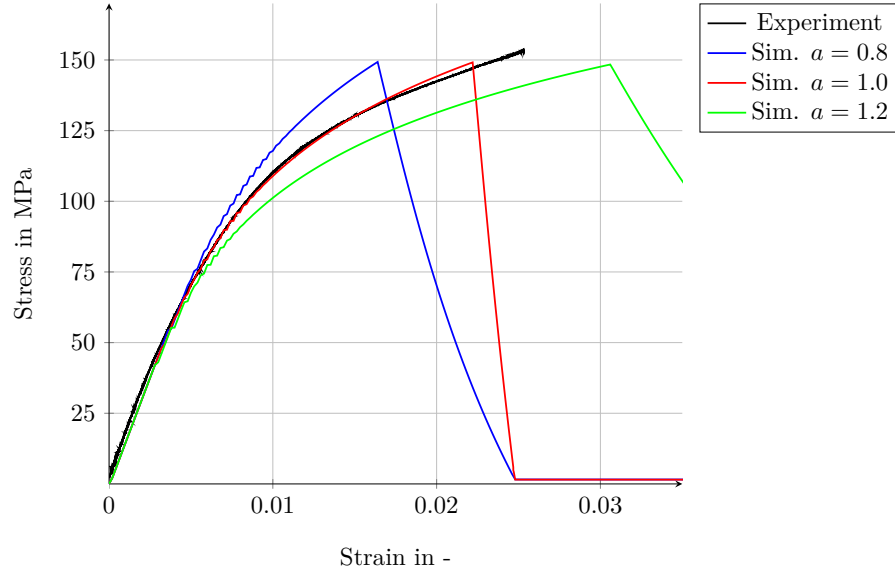


Figure 4.17: Comparison of experimentally and numerically determined stress-strain curves of a M21-T700GC $[\pm 45]_{2s}$ tensile test with different a -values

The parameter a_{66} weights the contribution of the shear stresses to the plastic behaviour of the material. Since values from the literature tend to suggest larger shear proportions for similar materials, different values of a_{66} were tested using the example of the $[\pm 45^\circ]$ test. This is possible because the goodness of fit (cf. Fig. 4.15) for different values of a_{66} differ only in the range of a few percent. The a_{66} values with their respective α and β parameters give only minor deviations in the stress-strain curves of the off-axis simulations, but differ significantly in the $[\pm 45^\circ]$ simulation.

As can also be seen in Fig. 4.17, a clear improvement occurs when using $a_{66} = 1.0$. The non-linear range is represented well and results in a good agreement with the measured strength and elongation at break are obtained in the physical test. If the parameter is increased further to $a_{66} = 1.2$, the modelling of the $[\pm 45^\circ]$ -test deteriorates again. The failure stress remains similar, but the material yields significantly more. Thus, the elongation at break increases. For this reason, the parameter a_{66} is set to 1.0 in the rest of the work.

For 8552-IM7, the same procedure is carried out on the basis of off-axis tensile tests from literature. The data from the off-axis tests and the resulting plasticity parameters can be found in Appendix E.

4.5.3 In-situ strengths

The effect of higher transverse tensile and shear strength of a ply, which is constrained by plies of different fibre orientations is called in-situ effect and was originally discovered by Parvizi [164]. The higher transverse tensile and shear strength compared to the same ply in a UD laminate is called in-situ strength. The occurring in-situ strengths depend on the number of clustered plies as well as on the orientation of the adjacent constraining plies [165].

It can be concluded that the consideration of in-situ strengths in stress-based failure initiation criteria, like the ones used in this work, is necessary for an accurate prediction. The extent of the influence of the in-situ strengths on the strength prediction is further investigated in Section 4.6.4. A method is therefore needed to determine the in-situ strengths.

In principle, the in-situ strengths, as shown by Chang and Chen [166] as well as Flaggs and Kural [167], can be determined experimentally. However, an elaborate experimental campaign for a pragmatic approach to design and analysis is not expedient. Since the UD strengths are usually available, an analytical method for determining the in-situ strengths from the UD strengths is preferred.

In this work, the approach of Camanho et al. [165] is utilised, as it is commonly used and is, for example, also included in the LaRC03/04/05 failure criteria [132, 168, 169]. Moreover, it has already been shown in some publications that it achieves good agreement with experimental results [168, 169, 170]. The theory [165] is based on crack analysis in thick, thin and embedded layers in the wake of Dvorak and Laws [171]. A slit crack is used as a macroscopic representation of an accumulation of microdefects and the crack growth is considered on the basis of fracture mechanics. Furthermore, the theory uses the Hahn-Tsai fit to incorporate the non-linear in-plane shear stress-strain behaviour with its fitting parameter β_{HT} [172].

Without further discussion of the analytical formulae of the theory, Tab. 4.5 compares the UD and the in-situ strengths of M21-T700GC. In this context, a distinction is made between a ply constrained from two plies (thin theory) and an outer ply which is only constrained from one side. The results were generated with $\beta_{HT} = 2.98 \cdot 10^{-8} \text{ MPa}^{-3}$ from [173] and a layer thickness of 0.13 mm. The analytical solutions from Camanho et al. [165] can be found in Appendix C.

Table 4.5: Comparison of UD and in-situ strengths of M21-T700GC

UD	in-situ (thin)	in-situ (outer)
R_{\perp}^t 78.0 MPa	$R_{\perp, is, thin}^t$ 158.0 MPa	$R_{\perp, is, outer}^t$ 100.0 MPa
$R_{\perp \parallel}$ 77.0 MPa	$R_{\perp \parallel, is, thin}$ 171.0 MPa	$R_{\perp \parallel, is, outer}$ 142.0 MPa

4.5.4 Parameters for failure criteria

The parameters for the FMC by Cuntze were determined at DLR using Arcan tests. A comprehensive explanation of the ARCAN tests and the parameter derivation for the FMC can be found in the same publication as the elastic and strength properties [119]. In the following, a brief overview of the parameter estimation based on the diploma thesis by Moll [159], supervised by the author, is given.

Friction values for Cuntze's FMC

To determine $\mu_{\perp\parallel}$ and $\mu_{\perp\perp}$, Petersen et al. [119] use Arcan experiments to generate IFF2 and IFF3 stress states in the material that are as pure as possible. To identify $b_{\perp\parallel}$, two points on the IFF3 curve are used for this purpose. In addition to the shear strength $R_{\perp\parallel}$, the stress state $(\sigma_2^c, \tau_{21}^c)$ marked as point A in Fig. 4.18 is used. This stress state can be achieved in a biaxial test. Using these two points, $b_{\perp\parallel}$ can be calculated as follows:

$$b_{\perp\parallel} = \frac{R_{\perp\parallel}^4 - (\tau_{21}^c)^4}{2\sigma_2^c(\tau_{21}^c)^2 R_{\perp\parallel}} \quad (4.65)$$

Assuming a linear Mohr Coulomb formulation, the relationship with the coefficient of friction can be approximated by a straight line between the points. This is described as follows:

$$\mu_{\perp\parallel} = \frac{\tau_{21}^c - R_{\perp\parallel}}{\sigma_2^c} = \frac{b_{\perp\parallel}}{2} \quad (4.66)$$

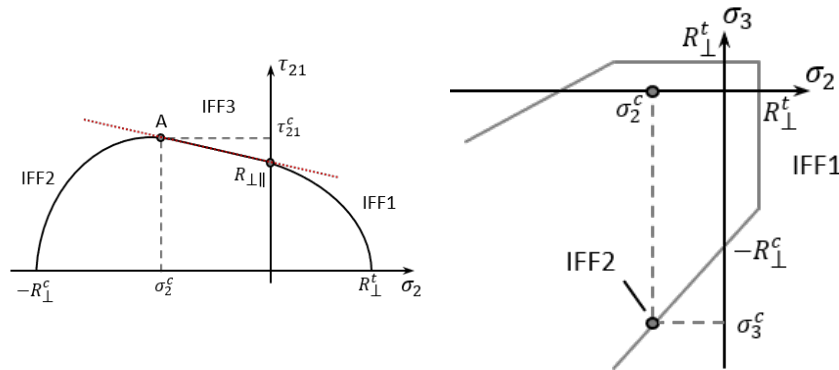


Figure 4.18: Cuntze σ_2 - τ_{21} -fracture curve (left) and σ_2 - σ_3 -fracture curve (right) adopted from [159]

In order to identify $b_{\perp\perp}$, a biaxial test is used to create a point on the IFF2 fracture curve which is assumed to produce pure IFF2 stresses in the material. The stresses σ_2^c and σ_3^c in this condition are shown on the right in Fig. 4.18. When inserting into the IFF2 fracture criterion and rearranging it, the result is:

$$b_{\perp\perp} = \frac{1 + (\sigma_2^c + \sigma_3^c)/R_{\perp}^-}{(\sigma_2^c + \sigma_3^c)/R_{\perp}^- + \sqrt{(\sigma_2^c + \sigma_3^c)^2/R_{\perp}^-}} \quad (4.67)$$

and

$$b_{\perp\perp} = \frac{1}{1 - \mu_{\perp\perp}} \quad (4.68)$$

An overview of all failure criterion coefficients can be found in Tab. 4.6. The interaction coefficient m , which evaluates the individual efforts Eff^{mode} to the total effort Eff^m , can be determined via test data according to Cuntze [83]. However, it has been found suitable to use the same coefficient m for each effort and to define it via empirical values. Cuntze recommends a range of 2.5 to 3.0, whereby a smaller value leads to lower failure stresses. As recommended by Petersen et al. [119], in this work a value of $m = 2.6$ is used.

Inclination parameters for Puck's APSC

The two inclination parameters $p_{\perp\parallel}^-$ and $p_{\perp\parallel}^+$ can be determined analogue to Cuntze's friction coefficients from the experimental $\tau_{21} - \sigma_2$ -fracture curve. They represent the inclination of the fracture curve at point A in Fig. 4.19, at which the transition from Mode A to Mode B takes place. Assuming a continuous curve, it corresponds to the coefficient of friction $\mu_{\perp\parallel}$ [174]. The simple determination is at a fracture angle Θ_{fp} of 0° in modes A and B. The effective plane of σ_2 and τ_{12} thus becomes the fracture plane with $\sigma_2 = \sigma_n$ and $\tau_{12} = \tau_{nt}$.

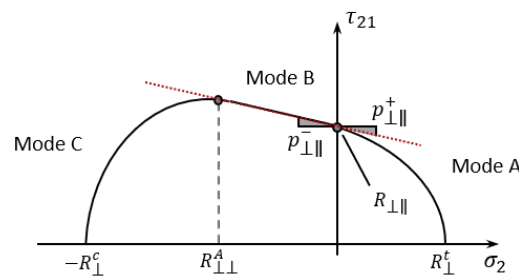


Figure 4.19: Puck $\sigma_2 - \tau_{21}$ -fracture curve adopted from [159]

The parameters $p_{\perp\parallel}^+$ and $p_{\perp\parallel}^-$ cannot be directly determined because the $\sigma_n - \tau_{nt}$ -fracture curve in the region around $\sigma_n \approx 0$ cannot be analysed experimentally. As described earlier, for a 3D stress state in Puck's APSC, it is necessary to determine the fracture angle numerically. However, in the plane stress state, there is an analytical solution for the calculation of Θ [130]. In this way, the parameter $p_{\perp\parallel}^-$ can be calculated assuming the

following parameter coupling:

$$\frac{p_{\perp\perp}^-}{R_{\perp\perp}^A} = \frac{p_{\perp\parallel}^-}{R_{\perp\parallel}} \quad (4.69)$$

with the crack resistance in the fracture plane:

$$R_{\perp\perp}^A = \frac{R_{\perp\parallel}}{2p_{\perp\parallel}^-} \left(\sqrt{1 + 2p_{\perp\parallel}^- \frac{R_{\perp\parallel}}{R_{\perp\parallel}}} - 1 \right), \quad (4.70)$$

subsequently results in:

$$p_{\perp\perp}^- = \frac{1}{2} \left(\sqrt{1 + 2p_{\perp\parallel}^- \frac{R_{\perp\parallel}}{R_{\perp\parallel}}} - 1 \right). \quad (4.71)$$

The required values are available from the experiments. Puck recommends assuming the $\sigma_n - \tau_{nt}$ -failure curve to be continuous and to set $p_{\perp\perp}^+$ equal to $p_{\perp\parallel}^-$. All values needed for Puck's APSC are also listed in Tab. 4.6. The same parameters are also used for the simulations with the 8552-IM7 material since both materials have a toughened epoxy matrix.

Table 4.6: Parameters for Cuntze's FMC and Puck's APSC

FMC	$b_{\perp\parallel}$ 0.44	$b_{\perp\perp}$ 1.266	m 2.6		
APSC	$p_{\perp\parallel}^t$ 0.22	$p_{\perp\parallel}^c$ 0.22	$p_{\perp\perp}^t$ 0.23	$p_{\perp\perp}^c$ 0.23	$m = s$ 0.5

4.5.5 Intralaminar fracture toughness

The developed intralaminar material model is based on CDM and uses an energy-based strain driven linear degradation model, cf. Section 4.4.3. The decisive parameter for adjusting the damage propagation to the specific material is the cERR or fracture toughness G_M . In total, five different fracture toughness parameters are needed for the energy-based degradation of the intralaminar material model. The two fracture toughness parameters for failure in fibre direction are distinguished by the loading in tension G_{ft} and compression G_{fc} . The remaining three parameters relate to the intralaminar matrix failure due to tension G_{mt} , compression G_{mc} , and shear G_{ms} loading.

The determination of intralaminar fracture toughness values is not standardised and is the subject of current research. As this is not the focus of this work, literature values are used:

Furtado et al. [175] studied the influence of ply thickness on the fibre related fracture toughness in tension for M21-T700GC, the material under investigation in this thesis. This

value is especially important for the accuracy of strength predictions.

By using double edge notch tension (DENT) specimens they found that the measured fracture toughness increases linearly with ply thickness. However, their hypothesis is that in mesoscale intralaminar damage models, like the one presented in this chapter, the fracture toughness should not be varied with ply thickness. This is explained by the fact that in laminates with thicker plies, subcritical damage occurs in the vicinity of notches which leads to stress redistribution and therefore a reduction of stress concentrations. Due to this, the measured effective fracture toughness associated with the longitudinal tensile failure is higher for thicker plies, but the intrinsic fracture toughness is not higher.

The damage mechanism described above is captured by mesomechanical models such as the model in this paper. Hence, the fracture toughness should be measured using specimens with a ply thickness that does not allow for subcritical damages like the thinnest ply thickness Furtado et al. [175] have used. Following this, the value of $G_{ft} = 83 \text{ N/mm}$, measured on DENT specimens with low-grade material (75 g/m^2), is used in this work.

For models which are not able to capture the subcritical damage around notches, like macromechanical ESL models, the researchers propose to use fracture toughness values measured with the actual ply thickness.

The value for fracture toughness associated with the longitudinal compression failure $G_{fc} = 60 \text{ N/mm}$ is also taken from Furtado et al. [175].

Using the example of the second composite material considered in this thesis 8552-IM7, Czabaj and Ratcliffe [176] found out that, the intralaminar fracture toughness, tested with a compact tension specimen, and the interlaminar fracture toughness, tested with Double Cantilever Beam (DCB) specimen, is similar. They suggest that at least the mode I matrix fracture toughness is independent from the fracture plane. In this work, it is assumed that this also applies to the other two matrix fracture toughness parameters. These are considered to be equal to the interlaminar mode II fracture toughness.

At this point, mode I and mode II fracture toughness from the interlaminar test campaign carried out within the scope of this work are adopted as intralaminar matrix values without further description of the tests. A detailed description of the characterisation of the interlaminar crack energies is presented in the following chapter.

Values for the second material 8552-IM7 are also taken from literature and are presented in Appendix E.

4.5.6 Summary of intralaminar material properties

The material parameters for the intralaminar model derived in this section for the material M21-T700GC are summarised in Tab. 4.7 below. Unless otherwise described, these parameters will be used for all simulations throughout the thesis.

Table 4.7: Material properties and model parameters for M21/T700GC

Elasticity	E_{11} 124.1 GPa	$E_{22} = E_{33}$ 10.3 GPa	$G_{12} = G_{13}$ 4.3 GPa	G_{23} 2.6 GPa	$\nu_{12} = \nu_{13}$ 0.29	ν_{23} 0.59
Plasticity	a 1.0	α 0.218	β 336.4			
Strength (UD)	R_{\parallel}^t 2214.0 MPa	R_{\parallel}^c 1521.0 MPa	R_{\perp}^t 78.0 MPa	R_{\perp}^c 207.0 MPa	$R_{\perp\parallel}$ 77.0 MPa	
Strength (in-situ)	$R_{\perp, is, thin}^t$ 158.0 MPa	$R_{\perp\parallel, is, thin}$ 171.0 MPa	$R_{\perp, is, outer}^t$ 100.0 MPa	$R_{\perp\parallel, is, outer}$ 142.0 MPa		
FMC	$b_{\perp\parallel}$ 0.44	$b_{\perp\perp}$ 1.266	m 2.6			
APSC	$p_{\perp\parallel}^t$ 0.22	$p_{\perp\parallel}^c$ 0.22	$p_{\perp\perp}^t$ 0.23	$p_{\perp\perp}^c$ 0.23	$m = s$ 0.5	
Fracture Toughness	G_{ft} 83.0 N/mm	G_{fc} 60.0 N/mm	$G_{mt} = G_{mc}$ 0.304 N/mm	G_s 2.33 N/mm		

4.6 Validation of the material model using open hole tension tests

The validation of the material model together with the determined material parameters is carried out using OHT specimens. This is presented in the following subchapter for the material M21-T700GC, starting with a description of the experimental tests. The results of the corresponding validation with the material 8552-IM7 can be found in Appendix F.

4.6.1 Experimental tests of open hole tension specimens

A total of five series of test specimens with five different layups were manufactured from M21-T700GC, with a nominal ply thickness of 0.131 mm.

The different layups are: $[0]_{18}$, $[90]_{32}$, $[-45/90/+45/0]_{4s}$, $[45/90/-45/0]_{3s}$ and $[0/90]_{8s}$. The first test specimen series has a laminate thickness of 2.36 mm, the second, third, and fifth 4.19 mm, and the fourth 3.57 mm. In the further course of the thesis, the specimen series will be referred to as UD-0, UD-90, QI-I, QI-II, and cross ply (CP). Further information on the sample geometries is given in Tab. 4.8. It should be noted that sample QI-II has a width of 18 mm, which is smaller than the other samples.

Table 4.8: Geometries of the M21-T700GC OHT configurations

Name	Width mm	Free length mm	Thickness mm	Hole diameter mm
UD-0	32.0	180.0	2.36	6.0
UD-90	32.0	180.0	4.19	6.0
QI-I	32.0	180.0	4.19	6.0
QI-II	18.0	180.0	3.14	6.0
CP	32.0	180.0	4.19	6.0

The plates are laid by hand, vacuum sealed and cured in an autoclave according to the manufacturer's recommended curing cycle. On the cured plates, $\pm 45^\circ$ -GFRP plates with a thickness of 1 mm were bonded as an end-tab to ensure a proper load introduction into the specimens during the test. The specimens were then cut from the plates with a diamond saw and the holes were drilled with a solid carbide drill at 750 rpm. During the drilling process, the specimens were supported at the top and bottom with 2 mm thick CFRP CP plates to prevent delaminations. The drilled surfaces were checked by optical microscopy. The tests were carried out in accordance with AITM 1-0007 [177] in a Zwick servomechanical testing machine (Zwick 1484) equipped with a 250 kN load cell. At an ambient temperature of $23 \pm 2^\circ\text{C}$, the specimens were loaded with a constant crosshead speed of 0.5 mm/min.

During testing of some of the specimens, 12 M ARAMIS system from Carl Zeiss GOM Metrology GmbH (GOM) was used as a DIC system to be able to measure the strain of the specimen between clampings without the influence of the testing machine rigidity.

The force-displacement curves of the experimental OHT tests are shown and discussed in the following sections together with the numerical results. In this section, the measured strengths and fracture behaviour are discussed in more detail.

All specimens show almost constant stiffness up to brittle failure. The specimens of the series UD-90, QI-I, QI-II as well as CP fail completely at the first load drop and show only very small scatter at the failure load.

For the UD-0 specimens, a clear drop in load was observed, which can be attributed to the longitudinal splitting of the specimens. This longitudinal splitting leads to a centre section of the same width as the hole diameter and thus reduces the load-bearing cross-section. The remaining cross-section bears further loads. Since this no longer represents the OHT case, the test was stopped after the load drop and longitudinal splitting occurred and the maximum force reached up to that point was considered as the failure load.

The resulting failure stresses are shown in Tab. 4.9.

Table 4.9: List of M21-T700GC OHT configurations and experimental results

Name	Laminate	Lay-up	No. of Spcms.	Peak Stress MPa
UD-0	100/0/0	$[0]_{18}$	4	348.3 ± 9.3
UD-90	0/0/100	$[90]_{32}$	6	40.9 ± 2.1
QI-I	25/50/25	$[-45/90/45/0]_{4s}$	6	397.1 ± 9.5
QI-II	25/50/25	$[45/90/-45/0]_{3s}$	5	356.0 ± 7.7
CP	50/0/50	$[0/90]_{8s}$	6	464.4 ± 15.8

4.6.2 Modelling of open hole tension specimens

The above introduced OHT specimens of the physical testing campaign are used for the validation of the developed intralaminar material model. In addition, on the basis of the OHT specimens, different versions of the material model are compared.

At first, some considerations are made regarding the set-up of the model. Girão Coelho et

al. [178] state that symmetry can be used to reduce the simulation expense, but not in the loading direction, since the restraining conditions may change the stress field. Although, in case of $\pm 45^\circ$ -plies in the layup there is no real symmetry in width or Y-direction. However, as it is common in literature, only half of the specimen width is modelled and a Y-symmetry is used. In addition, since the lay-up of all specimens is symmetric to the midplane also Z-symmetry is used. Therefore, all simulations are performed with Abaqus/Standard modelling 1/4 of the specimens. The geometry and boundary conditions of the model are shown in Fig. 4.20. The OHT specimens are loaded with a displacement load applied to one end. The time step is limited to a maximum value of 0.02.

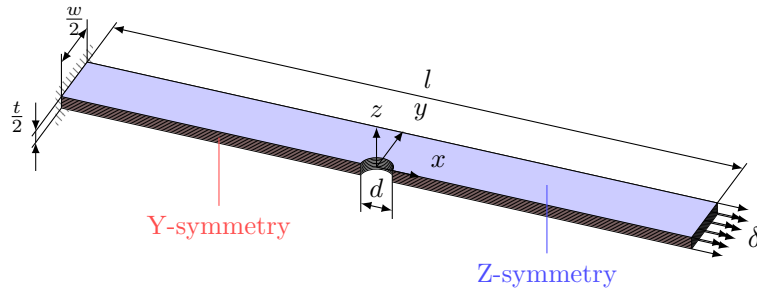


Figure 4.20: Sketch of model geometry and boundary conditions

4.6.3 Element type and mesh sensitivity

In order to save computation time and minimise the tendency for shear locking, reduced integrated linear solid elements (C3D8R) are used. The element size must be chosen in a way that complies with the premise of the CBA: The band width, in which the damage localises, is equivalent to the element dimension. Elements sized larger than the damage process zone would lead to a local snap back. Using the CBA with elements that are smaller than the width of the crack band would lead to a localisation of the deformation and, therefore, result into an incorrect stress field [150].

With Eq. 4.55, the smallest maximum element size $L^* = 0.91$ mm is determined for the transverse compression case. Since this is not likely to occur in OHT specimens the next larger element size $L^* = 1.70$ mm for the transverse tension case is used. Břzant and Oh [150] recommend using an element size of approximately half of the value calculated for L^* . In the case of the material parameter used for M21-T700GC this leads to an in-plane element size of about 0.85 mm. In order to check the determined element size, a strength prediction study with different meshes from 0.4 mm to 1.45 mm using the OHT specimen with QI-II layup is performed. With this range, all element edge lengths considered are smaller than the calculated critical, but not smaller than the recommended element size. As discussed in the section on choice of element type, cf. Section 4.2.3, in through-thickness direction, every ply is discretised by one element.

For each mesh size two different meshes are considered: a structured and an unstructured mesh. This is shown in Fig. 4.21 for configuration QI-II as an example. The motivation for this is to check if the alignment of the element edge to the fibre orientation has an

impact on the results. As can be seen from Fig. 4.21 the mesh has a small influence on the fracture path. While the damage develops orthogonally to the load direction in the structured mesh, it is slightly deflected to one side in the unstructured mesh.

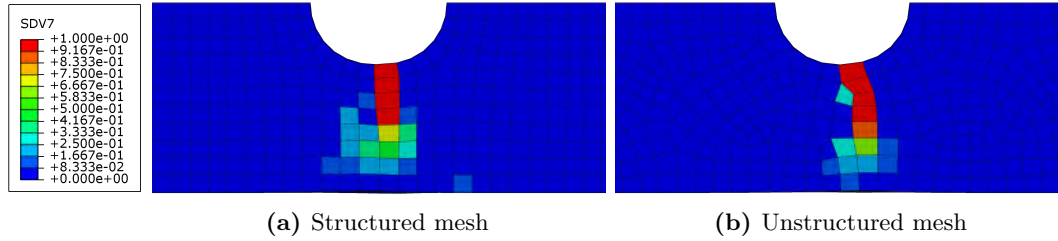


Figure 4.21: Comparison of fibre damage path d_f in OHT QI-II simulation models with structured and unstructured meshes

The strength results of the study with different element sizes are shown in Fig. 4.22. All simulated strengths are considerably lower than the experimental values. This is due to the fact that in-situ strengths were not used for this study, cf. Section 4.5.3 on in-situ strengths.

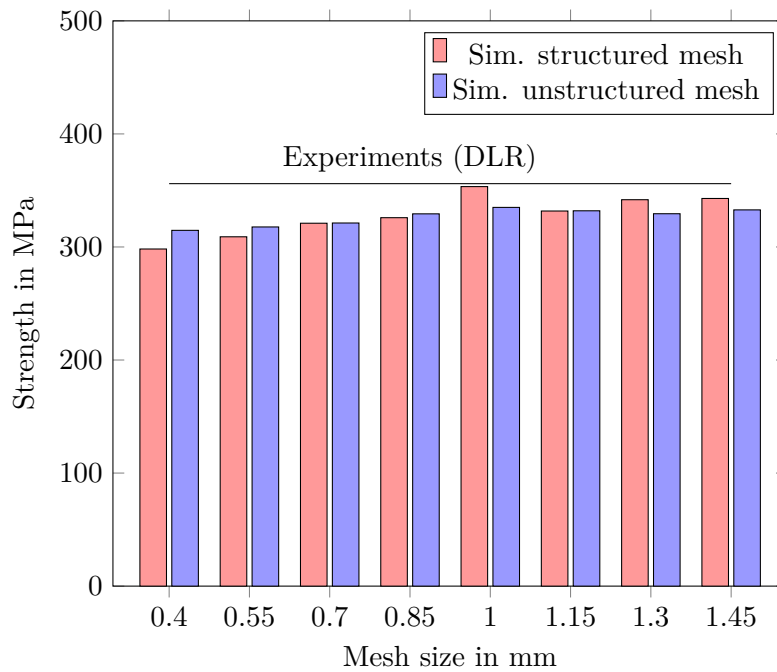


Figure 4.22: Mesh convergence of M21-T700GC 25/50/25 laminate (QI-II)

The above figure shows that the strengths decrease from coarse to fine mesh, with an outlier at 1 mm element size. It is noteworthy that this decrease is more pronounced for structured meshes. The models with structured meshes result in strength values between 298 MPa and 353 MPa, whereas unstructured meshes give strengths between 315 MPa and 333 MPa. The simulations with the unstructured meshes show lower results for coarser meshes and higher results for finer meshes compared to the structured mesh. Therefore,

the influence of mesh size on the predicted strength is lower for unstructured meshes. The differences between structured and unstructured meshes can be attributed to the slight influence of the element edge orientation on the damage path as shown in Fig. 4.22.

Since unstructured meshes are easier to generate, which complies with a pragmatic approach, and they are less sensitive to size changes, unstructured meshes are used in the following for the OHT simulations.

With results between 315 MPa to 330 MPa, the differences between the recommended mesh size of 0.85 mm and the smallest of 0.4 mm are considerably small. This supports the plausibility of the procedure for determining the mesh size proposed by Břzant and Oh [150]. For the simulations with M21-T700GC, an in-plane element size of 0.85 mm is used in the further simulations.

In the same way, the mesh size for 8552-IM7 is determined to 0.625 mm. A further discussion and explanation of mesh sensitivity in PDA can be found in [179] and [180].

4.6.4 Strength results of the numerical analyses

A comparison of the strength calculated using the simulation model described above with the experimental results is shown in Fig. 4.23 in form of a bar chart. All configurations introduced in Section 4.6.1 are simulated. The configurations UD-0 and UD-90, which contain only fibres in one direction are simulated using the normal UD strength only. As described in Section 4.5.3, no in-situ strength effect occurs in UD laminates. The multidirectional configurations QI-I, QI-II, and CP are simulated both using the normal UD as well as the in-situ strength. In this way, the use of in-situ strength for the mesoscale composite modelling in this work can be assessed.

Like all experimental results, the UD-0 test series shows little scatter. The mean strength of this series, considering the load at which the laminate splits into three parts, as described in Section 4.6.1, is 348.3 MPa. The failure mode observed in the UD-0 experiments could not be reproduced with the developed material model. No damage path develops in the direction of the load, starting from the hole edge. The damage propagates from the edge of the hole perpendicular to the load direction. For this reason, the forces achieved up to the load drop are with 727.8 MPa significantly too high. Since no pronounced damage progression is to be expected for UD-0 and the test specimens, as seen in the experiments, fail abruptly in the described mode after initiation of the damage, the stress at which the global material stressing effort $E f f^m$ reaches a value of 1.0 is used for comparison. With 443.5 MPa and a deviation to the experiment of 27.3 %, this value is still significantly higher than the experiment, but considerably lower than the stress at load drop. It must be noted that this approach is an approximation to define a comparable point between experiment and simulation. The prediction of the failure load of specimens with UD laminates having fibres oriented in the load direction using the presented material model needs to be further investigated in the future.

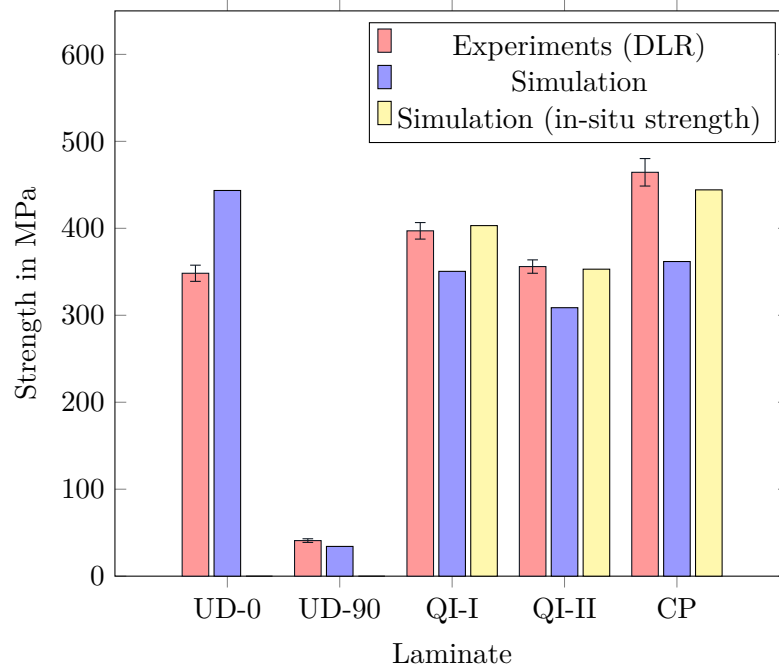


Figure 4.23: Comparison of experiments and simulations of M21-T700GC OHT tests

With a strength of 40.9 MPa, the UD-90 test specimens have by far the lowest strength and show negligible scatter. The simulation results is with 34.2 MPa 15.4 % lower than the experiment.

When looking at the multidirectional series, mean strength values between 356.0 MPa for QI-II and 464.4 MPa for the CP layup are observed. With 397.1 MPa, the configuration QI-I is in between. It needs to be mentioned that all three configurations show some scatter, but the scatter is clearly lower than the scatter of the UD-0 series. Without considering the in-situ strength, the OHT strengths determined with the simulations show deviations between -11.7% and -22.1% , which is significantly lower than the strength determined in the physical tests. Considering the higher in-situ strengths, the deviations are reduced to a range between -4.3% and 1.5% , which is considered a satisfying accuracy for this kind of simulations.

Hence, it can be concluded, that in-situ strengths should be used for multidirectional layups and that the simulations are, in general, in good correlation with the experimental results.

In the following using the example of QI-II, the stiffness of the model is compared to the experiment and the influence of pseudoplasticity is assessed. A more detailed analysis of the failure behaviour and occurring failure modes is given together with the comparison between Cuntze's FMC and Puck's APSC in the sections 4.6.6 and 4.6.7.

4.6.5 Stiffness and influence of intralaminar plasticity

The stiffness measured during the physical testing of one of the QI-II specimens by using a DIC system is consulted to assess the stiffness predicted with the models. In this scope, also the influence of the pseudoplasticity on the simulations results is evaluated. For this purpose the plasticity algorithm in the material model is deactivated. Both subjects are discussed using the stress-strain plot in Fig. 4.24.

As shown earlier, cf. Fig. 4.17, the influence of pseudoplasticity is considerably large for a $\pm 45^\circ$ -coupon. With the example of the OHT specimens QI-II, the influence is examined for layups typical for aircraft structures. So far, all simulations in the work have been performed with pseudoplasticity, unless otherwise described. However, it would save characterisation effort and simulation runtime if the plasticity could be neglected. The stiffness in the experiment is captured from both simulations, with and without plasticity, up to a strain of 0.005 and a stress above 300 MPa. From that strain on, the stiffness of the simulation without plasticity is slightly lower than the one measured in the experiment. The stiffnesses of the simulation with plasticity and the test agree even further up to a strain value of 0.0075. The difference slightly increases when reaching the point of specimen failure.

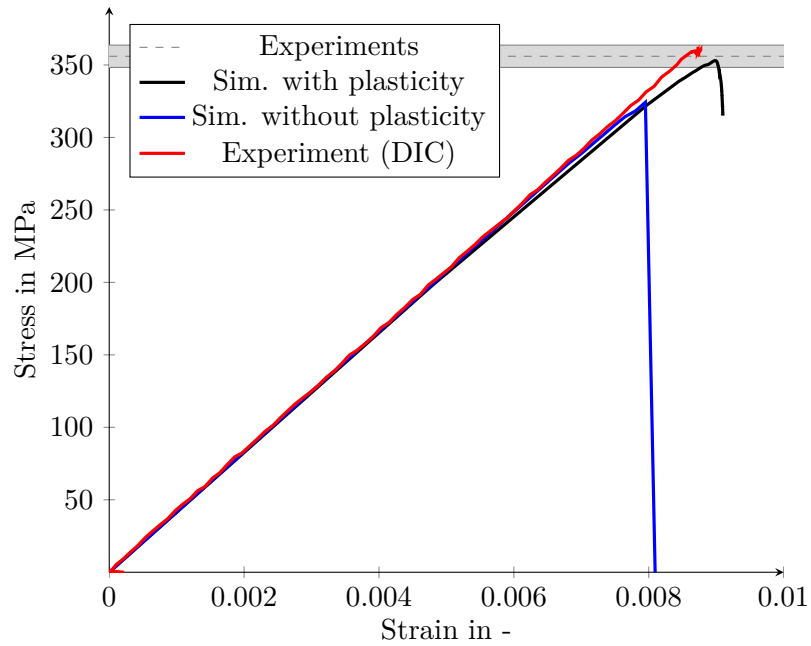


Figure 4.24: Comparison of stress-strain data of OHT simulations with and without plasticity with experimental data (M21-T700GC, QI-II, 25/50/25)

It is noteworthy that the influence of pseudoplasticity on the strength is significantly larger. The simulation without plasticity underestimates the average strength by 9.0 %, whereas the simulation with plasticity gives a higher strength and underestimates the average strength by 1.1 %. With this deviation, the simulation with plasticity lies within

the standard deviation of the experiment, which is represented by the grey area in the diagram. This higher strength is attributed to load redistributions after onset of yielding. In summary, it can be said that the stiffness is well represented with the material models in combination with the material data derived in Subchapter 4.5 up to a high loading but not until final failure.

The reason for the difference in stiffness at high stresses between the experiment and the simulation was assumed to be the highly localised loading in the OHT specimen, which probably cannot be captured by the chosen mesh size. However, simulations with finer meshes do not show any difference in terms of the stress strain curve. Therefore, this possible cause can be excluded. However, the true cause could not be conclusively determined. Although the simple plasticity model shows good agreement with the experiment for the $\pm 45^\circ$ -coupon, it is possible that the model reaches its limits with the present localised loading. Using the plasticity parameters prior to the calibration described in Section 4.5.2, does not improve the agreement between simulation and experiment either.

However, taking stiffness and strength into account the consideration of pseudoplasticity is recommended or should at least be checked in each individual case.

4.6.6 Fracture patterns

In this section, the experimental fracture patterns of the test specimens CP, QI-I, and QI-II are compared with the numerical results as examples. This is done by using the variable for damage due to IFF d_m . The reason for this is that elements are removed from the simulation when complete fibre damage is reached. Thus, no meaningful images can be obtained. The fracture patterns of the UD-0 and UD-90 specimens are not shown because they simply result in a straight crack.

Fig. 4.25 shows the experimental fracture patterns next to semi-transparent plan views of the simulations.

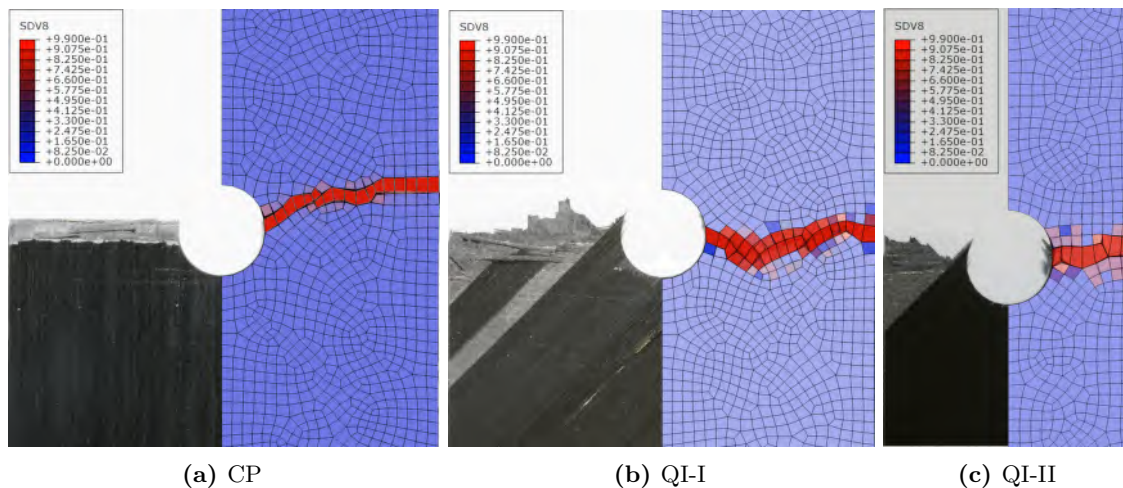


Figure 4.25: Comparison of experimental fracture pattern with numerical damage due to IFF

It can be seen from the figure that, as in the test, the damaged area in the QI layup is

wider than in the test specimen with CP layup. However, the fracture band in the simulation is, unlike in the experiments, not in the middle of the specimen. This is attributed to the unstructured mesh resulting in a slight preferential direction of damage. In general, it can be stated that the damage is qualitatively well captured. The fracture patterns in the simulations differs significantly for the two layups.

4.6.7 Detailed comparison of progressive damage analyses with Cuntze's FMC and Puck's APSC

In addition to the simulations using the FMC, the failure behaviour of the specimens is also predicted with the APSC failure criterion by Puck. On this basis, a comparison in terms of prediction accuracy and computation time between the two failure criteria used in combination with the proposed model is performed.

Four configurations, namely UD-0, UD-90, QI-II, and CP are used for this comparison. For the corresponding simulations with FMC and APSC, the same simulation models, ergo the same meshes and the same material data are used. The models differ only in the parameters for the failure criteria, cf. Section 4.5.4. The two specimens with multidirectional layups, QI-II and CP, are simulated using in-situ strengths.

It needs to be mentioned that strength results with the APSC are in all cases higher than with the FMC. However, the difference between FMC and APSC largely depends on the specimen under consideration.

At this point it should be said that the variant of the material model that uses the APSC as a failure criterion is also not able to correctly predict the failure behaviour of the UD-0 test specimens. The stress at the point where the maximum bearing capacity is reached is with 863.6 MPa even higher than with the FMC. For this reason, as in the case of the FMC, the point of damage initiation is shown in Fig. 4.26. However, this stress is in the APSC case with 494.7 MPa again higher compared to the FMC case with 443.5 MPa.

For the UD-90 a slightly higher strength results with the APSC than with the FMC. The deviation to the experiment reduces from -15.4 % to -13.9 % by changing to APSC. For the QI-II case, the APSC predicts a 6 % higher strength than the experiment. In this case, the FMC is considerably accurate, with only 0.8 % deviation to the experimental strength. Moreover, the strength of the CP specimen is 2.2 % overpredicted by the APSC model, compared to 4.2 % with the FMC model.

In general, it can be said that in cases where the APSC is more accurate than the FMC, the difference between the two failure criteria is relatively small. In the other two cases, UD-0 and QI-II, where the FMC is more accurate, the APSC deviates more considerably from the experimental values. For this reason, looking at all layups under consideration the accuracy of the FMC is rated higher.

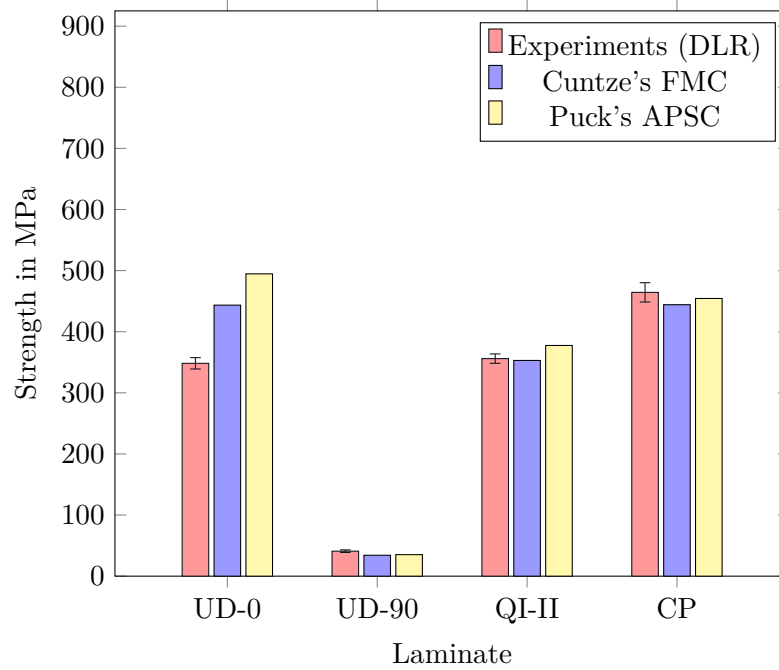


Figure 4.26: Comparison of strength prediction between Cuntze's FMC and Puck's APSC

The detailed comparison of the progressive damage analyses with Cuntze's FMC and Puck's APSC is performed with the example of the QI-II OHT specimen. However, the findings hold true also for the other specimens analysed. In Fig. 4.27 the resulting load-displacement curves from both analyses are plotted. It can be observed that the predicted stiffness of the specimen is the same for both versions of the material model. As with all analysed specimens, the predicted failure load with the APSC is bigger than the load predicted by the FMC. In order to gain further insights, the damage initiation points are marked in the diagram. The initial transverse matrix damage is marked by an d_m , while first matrix damage in shear is marked with d_s . The start of fibre damage is marked with point d_f . The subscript P assigns the points belonging to the prediction with Puck's APSC and the subscript C to the one with Cuntze's FMC. It can be seen that damage in fibre direction initiates first and at nearly the same load level. Transverse matrix damage is predicted at lower load level by the APSC (303 MPa) than with the FMC (318 MPa). The in-plane shear matrix damage with the material model using Puck's APSC ($d_{s,P}$) starts at the same load level as transverse matrix damage ($d_{m,P}$) due to the formulation of damage variables. This point is predicted much later, near to the point of total failure, with Cuntze's separate formulation for IFF under shear stress (IFF3), cf. $d_{s,C}$. It must be noted that, although first matrix damage is predicted at lower load levels with the APSC compared to the FMC, the calculated failure load is higher.

In order to assess the influence of the additional iterative fracture angle search as well as the additional algorithms to divide the damage portions from the interfibre fracture according to the fracture angle between the different stress components the computational

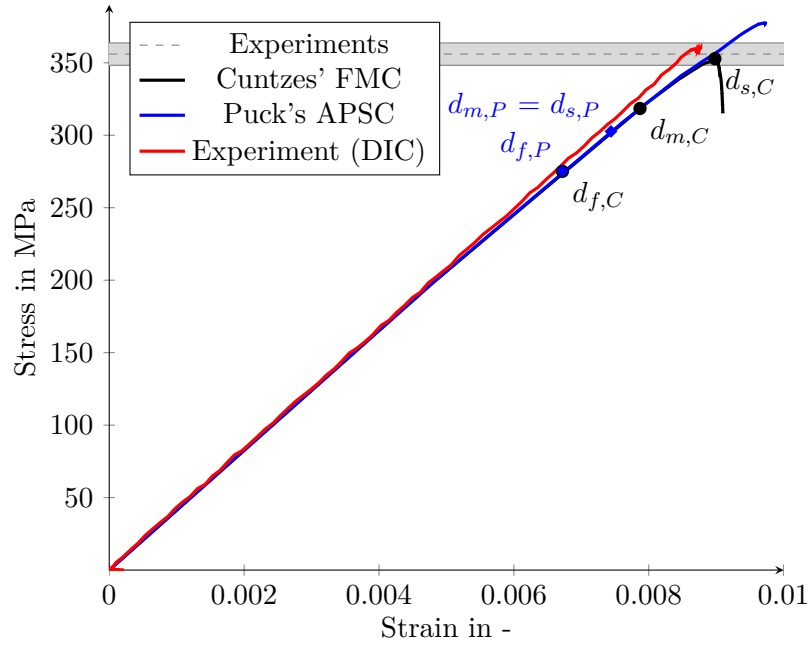


Figure 4.27: Comparison of stress-strain data from OHT simulations with Cuntze's FMC and Puck's APSC (M21-T700GC, QI-II, 25/50/25)

expenses of the simulations with the FMC and the APSC are compared. At this point it should be mentioned that the fracture angle search causes the majority of the additional computing time. Measures to increase the numerical efficiency of the APSC, such as the golden section search [181, 182], are not considered in this work. They shorten the computing time but, unlike the FMC, still require additional algorithms. All simulations were performed with the same solver settings on a workstation with an Intel® Xeon® E5-2670 v3 processor and 48 GB RAM using eight CPU cores. The models consist of about 12,000 elements with about 32,000 equations in total. The simulations are evaluated at fixed time increments by a Python script and the analysis is terminated if a load drop of at least 7.5 % has occurred. In this way, comparability between the simulations is ensured. The results regarding the number of increments, the total CPU time and the average time per increment are listed in Tab. 4.10. Since the damage progression of UD-0, as described in Section 4.6.4, is not properly represented in the simulations, this configuration is not used to compare the computation times.

It can be seen that the analysis of the same model always takes more increments as well as more CPU time when using the APSC. The simulation of the QI-II specimen with Puck's APSC was aborted before reaching the specified load drop of at least 7.5 % after 50,000 increments because of slow convergence. However, as can be seen in Fig. 4.27, a slight drop in stress is noticeable.

The higher number of increments needed for the model with Puck's APSC can partly be attributed to the fact that the load-bearing capacity is preserved for a longer time

after the damage has been initiated, compared to the prediction with Cuntze's FMC. This effect is intensified by the fact that the time step decreases with the onset of the damage. Furthermore, the average time per increment is always higher if the APSC is used. This can be explained by the additional effort required for the iterative fracture angle search and the split of the interfibre damage. The model with Cuntze's FMC is, as expected, more efficient in the calculation.

Table 4.10: Comparison of computational expense of proposed material model with different failure criteria on the basis of OHT specimens with different layups

Failure criterion	Specimen	No. of increments	Total CPU time in s	Average time per increment in s
Cuntze's FMC	UD-90	160	4,410	27.6
	QI-II	2,648	32,711	12.4
	CP	300	10,167	33.9
Puck's APSC	UD-90	241	7,249	30.1
	QI-II	50,000*	762,751	15.3
	CP	680	25,161	37.0

* aborted before 10% load drop after 50,000 increments

4.7 Simplified versions of the intralaminar model

For further studies, some simplified versions of the material model are derived. One simplification, namely the neglect of pseudoplasticity and therefore, linear-elastic version up to damage, was already discussed in Section 4.6.5. In addition, a version for continuum shell elements (SC8R) as well as a version for Abaqus/Explicit are presented in the following.

4.7.1 Version for continuum shell elements

Continuum shell elements have an unlimited z-stacking capability and for this reason, they are suitable for the considered LWT approach, cf. Section 4.2.2. With the example of the Pagano solution in Section 4.2.3 it is shown, that the computation time for the SC8R reduced integrated continuum shell elements is a little higher than the one for baseline C3D8R elements, but the former are even more accurate. Therefore, in principle, they are appropriate for the planned application.

It needs to be mentioned that the version for continuum shell elements differs from the solid element version in that not a full 3D stress state is implemented, but a 2D plane stress state. Therefore, the constitutive model, the plasticity model, the failure criterion, the stiffness degradation, and the algorithm for the tangent stiffness matrix have to be altered to the plane stress case. Except for the FMC by Cuntze for the 2D case, all changes are made in accordance with the publication of Din et al. [138]. The 2D version of Cuntze's FMC can be found in [145].

As for the other in-depth comparisons, the OHT example QI-II was chosen as a representative case for the comparison of solid and continuum shell variants of the material model. The resulting stress-strain curve can be found in Fig. 4.28.

The comparison of the two models, using solid and continuum shell elements respectively

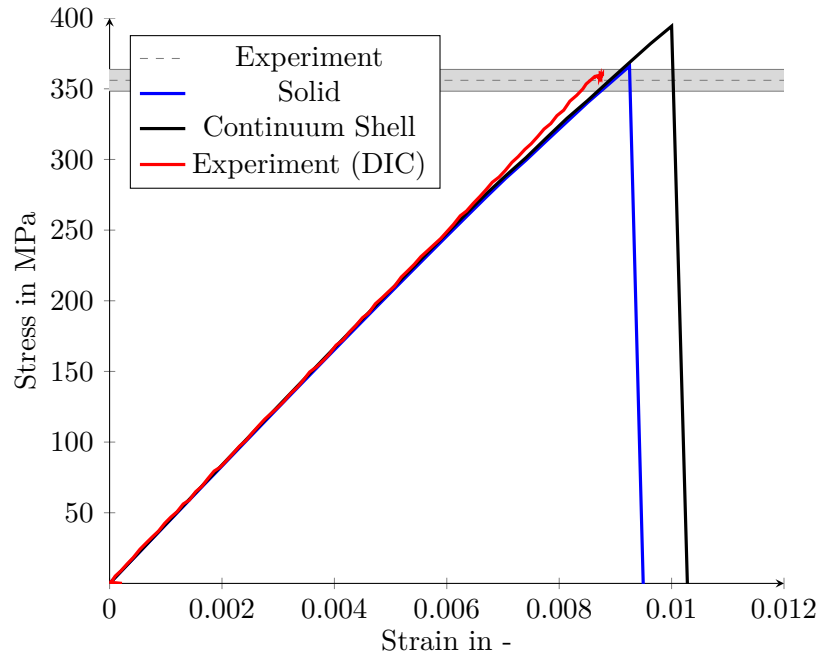


Figure 4.28: Comparison of solid and continuum shell based modelling at the example of open hole tension test (QI-II)

shows that the resulting stiffness of both simulations is in good agreement. For the purpose of comparison, the stress-strain curve recorded with DIC during one test is also plotted in the above diagram. The difference between the models is a considerably higher strength of 394 MPa calculated with the continuum shell version. This may be attributed to the neglect of damage in through-thickness or z-direction and could be overcome by combining it with discrete modelling of interlaminar damage. At the end of Chapter 5, after the interlaminar modelling technique is chosen and the interlaminar material properties are determined, this is done on the basis of OHT specimens. The detailed analysis of the differences between solid and shell element-based simulations is also carried out in Subchapter 5.6.

4.7.2 Implementation as (V)UMAT for Abaqus/Explicit

The simulations presented so far have all been solved with the UMAT for Abaqus/Standard introduced in Section 4.4.4. With the combined method for the entire bonded joint, further non-linearities are added by including cohesive contacts or elements as well as elastoplastic material behaviour of the adhesive. This can lead to convergence problems with the implicit solver Abaqus/Standard. For this case, the presented intralaminar material models are also implemented for Abaqus/Explicit as (V)UMAT. The routine is much simpler because for Abaqus/Explicit, the material model only needs to calculate updated stresses and does not have to provide the tangent stiffness matrix. Without going further into detail about the changes to the routines, with the OHT QI-II example it is demonstrated below that both implicit and explicit routines provide comparable results.

In Fig. 4.29 the stress-strain results calculated with the two material models are shown alongside the results from the experiments.

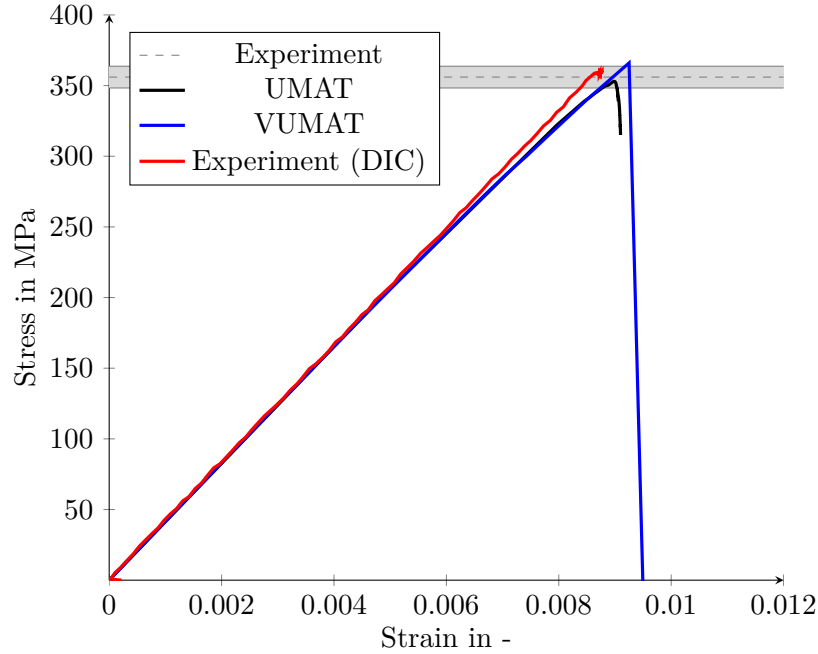


Figure 4.29: Comparison of stress-strain data of OHT simulations with UMAT (dynamic implicit solver) and VUMAT (explicit solver) (M21-T700GC, QI-II, 25/50/25)

It can be said that the simulations agree in terms of stiffness. The strength of 366 MPa predicted with the VUMAT is slightly higher than the strength of 352 MPa resulting from the dynamic implicit simulation using the UMAT. It is also slightly higher than the experimental mean strength of 356 MPa.

The cause for this difference was investigated but could not be finally answered. A simulation of the OHT specimen with continuum shell elements using the Abaqus built-in Hashin material model results in the same stress-strain both for Abaqus/Standard and Abaqus/Explicit. Hence, the described difference originates from the user-defined material model. Single element tests of the UMAT and the VUMAT with the M21-T700GC material parameters, cf. Appendix D, are the same except for the degradation behaviour in the fibre direction. While the VUMAT shows, as desired, a linear degradation, the UMAT provides a non-linear curve. This may be caused by an error in the numerical estimation of the tangent stiffness matrix in the UMAT, which unfortunately could not be eliminated in the course of the work.

However, the 4.0% difference of the explicit simulation to the implicit simulation and the 2.8% difference to the experiment, are not considerably large. Accordingly, it can be concluded that explicit simulations using the VUMAT variant of the material model give comparable results to the implicit simulations and can be used for further work.

4.8 Conclusions and recommendations for the holistic approach

This chapter focuses on the intralaminar modelling of the composite adherends for the holistic progressive damage model. For this application, the LWT approach is chosen. For this purpose, a user-defined 3D intralaminar material model including transverse isotropic pseudoplasticity has been developed, implemented, and validated. In order to do so, the intralaminar material properties of two materials, M21-T700GC and 8552-IM7, were determined. For the first material, the determination of the characteristic values is primarily based on tests carried out at DLR, while the determination of the characteristic values for the second material is based on literature data. The material model was successfully validated on several OHT test specimens made of both materials and different multidirectional layups. However, the strength and failure mode prediction of specimens with UD-layups with fibres oriented in the load direction needs further investigation.

After that, studies regarding the choice and necessity of different modelling features were carried out. For the holistic model, it can be concluded, that pseudoplasticity should be considered not only for fibre composites with thermoplastic matrix material but also for toughened epoxy materials like M21 and 8552. In this context, a question was whether pseudoplasticity could be neglected to save computational effort. The influence of pseudoplasticity depends on the layup but must be evaluated on a case-by-case basis. Even for QI layups, significant difference in predicted strengths were found.

Another finding is that in-situ strength should be used in multidirectional layups to increase accuracy of the predictions.

When comparing the failure criteria of Cuntze and Puck, it can be concluded that the FMC by Cuntze is more accurate and also more efficient regarding computation times.

However, the element choice for composite adherends in the holistic model needs further investigations. When using reduced integrated solid elements (C3D8R), accurate results are achieved without discrete delamination modelling. Yet, the use of reduced integrated continuum shell elements (SC8R) results in an overprediction of strength. This circumstance will be examined in Section 5.6.1 when combined with discrete interlaminar damage modelling. Up to now, the baseline is C3D8R without additional modelling of delaminations.

After having developed the modelling of the intralaminar behaviour of the composite adherends, the following Chapter 5 will examine the interlaminar behaviour and its modelling in the holistic PDA approach.

CHAPTER 5

Numerical modelling of interlaminar damage growth

Which approaches are suitable to model the interlaminar behaviour of the adherends, how can the necessary parameters be determined, and should different interface ply orientations be considered?

Apart from the intralaminar behaviour, the interlaminar behaviour is decisive for the failure behaviour of the adherends made of fibre composites. Within this chapter, the question is answered whether and how interlaminar behaviour should be considered in the holistic PDA approach.

Parts of this chapter have previously been published in [8].

5.1 Structure and approach

The chapter starts with a brief overview of the state of the art in delamination observed in multidirectional laminates and its experimental characterisation. After that, mesoscale modelling approaches for the holistic PDA approach are identified and analytical methods for data reduction as well as for verification are presented. An experimental test campaign for the full characterisation of four different interfaces is performed. This is accompanied by a verification of the identified parameters using the numerical and the analytical models. Then, the numerical modelling approach developed in this way is applied to the OHT test specimens from Chapter 4. The chapter closes with a recommendation for the modelling of the composite adherends in the holistic PDA approach.

5.2 Delaminations in multidirectional composite structures

In this subchapter, a brief overview of delamination in multidirectional composite structures and its characterisation is given.

5.2.1 Interlaminar failure mechanism

A comprehensive overview of the role of delamination in the failure of fibre composites is provided by Wisnom [183] and the following paragraph is a brief summary of his description. Interlaminar damage or delamination differentiates the behaviour of fibre composites structures from metallic ones and is a critical failure mechanism. Delaminations arise due to high interlaminar stresses and low through-thickness strength. This low strength through the thickness can be explained by the architecture of typical fibre composite structures.

There is no reinforcement in through-thickness direction because fibres lie only in the plane of the laminates. For this reason, load through the thickness is carried by the weak matrix only.

Wisnom points out that most studies investigate delamination under through-thickness stresses. However, they also play an important role in determining in-plane strength: Released energy due to the unloading of fibres drives the in-plane failure of fibre composites. This unloading can be caused by two different phenomena. On the one hand, by fracture of the fibres themselves, and on the other hand, by the joining up of matrix cracks and delaminations producing fracture surfaces without FFs.

Fig. 5.1 shows the possible fracture modes, caused by different load cases. Mode I represents crack growth under peel loading, where the crack propagates perpendicular to the loading direction. Crack growth parallel to the direction of loading is caused by shear in mode II. The fracture mode III is also caused by shear with crack growth occurring transversely to the direction of loading. Combinations of the individual modes are possible and are referred to as mixed mode.

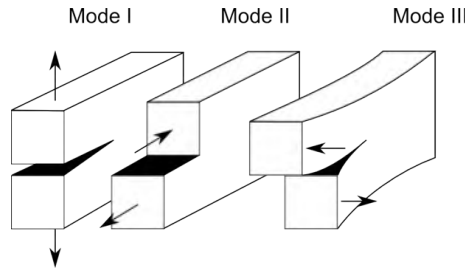


Figure 5.1: Fracture modes under peel and shear loading in and normal to the plane of crack propagation

An established method to determine failure loads for CFRP is the use of cERR. According to Griffith [184], the loss of energy per area is assumed to be an inherent material characteristic value G_c . These G_c values can be determined from static crack propagation experiments with beam type specimens and artificial precracks.

5.2.2 Static crack propagation experiments

To represent nearly pure fracture modes and characterise the respective fracture resistance, several static experiments have been established for use with UD CFRP. The DCB test is the only standardised test for determining the cERR in mode I quantified as G_{Ic} [185]. In the DCB test, a peel load is applied directly to the crack, which is globally equivalent to a pure mode I load. However, if the upper and lower beams have different elasticity characteristics, local parasitic shear modes may occur [186]. In the experimental reproduction of pure mode II to determine G_{IIc} , the challenge is to apply the interlaminar shear load between the lower and upper arm of the specimen and thus correctly at the crack. Therefore, bending tests are usually considered. An example for this is the most commonly used End Notched Flexure (ENF) test, which is also standardised [187]. In the ENF test,

a three-point bending setup is used and a moment creates a relative displacement between the upper and lower test specimen leading to shear in the interface. Nevertheless, it needs to be mentioned that a disadvantage for the correct determination of G_{IIc} is the indirectly applied shear load, as well as the effect of additional energy dissipation due to frictional effects in the crack interface. A comparison between the ENF test in 3-point and 4-point bending setup by Wang et al. [188] shows 2% higher values for the 4-point bending test. Furthermore, Schuecker et al. [189] could not determine a significant difference between the two tests, if compliance and crack length were considered accurately. It is noteworthy that pure mode I or mode II loads rarely occur in real structures, but mostly mixtures of the modes. In order to also be able to characterise the behaviour under these mixed mode loads, various experiments were developed in the past. Yet, most tests have not gained acceptance because they either allow only a limited range of mixed mode ratios or the interpretation of the test data is difficult and requires FEM analyses [190]. For these reasons, the Mixed Mode Bending (MMB) test from Crews and Reeder [191] has become popular as it allows the testing of any mixed mode ratio and is relatively easy to evaluate.

5.2.3 R-curve behaviour

During crack growth, there may be an increase in the cERR, so that different values exist for crack initiation and propagation. This resistance, also called R-curve behaviour, originates from micromechanical processes. In particular, the bridging of the gap by individual fibre bundles causes an increase of the delamination resistance during crack propagation, as shown schematically in Fig. 5.2.

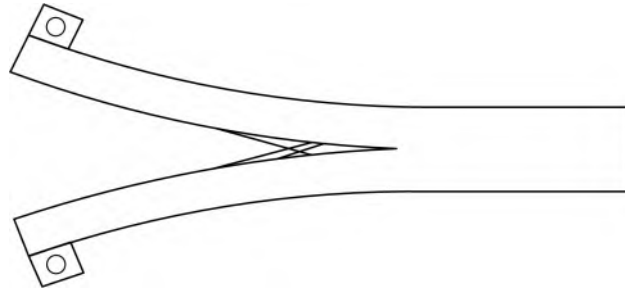


Figure 5.2: Schematic illustration of fibre bridging in the DCB test

The first researchers to investigate this behaviour were Johnson and Mangalgiri [192]. They showed that an increase of fracture resistance is accompanied by an increase of fibre bridging. Especially in the case of interface layers of the same orientation, UD 0° fibre bundles cause the layers to penetrate each other. However, R-curve behaviour is not a pure material property. In fact, it depends on the geometry of the test specimen [193].

5.2.4 Interface-orientation-dependent fracture toughness

This leads to varying cERR for different layers adjacent to the interface, like occurring in multidirectional laminates. Composite layups are in general composed of laminas with varying orientation to adapt stiffness and strength in accordance with the main load directions. The delamination can occur between layers of different orientations as, in

general, layers of 0° , 90° and $\pm 45^\circ$ orientations are used. Andersons and König [92] show in their review that the cERRs in multidirectional laminates depend on the fibre orientation adjacent to the interface under consideration.

Pereira et al. showed that G_{Ic} values depend on the orientation of the adjacent layers in the interface and higher values occur for $0^\circ//0^\circ$ interfaces than for $0^\circ//45^\circ$ and $0^\circ//90^\circ$ interfaces [186, 194]. On the contrary, in mode II $0^\circ//0^\circ$ interfaces show lower G_{IIc} values than multidirectional interfaces [195]. Conflicting results are presented by Bienias [196], where G_{IIc} is observed to decrease with increasing ply angle difference. Andersons and König present a review of experimentally determined cERR for different interfaces of adjacent layers and external loading direction [197]. They state that G_{Ic} values of a UD interface increase strongly with an increase of loading direction from parallel to transverse loading to fibre orientation, meaning that an interface of $0^\circ//0^\circ$ has a lower fracture toughness than a $90^\circ//90^\circ$ interface. On the contrary, in mode II the UD interface shows a small decrease of G_{IIc} with increase of the loading direction.

Two more recent studies from Blondeau et al [198] and Yu et al. [199] investigate the R-curve behaviour of multidirectional carbon/epoxy prepreg laminates with different interface orientations under mode I loading. Both studies conclude that the steady state cERR is much more influenced than the initiation cERR. It needs to be mentioned that the work from Pichler et al. [199] is much more holistic since they investigate a carbon/epoxy prepreg material under mode I, mode II and mixed mode loading using DCB, 4ENF and MMB tests. The findings regarding the cERR are comparable to those in [198, 199]. However, they highlight that almost all studies examine behaviour in one mode only, but that there is a lack of studies that examine all relevant modes.

An explanation lies in the cERRs determined on macroscopical level. On this level an idealised fracture surface perpendicular to the adjacent layers is assumed. On micromechanical level a delamination shows different fracture characteristics as can be identified by scanning electron microscopes [200]. Pure resin failure is combined with interface failure between fibres and resin. The crack follows the fibres, leading to a coarse and increased fracture surface. All the phenomena and especially the increased fracture surface are included in the macroscopical effective cERR leading to different G_c values for different combinations of adjacent layer orientation. As laminates in general are composed of layers with multidirectional orientations, the cERRs have to be determined for all possible layer combinations.

5.2.5 Experimental characterisation of multidirectional laminates

Investigations by Pereira et al. [186] have shown that without generating a natural precrack cERR in DCB experiments can be considerably lower for multidirectional interfaces. For UD interfaces, on the other hand, no serious difference was found. In mode II, the resin accumulation at the ends of the foil can increase the crack resistance. This results in higher cERRs for artificial precracks, especially for $0^\circ//0^\circ$ interfaces [195]. Nevertheless, the introduction of a natural mode II precrack is very difficult, since a total failure of the specimen can already occur due to sudden crack propagation. The otherwise common procedure of shortening a DCB test specimen and using it as an ENF specimen is not possible for multidirectional laminates due to an inhomogeneous crack front and observed crack jumping.

For the investigation of multidirectional interfaces or those between different materials, an asymmetrical layup of the specimens is inevitable. This leads to undesired fracture modes in addition to the dominant fracture mode, which is especially caused by undesired torsion in $\pm 45^\circ$ -layers [195, 201, 202]. The result is an inhomogeneous crack front over the specimen width.

It is possible to consider the influence of the asymmetry on the mode ratio and to determine the individual mode portions [203, 204].

To determine almost pure mode cERR values the influence of the asymmetry can be reduced by balanced layups, which have low laminate coupling terms [197, 205]. Recommendations exist for specimens with multidirectional interfaces, which must be fulfilled for both the upper and the lower specimen arm. For the coupling of the bending terms, Prombut et al. [206] propose the following limit:

$$D_c = \frac{D_{12}^2}{D_{11}D_{22}} \leq 0.25. \quad (5.1)$$

In addition, the bending-torsion coupling should fulfil the condition,

$$B_t = \left| \frac{D_{16}}{D_{11}} \right| \ll 1 \quad (5.2)$$

These equations help to find layups which are a compromise between real world layups and the influence on the testing method.

A special phenomenon in multidirectional specimens is called ‘crack jumping’ and has, for instance, been investigated by Tao et al. [207] for mode II crack propagation. The crack leaves the interface under investigation by ‘jumping’ transversely through an adjacent layer and continues in another interface. The intralaminar crack growth dissipates energy and after crack jumping, the crack propagates in an undesired interface. Hence, the determined cERR does not describe the fracture toughness of the interface intentionally under investigation. As Choi et al. [208] investigated for $45^\circ// -45^\circ$ interfaces, edge inserts could be used to prevent crack jumping.

Since there is very little work on a holistic interlaminar characterisation of multidirectional laminates, a characterisation of M21-T700GC is performed in this work. Four different interfaces, including $0^\circ//0^\circ$, $0^\circ//45^\circ$, $0^\circ//90^\circ$, $+45^\circ// -45^\circ$, are investigated. R-curve behaviour is examined under mode I loading, since the chosen and most used ENF test prevents the measuring of mode II R-curve due to unstable crack growth [209]. In addition, the fracture surfaces and crack paths as well as the crack front shapes are also investigated. Thus, a complete set of parameters is available for each interface under investigation. All characterisation tests are simulated using CZM to validate the determined effective interlaminar material properties. This leads to the description of the mesoscale modelling approach for interlaminar damage in the following subchapter.

5.3 Mesoscale numerical modelling approach

The objective of this work is to develop a description of delaminations in multidirectional laminates for mesoscale FEM analyses. State-of-the-art for modelling delaminations in this kind of analyses are the CZM [210] and the VCCT [67]. In this work the CZM is preferred because no initial crack is needed, it can be used as element- or surface-based behaviour, it needs less run-time compared to VCCT, can model both initiation and propagation, and it has the possibility to model R-curve behaviour [211, 212]. However, for the evaluation of mode mixture, especially in the specimens with multidirectional layup and interfaces, some VCCT analyses are performed.

In the CZM approach, cohesive traction is associated with a separation at an interface where a discrete crack may occur. The damage is initiated, if a maximum interface strength, also called traction, is reached. The relationship of cohesive traction and the displacement at the interface is called traction-separation law. It needs to be mentioned that there are several different types of traction-separation laws mentioned in literature. Baseline in this work is a bilinear law where the area under the traction-separation law is equal to the fracture toughness G_c of the interface [213].

For the use of CZM, regardless of element or surface-based behaviour, several numerical parameters must be chosen. The following sections describe the selected approaches to choose values for the different parameters.

5.3.1 Elastic behaviour

In CZM analyses the cohesive stiffness is a numerical parameter. Turon et al. [213] published an analytical solution to estimate the cohesive stiffness with the aim that the effective elastic properties of the composite would not be affected by the cohesive behaviour. Otherwise the delamination onset would be delayed. This is given whenever $E_3 \ll K$, i.e.,

$$K = \frac{\beta_{comp} \cdot E_3}{h} \quad \text{with} \quad \beta_{comp} \gg 1, \quad (5.3)$$

where h is the half beam thickness of the adjacent sub-laminate, β_{comp} is the parameter to ensure compliance which is much larger than 1 ($\beta_{comp} \gg 1$), and E_3 is the stiffness of the laminate in thickness direction.

Overall structural stiffness is correctly modelled above a certain value of K . However, considerably high values of K , for instance 10^7 or 10^8 N/mm³, lead to significant oscillations in the loading behaviour during the delamination propagation process. These oscillations can result in over-predictions of the structural failure load [214].

The stiffness has a strong impact on computational efficiency since the stable time increment in explicit analyses is inversely proportional to the interface stiffness. Thus, the number of required increments increases with higher stiffness. As a result, the goal is to keep the interface stiffness as low as possible.

An overview of commonly used stiffness values is given by Lu et al. [214]. Values between 10^5

to 10^6 N/mm³ are considered appropriate candidate choices for carbon/epoxy composites, allowing for both accuracy and feasibility of the simulation. As a starting point, $K = 10^5$ N/mm³ is chosen in this study. If necessary, it will be adjusted to higher values during calibration.

5.3.2 Interface strength and element edge length

In the following, it will be explained why the element size and the cohesive strength of the interface cannot be considered separately. Here, it needs to be mentioned that both depend on the cohesive zone length l_{CZ} . The physical l_{CZ} is defined as the length over which a degradation of the interface in front of the crack has occurred, whereas the numerical l_{CZ} is defined by the length over which the interface elements are degraded in front of the crack. This means that they lie in the softening part of the traction-separation response [215]. The l_{CZ} depends on the mechanical parameters of the interface. In the relevant literature, different numbers are mentioned for the minimum required elements modelling the fracture process zone. Some authors state that at least two elements are required over the zone length, but others demand up to ten elements as a minimum [213]. The majority of authors specify the required number of elements to at least three [213, 215]. There are several equations to calculate the characteristic length of the numerical cohesive zone to determine the required element length of the mesh. The original equation for isotropic materials was developed by Hillerborg et al. [216] for the use of cohesive zone models in concretes:

$$l_{ch} = E \frac{G_c}{(\sigma_{max})^2} \quad (5.4)$$

Yang and Cox developed a modified version of Eq. 5.4 for orthotropic materials where E' is an elastic modulus [217]:

$$l_{ch,I} = E'_I \frac{G_{Ic}}{(\sigma_{I,max})^2} \quad (5.5a)$$

$$l_{ch,II} = E'_{II} \frac{G_{IIc}}{(\sigma_{II,max})^2} \quad (5.5b)$$

This version was further modified by the same authors for the use with slender laminates [217]:

$$l_{ch,slender,I} = \left(E'_I \frac{G_{Ic}}{(\sigma_{I,max})^2} \right)^{\frac{1}{4}} h^{\frac{3}{4}} \quad (5.6a)$$

$$l_{ch,slender,II} = \sqrt{\left(E'_{II} \frac{G_{IIc}}{(\sigma_{II,max})^2}\right) h} \quad (5.6b)$$

Nevertheless, Yang and Cox do not give a definition of a slender body. Harper and Hallet [215] suggest calculating the characteristic length with both normal orthotropic and the slender orthotropic equations and then taking the minimum value to be conservative.

As can be seen from the equations 5.4 to 5.6b the characteristic length and hence the maximum element size depend on the interface strengths σ_{max} . Interface strength is a parameter that is difficult to measure. From unfolding tests with L-profile specimens, Petersen et al. [218] derived strengths $\sigma_{I,max}$ of 79 MPa to 94 MPa for the material considered in this work.

These values result in characteristic lengths of $l_{ch,I} = 0.36$ mm and $l_{ch,II} = 0.50$ mm and thus element lengths of $l_{el} = 0.12$ mm and $l_{el} = 0.17$ mm for three elements in the cohesive zone. For the mesoscale analysis of a coupon or even a structural detail as target application, these element lengths are too small to achieve reasonable computing times.

Element lengths of $l_{el} = 0.75$ mm to $l_{el} = 1.0$ mm can typically be found in mesoscale analysis using CDM approaches to model the intralaminar failure behaviour of the composite structure [6]. As an engineering solution, Turon et al. [213] propose the reduction of the strength, so that the cohesive zone becomes so large that even with the target element size, a minimum number of elements lie in the cohesive zone.

This can be justified by the fact that as soon as a crack is initiated and a cohesive zone exists in the structure, only the fracture toughness value is critically important. At this stage, the results are relatively insensitive to the interface strength values [213]. This approach is also followed in this work. However, not the equation proposed by Turon et al. [213] but the equations 5.4 to 5.6b presented above are used to calibrate the interface strength. The correction factor M , introduced by Harper and Hallett [215] to gain a close match between experimental and numerical results, is not applied in this work since all results show a good agreement without further down scaling the element size.

The apparent interlaminar shear strength in mode II is determined by using short-beam-shear tests. The determined value of $\sigma_{II,max} = 110$ MPa does not need to be reduced since the characteristic length is more than three times larger than the targeted element size.

5.3.3 Initiation criterion

The initiation of damage can be predicted using a stress-based quadratic power law as proposed by Ye [219]:

$$\left(\frac{T_I}{T_I^0}\right)^2 + \left(\frac{T_{II}}{T_{II}^0}\right)^2 + \left(\frac{T_{III}}{T_{III}^0}\right)^2 = 1 \quad (5.7)$$

The criterion was successfully applied in previous studies [210, 220, 221] and is also used in this work.

5.3.4 Propagation criterion

A crack propagates if the energy release rate (ERR) exceeds the fracture toughness or cERR. For pure modes, the ERR can be compared to the determined cERR in this mode. Though, in real structures, mixed mode loading conditions will occur. For that reason, a propagation criterion, which includes the mode interaction, is necessary. As discussed by Turon et al. [68], the power law criterion by Wu and Reuter [222] is the most widely used one:

$$\left(\frac{G_I}{G_{Ic}}\right)^{\alpha_{PL}} + \left(\frac{G_{II}}{G_{IIc}}\right)^{\alpha_{PL}} + \left(\frac{G_{III}}{G_{IIIc}}\right)^{\alpha_{PL}} = 1 \quad (5.8)$$

However, even though Camanho et al. [210] state that the power law criterion is good for thermoplastic composites using $\alpha_{PL} = 1$, it failed to describe the mixed mode fracture toughness of epoxy-based composites with $\alpha_{PL} = 1$ and $\alpha_{PL} = 2$. As a result, the criterion by Benzeggagh and Kenane (BK) [190] is considered to be better suited for epoxy composites. Therefore, it is used in this work.

$$G = G_{Ic} + (G_{IIc} - G_{Ic}) \left(\frac{(G_{II} + G_{III})}{(G_I + G_{II} + G_{III})} \right)^{\eta_{BK}} \quad (5.9)$$

The interaction exponent η_{BK} is determined with the help of MMB tests in this work.

5.3.5 Modelling R-curve behaviour

Davila et al. [212] showed that R-curve behaviour can be modelled by superposing two bilinear cohesive laws with different stiffnesses, interface strengths, and fracture toughnesses. The superposition of two bilinear laws resulting in a trilinear law is shown in Fig. 5.3.

The two bilinear laws may be considered as representations of different phenomena. While the first law with the subscript 1 has a high traction peak T_{n1}^0 , a short critical opening displacement δ_{c1} , and may be seen as representation of the quasi-brittle delamination

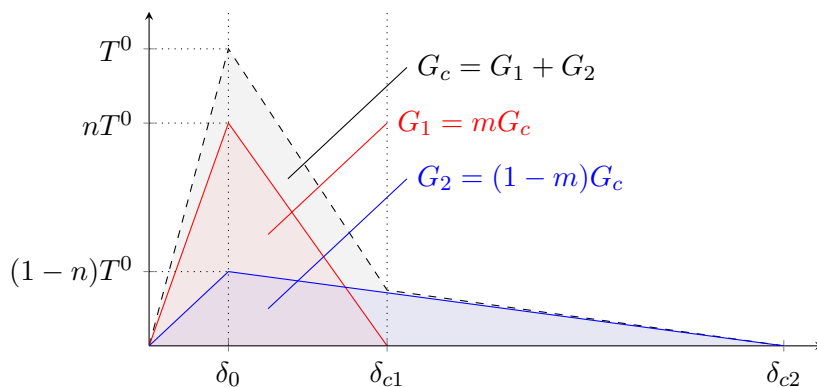


Figure 5.3: Trilinear traction-separation-law obtained by superposing two bilinear laws

fracture, the second bilinear law with subscript 2 can be regarded as a description of fibre bridging. It is noteworthy that it has a lower peak stress and a much longer critical opening displacement δ_{c2} compared to the first law. However, the two bilinear traction-separation laws are used for simplicity and do not necessarily correspond to two different failure modes that might peak at different displacement jumps. Actually, the bridging strength does not significantly contribute to the peak strength related to the intrinsic fracture process prior to fibre bridging. To obtain the characteristic values for the somehow pragmatic approach, the total interface strength T^0 and the total fracture toughness G_c are subdivided in the following manner:

$$T_1^0 = nT^0; \quad T_2^0 = (1 - n)T^0 \quad (5.10)$$

$$G_1 = mG_c; \quad G_2 = (1 - m)G_c \quad (5.11)$$

The stiffnesses are chosen in a way so that the maximum tractions of both bilinear laws occur at the same separation. Several publications have proven that this approach is able to model R-curve behaviour in numerical analyses [212, 223, 224, 225, 226]. To add, de Moraes proposes a closed-form analytical solution with a similar trilinear traction-separation law [227]. The difficulty arises in determining the parameters of the two traction-separation laws. Determination of m from the initial and the steady-state fracture toughness values is straightforward using the following equation from [224]:

$$m = \frac{G_1}{G_c} = \frac{G_{c-init}}{G_{c-ss}} \quad (5.12)$$

However, there is no commonly accepted approach to find n . In this study, the semi-empirical approaches of [212] were used first. Though, this approach did not result in a satisfying correlation with the experiments. Airolidi et al. [224] performed several parametric analyses and minimised the error between averaged experimental and numerical force-displacement curves. In this study, as in the publications [225] and [226], the determination of n is achieved by very simple means, through adjustment by testing or trial and error. The parameter n controls the interface strength T^0 . Higher values of n eliminate the pre-peak non-linearity and vice-versa. For the specimens with $0^\circ/45^\circ$ interface the numerical results with two different values for n are shown in Fig. 5.10(b).

Another approach is to modify the fracture toughness value with crack growth during simulation [228, 229, 230]. This approach is simpler in application because the values can be taken directly from the R-curves. In this way, it circumvents the lack of methods to calibrate the parameters of the superposed cohesive laws. Nevertheless, in this work the superposition approach is followed. The modelling of the R-curve behaviour is only one aspect of the holistic description of multidirectional interfaces and for the approach of for example Raimondo et al. [230], a user-defined material model is required, which is beyond the scope of this work.

5.3.6 Simulation models

FE models are used to validate the determined fracture toughness values on the basis of experimental and numerical force-displacement curves. Furthermore, the mode mix, the shape of the crack front, and the intralaminar material stressing efforts in the beams are investigated. For this reason, detailed 3D models with a layer-wise approach for the fibre composite are used. The analyses of the 3D model were solved explicitly using Abaqus / Explicit Version 2020.

In addition, the composite beams of the specimens are modelled with a layer-wise approach using reduced integrated 8-node linear solid elements (C3D8R) with an in-plane edge-length of 2.5 mm and one element per layer in through-thickness direction. In the region of interest the in-plane edge-length in crack growth direction is reduced to 0.75 mm. Deviating from this and following the recommendations from Daricik [231], a mesh refined to 0.25 mm by 0.25 mm in-plane edge length in the area around the crack is used for the VCCT analyses. The composite beams are modelled as linear-elastic transversally isotropic material using the material data from Petersen et al. [119]. In this work the element-based CZM approach is used to model the delamination because the superposition of two bilinear traction-separation laws does not work with the surface-based approach in Abaqus. As previously described, the target element size lies between 0.75 mm and 1.0 mm. The previously described procedure results in a mode I interface strength of 20 MPa for the $0^\circ//0^\circ$ interface for the element edge length of 1.0 mm and three elements in the process zone. The mode II interface strength is set to the interlaminar shear strength of 110 MPa. If the element edge length is reduced to 0.75 mm, like in this study, these strengths result in four elements in the process zone. As the ERR of the other interface variants are higher, the process zones are larger and therefore modelled with more elements. Hence, the use of the $0^\circ//0^\circ$ values can be considered as a conservative approach.

The aluminium parts, to which the hinges are attached in the experiment, are also modelled with solid elements (C3D8R) and are connected to the composite beams with tied contacts. Furthermore, translatory degrees of freedom of the middle row of nodes on the upper aluminium part are locked. At the same node set the reaction forces are taken and summarised for evaluation. A displacement in loading direction is applied to the middle row of nodes of the lower aluminium part and the remaining two translatory degrees of freedom are locked. The model of the DCB specimen is shown in Fig. 5.4.

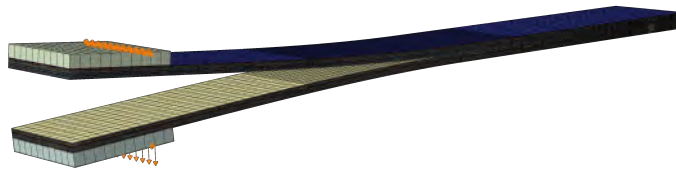


Figure 5.4: DCB model for mode I parameter calibration

In the case of the ENF specimen, cf. Fig. 5.5, the translatory degrees of freedom are locked at the nodes of the lower outer edges. At these nodes, the reaction forces are also taken for summation and evaluation. The pin, which moves down and applies the force to

the specimen, is modelled as a rigid body. A displacement is applied in loading direction at the control point and the other two translatory degrees of freedom are locked. All other modelling is the same as for the DCB specimens.

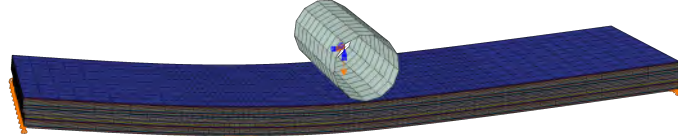


Figure 5.5: ENF model for mode II parameter calibration

The MMB specimen itself, cf. Fig. 5.6, is modelled like the DCB specimen described above. In addition, a lever is modelled with shell elements of very high stiffness to represent the movable part of the fixture. It is connected to the specimen via equation constraints, in which the translatory degrees of freedom are coupled. At the front edge of the lower load block, the translatory degrees of freedom are locked, whereas the specimen at the lower edge of the rear end is simply supported to simulate the bearing of the fixture. A displacement load is introduced at the lever edge representing the saddle of the fixture.

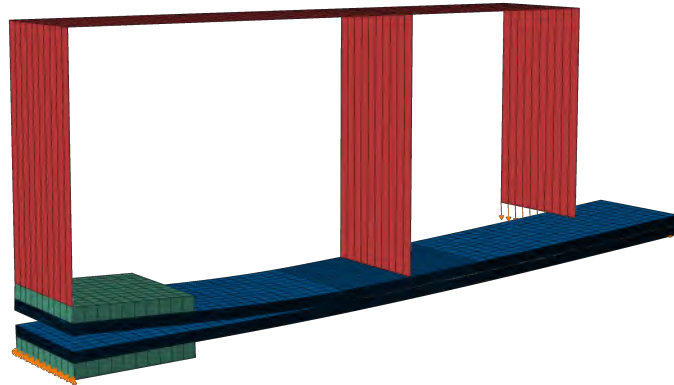


Figure 5.6: MMB model for mixed-mode parameter calibration

5.3.7 Evaluation of laminate stressing effort

As described before, crack jumping from the original plane, namely the plane with the precrack, to another interface could occur in the multidirectional specimens. This process implies that the crack migrates as a matrix crack from one interface to the other [232]. In order to assess the tendency towards crack jumping, the material stressing effort is calculated in post for the plies adjacent to the original crack plane using the FMC by Cuntze [6, 119]. With the FMC the stressing efforts in five failure modes are calculated. These are FF1 and FF2 for FF in tension and compression as well as IFF1 to IFF3 for IFF in tension, compression and shear.

5.4 Analytical methods

In this work, analytical solutions are used to verify the FE models and to quickly determine trends due to the change in fracture toughness. As suggested in the corresponding ASTM standards, the Corrected Beam Theory (CBT) is used in this work. CBT corrects the displacement for shear deformation as well as for local deformations occurring around the crack tip. The following equations used for mode I and mode II are taken from Harper and Hallet [215].

$$\delta_I = \frac{2P(a + \chi h)^3}{3E_{11}I} \quad (5.13)$$

The tip displacement δ_I can be calculated using Eq. 5.13, in which P is the applied force, a is the crack length, and h is the half beam thickness. Further, the stiffness E_{11} and the bending stiffness $I = Bh^3/12$ have to be considered. The parameter χ is calculated with:

$$\chi = \sqrt{\frac{E_{11}}{11G_{13}} \left[3 - 2 \left(\frac{\Gamma}{1 + \Gamma} \right)^2 \right]} \quad (5.14)$$

where Γ results from the following equation:

$$\Gamma = 1.18 \frac{\sqrt{E_{11}E_{22}}}{G_{13}} \quad (5.15)$$

With a linearly increasing tip displacement, the load P increases up to the point where $G_I = G_{IC}$. Then the crack starts to propagate and the load-displacement relationship for each increment of crack growth is found by combining the equations 5.13 and 5.16, where G_I is set equal to G_{IC} .

$$P_I = \sqrt{\frac{G_I(a + \chi h)^2}{BE_{11}I}} \quad (5.16)$$

The analytical load-displacement curves for ENF and MMB are calculated in the same way. Only the equations for the tip displacement and the ERR change:

$$\Delta_{II} = \frac{3P(a + 0.42\chi h)^3 + 2PL^3}{96E_{11}I} \quad (5.17)$$

$$P_{II} = \sqrt{\frac{G_{II}64BE_{11}I}{3(a + 0.42\chi h)^2}} \quad (5.18)$$

The solution for MMB is taken from the ASTM D 6671-06 standard, while the BK-criterion is used to calculate the cERR G_{Tc} under mixed mode loading.

$$\Delta_{MM} = \frac{P_{MM}}{8bE_{11}h^3L^2} [4(3c - L)^2(a + h\chi)^3 + (c + L)^2(2L^3 + 3(a + 0.42h\chi)^3)] \quad (5.19)$$

$$P_{MM} = \sqrt{\frac{\frac{4}{3}G_T b^2 E_{11} h^3 L^2}{(3c - L)^2(a + h\chi)^2 + \frac{3}{4}(c + L)^2(a + 0.42h\chi)^2}} \quad (5.20)$$

It needs to be considered that the CBT equations are intended for the use with UD laminates. To adapt the equations for the use with multidirectional laminates, in this work, for all specimen types, except the one with $0^\circ//0^\circ$ -interface, homogenised properties from the ABD matrix of the laminates can be used. This is done using the CLT. However, with CBT it is not possible to account for different properties of the lower and upper beam in case of non symmetric lay-ups [233]. The Extended Beam Theory [201, 202] does account for this effect and would probably provide better results. However, due to simplicity reasons and because the stiffness of the chosen layups for upper and lower beam are nearly identical, the author sticks to CBT like recommended in the ASTM standards.

5.5 Experimental test campaign for parameter identification

The following section describes the interface orientation dependent parameter identification for the CZM-based interlaminar modelling using DCB, ENF, and MMB specimens.

5.5.1 Specimen manufacturing

Manufacturing of the DCB, ENF, and MMB test specimens is done using UD CFRP prepreg material by Hexcel (HexPly M21/35%134gsm/T700GC) with a nominal ply thickness of 0.13 mm. In order to investigate the interlaminar behaviour of multidirectional interfaces, the laminate stacking sequence needs to be adjusted. As discussed in Section 5.2.5, the resulting laminate layups are inevitably asymmetric. However, by employing laminate layups conforming to the conditions proposed by Prombut et al. [206] in equations 5.1 and 5.2 parasitic ERR effects are reduced. The resulting laminate layups for the interfaces $0^\circ//0^\circ$, $0^\circ//45^\circ$, $0^\circ//90^\circ$, and $45^\circ//45^\circ$ are presented in Tab. 5.1. As can be seen, the requirements for D_c and B_t are well met, thus indicating minimised effects by parasitic modes.

Table 5.1: Laminate layups for multidirectional interface testing

Interface	Layup	D_c [-]	B_t [-]
$0^\circ//0^\circ$	[0 ₃₄]	0.00647	0.00000
$0^\circ//45^\circ$	[(0 ₂ /90) ₆ /0 ₂ // + 45/(0 ₂ /90) ₆ /0 ₂]	0.00191	0.00000
$0^\circ//90^\circ$	[(0 ₂ /90) ₆ /0 ₂ //90/(0 ₂ /90) ₆ /0 ₂]	0.00191	0.00000
$45^\circ//45^\circ$	[-45,0, + 45 ₂ ,0, - 45, + 45,0, - 45 ₂ ,0, + 45// -45,0, +45 ₂ ,0, + 45, - 45,0, - 45 ₂ ,0, + 45]	0.22293	0.00000

Furthermore, the use of sub-laminates within the multidirectional specimens minimises coupling effects and generates nearly isolated fracture modes. The asymmetric layups of the $45^\circ// -45^\circ$ sample originates from the investigation of edge effects in the DCB experiment [208, 234]. Moreover, the set-ups for $0^\circ//90^\circ$ and $0^\circ//45^\circ$ have also been successfully used in DCB and ENF experiments to determine the corresponding characteristic values [206, 207].

The plates are laid by hand, vacuum sealed, and cured in an autoclave using the manufacturer's recommended cure cycle. The initial precrack is introduced into the laminate during the hand layup process by insertion of a double-layered polytetrafluoroethylene (PTFE) foil of 25 μm in thickness. Subsequent to the autoclave process, the specimens are cut to size using a diamond saw and are measured with a caliper gauge. Manufacturing of the DCB and MMB specimens further requires the application of load introduction elements according to ASTM D5528 and ASTM D6671. In the present case, piano hinges are bonded onto the ends of the specimens using a film adhesive. The last step in fabricating the DCB specimens consists of applying marks on the side of the DCB specimen for determination of the position of the crack tip during experimental testing. For this purpose, the side of the DCB specimen is coated with a thin layer of white chalk ink. Black lines indicating the distance from the initial crack tip are finally added. After manufacturing, all specimens are stored at $23\pm 3^\circ\text{C}$ and $50\pm 10\%$ relative humidity until testing.

5.5.2 Test setup and procedure

Investigation of the mode I, mode II, and mixed mode interlaminar behaviour of multidirectional interfaces is conducted using the DCB set-up according to ASTM D5528, the ENF set-up according to ASTM D7905, and the MMB setup according to ASTM D6671. The specimens are tested in a servo-mechanic testing machine by Zwick (Zwick 1484), which is equipped with a 20 kN load cell.

The DCB setup in Fig. 5.7 is extended with a consumer full-frame mirrorless camera with a resolution of 42 megapixels and a spotlight in order to be able to analyse crack propagation during the DCB test. The set-up allows to take pictures at a frequency of 1 Hz synchronised with the testing machine's force and displacement output data for determination of R-curves after testing. As explained in Section 5.2.5, in the case of DCB testing, a natural precrack is introduced in the delamination plane prior to the actual test. Therein, the DCB specimen is mounted inside the testing rig and the specimen halves are separated manually until the initial crack of 40 mm in length defined by the PTFE insert is increased by 3 mm to a total precrack length of 43 mm. After introduction of the natural precrack, the specimen halves are unloaded in order to conduct the actual DCB test at a constant crosshead speed of 1 mm/min.

In Fig. 5.8, an ENF specimen inserted inside a 3-point bend setup is shown. The specimen is supported by two bottom legs, while the bending load is introduced using the centre stamp at a constant crosshead speed of 0.5 mm/min. The crack length is defined by the distance from the inserted foil to the closest bottom leg. Therefore, markings on the specimens are applied in order to facilitate the installation of the specimen inside the 3-point bend set-up and to assure correct alignment. As crack propagation during ENF

testing occurs abruptly, the crack propagation behaviour is not monitored and, therefore, no camera equipment is needed. One specimen of each test series is used to determine the correction parameters for the Compliance Calibration (CC) method recommended in ASTM D7905. Therein, the second specimen in each series is loaded to 50% of the failure load of the respective interface for crack lengths of 15, 25 and 35 mm and force-displacement data is saved for the subsequent data reduction procedure.

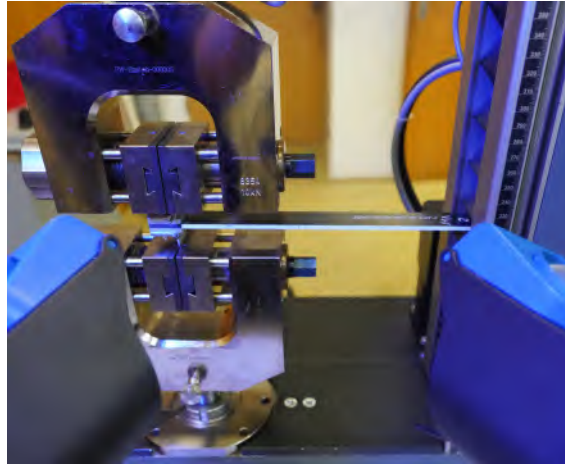


Figure 5.7: DCB specimen inside fixture according to ASTM D5528

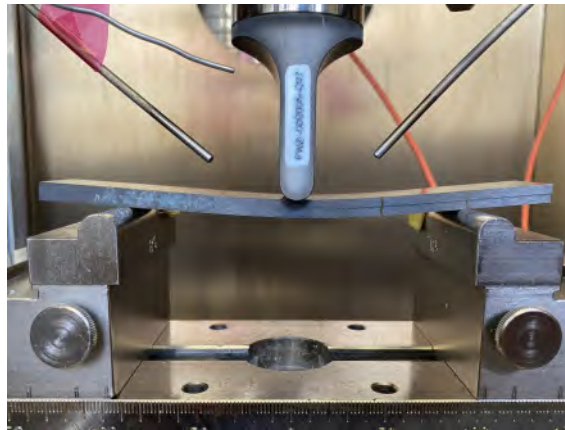


Figure 5.8: ENF specimen inside 3-point bend setup according to ASTM D7905

The experimental setup of the MMB tests is shown in Fig. 5.9. The fixture used was manufactured according to ASTM D6671. A steel base bears the lower hinge clamp and the holder for the rear roller. The upper hinge clamp as well as the middle roller are connected to an aluminium lever. At the end of the lever, a moveable saddle is mounted to adjust the mixed mode ratio. The load is introduced at this saddle via a loading yoke which is connected to the testing machine and a displacement is applied with a constant crosshead speed of 1 mm/min. Since only unstable crack propagation was observed, the evolving crack distance was not recorded.



Figure 5.9: MMB specimen inside fixture according to ASTM D6671

5.5.3 Data reduction methods

The data reduction methods proposed in the standards for DCB, ENF, and MMB testing are adopted here for determination of the interlaminar properties. As previously described, mode interaction due to parasitic ERR effects are reduced by adjustment of the laminate layup. Therefore, perfectly isolated cERR modes are assumed within the application of the data reduction methods. However, the actual mode mixture in the different specimens is evaluated using numerical analysis with the VCCT to check if the assumption of perfectly isolated modes holds true. The outcome is discussed in the results section. As recommended in ASTM D5528, data reduction of the DCB results is based on the Modified Beam Theory (MBT). Therein, deviations from the beam theory due to rotation of the beams at the delamination front are taken into account by artificially increasing the delamination length $a + \Delta$. The DCB specimen is thus treated as if the delamination length was slightly increased. The correction parameter Δ is defined by the intersection of the linear regression curve with the abscissa when plotting the specimen compliance δ/P over the delamination length a . The corrected ERR in mode I G_I based on the MBT method is

$$G_I = \frac{3P\delta}{2b(a + |\Delta|)} \quad (5.21)$$

with the crossbeam displacement δ , the applied load P and the specimen width b .

According to ASTM D7905, the CC method represents the only acceptable data reduction method for ENF testing. As described in the previous section, one specimen from each series is used to determine the CC coefficients by loading the specimen to 50% of the maximum force of a given interface at variable crack lengths a . Compliance of the specimen δ/P at different crack lengths of 15, 25 and 35 mm are then plotted over the respective

cubed crack length a^3 , where the slope of the linear regression curve m represents the CC correction parameter. The corrected ERR in mode II G_{II} based on the CC method is

$$G_{II} = \frac{3mP_{max}^2a_0^2\delta}{2b} \quad (5.22)$$

with P_{max} as the maximum force at crack initiation, δ as the cross-head displacement and a_0 as the initial crack length.

For the data reduction of the MMB tests the procedure proposed in ASTM D6671 based on CBT is used. The ERR in mode I is calculated with the following equation:

$$G_I = \frac{12P^2(3c-L)^2}{16b^2h^3L^2E_{1f}}(a+\chi h)^2 \quad (5.23)$$

In mode II, the ERR can be calculated as follows:

$$G_{II} = \frac{9P^2(c+L)^2}{16b^2h^3L^2E_{1f}}(a+0.42\chi h)^2 \quad (5.24)$$

In the equations above, E_{1f} is the bending modulus of the laminate. With the two ERRs, the total mixed mode ERR is determined with $G_T = G_I + G_{II}$. The mode mixture is then calculated by dividing the ERR in mode II with the total G_{II}/G_T . All ERRs described above can be calculated for any loading condition. However, delamination growth is associated with the cERR. These values are identified when the critical loading P_c is used instead of P . The ASTM standard describes three different ways to calculate P_c . In this work, the most reproducible value $P_{5\%max}$ is chosen. The cERR of the corresponding DCB, ENF, and MMB tests are then used to determine the interaction exponent η by a numerical curve fit of Eq. 5.9 using a Python script.

The following section covers the experimental as well as the numerical results and discussion of the multidirectional laminates under mode I, mode II, and mixed mode loading. It is organised in subsections per mode respective test type. In each mode-specific subsection, an overview of the derived fracture toughness values from each layup with a brief discussion is given first. This is followed by a detailed presentation and discussion of all performed investigations.

5.5.4 Double cantilever beam test for mode I parameters

The experimentally determined cERR values at crack initiation for the different interfaces considered, are presented in Tab. 5.2. A comparison of the cERR values reveals an effect of ply-angle difference on the interlaminar toughness of multidirectional interfaces. Starting from the $0^\circ//0^\circ$ interface with the lowest cERR, the interface toughness value at crack initiation increases slightly for the $0^\circ//45^\circ$ interface and reaches the highest values for $0^\circ//90^\circ$ and $45^\circ// -45^\circ$ interfaces, both having a ply-angle difference of 90° at the delamination plane.

Table 5.2: Summary of calibrated mode I parameters

Parameter	Unit	0°//0°	0°//90°	0°//45°	45°//−45°
n_{SP}	-	12	10	10	10
G_{Ic}	kJ / m ²	0.304	0.650	0.366	0.610
$\sigma_{G_{Ic}}$	kJ / m ²	±0.014	±0.164	±0.095	±0.138
G_{Iss}	kJ / m ²	-	1.063	0.639	-
$\sigma_{G_{Iss}}$	kJ / m ²	-	±0.109	±0.099	-
G_{I1}	kJ / m ²	-	0.650	0.366	-
G_{I2}	kJ / m ²	-	0.413	0.273	-
K_I	N/mm ³	10 ⁵	10 ⁵	10 ⁵	10 ⁵
K_{I1}	N/mm ³	-	9.5 · 10 ⁴	9.5 · 10 ⁴	-
K_{I2}	N/mm ³	-	5.0 · 10 ³	5.0 · 10 ³	-
T_I^0	MPa	20	20.0	20	20
T_{I1}^0	MPa	-	19.0	19.0	-
T_{I2}^0	MPa	-	1.0	1.0	-
m_I	-	-	0.61	0.57	-
n_I	-	-	0.95	0.95	-

Experimentally determined force-displacement curves

The experimental force-displacement data of the DCB tests for 0°//0°, 0°//45°, 0°//90°, and 45°//−45° interfaces are presented in figures 5.10(b)-5.10(d). While the 0°//0° interface exhibits a rather smooth decay in force after crack initiation indicating self-similar crack propagation, the behaviour of the 0°//45° and 0°//90° interfaces is characterised by an increase in force after crack initiation as well as crack propagation at an elevated load level indicating an R-curve behaviour. In case of the 45°//−45° interface, substantial scatter is present as soon as crack propagation is initiated. This behaviour is a result of significant fibre-bridging occurring during testing, where the rip off of fibre bundles leads to severe and sudden load drops in the force-displacement curves.

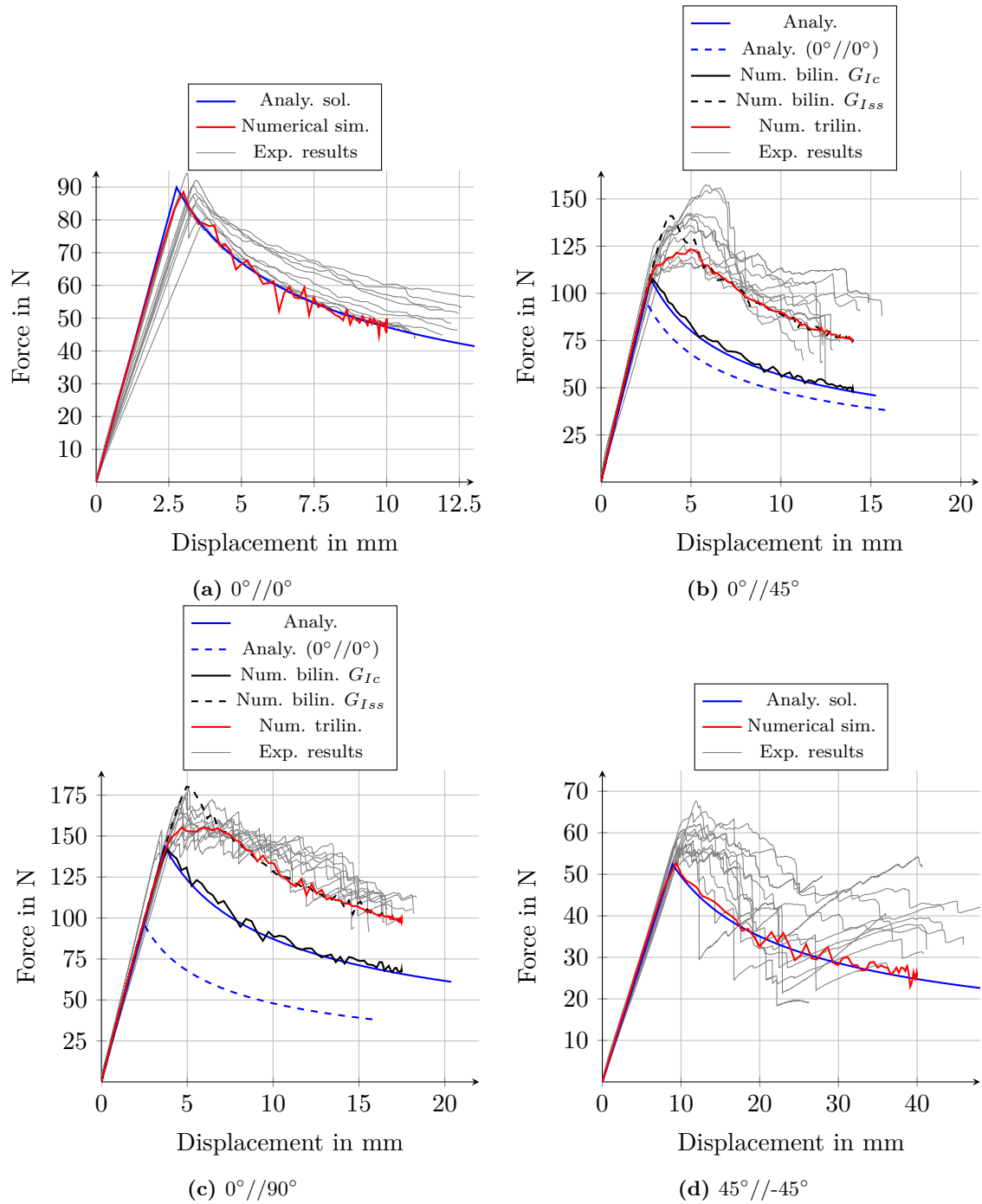


Figure 5.10: Experimentally, analytically and numerically determined load-displacement curves of DCB test

R-curve behaviour

In Fig. 5.11 the evolution of the cERR with the crack extension $\Delta\alpha$ is shown for all four interfaces under investigation. In this plot, the mean value at each crack extension is shown with an error bar to indicate the standard deviation.

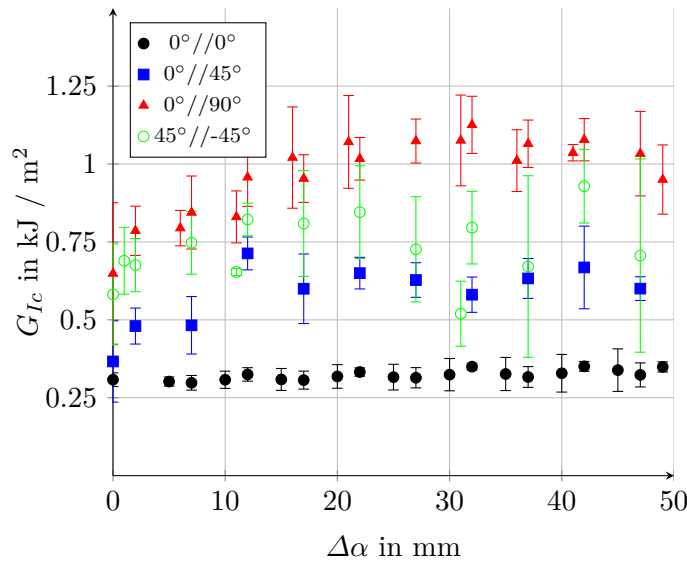


Figure 5.11: Resistance curves of DCB tests with different interfaces (MBT)

As can be expected from the characteristic behaviour of the force-displacement curves, the $0^\circ//45^\circ$ and $0^\circ//90^\circ$ interfaces exhibit an R-curve behaviour. For both interfaces a lower cERR at initiation increases until an elevated plateau is reached at crack extensions larger than 20 mm. The plateau can be interpreted as a steady-state region with self-similar crack propagation behaviour. The ERR at both, initiation and steady-state conditions, exhibit some scatter, however, on average, the behaviour is consistent. The cERR of the $0^\circ//45^\circ$ increases by 63.5 % whereas the increase in cERR of the $0^\circ//90^\circ$ specimens is slightly larger with 74.6 %. The cERR of the $45^\circ//45^\circ$ specimens also increases. However, the effect is not as pronounced as with the interfaces discussed before and the cERR is affected with a large scatter. The specimens with a standard $0^\circ//0^\circ$ -interface do not show any increase in cERR.

Analytical solutions

When comparing the experimentally determined force-displacement curves with the analytical solution based on the MBT [215], agreement between the curves is considerably good for all interfaces up until crack initiation, despite the fact that the analytical solution is derived for perfectly identical sublaminates. Strictly speaking, this assumption is not valid for the present laminate stackings. However, the comparison of analytical and experimental data indicates that the deviation in properties is negligible. When considering the crack propagation regime of the experimental force-displacement curves, only the $0^\circ//0^\circ$ interface exhibits self-similar crack propagation. Hence, the qualitative behaviour of analytical

and experimental force-displacement curves is in agreement for that interface only. The remaining interfaces are all affected by fibre-bridging and crack jumping to some extent. The analytical solution is not capable of accounting for such effects, thus, limiting its applicability to the behaviour up until crack initiation.

Numerical simulations

It can be said that the simulation of the $0^\circ//0^\circ$ specimens according to ASTM D5528 using a bilinear traction-separation law is in good agreement with the experimental results, cf. Fig. 5.10(a). Since no R-curve behaviour was observed in the experiments, the superposition approach is not applied for this interface configuration.

For the $0^\circ//45^\circ$ specimens a distinct R-curve behaviour could be observed, cf. Fig. 5.11. Due to this reason, several simulations were performed for this configuration. The two bilinear simulations show that, regardless of whether the initiation or the progression fracture toughness is used, the experimental curves cannot be reproduced satisfactorily, cf. Fig. 5.10(b). Using the initiation value the point of initiation is met, but the progression is significantly underestimated. Using the steady-state progression fracture toughness, the progression is well modelled, but the initiation is largely overestimated. The two trilinear simulations show that the superposition approach is able to capture the initiation as well as the progression behaviour. Moreover, the simulation using $n = 0.95$ fits qualitatively better than with $n = 0.90$. This is underlined by comparing the numerical and the experimental R-curves. Here, the steady-state phase is captured better by the simulation using $n = 0.95$. Again, bilinear simulation and analytical solution agree well. The analytical solution using the fracture toughness value of the ‘standard’ $0^\circ//0^\circ$ -values shows that using the standard procedure for this interface configuration is conservative in terms of initiation as well as progression.

For the simulation of the $0^\circ//90^\circ$ specimens, the same observations apply as for the $0^\circ//45^\circ$ specimens. As can be seen in Fig. 5.10(c) in this case using the $0^\circ//0^\circ$ -value is even more conservative.

Since the analysis of the $45^\circ//45^\circ$ R-curve did not reveal a distinct R-curve behaviour, this configuration was numerically analysed using the bilinear simulation approach only. As shown in Fig. 5.10(d), analytical and numerical solutions agree well. The initiation is captured with reasonable accuracy. However, the prediction of the progression is considerably conservative. This could be attributed to the difficult parameter determination due to the large scatter in the experimental results.

It can be concluded that the strategies to estimate the interface stiffness and strength under consideration of the element size provide reasonable values which lead to satisfactory results. This holds true for all simulations performed. All mode I simulations display slight oscillations of the curve in the crack progression regime. This is attributed to the explicit integration scheme of the simulations.

Crack path and fracture surface

In order to assess crack jumping between adjacent interlaminar fracture planes, which is also called delamination migration, images of the fracture surfaces as well as from the crack paths are evaluated. Fig. 5.12 illustrates the conjugate post-mortem fracture surfaces of the top and bottom beam of one representative specimen of each interface configuration.

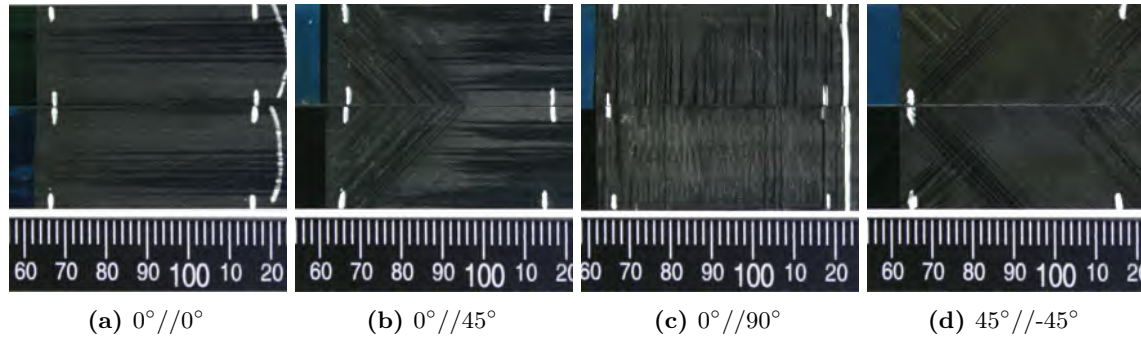


Figure 5.12: Fracture surfaces of DCB specimens [235]

In addition to the in-plane delaminations, ripped-off fibre bundles are visible in all four interfaces. This means that all four interface configurations show crack propagation both within adjacent plies (intralaminar) and between adjacent plies (interlaminar), albeit to different degrees. The crack in the $0^\circ//0^\circ$ -specimen stays in the intended fracture plane. This is different for the test specimens with the $0^\circ//45^\circ$ interface shown. As can be seen in Fig. 5.12(b) starting from the insert, the crack is intralaminar in the 45° -ply and then jumps to the $0^\circ//0^\circ$ interface in the lower beam and propagates in this interface with inter- as well as intralaminar shares. Again, another behaviour can be observed in the $0^\circ//90^\circ$ -interface specimen, cf. Fig. 5.12(c). Here, the crack jumps through matrix cracks in the 90° -ply between the 0° -plies in the upper and lower beam. Fig. 5.12(d) shows a fracture surface of a $45^\circ//45^\circ$ -specimen. There are two areas at the beginning and at the end which show large ripped-off fibre bundles and interlaminar crack growths in between. In addition to the fracture surfaces, Fig. 5.13 shows images taken from the side of one representative specimen for each interface during testing with significant crack extension. Overall, it can be said that the findings in the crack path images fit with the one from the fracture surfaces. The $0^\circ//0^\circ$ interface shows no noticeable jump in the crack plane and no fibre bundles. In the $0^\circ//45^\circ$ specimen, a slight zigzag shape of the crack path as well as some fibre bundles can be observed. In the $0^\circ//90^\circ$ specimen, however, the zigzag shape of the crack path is strongly pronounced. This matches the fracture surface. As can be seen in the side view of the $45^\circ//45^\circ$ specimen, also agrees with the fracture surface. At the beginning of the crack path, some fibre bundles are visible, but after that, a smooth crack path without jumps is apparant. At the crack tip in the image, some fibre bundles might start to form again.

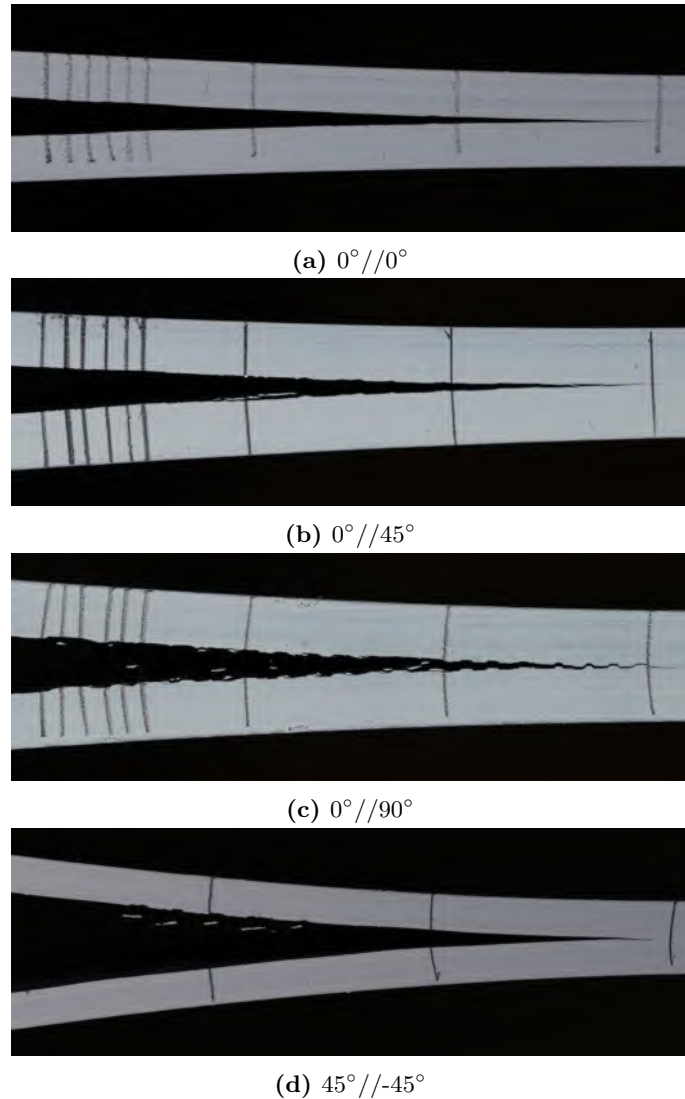


Figure 5.13: Crack paths in DCB specimens

Nevertheless, the evaluation of the failure modes by Cuntze reveals that in the simulation no FF or IFF is detected in the plies adjacent to the initial delamination plane, cf. Tab. 5.3. All stress efforts are significantly below 1.0, which would indicate a laminate failure. As expected, the values for IFF are the highest due to a tension load. The highest value is calculated for the $45^\circ//45^\circ$ -interface with 0.42. This translates to a material stressing effort of 42 % and underlines the need of effective properties in such simulations because matrix cracking with subsequent crack jumping can not be captured in this kind of mesoscale simulations.

Table 5.3: Cuntze failure mode material stressing effort (DCB)

Interface	FF1	FF2	IFF1	IFF2	IFF3
$0^\circ//0^\circ$	0.10	0.00	0.21	0.04	0.06
$0^\circ//45^\circ$	0.12	0.00	0.27	0.04	0.12
$0^\circ//90^\circ$	0.14	0.01	0.38	0.05	0.05
$45^\circ//45^\circ$	0.15	0.02	0.42	0.11	0.23

Crack front shape

Data reduction schemes and analytical solutions assume that the crack length is constant across the specimen width. Yet, this is not always the case in real tests. Urcelay [229] describes two kinds of deviations from a constant crack length across the width. First, the lack of uniformity, which means that the crack lengths at the edges differ from the length in the middle. Second, the lack of symmetry, which means that the crack length at the left and right edge differ. In this work, the crack front shape of the proposed layups is investigated for the DCB specimens with ultrasonic C-scan inspection, which is then compared with simulation results. The results are shown in Fig. 5.14. Blue elements show still fully bonded elements whereas red elements indicate completely degraded interfaces. Moreover, the crack grows from right to left.

The crack fronts of the $0^\circ//0^\circ$ and $45^\circ//45^\circ$ interfaces are both convex shaped meaning that the crack front in the middle of the specimen precedes. These crack fronts are non uniform but nearly symmetric. The crack front of the specimen with $0^\circ//45^\circ$ interface, on the other hand is inclined towards one end and therefore asymmetric. Furthermore, a straight crack front can be observed at the $0^\circ//90^\circ$ interface. In the ultrasonic C-scan image, a partially weak echo indicates the pronounced delamination migration which is described in the previous section. All in all, a good qualitative agreement between simulation and ultrasonic inspection can be observed as only the $0^\circ//45^\circ$ interface results in an asymmetric crack front. In future tests, this kind of specimen should be inspected from both sides during crack extension measurement. It is noteworthy that the crack front at the $45^\circ//45^\circ$ interface is not significantly less uniform than the one of the standard $0^\circ//0^\circ$ interface. The quantitative measurements of the crack front shapes are taken from the simulations and are summarised in Tab. 5.4. In summary, the chosen layups of the multidirectional specimens work satisfactorily.

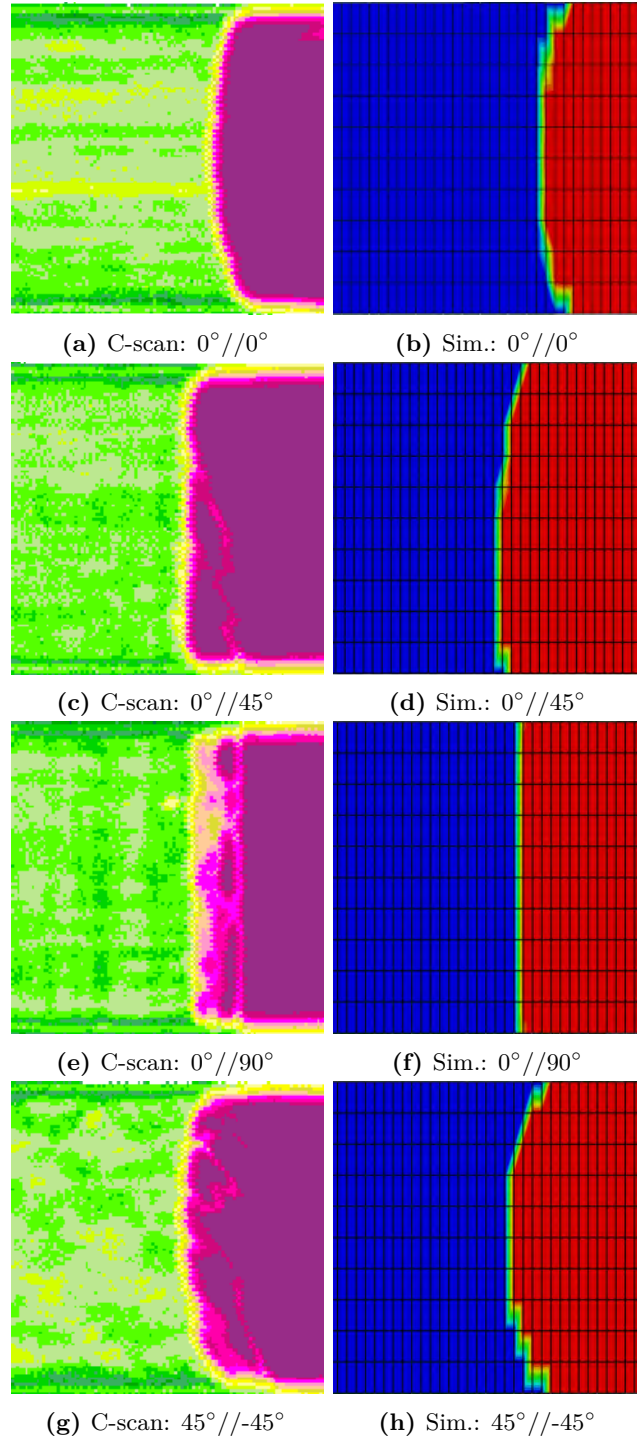


Figure 5.14: Comparison of crack front shape from ultrasonic C-scan inspection and simulation results of DCB specimens

Table 5.4: Crack front shape: Distances of the right and left edges to the most advanced point of the crack front

Interface	Left edge in mm	Right edge in mm
0°//0°	2.25	2.25
0°//45°	0.75	3.00
0°//90°	0.00	0.00
45°//−45°	3.0	3.00

Mode mixture

As described earlier the data reduction schemes as well as the analytical solutions assume perfectly isolated modes. However, multidirectional layups can lead to a mixed mode loading of the delamination plane. To check if the layups chosen with respect to a reduction of coupling work, VCCCT analyses are performed to evaluate the mode mixture. The values reported in Tab. 5.5 are the observed maximum values along the width of the specimen and taken after the onset of delamination. The maximum values of the parasitic modes occurred at the free edges of the specimen. From the values, it can be concluded that in the DCB tests nearly pure mode I loading is achieved. The 0°//45° specimen shows the highest mode II and mode III components. However, these are with less than 3 % from the average total cERR G_{tot}^{av} negligible. This corresponds to the comparably low D_c and B_t values shown in Section 5.5.1.

Table 5.5: ERR components and mode mixture for different interfaces (DCB)

Interface	G_I (kJ/m ²)	G_{II} (kJ/m ²)	G_{III} (kJ/m ²)	G_{II}/G_{tot}^{av}	G_{III}/G_{tot}^{av}
0°//0°	0.333	0.000	0.000	0.000	0.000
0°//45°	0.402	0.009	0.004	0.022	0.010
0°//90°	0.712	0.005	0.004	0.007	0.006
45°//−45°	0.669	0.013	0.003	0.019	0.004

5.5.5 End notched flexure test for mode II parameters

In the following, the mode II results are presented and discussed in the same way as the mode I results before. Apart from the cERRs determined with the data reduction schemes discussed earlier, a summary of all mode II parameters used for the analytical and numerical analysis can be found in Tab. 5.6.

Similar to the DCB results, the cERR of the 0°//0° interface is again the lowest and the interfaces with a ply-angle difference of 90° still produce similar cERR values, however, the behaviour of the 0°//45° interface breaks the pattern. Thus, contrary to the DCB results, no distinct dependency of the cERR in mode II on the difference in ply-angle between the interface layers can be observed.

Experimentally determined force-displacement curves

The force-displacement curves from the experimental ENF tests of the 0°//0°, 0°//45°, 0°//90°, and 45°//−45° interfaces are presented in Fig. 5.15. Compared to the DCB results, the force-displacement curves in mode II exhibit more scatter with respect to both initial

Table 5.6: Summary of calibrated mode II parameters

Parameter	Unit	0°//0°	0°//90°	0°//45°	45°//−45°
n_{SP}	-	9	9	10	9
G_{IIc}	kJ / m ²	2.330	2.444	2.776	2.475
$\sigma_{G_{IIc}}$	kJ / m ²	±0.122	±0.139	±0.177	±0.103
K_{II}	N/mm ³	10 ⁵	10 ⁵	10 ⁵	10 ⁵
T_{II}^0	MPa	110.0	110.0	110.0	110.0

stiffness and initiation of crack propagation. This could possibly be due to the manual alignment of the specimens in the 3-point bend set-up during testing.

Analytical solutions

Good agreement between the experimental force-displacement curves and the analytical solution can be observed for the 0°//0° interface. Nevertheless, in the cases of the remaining interfaces, agreement is less pronounced. While the analytically determined initial stiffness is slightly larger than the experimental stiffness of the 0°//45° and 0°//90° interfaces, the analytically determined initial stiffness in the case of the 45°//−45° interface is considerably lower than in the experiment. Resulting from this difference in stiffness, the points of crack initiation in the force-displacement curves of the 0°//45°, 0°//90°, and 45°//−45° interfaces are either slightly over- or underestimated.

Numerical simulations

In general, compared to the bilinear mode I simulations, a lower agreement of the mode II simulations with the analytical solutions can be observed, cf. figures 5.15(a) to 5.15(d). The stiffness observed in the experiments is better captured by the numerical simulations than by the analytical solutions. In all simulations except for the 0°//0° interface model the stiffness of the tests agrees well until load drop. The simulation with the 0°//0° interface shows a non-linearity prior to the load drop which cannot be observed in the experimental results and the forces as well as displacements at crack initiation also differ significantly between the numerical and analytical solutions. Again, the agreement with the experiment is better for the simulations. The crack initiation force is a bit low for the 0°//0° interface, but well captured for all other interfaces.

Since due to the unstable crack growth no R-curves were recorded during experimental testing, configurations are only modelled with the bilinear approach and not with a superposed trilinear traction-separation law. However, the bilinear approach works reasonably well in mode II. As observed in the mode I results, the analytical solution using 0°//0°-values shows that using this ‘standard’ value is always conservative compared to the analytical solution with the interface-specific value.

Fracture patterns

For the ENF specimens no side view images of the crack paths are available. However, the post-mortem fracture surfaces of the experimentally tested specimens, cf. Fig. 5.16, can

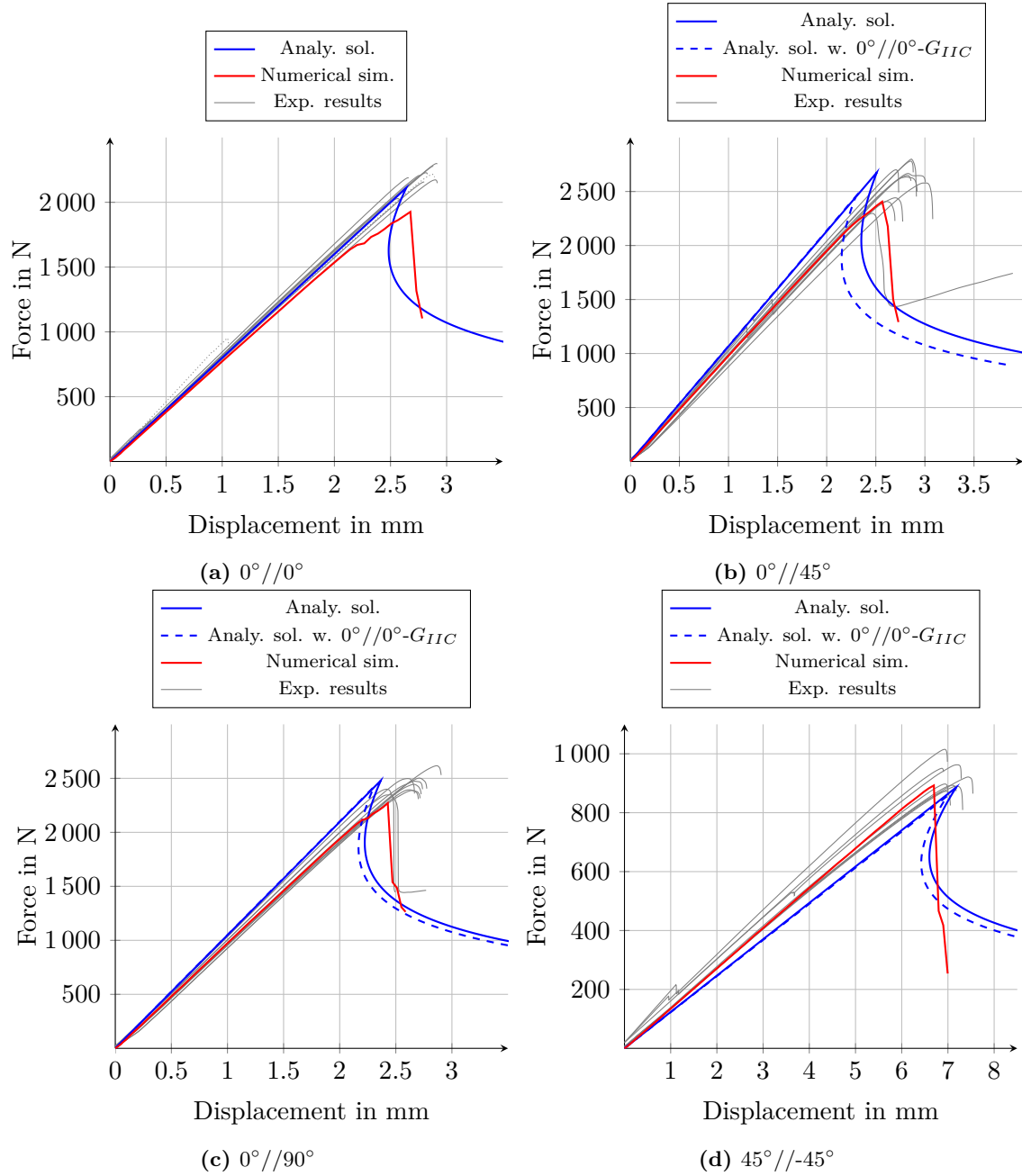


Figure 5.15: Experimentally, analytically and numerically determined load-displacement curves of ENF tests

be used in combination with the material stressing efforts summarised in Tab. 5.7. These material stressing efforts are calculated from the stresses determined with the numerical analyses in the plies adjacent to the intended fracture plane.

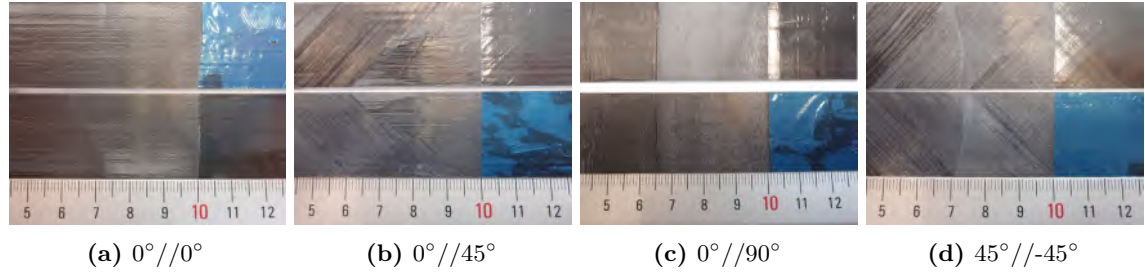


Figure 5.16: Fracture surfaces of ENF specimens [235]

The fracture surface of the specimen with the 0°//0° interface shows no delamination migration. However, some ripped-off fibre bundles, which are attributed to fibre bridging, are visible. In contrast to that, the crack in the specimen with the 0°//45° interface initially grows in the intended interface in an interlaminar manner. With progressing crack growth, intralaminar damage comes into play. At the end of testing, the crack is completely migrated to an intralaminar crack in the 45° ply. It needs to be mentioned that the remaining interfaces show a much simpler fracture pattern. For instance, the crack in the 0°//90° specimen stays in the intended interface. The fracture surface of the 45°//45° specimen again shows some ripped-off fibre bundles, but all of them are oriented with 45° which leads the author to conclude that the crack grows in the intended interface.

Unlike with the DCB specimens for every ENF specimen, a failure mode reaches the value of 1.0, which means that a damage in the ply can be expected. The evaluation of the material stressing efforts for the 0°//0° results in an IFF due to shear loading (IFF3) and for all other specimens in an IFF due to tension loading (IFF1). This result supports the experimental observations.

Table 5.7: Cuntze failure mode material stressing effort (ENF)

Interface	FF1	FF2	IFF1	IFF2	IFF3
0°//0°	0.37	0.53	0.27	0.19	1.0
0°//45°	0.27	0.62	1.0	0.47	0.55
0°//90°	0.02	0.54	1.0	0.19	0.52
45°//45°	0.34	0.48	1.0	0.67	0.58

Crack front shape

In Fig. 5.17 the crack front shapes determined by simulation for all four interfaces are shown. Except for the specimen with the 45°//45° interface, all interfaces show a straight crack front which is uniform and symmetric. The crack front in the 45°//45° specimen is inclined and slightly curved. Therefore, it is non-symmetric and non-uniform.

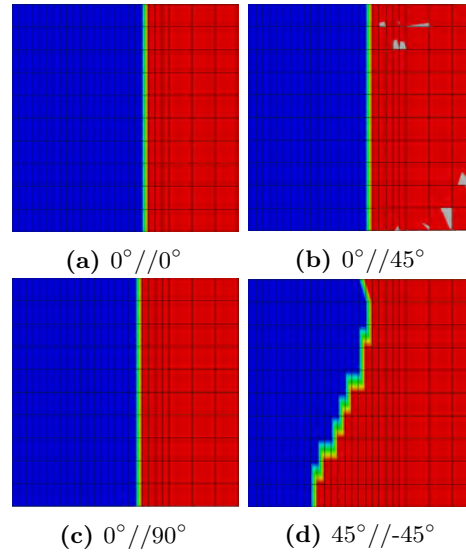


Figure 5.17: ENF crack front shapes observed in numerical simulations

Mode mixture

Like for the DCB specimen, again VCCT analyses are performed to determine the mode mixture for the different specimens. The highest values for each ERR component are shown in Tab. 5.8. The high mode I and mode III values occur in small regions from the edges towards the middle of the specimens, as also shown by Garulli et al. [236] for different layups. As desired, mode I is small in every configuration. The highest mode I share can be found in the 45°//45° specimen. However, with 1.3% it is rather small. Though, there are pronounced mode III components between 21% and up to 82.5%. Nevertheless, it needs to be mentioned that these high mode III components are very localised and even in the standard 0°//0° specimen there are areas with 30% mode III with respect to G_{tot}^{av} . The largest edge region with parasitic mode III fraction was observed in the 0°//45° specimen with 3 mm from the edge towards the center of the specimen. As can be seen from Tab. 5.8 in the middle of the specimens pure mode II loading is achieved. Due to the small and local character of the parasitic modes, the authors assess the standard evaluation methods as applicable.

Table 5.8: Highest (h) and in the middle (m) measured ERR components and mode mixture for different interfaces (ENF)

Interface	G_I (kJ/m ²)		G_{II} (kJ/m ²)		G_{III} (kJ/m ²)		G_I/G_{tot}^{av}		G_{III}/G_{tot}^{av}	
	h	m	h	m	h	m	h	m	h	m
0°//0°	0.017	0.003	2.533	2.088	0.774	0.000	0.007	0.001	0.306	0.000
0°//45°	0.017	0.001	3.048	2.971	1.556	0.000	0.006	0.000	0.510	0.000
0°//90°	0.001	0.000	3.045	2.854	0.640	0.000	0.000	0.000	0.210	0.000
45°//45°	0.032	0.006	2.632	2.491	2.172	0.001	0.013	0.000	0.825	0.000

5.5.6 Mixed mode bending tests for mixed mode parameters

MMB tests are used to determine G_T for an intended mixed mode ratio of 0.71. The $45^\circ//45^\circ$ interface produces the highest G_T value with 1.146 kJ/m^2 . Nearly the same cERR is determined for the $0^\circ//0^\circ$ and $0^\circ//45^\circ$ interfaces with 0.895 and 0.923 kJ/m^2 respectively. The $0^\circ//90^\circ$ interface results in the lowest cERR, which is under the tested mixed mode loading ratio with 0.735 kJ/m^2 . In Fig. 5.18, the cERRs are shown together with the DCB and ENF results for all interfaces.

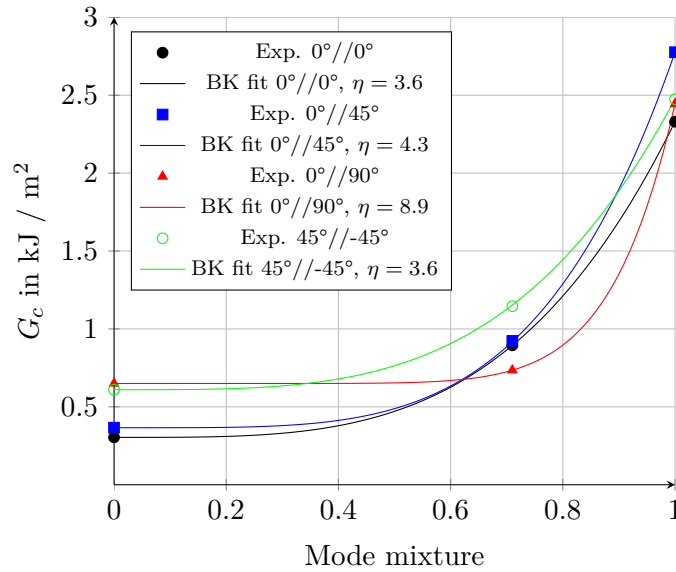


Figure 5.18: Fracture toughness vs. mode mixture curves

When comparing the cERRs of the different test types and respective loading modes no clear trend of high and low cERR for the different interfaces can be observed. For instance, the $0^\circ//90^\circ$ interface shows the highest values in mode I, but the lowest under mixed mode conditions, whereas for mode II loading, the $0^\circ//90^\circ$ interface lies in the middle of the tested interfaces.

Using the DCB, ENF, and MMB results, a curve fit with a Python script was performed to find the exponent η_{BK} of the BK law. The exponent is found to be the same for the $0^\circ//0^\circ$ and $45^\circ//45^\circ$ interfaces with $\eta = 3.6$. Furthermore, with 4.3, the fitted value for the $0^\circ//45^\circ$ interface is comparable. With $\eta_{BK} = 8.9$, a much higher η_{BK} is determined for the $0^\circ//90^\circ$ interface. These values for η_{BK} are used for the analytical and numerical analyses presented in the following.

Experimentally determined force-displacement curves

The force-displacement curves recorded during MMB testing are shown in figures 5.19(a) to 5.19(d). It is noteworthy that the experimentally determined curves of the specimens with $0^\circ//0^\circ$ and $0^\circ//90^\circ$ interfaces have the same characteristic shape. The force increases

nearly linear until a small load drop occurs. After the load drop, the force rises again. This is different for the specimens with the $0^\circ//45^\circ$ interface where only a slight load drop is noticeable. The specimen with the $45^\circ//45^\circ$ interface shows no load drop at all. For this specimens, a reproducible knee point with a change in stiffness can be observed. After the knee point, the force increases more slowly.

Analytical solutions

The results of the analytical solution, cf. figures 5.19(a) to 5.19(d), can be summarised for all interfaces. The stiffnesses of experimental and analytical results are in good agreement until the load drop or change in stiffness in the experimental curves. However, the behaviour after this points is not well captured and the analytical solution overestimates the maximum forces in every case.

Numerical simulations

Same as for the analytical solutions, the stiffness observed in the experiments is well modelled with numerical simulations. As can be seen in figures 5.19(a) and 5.19(b) there is a good agreement between numerical solutions and the experiment for the $0^\circ//0^\circ$ and $0^\circ//45^\circ$ interface both for crack initiation as well as progression. Compared to the experiment the maximum force for the remaining two interfaces is overestimated, cf. figures 5.19(c) and 5.19(d). In addition, the shape of the force-displacement curve in the $45^\circ//45^\circ$ case is not well captured. There is a sudden load drop in the simulation results which could not be observed in the experiments. To check if the overestimation of the maximum force in the $0^\circ//90^\circ$ case must be attributed to the interface-specific values, a second simulation using the standard $0^\circ//0^\circ$ interface values was performed. This resulted in a slightly lower but still existing overestimation. This leads to the conclusion that the overestimation may be caused by damage processes in the real specimens which are not modelled in the numerical simulation. Hence, the $0^\circ//90^\circ$ and $45^\circ//45^\circ$ interfaces are the only cases, in which the numerical simulation is less conservative than the analytical solution.

Fracture patterns

As with the ENF tests, only post-mortem images of the fracture surfaces are available for the MMB tests, cf. Fig. 5.20. In addition, like for DCB and ENF, the material stressing efforts of the plies adjacent to the intended fracture plane are given in Tab. 5.9. In general, it can be said that the fracture surfaces are comparable to the ones of the ENF specimens. The fracture surface of the $0^\circ//0^\circ$ interface shows no delamination migration and there are only some ripped-off fibre bundles visible, whereas the specimen with the $0^\circ//45^\circ$ interface first shows intralaminar crack growth in the 45° ply. With progressing growth the crack then migrates to an interlaminar crack and an intralaminar crack in the 0° ply respectively. This is not totally clear. The fracture pattern of the $0^\circ//90^\circ$ specimen is significantly more uneventful as the crack stays in the intended interface. The last specimen type with the $45^\circ//45^\circ$ interface shows interlaminar crack growth in the intended interface but with some ripped off fibre bundles oriented under 45° . The findings from the fracture surfaces in general fit with the calculated material stressing efforts. For the $0^\circ//0^\circ$ specimen, all

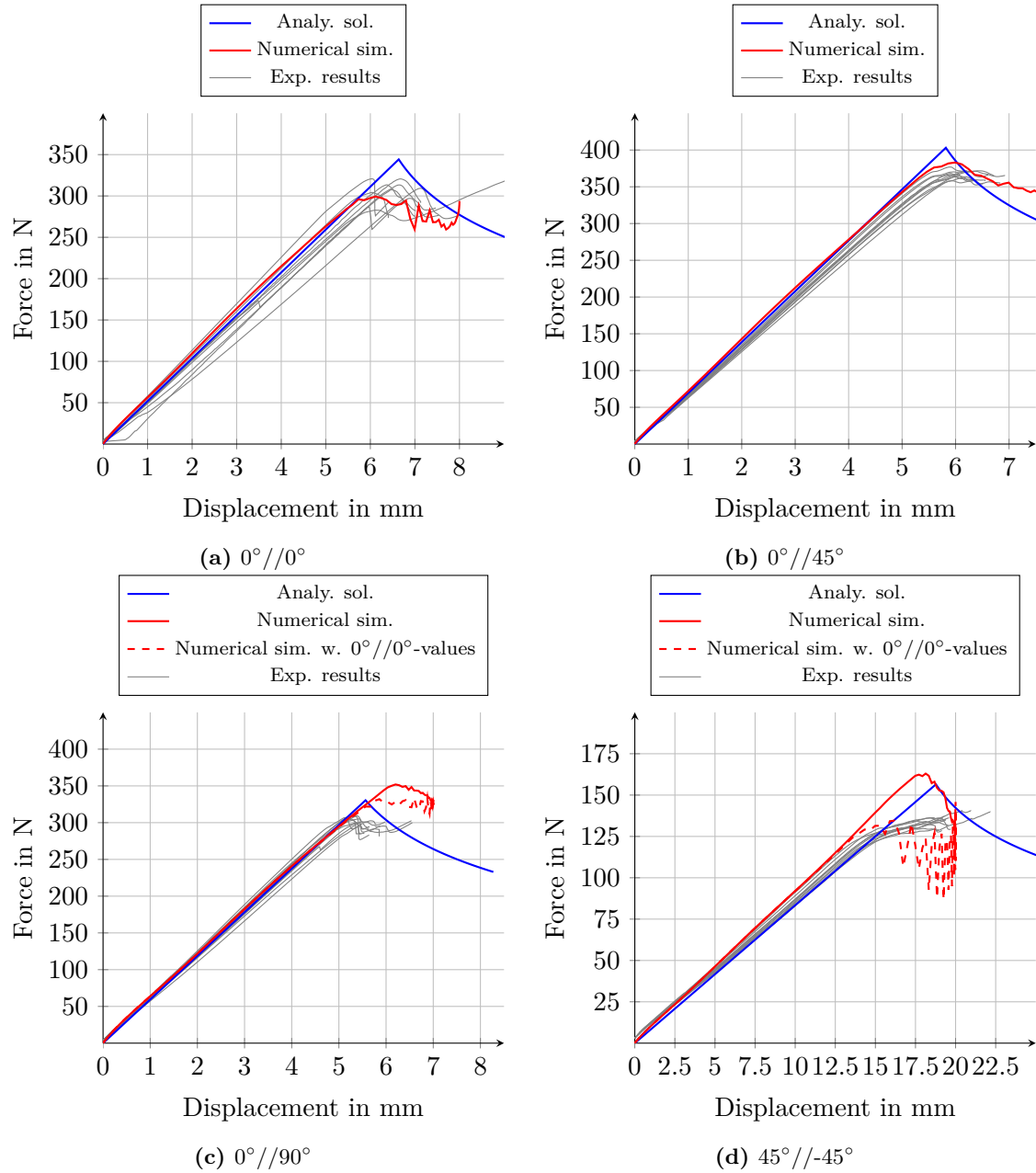


Figure 5.19: Experimentally, analytically and numerically determined load-displacement curves of MMB tests

stressing efforts are clearly below 1 which means no failure at all. For the $0^\circ//45^\circ$, again all failure modes are below 1. However, with 0.85 the IFF1 effort is significantly closer to failure than with the $0^\circ//0^\circ$ specimen. Furthermore, IFF are visible in the fracture surface. The next specimen with $0^\circ//90^\circ$ interface, is predicted to have IFFs, but the fracture pattern shows, at least no obvious IFF. The highest stressing efforts overall are calculated for the $45^\circ//45^\circ$ specimen, but only the IFF1 value reaches 1. This fits with the ripped-off fibre bundles visible in the fracture surface image.

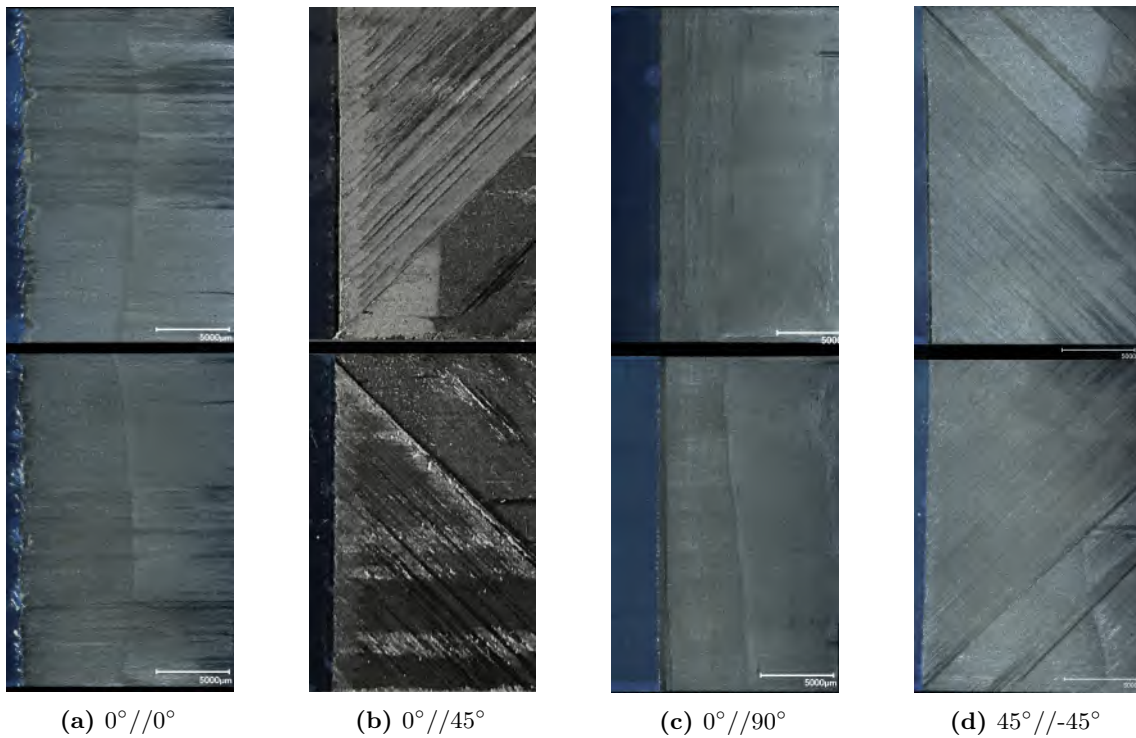


Figure 5.20: Fracture surfaces of MMB specimens [235]

Table 5.9: Cuntze failure mode material stressing effort (MMB)

Interface	FF1	FF2	IFF1	IFF2	IFF3
$0^\circ//0^\circ$	0.31	0.20	0.25	0.08	0.42
$0^\circ//45^\circ$	0.16	0.00	0.85	0.06	0.37
$0^\circ//90^\circ$	0.04	0.20	1.00	0.05	0.40
$45^\circ//45^\circ$	0.32	0.23	1.00	0.30	0.54

Crack front shape

In all four simulations a straight and therefore uniform and symmetric crack front could be observed. Due to this reason the crack fronts are not shown in a figure.

Mode mixture

In this work, VCCT analyses are used to assess the parasitic modes in the test specimens with multidirectional layups. Since the mode mix of the MMB specimens lies between the DCB and ENF specimens, VCCT analyses were not performed for the MMB specimens.

5.5.7 Summary of interlaminar material properties

Tab. 5.10 summarises the determined interlaminar material properties of M21-T700GC for the different interfaces tested. These material properties are used for all subsequent analyses. The material data for the second material under consideration is taken from literature and is summarised in Tab. E.2 in the Appendix E.

Table 5.10: Summary of calibrated M21-T700GC CZM parameters for different interfaces

Property	0°//0°	0°//45°	0°//90°	45°//−45°	Unit
$K_I = K_{II} = K_{III}$			10^5		N/mm ³
G_{Ic}	0.304	0.366	0.650	0.610	N/mm
$G_{IIc} = G_{IIIc}$	2.330	2.776	2.444	2.475	N/mm
T_I^0			20.0		MPa
$T_{II}^0 = T_{III}^0$			110.0		MPa
Initiation. Criterion			QUADS		
Propagation Criterion			BK		
η_{BK}	3.6	4.3	8.9	3.6	

5.6 Application to open hole tension specimens

In this subchapter, the interlaminar modelling developed in the preceding sections is applied to OHT specimens, which were already used for validation of the intralaminar modelling in Chapter 4. At the end of Chapter 4, a question regarding the intralaminar modelling was raised which shall be answered in this subchapter. It should be mentioned that the modelling for the OHT specimens using solid elements only resulted in valid predictions of the failure loads. However, the sole use of continuum shell elements yields a failure load that is significantly too high for the simulated QI-II specimen. This is attributed to the neglect of damage in through-thickness direction in Section 4.7.1. In this context, the combination of continuum shell elements with discrete interlaminar damage modelling with cohesive surfaces could provide relief.

Four different modelling approaches for the composite are conceivable. The sole use of solid elements, the sole use of continuum shell elements and in each case the combination with cohesive surface-based interlaminar modelling. These four approaches are applied to different OHT specimens and are compared with each other.

For this, the multidirectional OHT specimens QI-I, QI-II, and CP, introduced in Section

4.6.1, are under consideration. All of above-mentioned specimens were analysed. However, the specimens QI-I and CP are not considered suitable for the evaluation because they do not show any delamination prior to total failure. Therefore, all approaches predict the same failure load.

The remaining specimen series QI-II shows delamination prior to total failure. Since only one series remains for the investigation, a second series of six specimens referred to as QI-III was manufactured and tested.

These tests were carried out subsequently to the other OHT tests described in Chapter 4. Nevertheless, during the work on this thesis, the M21-T700GC material was discontinued in the originally used thickness. At this time, it is only available in double thickness. Consequently, the QI-III specimens have a cured ply thickness of 0.26 mm instead of 0.13 mm. Although this reduces the consistency of the study, thicker plies are assumed to provoke delaminations [183]. Therefore, the thicker plies are actually beneficial in this examination. The dimensions of the QI-III specimens are 32.0 mm in width and 4.25 mm in thickness, while the hole diameter is 6.0 mm. The free length during testing was 180 mm and the layup is $[45,90,-45,0]_{2s}$.

This series was also used to evaluate the delamination area by ultrasonic inspection. To do so, three specimens were tested up to failure and the tests of the remaining three specimens were aborted at 93 %, 95 %, and 97 % of the previously determined mean failure load of 56.87 ± 1.08 kN.

The two series QI-II and QI-III are also used to test the orientation specific ERRs at the end of this subchapter.

5.6.1 Comparison of composite modelling approaches

The four modelling approaches introduced above are compared on the basis of the QI-II and QI-III specimens. For the comparison, simulation models as described in Section 4.6.2 are used. It needs to be noted that a change of the fracture toughness under fibre tension G_{ft} was necessary for the QI-III specimen. With the original value of $G_{ft} = 83.0$ N/mm, taken from Furtado et al. [175], the predicted failure load was significantly too low. In their study, Furtado et al. [175] determined G_{ft} for different ply thicknesses. The value was changed to 252.0 N/mm which is the value determined by Furtado et al. for the corresponding ply thickness. With this value plausible results for QI-III are achieved.

Fig. 5.21 shows the QI-II stress-strain curves resulting from the different modelling approaches as well as a DIC measurement during the experiment and the mean experimental failure stress. Up to a stress of 325 MPa and a strain of 0.008, all modelling approaches capture the stiffness of the specimen well. As already described in Section 4.7.1, for this specimen, the modelling using solid elements results in an acceptable prediction of the failure load with a deviation of +2.8 % to the mean failure stress, whereas the simulation using continuum elements overshoots the experimental failure stress by +10.8 %.

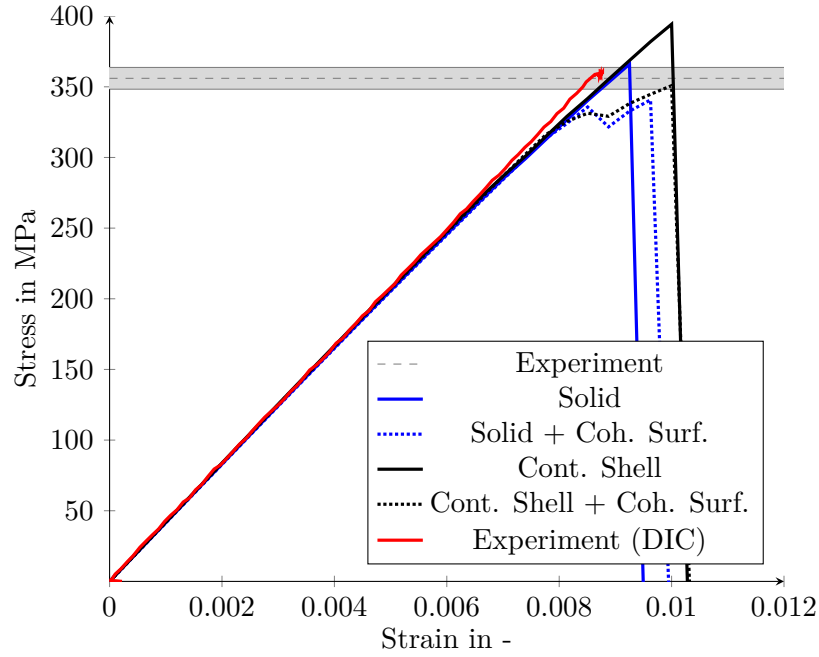


Figure 5.21: Comparison of modelling approaches with the example of QI-II OHT tests

It is noteworthy that the combination with cohesive surfaces reduces the failure load. This is independent of the use of solid or continuum shell elements. However, both models using cohesive surfaces show a behaviour prior to the maximum loading which was not observed in the experiment. After a first load drop, the load increases again up to a second load drop, after which the specimens in the simulations cannot bear further load. Looking at the damage variables in the simulations, at the first load drop the first elements are already fully damaged due to FF and are thus deleted. Additionally, clearly pronounced delaminations are predicted around the hole. At the second load drop, more elements are deleted and the delaminations have spread over the whole width of the specimen. For this reason, the first peak load is taken for the evaluation of the modelling approaches. On the one hand, this results in 335.7 MPa for the combination of solid elements with cohesive surfaces which represents a deviation of -5.7% from the experiment. On the other hand, the combination of cohesive surfaces with continuum shell elements results in a slightly lower value of 331.3 MPa and a deviation of -6.9% from the experiment.

The stress-strain plot, cf. Fig. 5.22, for the QI-III specimen delivers basically the same findings as the one for QI-II.

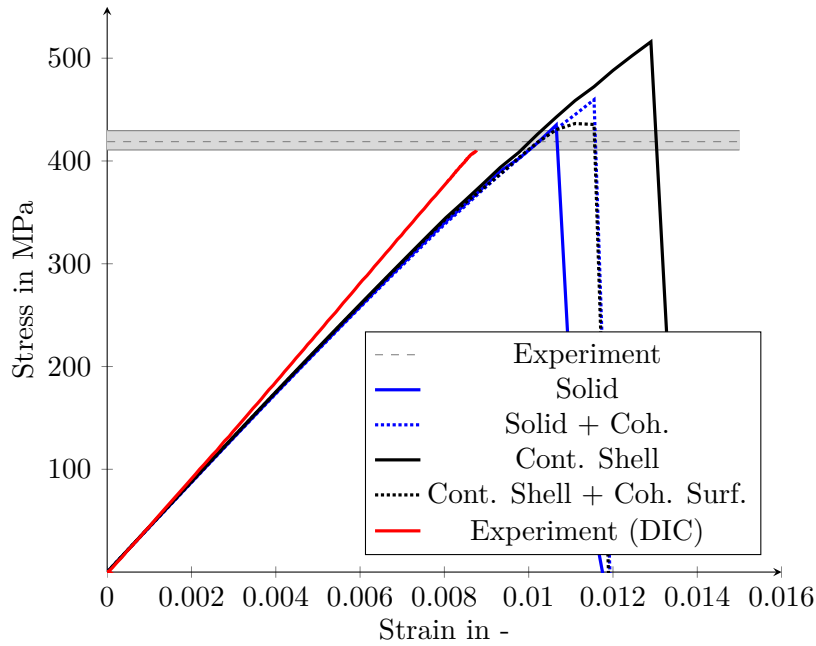


Figure 5.22: Comparison of solid and continuum shell based modelling with the example of QI-III OHT tests

With a +3.9 % higher failure stress than the experimental mean, the solid only modelling has a considerably good accuracy, whereas the sole use of continuum shell elements overpredicts the strength by 23.2 % and therefore even more than for the QI-II example. As for the previously discussed QI-II specimen, the addition of cohesive surfaces to the continuum shell modelling reduces the failure load to 436.5 MPa, which is, with +4.2 %, significantly closer to the experiments. Unlike for the QI-II test specimen, the failure stress for the solid modelling increases when cohesive surfaces are added. With a failure stress of 459.6 MPa, the deviation is now +9.7 %.

It must also be noted that the stiffness from the experiment is captured less accurately by the simulations than in the previous example. This could be due to the higher ply thickness which could result in a slightly different stiffness of the material. The experimental force-displacement curve measured by DIC is nearly linear, whereas the simulations are more non-linear, especially above 150 MPa.

The failure stresses resulting from experiments and simulations as well as their deviations are summarised in Tab. 5.11. A preliminary conclusion is that either pure solid modelling or the combination of continuum shell and cohesive surface should be used. For both specimens, these two approaches provide good accuracy in predicting the strength.

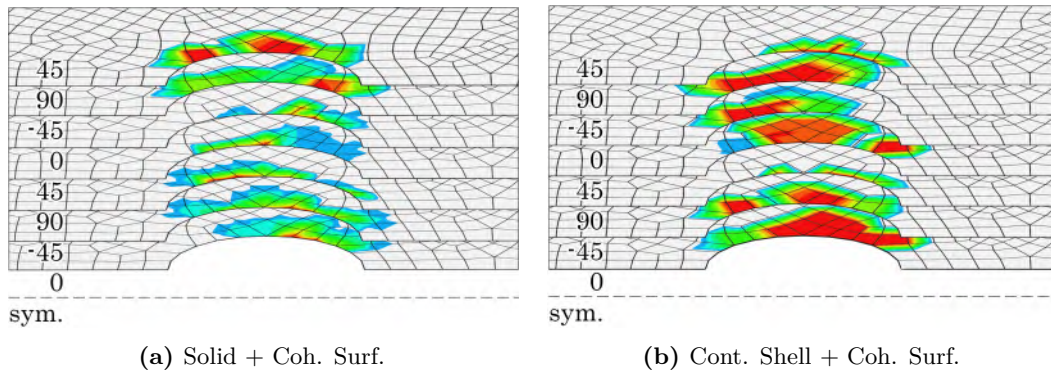
Table 5.11: Comparison of failure loads of OHT specimens with different modelling approaches from experiment and simulation

	QI-II		QI-III	
	σ_{max} in MPa	Diff. to Exp. in %	σ_{max} in MPa	Diff. to Exp. in %
Experiment	356.0 ± 7.7		418.8 ± 7.9	
n_{sp}	5		3	
Solid	366.0	+2.8	435.0	+3.9
Cont. Shell	394.3	+10.8	516.0	+23.2
Solid + Coh. Surf.	335.9	-5.7	459.6	+9.7
Cont. Shell + Coh. Surf.	331.3	-6.9	436.5	+4.2

In the simulation results with cohesive surfaces, it is observed that, depending on the use of solid or continuum shell elements, the predicted delamination areas are different. This is further investigated in the following section.

5.6.2 Comparison of delamination areas with experimental results

Fig. 5.23 shows the predicted delamination areas at nearly the same load level, namely 53.5 kN for the combined solid and 53.7 kN for the combined continuum shell modelling, corresponding to 95 % of the experimental mean failure load which is 54.0 kN.

**Figure 5.23:** Comparison of predicted delaminations areas between individual plies

At this load level one of the experimental test was aborted and subjected to an ultrasonic inspection. During the test, a crackling sound was heard shortly before the termination load level was reached. This indicates the formation of delaminations and IFF. However, the test specimen did not show any visible damage after the test was stopped.

In general, it can be observed that the delamination areas between the individual plies are significantly higher when using continuum shell elements. Only at the $0^\circ// -45^\circ$ interface, smaller delamination areas are predicted with the solid-based modelling.

In Fig. 5.24, the delamination areas determined with the ultrasonic inspection are com-

pared with the numerical predictions.

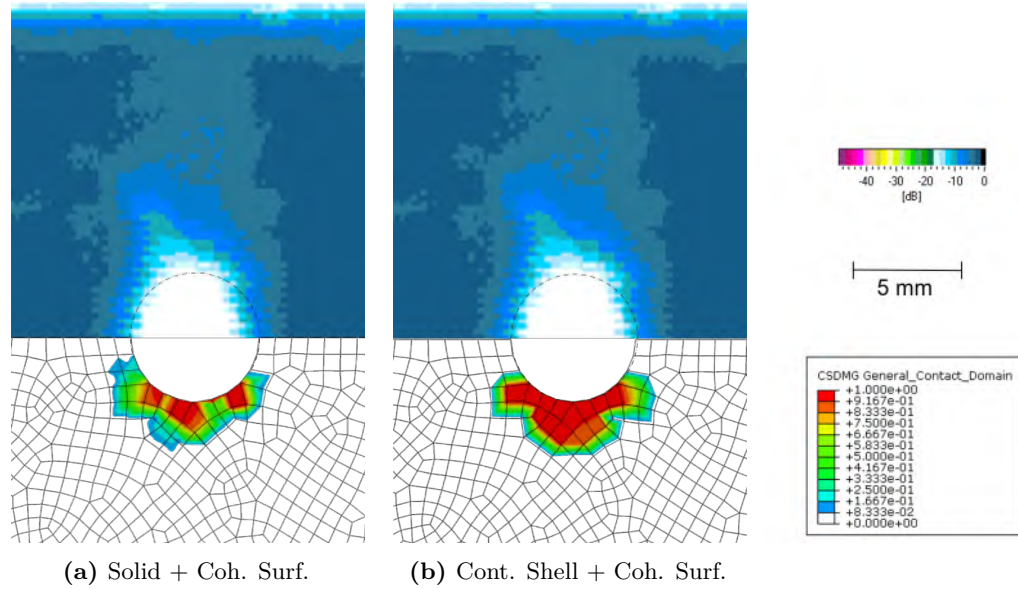


Figure 5.24: Comparison of predicted delaminations areas with experimental results

In the top part of the two images, the floor echo of the water basin is shown, whereas the delamination areas from the simulations are depicted in the bottom part. In the images from the ultrasonic inspection, deep blue colour means that no delamination occurred and light blue to mint colours indicate delaminated areas. For the images of the simulations, the debonded areas between the individual plies from Fig. 5.23 are superimposed. The largest occurring damage value across all seven contact surfaces is shown in plan view. In this superimposed illustration, the difference between the two simulations that can be clearly seen in Fig. 5.23, is not as visible.

Both simulations result in a qualitatively acceptable agreement with the experiment in terms of shape and size of the debonded regions. However, no definitive statement can be made as to whether the delamination areas are predicted more precisely using a solid- or a continuum shell-based modelling. A more comprehensive study is required to be able to provide more detailed assessments. Nevertheless, for this example, both approaches provide plausible predictions compared to the experiment.

Overall, with these examinations the hypothesis is supported that damage caused by stresses in the thickness direction is distributed between the interface and the layer when solid elements are used. In the case of continuum shells, stresses in the thickness direction only lead to interface damage, which results in a larger damaged area.

5.6.3 Use of interface orientation-specific ERRs

In the DCB, ENF, and MMB tests described in this chapter, it was found that cERR is dependent on the orientation of the respective interface layer. Furthermore, it was found that the cERRs for the same difference in orientation angle between adjacent plies are comparable. This can be seen from the results of the $0^\circ//90^\circ$ and the $45^\circ// -45^\circ$, cf. Tab. 5.10. The difference in the orientation is 90° for both interface configurations and the corresponding cERRs are very close to each other. With this finding, the hypothesis is that for cohesive surfaces in simulation models of multidirectional specimens, ERRs that are determined from tests with the same difference in orientation should be used.

The layups of the two examples under investigation in this section, QI-II and QI-III, have only 45° increments from ply to ply. With the consideration above, $0^\circ//45^\circ$ -values should be used. To investigate the use of interface orientation-specific cERRs, simulations with the $0^\circ//45^\circ$ ERRs from Tab. 5.10 are performed and compared to the simulations discussed above with the standard $0^\circ//0^\circ$ -values.

The resulting stress-strain curves are plotted in Fig. 5.25 for QI-II and in Fig. 5.26 for QI-III.

In the case of QI-II, the use of orientation specific cERR values increase the failure stress slightly from 331.3 to 338.0 MPa, when the first load drop in the simulation using standard values is considered, cf. discussion in Section 5.6.1. With this slight increase in strength, the deviation to the experiments is reduced to -5.1% .

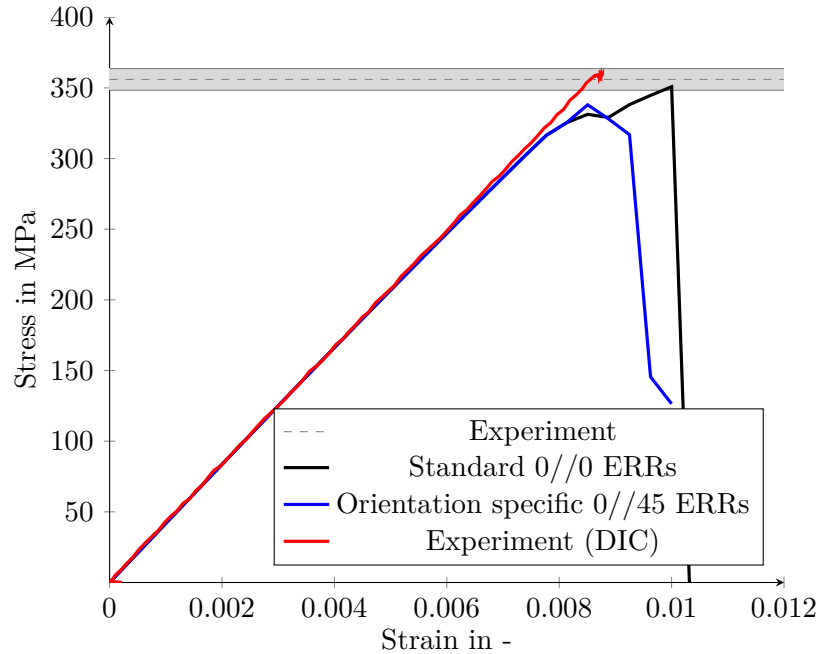


Figure 5.25: Comparison of standard and orientation specific ERRs with continuum shell + cohesive surface based modelling with the example of QI-II OHT tests

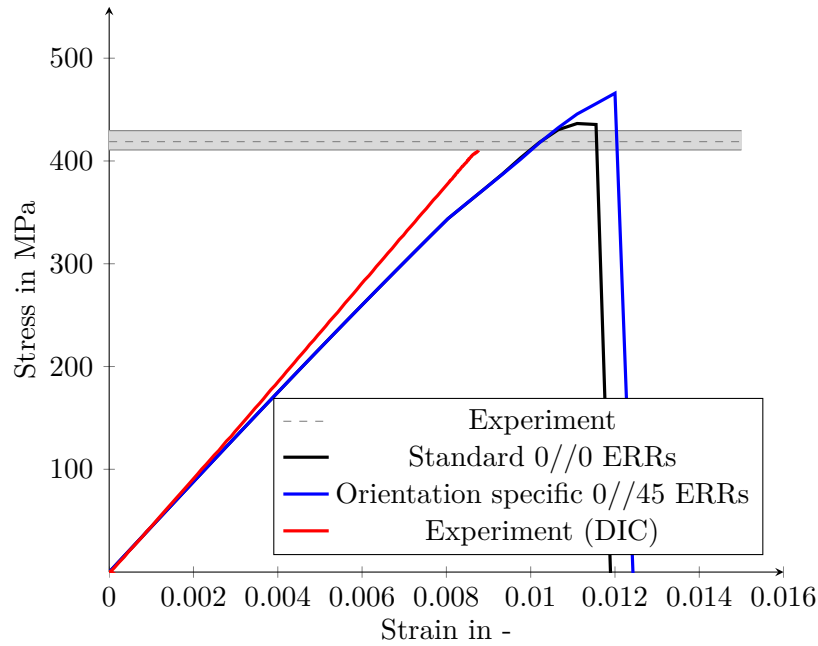


Figure 5.26: Comparison of standard and orientation specific ERRs with continuum shell + cohesive surface based modelling with the example of QI-III OHT tests

For the second specimen QI-III, the failure stress is also increased when using orientation specific cERRs. However, the simulation with the standard cERR already overshoots the experiments by +4.2 %. The deviation with orientation-specific cERRs is +11.2 %. In both cases, QI-II and QI-III, with the standard $0^\circ//0^\circ$ cERRs, a strong non-linear region prior to the maximum load can be seen in the stress-strain curve. This non-linearity is reduced with the orientation-specific $0^\circ//45^\circ$ cERRs and thus fits better with the experiment.

In summary, it needs to be said that no clear trend can be observed. Accordingly, the use of interface orientation-specific cERRs needs further investigation and the cERRs determined in this work are a good basis for this. However, in the further course of this work, the standard $0^\circ//0^\circ$ -values are used.

5.7 Conclusions and recommendations for the holistic approach

In this chapter, the modelling and characterisation of the interlaminar behaviour of the composite adherends were investigated with the example of M21-T700GC material. With the results in this chapter, recommendations regarding the holistic PDA approach for the interlaminar and the composite modelling in general can be drawn.

First, an experimental and numerical study on the influence of interface ply orientation on mode I, mode II, and mixed-mode fracture toughness in multidirectional laminates has been conducted in Subchapter 5.5. It could be revealed that the effective fracture toughness of the same composite material largely depends on the interface orientations.

Furthermore, the R-curve behaviour in mode I has been investigated. It is noteworthy that whether an R-curve effect occurs or not depends on interface orientation. R-curve behaviour in mode II and mixed-mode should be investigated in future work. For this purpose, the selected ENF specimen is unsuitable due to its unstable crack growth. To what extent these phenomena are attributed to fibre bridging, delamination migration, or other effects cannot be answered definitively.

With respect to the numerical investigation of the characterisation specimens, also discussed in Subchapter 5.5, it was shown that the proposed procedure to reduce the mode I interface strengths to allow for larger elements is a valid approach. In addition, it could be shown that analytical solution and numerical results with bilinear traction-separation laws are in good agreement. The use of the $0^\circ//0^\circ$ -interface cERR value for other interface orientations, the procedure according to the standards, results in considerably conservative predictions. In turn, the use of effective interface-specific cERR values improves simulation accuracy for the characterisation specimens.

Even though this way does not accurately describe the physics, it can be a viable way for simulations in which IFF are modelled using CDM, as in this simulation the modelling of crack jumping due to the stress peaks at the crack tip of interfibre crack cannot be achieved. Furthermore, it could be confirmed that superposition of two bilinear traction-separation laws is a suitable solution to model R-curve behaviour. A summary of the determined parameters can be found in Section 5.5.7.

In order to develop a recommendation for the holistic modelling approach, the investigations moved away from the characterisation specimens. The determined material parameters were used to model OHT specimens with different modelling approaches. This study can be found in Subchapter 5.6.

Moreover, the open question from Chapter 4 regarding the significantly too high strength predictions when using continuum shell elements, could be answered. The addition of CZM-based delamination modelling to the continuum shell-based modelling reduces the predicted strength. With this additional modelling feature, the same accuracy in terms of strength prediction as for the modelling with solid elements only can be achieved. In turn, this means that the exclusive use of continuum shell elements cannot be recommended. If no specific information about delamination areas are needed, solid elements should be used instead. Whether solid or continuum shell elements should be combined with CZM-based delamination modelling if the delamination information is needed cannot be definitely answered yet. This is further investigated in Chapter 7 together with the validation of the holistic model using single lap joints.

Another aspect that needs further investigation outside of this work is the use of interface orientation-specific cERRs on structures other than the characterisation specimens. The application of these values to OHT specimens in Section 5.6.3 could not provide a clear indication for this.

Having investigated the intralaminar and interlaminar modelling of the composite adherends including the determination of the required material parameters for the holistic PDA approach in chapters 4 and 5, both the modelling approach and the material parameters for the adhesive are missing to cover all constituents of the entire bonded joint. This is addressed in the subsequent chapter.

CHAPTER 6

Plasticity and damage modelling of structural epoxy film adhesives

What kind of plasticity and damage models are needed to model the behaviour of the structural film adhesive and how can the adhesive be characterised for the chosen approach?

Modelling the behaviour of the adhesive bondline is a central element in the holistic PDA approach for predicting strength and failure mode of the entire joint. In terms of a pragmatic method, the question is which approach for modelling damage onset and progression represents the best compromise between accuracy and effort.

Parts of this chapter have also been published in [5].

6.1 Structure and approach

None of the state-of-the-art approaches for the entire joint presented in Section 2.3.3 take into account the non-linear behaviour of the adhesive with a plasticity model. All of them prescribe the fracture path. This leads to the main questions for this chapter: Does plasticity need to be explicitly modelled and is it permissible to specify the fracture path? To answer this question for the use case in the present work, after a brief overview on the state of the art of adhesive modelling, three different modelling approaches are presented. They differ in terms of numerical cost and material characterisation effort. Two of the approaches also include a distinct plasticity model. The needed material parameters of an aerospace grade film adhesive are determined for all three approaches. With these properties, comparative calculations are carried out on TAST specimens and a recommendation is made for the holistic PDA approach.

6.2 Adhesive selection

The holistic method is intended to be used for bonded joints in aerospace structures. Although the method can be extended to other applications in the future, a typical aerospace adhesive is used in this work. The choice is a high-strength epoxy film adhesive widely used in the aerospace industry: Henkel Loctite EA9695 050 NW AERO. In the further course of this work it will be referred to as EA9695.

It needs to be mentioned that film adhesives have some process advantages over paste adhesives [26]. Since the former are one-component systems, no dosing and mixing is necessary and, therefore, no limited pot life has to be considered. Furthermore, because

the adhesive material is applied to a carrier fabric, resulting bondline thicknesses are more constant. Film adhesives are already in use for co-bonded stiffeners in the Airbus A350 and composite repairs for example. Due to the processing advantages, scatter in experimental data is expected to be reduced. This may lead to a better evaluation of experimental results.

Furthermore, other quite similar film adhesives are available. For instance, FM73, FM94, and FM300 from Cytec / Solvay can be mentioned in this context. However, for the purpose of simplicity, the adhesive material is not varied in this work.

6.3 On the state of modelling structural adhesives

In this subchapter, a brief outline is given on why damage modelling approaches to determine the strength of adhesive layers have emerged.

In principle, to predict the strength of adhesive layers, one can apply analytical or numerical methods. An overview of available linear and non-linear analytical approaches is provided by da Silva et al. [61, 62] and Rodriguez et al. [237]. Analytical approaches are computationally efficient but have some drawbacks which prevent using them for the purpose considered in this work. While linear analytical analyses tend to give safe predictions but are usually conservative, whereas non-linear analyses can be less conservative but are considerably expensive and the advantage over FEA is disputable. In addition, it needs to be considered that the exclusive use of analytical models is only applicable to the analysis of single joints. Unlike the state-of-the-art analytical models, continuum mechanics FEM-approaches are appropriate for global structural design. Reviews of design methods for adhesive joints that are based on FEA are given by He [47] and Jia [238]. Continuum mechanics modelling relies on the comparison of the actual stress or strain state to a limit value [239]. Tomblin et al. [240] state that the majority of industrial practitioners verify the adequacy of the adhesive joint design by analysing average shear stresses. In this context, several requirements have to be met to ensure that this approach is valid. For instance, the overlap length cannot be increased arbitrarily to reduce the average shear stress, because the peak stresses at the end of the joint are only decreased to a certain amount with this measure. Thus, with this method also high safety factors have to be used.

The application of less complex analytical and continuum mechanics methods can be suitable to predict the strength of an adhesive layer with the use of safety factors. However, damage growth, which is a requirement for the holistic approach, cannot be modelled.

In order to overcome these limitations, researchers use damage mechanics approaches to be able to model damage initiation and propagation due to local stress concentrations. An extended review about available methods is presented by Pascoe et al. [241]. The CZM [242] and the VCCT [67] are common methods to incorporate damage mechanics in FEM models. Both methods, VCCT and CZM, have already been presented in more detail in Subchapter 5.3. For this reason, a detailed description is not given in this chapter. While the VCCT is eligible only for very brittle materials and needs an initial crack, CZM is the common approach for adhesive joints and is also chosen in this work [243].

Since these approaches rely on a stress-based damage initiation combined with an energy-based damage propagation, they do not suffer from large mesh dependencies due to the

stress concentration at the edges of the adhesive layer, like the above mentioned analytical and continuum mechanics approaches do. There are different CZM-based approaches varying in accuracy and complexity. In the following, the CZM-based approaches, which are under consideration in this work, will be presented. As with the approaches for modelling the other components of the bonded joint in the holistic approach, a compromise between efficiency and accuracy favourable.

6.4 Cohesive zone modelling-based approaches

Three different CZM-based approaches are common in the relevant literature and are thus under consideration in this work. They are illustrated in Fig. 6.1 and will be introduced in order from simple to complex in the following.

6.4.1 Cohesive elements (ACZ)

Cohesive elements represent the simplest damage mechanics approach. With this approach, the entire adhesive layer is replaced by special-purpose cohesive elements. In this approach, the adherends as well as the cohesive zone represented by the cohesive elements are modelled. Therefore, following Pardoen et al. [94], this approach is referred to as Adherend + Cohesive Zone (ACZ) in this thesis. It is shown in Fig. 6.1(a).

In ACZ models the adherends are modelled as continua and the adhesive layer is only represented by the cohesive zone's traction-separation response. This type of modelling is considerably attractive because only a limited number of parameters is needed, and mixed-mode loading can easily be incorporated. However, representing the whole mechanical behaviour of the adhesive with a single cohesive zone is a strong simplification.

Publications from a group of researchers around Campilho [243, 244] show the difficulties of the widely used ACZ technique. Neto et al. [244] determined the failure loads of single lap joints made of UD carbon epoxy prepreg with 0° plies experimentally and numerically using the ACZ technique. The specimens with varying overlap lengths were bonded either with a brittle or with a ductile adhesive. For the specimens with the brittle adhesive, satisfactory correlations between experimental and numerical failure load were achieved. However, specimens with the ductile adhesive could not be predicted with an acceptable accuracy. The authors attribute this to the used triangular-shaped cohesive law, which is probably not suited for ductile adhesives.

Later, Campilho et al. [243] numerically predicted the same specimens with the ACZ technique but under variation of the cohesive law shape. They found that the influence of the cohesive law shape is neglectable for brittle adhesives but has a large influence for ductile adhesives. A trapezoidal shape results in better predictions.

Overall, it can be stated that it is not straightforward to capture the plastic effects of the adhesive in the ACZ approach without a continuum mechanics plasticity model.

6.4.2 Elastoplastic solid elements combined with cohesive surface (AACZ)

A more versatile model is necessary to include multi-axial plastic deformation. This can be achieved with the Adherend + Adhesive + Cohesive Zone (AACZ) approach, cf. Fig. 6.1(b).

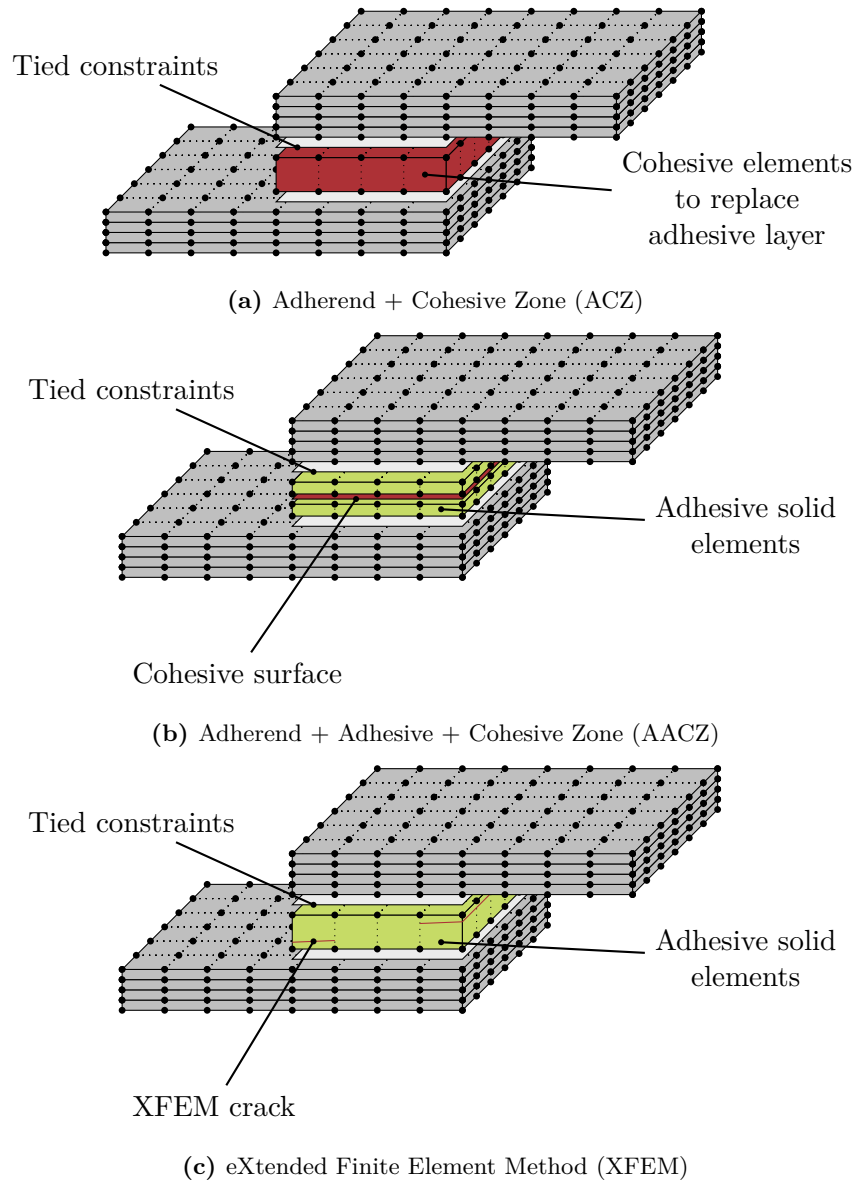


Figure 6.1: Illustration of ACZ (a), AACZ (b) and XFEM-based (c) CZM techniques

In this approach, not only the adherends are modelled as continua but it also includes solid elements to model the adhesive as an elasto-plastic material. In the middle of the adhesive layer modelled with solid elements, a single row of zero-thickness cohesive elements or cohesive contacts is embedded to model fracture within the adhesive.

There are only few publications on models using the AACZ technique for strength prediction of composite bonded joints [245, 246, 247, 248]. As an example, the work of Liljedahl et al. [245] from 2006 shall be discussed in more detail.

The researchers use the AACZ technique to predict the strength of carbon fibre composite SLS joints amongst other joints with aluminium adherends. The adherends are made from an epoxy-based carbon fibre prepreg, which is widely used in aerospace application (Hexcel 8552-IM7), and a toughened-epoxy film adhesive (Cytec FM73). The experimentally observed failure mode is purely cohesive, which justifies the limitation of the damage modelling to the adhesive. To achieve a good correlation between experimentally and numerically determined failure load, the incorporation of adhesive yielding using von Mises (v.M.) plasticity was not sufficient. It was found that only the use of a plasticity model considering hydrostatically sensitive yielding, in the present case a linear Drucker-Prager (lin.D.-P.) model, produces adequate predictions of the failure load.

In a study of Pirondi et al. [247], ACZ and AACZ were compared on the basis of DCB and T-peel joints. They conclude that the use of AACZ did not improve results compared to ACZ. However, this could probably be attributed to a mode I dominated loading and therefore less to none plastic yielding.

In contrast to the ACZ technique, the experimentally determined fracture energy G_c or cERR cannot be used directly with the AACZ technique. The fracture toughness G_c is the sum of energy dissipation to create a new surface and the plastic dissipation in ductile materials. While damage in ACZ is ruled by both dissipations, in models using AACZ technique the plastic dissipation is represented by continuum elements and only the dissipation by separation of the fracture surfaces controls the damage in the cohesive zone. Thus, an intrinsic fracture energy must be considered in the traction-separation-law [249]. To find this intrinsic fracture energy of the softening part, the energy from the elastic and hardening part is subtracted from the total critical energy. This parameter modification is described in Section 6.8.5.

In summary, the ACZ technique is suitable for brittle adhesives, whereas this technique reaches its limits for more ductile adhesives, as plasticity can only be taken into account by adjusting the shape of the traction-separation laws. The AACZ technique, on the other hand, should work for a wider range of adhesives, since more complex plasticity models can be incorporated. Although, it is more difficult to apply. However, with both approaches the crack path is prescribed since cracks can only grow where special purpose cohesive elements or cohesive surfaces are inserted in the FEM model.

6.4.3 eXtended Finite Element Method combined with cohesive surfaces (XFEM)

The classical FEM does not allow arbitrary discontinuities in the displacement field of the discretised region. To model discontinuities, the element edges of the finite element mesh must match the crack geometry. Therefore, the possible crack path is a priori defined, or the region has to be remeshed in every calculation increment. The eXtended Finite Element Method (XFEM) allows arbitrary crack growth in the FEM model without the need of remeshing. XFEM is an extension of the classical FEM, which allows to model discrete cracks in a continuum through an enrichment of the displacement field with discontinuous functions, cf. Eq. 6.1, developed by Belytschko and Black [250]. These enrichment functions allow the inclusion of priori unknown fracture planes and singular

expressions in the existing finite element mesh.

$$\mathbf{u}^h = \sum_{i=1}^N N_i(x) \mathbf{u}_i + \sum_{i=1}^N M_i(x) a_i. \quad (6.1)$$

The approximation of the XFEM displacement field \mathbf{u}^h consists of the standard FEM function at node i $N_i(x)$ and the related unknown \mathbf{u}_i as well as the enrichment part with the local enrichment function $M_i(x)$ and the unknown of the enrichment a_i both at node i [251]. The enrichment is only active when a crack exists. It enables the establishment of phantom nodes which subdivide the element into two subelements formed by the original and the phantom nodes. The displacement fields of these two subelements are completely independent from each other and replace the original element. Whether or not a crack exists in a finite element depends on the evaluation of a crack initiation criteria. If a crack is initiated, CZM or VCCT can be used for crack propagation. As mentioned above, for this work, CZM is the preferred choice. It needs to be mentioned that all of the studies discussed below use XFEM in combination with CZM.

Campilho et al. [252] performed strength predictions of single and double lap joints with a brittle adhesive and aluminium adherends with overlap lengths l between 5 and 20 mm. With the maximum principal stress criterion used for crack initiation, damage growth could not be simulated with XFEM. Mubashar et al. [253] used XFEM to model cracks in the adhesive fillet region of single lap joints and CZM for the interfacial region. They showed that crack growth in the fillet could be well modelled. However, like Campilho et al. [252], they also showed that XFEM with a maximum principal stress criterion for crack initiation is not able to model crack propagation in the adhesive layer as the crack grows towards the adherends. This behaviour does not represent the experimental observations. Xará and Campilho [254] further studied the influence of different XFEM damage initiation criteria on the strength prediction. They showed that the maximum principal stress criterion used by Campilho et al. [252] and Mubashar et al. [253] is the most inappropriate one in this context. With the quadratic stress criterion, the difference in strength between experiment and numerical prediction is less than 10 %. Apart from this, they also performed strength predictions with CZM and observed that the computation times between CZM and XFEM, at least when using an implicit solver, are comparable. All of the mentioned studies, used v.M. as elastic-plastic material model for the adhesives.

Similar to the AACZ approach, the ERRs for the crack propagation must be derived from the measured cERR.

6.4.4 Damage initiation and propagation

All three approaches introduced above require a damage initiation as well as a damage propagation criterion. In this section, a brief summary of the criteria used is given. A bilinear traction-separation law is used for all approaches.

In Abaqus 2020 six different stress- and strain-based criteria are available. For this work,

only the quadratic nominal stress criterion (QUADS), cf. Eq. 6.2, is considered as it is stated to be best suited for the most joint/adhesive configurations by Xará and Campilho [254].

$$f = \left\{ \frac{\langle T_I \rangle}{T_I^0} \right\}^2 + \left\{ \frac{T_{II}}{T_{II}^0} \right\}^2 + \left\{ \frac{T_{III}}{T_{III}^0} \right\}^2 \quad (6.2)$$

With regard to damage propagation, the relevant literature is somewhat ambiguous. Rocha and Campilho [255] conclude in their study that a power law criterion with $\alpha_{PL} = 1$, cf. Eq. 6.3, generally yields the best results for different types of adhesives with the exception of highly ductile adhesives.

$$\left(\frac{G_I}{G_{Ic}} \right)^{\alpha_{PL}} + \left(\frac{G_{II}}{G_{IIc}} \right)^{\alpha_{PL}} + \left(\frac{G_{III}}{G_{IIIc}} \right)^{\alpha_{PL}} = 1 \quad (6.3)$$

However, the BK criterion, introduced in Section 5.3.4 for interlaminar modelling, provides similar results for brittle adhesives, but deviates for other types of adhesives. For this reason, both propagation criteria will be tested in this work.

6.5 Plasticity models with pressure dependent flow criteria

Prior to damage in the form of discrete cracks, adhesives show inherent non-linear material behaviour. Therefore, two of the three modelling approaches use elastic-plastic material models to describe the adhesives' behaviour until fracture in FEA. In order to predict the transition between the elastic and the plastic regime, all of these material models require a suitable yield criterion which is valid for the adhesive under consideration [256]. In contrast to metals, the plastic behaviour of adhesives is sensitive to the hydrostatic stress component [239]. These hydrostatic stress states are generated due to constraints imposed by the stiff adherends in the thin adhesive layer [256]. For this reason, a suitable yield criterion should take into account the influence of the hydrostatic stress on the yield point. Without any claim of completeness, four possible yield criteria for the simulations in this work will be discussed in the following.

6.5.1 Von Mises

The v.M. yield criterion [257] predicts the onset of yielding when the equivalent stress q or rather the second deviatoric invariant J_2 reaches the critical values σ_y [257], cf. Eq. 6.4.

$$F_{vM} = \sqrt{3J_2} - \sigma_y = q - \sigma_y = 0 \quad (6.4)$$

Since the v.M. material model does not account for the influence of the hydrostatic component of stress on the yield point, it does not fulfil the demand stated above and is not well suited for adhesives. Nonetheless, it is widely used in literature and will be the baseline for the simulations in this work because of its easy parameter setting.

6.5.2 Linear Drucker-Prager

The lin.D.-P. criterion is a yield criterion where the onset of yielding is linearly dependant on the hydrostatic stress p [258], cf. Eq. 6.5.

$$F_{linDP} = q - p \cdot \tan(\beta_{linDP}) - d = 0 \quad (6.5)$$

The sensitivity of yielding to the hydrostatic stress p is characterised by the hydrostatic stress sensitivity parameter β_{linDP} being material dependant. The cohesion d is related to the shear yield stress τ_y with $d = \frac{\sqrt{3}}{2}\tau_y(1 + \frac{1}{K})$.

According to the results of Dean et al. [256], the lin.D.-P. model is improper for the investigated epoxy adhesives but appears to describe the behaviour of the investigated acrylic adhesives by Dean et al. [256]. The adhesive under consideration in the present work is epoxy-based and therefore, the lin.D.-P. criterion is not further considered.

6.5.3 Exponent Drucker-Prager

For the epoxy-based adhesive under consideration, the dependence of hydrostatic stress on the yield point is non-linear. This can be seen in the evaluation of the experimental tests later in this chapter, cf. Fig. 6.8. For this reason, the exponent Drucker-Prager (exp.D.-P.) criterion [258] is considered as a third yield criterion. Unlike the lin.D.-P. criterion, the exp.D.-P. criterion forms a hyperbolic yield surface with the material parameter a_{expDP} , the exponent parameter b_{expDP} , and the hardening parameter p_t . The yield surface can be described with the following equation:

$$F_{expDP} = a_{expDP} \cdot q^{b_{expDP}} - p - p_t = 0 \quad (6.6)$$

Originally developed for soil mechanics, it is used for adhesives by several authors [239, 259, 260, 261, 262] to be able to describe the dependency of hydrostatic stresses on yielding. The FM94 adhesive under investigation in the study of Quan and Alderliesten [262] is similar to the adhesive in this work, as both are aerospace grade film adhesives. Since this yield criterion is available by default in both Abaqus/Standard and Abaqus/Explicit, this criterion will be used in addition to v.M. in the remainder of the work.

6.5.4 Mahnken-Schlimmer

A fourth yield criterion to be mentioned is the one that Mahnken and Schlimmer [263] have especially developed for adhesives. The criterion, cf. Eq. 6.7, takes into account the first stress invariant I_1 , the second deviatoric stress invariant J_2 as well as an initial yield stress Y_0 and two material parameters a_1 and a_2 . This expression is then compared with the actual yield stress Y .

$$F_{MS} = \sqrt{3J_2 + a_1Y_0I_1 + a_2I_1^2} - Y \leq 0 \quad (6.7)$$

Apart from Mahnken and Schlimmer themselves [263], Jousset and Rachik [93, 264] also use the criterion with good accuracy. Moreover, it is also used by Burbulla in a

modified form [265]. However, the yield criterion is not available by default in Abaqus and the parameters can only be identified inversely by optimisation [264]. For the mentioned reasons, the Mahnken-Schlimmer criterion is not further considered in this work.

6.6 Experimental tests for elastoplastic properties

The characterisation of the mechanical behaviour of the film adhesive starts with the elastoplastic properties for the v.M. as well as the exp.D.-P. yield criterion. It is followed by the fracture mechanical property characterisation in Subchapter 6.8.

As explained in Subchapter 6.5 the elastoplastic behaviour of structural adhesives strongly depends on loading and more specifically, on the ratio of deviatoric to hydrostatic stress components resulting from different ratios of shear and normal stress in the adhesive. Therefore, characterisation experiments must be performed with different ratios of shear and normal stress. In the relevant literature, several different approaches are used to produce the desired loading ratios.

Arcan tests, similar to the tests used to determine the parameters for the intralaminar failure criteria in Section 4.5.4, can be used [266]. Nonetheless, in Arcan tests, the use of strain gauges to record the strains in the bondline is rather difficult. Another possibility is the use of tubular Butt Joint (BJ) loaded in tension as well as with a combination of tension and shear. Such tests were, for example, used by Mahnken and Schlimmer [263] to determine the properties for their yield criterion to characterise a paste adhesive used in the automotive industry.

This type of experiments was also carried out in a cooperation between DLR and Fraunhofer Institut für Fertigungstechnik und angewandte Materialforschung / Institute for Manufacturing Technology and Advanced Materials (IFAM) for the adhesive under investigation in this work [267, 268]. However, the thin bondline of the film adhesive between 0.1 and 0.2 mm in contrast to 2.0 mm for the automotive paste adhesive, makes the control of the testing machine to achieve constant load ratios very difficult. This is due to the fact that the travel distances of the testing machine are very small while the forces are high.

For this reason, different types of test specimens are utilised in this work. The behaviour under shear loading is characterised with the help of TASTs. The behaviour under normal loading is studied with BJ tests and the behaviour under a combined loading is investigated with Inclined Butt Joint (IBJ) tests.

Furthermore, the Poisson's ratio was determined at DLR using pure resin dog-bone specimens in line with DIN EN ISO 527-2. These tests, however, will not be discussed in detail.

6.6.1 Thick adherend shear tests

This section describes the geometry, manufacturing and testing of the TAST specimens. The geometry of the TAST specimen is represented in Fig. 6.2 and was chosen according to ASTM D 5656 [269].

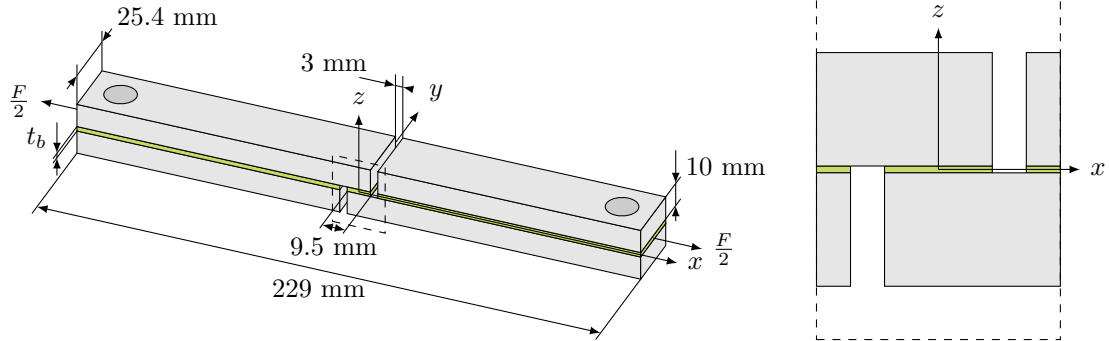


Figure 6.2: Sketch of a TAST specimen

Two different bondline configurations were manufactured. A series with one film adhesive layer and another series with two adhesive layers. In contrast, the series with one adhesive film layer is used for characterisation since the bonded composite structures under investigation also use only one layer. The second series with two layers of film adhesive is used for strain evaluation with a DIC system. The thicker bondline allows for the measurement of the strain field in the bondline itself, whereas the DIC system reaches its resolution limits with the thin bondline. The first tests were performed in 2017 with EN AW 5083 aluminium adherends deviating from the standard. A second campaign, only with one adhesive layer, was performed in 2021 with EN AW 2024 aluminium.

First, the aluminium plates with a thickness of 10 mm were sandblasted with white corundum (grain number F180) and then cleaned with acetone and isopropyl alcohol. After surface preparation, the adhesive film was applied and the bonded aluminium plates were vacuum bagged for one hour. For a nominal adhesive bondline thickness of $t_b = 0.1$ mm, one layer of adhesive film was needed and for a thickness of $t_b = 0.2$ mm two layers were used. The curing of the adhesive was performed in a heat press with temperature and pressure according to the data sheet of the adhesive [270] in an evacuated press chamber. After curing, the plates were cut in strips with a band saw. Then the final specimen geometry including the two holes were machined with a Computerised Numerical Control mill.

The tensile testing of the TAST specimen was performed at room temperature in a Zwick 1476 servo-mechanic testing machine equipped with a 100 kN load cell. The tests were carried out with a constant crosshead speed of $v_{ch} = 0.05$ in/min. For each of the two configurations in 2017, four specimens were tested. The campaign in 2021 consisted of six specimens. In addition to the load-displacement data gathered, data for DIC evaluation was recorded with a consumer full-frame mirrorless camera and a macro lens to capture full-field strain fields of the adhesive layer. For the DIC measurements the challenge is the very thin adhesive layer of the film adhesives compared to paste-bonded joints. For this reason, no off-the-shelf systems are suitable and it was necessary to develop an individual measurement set-up including a very fine speckle pattern.

This DIC set-up is shown in Fig. 6.3 (a) and the speckle pattern applied to the measurement area of the TAST specimen is shown in Fig. 6.3 (b). The camera was coupled to the testing

machine with a self-developed interface box in order to correlate the data of the load cell with the recorded images. Afterwards, the recorded image data was evaluated with the Software Correlate Professional 2017 from GOM. A detailed description of the DIC setup and the data processing can be found in Kosmann et al. [268].

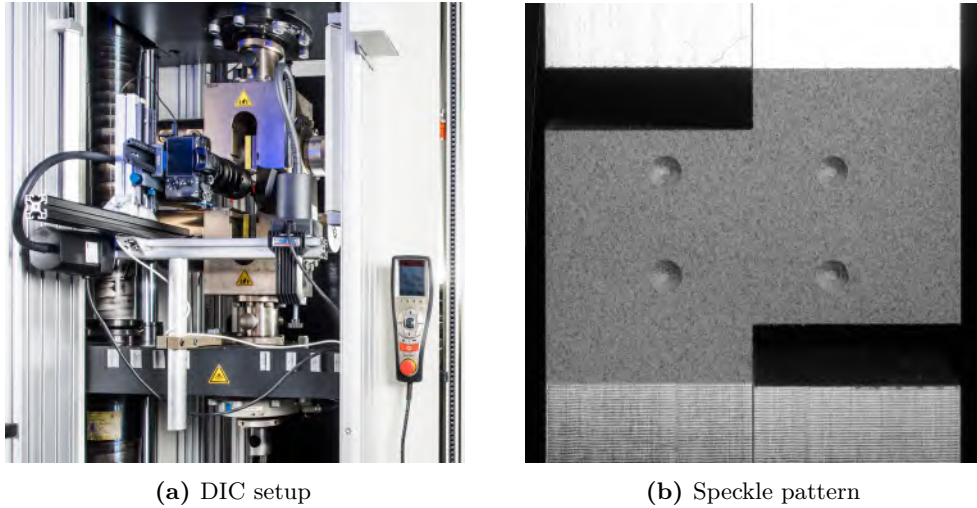


Figure 6.3: DIC setup for thick adherend shear tests

Fracture pattern

In Fig. 6.4, the typical fracture surfaces of the tested TAST specimens are shown for the bondline thickness of $t_b = 0.21$ mm as an example. It can be observed that there is adhesive on both adherend surfaces which means that a cohesive failure in the bondline occurred. It may be concluded that the surface preparation before bonding and the curing of the adhesive were sufficient.

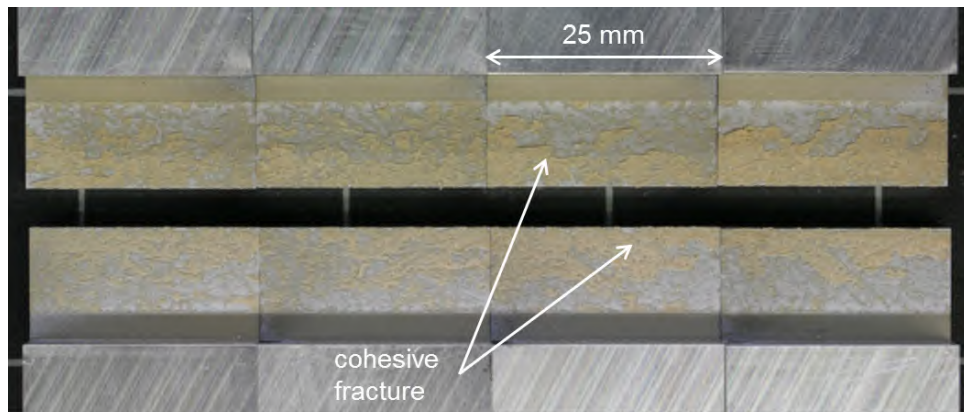


Figure 6.4: Failure surface of the specimen with $t_b = 0.21$ mm

To add, each adherend has one overlap edge with more adhesive left on the surface than the other side and a transition zone in the middle. Therefore, it can be deduced from the fracture pattern that the cracks started near the interface at both overlap edges and then

changed the direction in the middle of the overlap length. This behaviour is reported in literature for brittle adhesives [271].

Experimental force-displacement curves

In Fig. 6.5 the recorded crosshead displacement-force data is plotted. It can be seen that all specimens of the individual series lie very closely together and that there is not much difference between the two different bondline thicknesses. The determined failure loads in the 2017 campaign are $F_f = 11993 \pm 193$ N for the thin bondline and $F_f = 11607 \pm 463$ N for the thicker bondline. These findings are in agreement with the general assumption that thinner bondlines bear higher loads when loaded in shear [272]. However, the differences between the two series lie in the range of scatter.

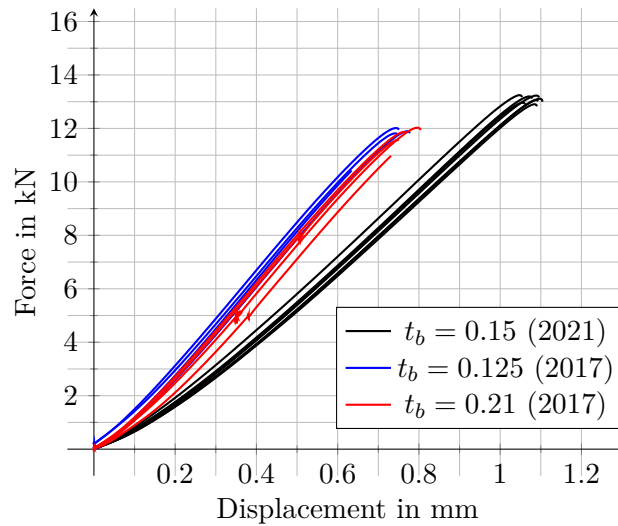


Figure 6.5: Force-displacement data from TAST experiments

It needs to be mentioned that the test campaign performed in 2021 resulted in higher recorded crosshead displacements. Moreover, with $F_f = 13100 \pm 133$ N, the failure load is also higher. These differences may be attributed to several changes in the test setup. As mentioned earlier in this section, the aluminium alloy of the adherends was changed and the specimen fixture inside the test machine was redesigned to allow for less impairment of the degrees of freedom. The ball-head fixtures used in 2021 are probably the reason for the larger crosshead travel. The higher failure load is attributed to the use of a new material batch which also resulted in a slightly higher adhesive thickness of $t_b = 0.15$ mm compared to $t_b = 0.125$ mm in 2017. Unless otherwise stated, the data from the 2021 campaign is used for parameter identification. It needs to be mentioned that the manufacturing process is identical for all test series.

6.6.2 Butt joint and inclined butt joint tests

As the tests with tubular BJs were not successful, BJ and IBJ tests were used for normal and combined normal/shear loading. These tests were carried out as part of a joint project

by Fraunhofer IFAM and are published in [273]. For this reason, only a brief description of the experiments will be given here. It needs to be noted that yield and failure stresses of the different tests are published. However, stress-strain curves are not available.

The geometry of the specimens is shown in Fig. 6.6 and the external dimensions of the two types of test specimens are the same. Nevertheless, the difference is that the bondline of the IBJ is not perpendicular to the loading direction but is inclined by 20° .

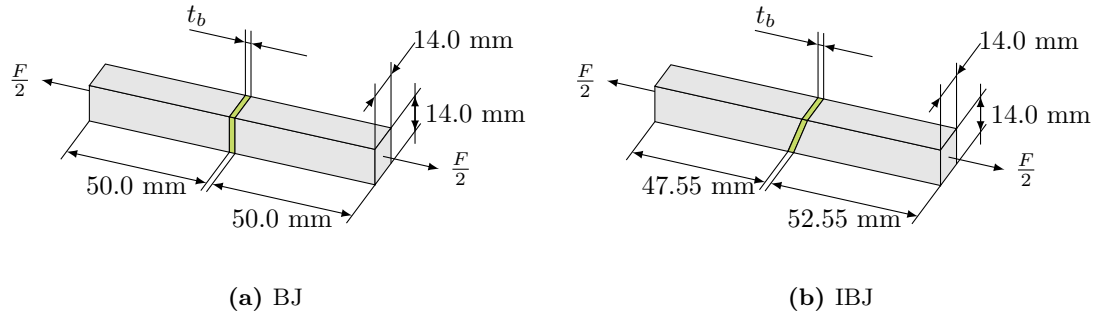


Figure 6.6: Sketches of BJ and 20° IBJ specimen

The adherends were made out of mild steel and the specimens were individually bonded with a joining device. The device used for bonding applies a springload to the specimens during curing. The specimens were cured in a convection oven heated to 130°C and held for two hours. The resulting bondline thickness is 0.135 mm, which is in between the values of the TAST specimens tested at DLR. Tests were performed at room temperature using a Zwick Z050 testing machine. Other than with the TAST tests at DLR the tests were performed strain controlled with a nominal strain rate of 0.001 per second. The strain measurements were performed with four Crack Opening Displacement clips symmetrically distributed around the adhesive layer with an initial distance of 5.0 mm.

The identified yield and failure stresses are summarised in Tab. 6.1. Nagel and Klapp also tested Thick Adherend Shear Joint (TASJ) similar to the TASTs performed at DLR. For the purpose of consistency, yield stress under shear determined by Nagel and Klapp is used for the exp.D.-P. parameter identification.

Table 6.1: TASJ, BJ and IBJ yield and failure stresses from [273]

			σ_y	σ_f	τ_y	τ_f
TASJ	mean	MPa			32.78	51.28
	std. dev.	MPa	-	-	2.73	7.22
	n_{sp}	-			6	9
BJ	mean	MPa	46.78	51.94		
	std. dev.	MPa	1.62	2.41	-	-
	n_{sp}	-	9	10		
IBJ	mean	MPa	38.67	43.69		15.90
	std. dev.	MPa	3.91	4.41	-	1.61
	n_{sp}	-	9	9		9

6.7 Identification of elastoplastic material parameters

This subchapter describes the identification of the elastoplastic parameters of the film adhesive from the experimental tests presented above.

6.7.1 Elastic properties

The shear modulus is determined with the TAST experiments to $G = 810.3$ MPa. With the Poisson's ratio $\nu = 0.361$ from the pure resin dog-bone tests, a Young's modulus of $E = 2205.6$ MPa is calculated.

6.7.2 Hardening curve

To describe the material behaviour after onset of yielding, Abaqus requires a hardening curve as an input. In this work, the hardening curve is derived from the TAST campaign in 2021 described in Section 6.6.1, according to the procedure described in ASTM D5656. The τ - γ -data derived from the test are shown in Fig. 6.7(a).

At first, the yield stress τ_y has to be determined to obtain a shear stress - plastic strain curve. This data was then used to calculate a true stress - true strain curve. The hardening curve for the Drucker-Prager models has to be given in terms of cohesion d and effective true plastic strain ϵ_{eff}^p . In contrast, the hardening curve for the v.M. model has to be specified in Abaqus in terms of effective stress σ_{eff} and effective plastic strain ϵ_{eff}^p . The data can be converted with the equations 6.8 - 6.10.

$$\sigma_{eff} = \sqrt{3}\tau \quad (6.8)$$

$$d = \frac{\sqrt{3}}{2}\tau\left(1 + \frac{1}{K}\right) \quad (6.9)$$

$$\epsilon_{eff}^p = \frac{1}{\sqrt{3}}\gamma^p \quad (6.10)$$

The yield surface shape in the deviatoric stress plane is described by the parameter K . In this thesis, the parameter K is set to 1, which means that the flow stress in triaxial tension is equal to the flow stress in triaxial compression [65]. In this case, the hardening curve for the v.M. and the Drucker-Prager models are the same.

To generate a mean hardening curve as simulation input, each hardening curve derived from the individual measurements is cut off after the lowest occurring maximum plastic strain value and fitted with a cubic spline fit. With the help of these spline fits, hardening curves with stress values at the same equidistant plastic strain intervals are generated. After that the mean stress values at each plastic strain value are calculated, which then results together with the equidistant plastic strain interval in the final mean hardening curve. This final hardening data used for all simulations is shown in Fig. 6.7(b) together with the hardening curves from the individual specimens.

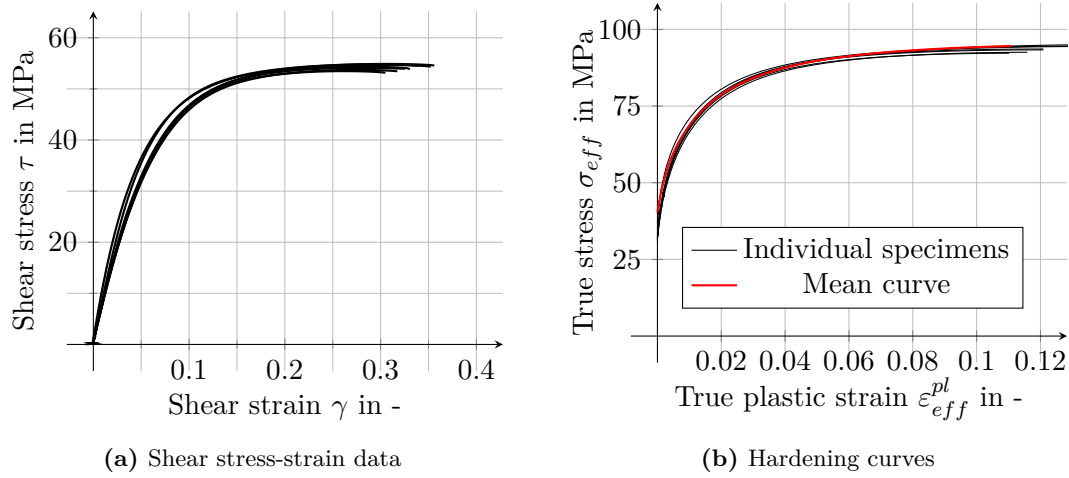


Figure 6.7: Hardening curve derived from TAST shear stress-strain data

6.7.3 Parameters for yield criteria

For the v.M. yield criterion, no additional parameters are necessary. Only the hardening curve derived above is needed as an input.

However, the exp.D.-P. model requires three additional parameters. In order to determine the parameters a_{expDP} , b_{expDP} , and p_t for the exp.D.-P. yield criterion, the flow function Eq. 6.6 is fitted with a least square fit using a Python script through the mean yield stresses from the TASJ, BJ and IBJ tests introduced in Section 6.6.2. The fitted function is shown in Fig. 6.8 and the determined values for the parameters a_{expDP} , b_{expDP} and p_t are summarised in Tab. 6.2.

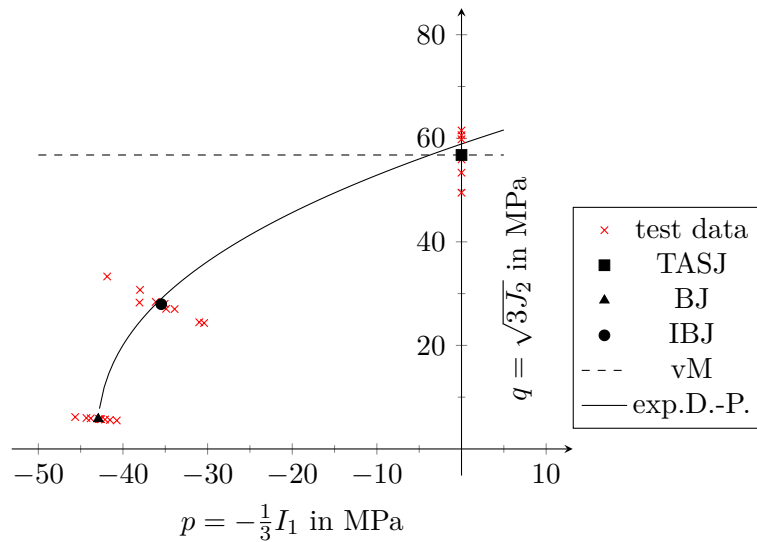


Figure 6.8: Yield data expressed in hydrostatic p and deviatoric q stresses

Table 6.2: Fitted exp D.-P. parameters for LOCTITE EA 9695 050 NW AERO epoxy film adhesive

Property			
Material parameter	a	0.00219	
Exponent parameter	b	2.448	
Hardening parameter	pt	43.082	MPa

6.7.4 Verification of plasticity models on the basis of TAST specimens

As mentioned in Section 6.6.1, DIC data was recorded during the experimental tests. The resolution of the chosen setup enables the computation of several strain data points in thickness direction of the adhesive layer during post processing of the DIC data. This data is used to compare the strain distribution in FE-models, calculated with both the v.M. and the exp.D.-P. models presented in Subchapter 6.5, with the experimental data. By doing so, the material models in combination with the chosen material parameters can be verified.

The numerical analyses used for the verification were carried out as quasi-static implicit dynamic simulations with Abaqus/Standard. Although two-dimensional plane strain simulations would be numerically much more efficient, full 3D simulations are used because the strains conducted by the DIC system were measured at the side surface of the specimen. The measured strains in this area cannot be compared to strains from a two-dimensional plain strain analysis, which represents a mid-section cut through the specimen. As a result of a mesh convergence study the adhesive layer was discretised with five reduced integrated linear brick elements (C3D8R) in through-thickness direction and an element edge length of 0.1 mm in the other two directions. The adherends are also modelled by reduced integrated C3D8R linear brick elements with a edge length of 1.0 mm. As can be seen in Fig. 6.9, the model takes advantages of the symmetry in the x-z-plane of the specimen to save computation time. The interface between adhesive and adherend is modelled with a tied contact.

In Fig. 6.10 the strains ϵ_x and ϵ_{xy} are plotted at a loading of 1.5 kN. At this loading the material behaviour is assumed to be linear-elastic because the calculated stresses are lower than the yield stresses presented by Nagel and Klapp [273]. Since the strains in y-direction ϵ_y are about zero, they are not presented. The strains are plotted from the edge of the bondline at $x = -4.75$ mm until the half overlap length $x = 0$ mm because the measurement field of the DIC system covers only 7.2 mm by 4.8 mm. It is apparent that there is some noise in the DIC strain data but nevertheless, the strains ϵ_x are in good agreement with the experimental data. Compared to the experiment, both simulations slightly overestimate the shear strains ϵ_{xy} . In addition, it can be noted that both material models reveal the same strains. This is an expected result as the two materials models do not differ from each other in the linear-elastic regime.

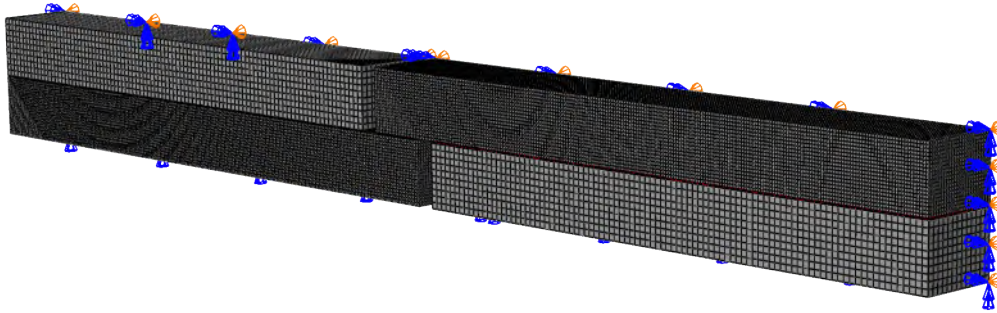


Figure 6.9: 3D FE-model of half TAST specimen using x-z symmetry plane and tied contact between adhesive and adherends

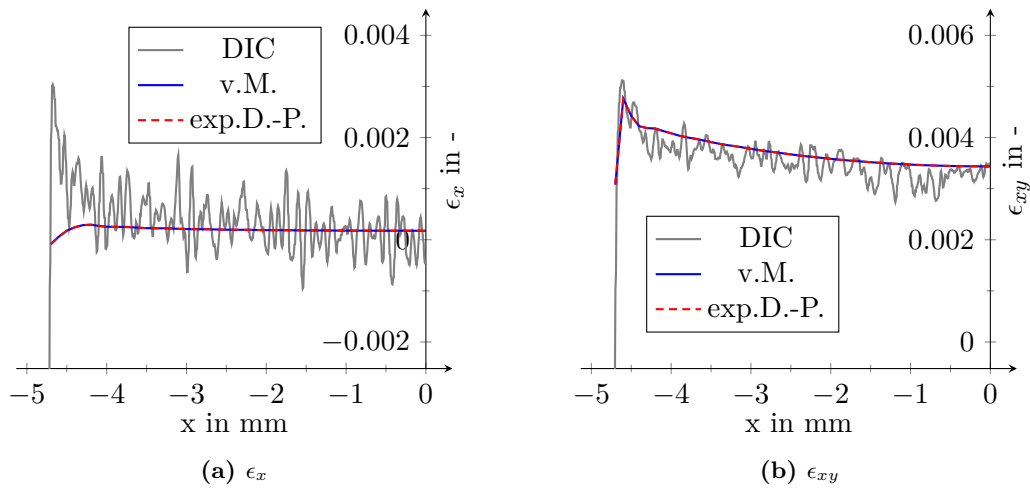


Figure 6.10: TAST strain comparison at 1.5 kN

In order to compare strain fields after onset of yielding, in Fig. 6.11 the strains ϵ_x and ϵ_{xy} are plotted at a loading of $F = 6$ kN. It can be noted that the v.M. model and the exp.D.-P. model give the same results. Similar to the findings for the 1.5 kN loading, the ϵ_x strains from the experiment and the numerical simulations are in good agreement. Also, the numerical data only differs slightly at the outer boundary of the overlap at $x = -4.75$ mm and the ϵ_{xy} -values of both simulations at the overlap edge are in good agreement with the experimental values. However, in the middle of the overlap, the numerical values are higher. At this point, the numerical values are in the range of the peaks of the DIC measurement.

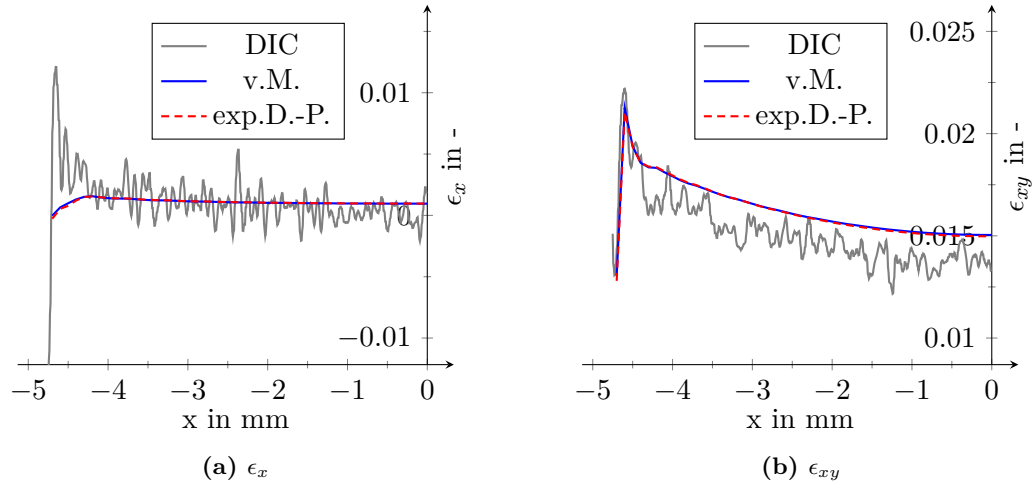


Figure 6.11: TAST strain comparison at 6.0 kN

A second data set after onset of yielding is recorded at $F = 10$ kN. The results are shown in Fig. 6.12.

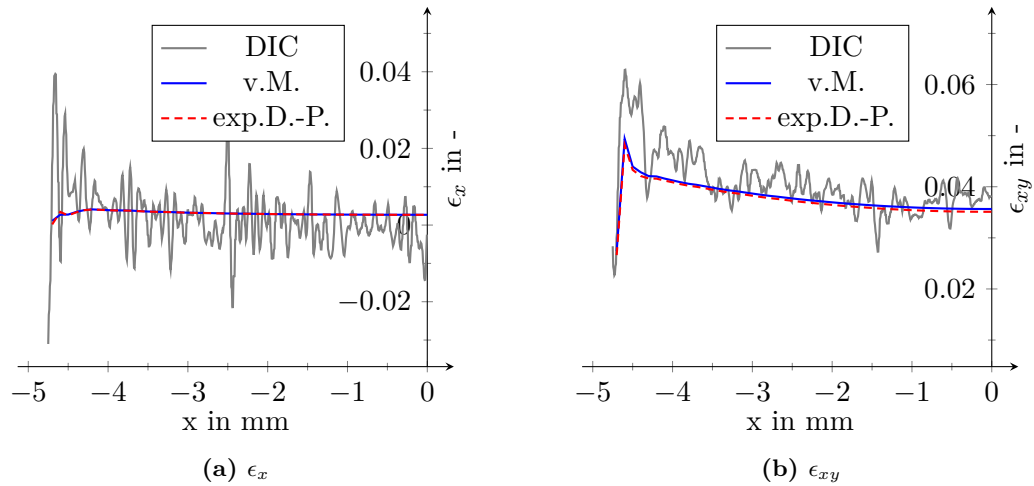


Figure 6.12: TAST strain comparison at 10.0 kN

Again, the numerically determined strains ϵ_x are in good agreement with the experimental test. At this loading, the shear strains ϵ_{xy} predicted with the v.M. model are slightly higher than the ones predicted with the exp.D.-P. model. However, the difference is considerably small. Compared with the results at 6 kN the findings for ϵ_{xy} are the opposite. The peak strains at the overlap edges are underestimated, but the strains in the middle of the overlap length are well captured by both numerical models.

As a result, it can be concluded that both material models can describe the experimental behaviour adequately. The slight difference in the ϵ_{xy} -distribution might stem from measurement inaccuracy or the material parameters since the DIC measurements were

performed on specimens with a bondline thickness of $t_b = 0.2$ mm from 2017 and the parameter identification was performed with the recent specimens with $t_b = 0.15$ mm from 2021. Accordingly, further testing with a more extensive number of specimens has to be conducted. The good performance of the v.M. model could be attributed to the low hydrostatic stress component in the TAST specimens [274].

6.7.5 Comparison of plasticity models on the basis of butt joint tests

The comparison of the DIC measurements on TAST test specimens with simulations shows good agreement, but no major differences between the two yield models under consideration. Because high hydrostatic stresses are caused by normal loading, differences should occur in BJ specimens. As no own tests have been carried out in this configuration, the previously introduced tests by Nagel and Klapp, cf. Section 6.6.2, are used to compare the two yield criteria.

For this purpose, the test specimen is simulated with the dimensions given in Fig. 6.6. The adhesive layer is discretised with two elements through the thickness and an in-plane element edge length of 0.5 mm. During the simulation the specimens are loaded with 10 kN, which corresponds to the failure load of the experimental tests. Since no stress-strain data is available from these tests, the simulations are only used to compare the two yield models and not for verification purposes.

The results from the simulations in terms of force-displacement data are shown in Fig. 6.13.

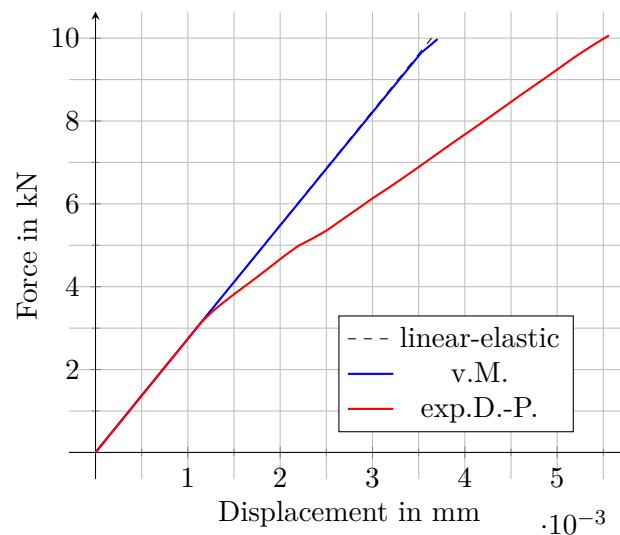


Figure 6.13: Force-displacement data from BJ simulations

It can be seen that the initial stiffness of the two models is equal up to a loading of approximately 3.5 kN. At this loading, the simulations with the exp.D.-P. model predicts yielding of the adhesive. Yet, the simulations with the v.M. model show a linear behaviour

up to above 9.5 kN. Thus, yielding begins immediately before the experimental failure load of 10 kN is reached.

It can be concluded that the two models behave differently under loading with high hydrostatic stress components. However, for further verification, strain fields from BJ tests should be recorded with the same DIC technique used for the evaluation of the TAST specimen in the future.

6.8 Identification of fracture mechanical properties

The following subchapter describes the identification of the fracture mechanical properties of the EA9695 film adhesive. This is done as an extension of the master thesis of Klimmeck [275] supervised by the author of this thesis.

The DCB, ENF and MMB specimens for the interlaminar composite material characterisation described in Chapter 5 are used as a basis. For this reason, not the entire experimental set-up and the evaluation are described here. Instead, it is referred to Subchapter 5.5 and only the differences to the interlaminar test programme are described in this chapter.

The DCB and ENF tests are performed with both composite materials under consideration as adherend materials. Like with the interlaminar test programme, plates are manufactured and then cut down to six specimens from each plate. Different to the interlaminar specimens which are manufactured in one curing cycle, the specimens for adhesive characterisation are manufactured in a two-step process. At first, the composite adherends are manufactured and cured. Thereafter, the surfaces to be bonded are cleaned and pretreated. This is described in the following section in more detail. After that, the film adhesive and a PTFE foil for the initial crack are placed between the composite plates. Then, the film adhesive is cured in a second autoclave process according to the manufacturer's instructions. This process is called secondary bonding, cf. Fig. 2.4.

If not stated otherwise, the data reduction methods as well as the analytical solutions are the same as for the interlaminar test programme. They are described in Subchapter 5.5.3 and Section 5.4. Also, the simulations models used for verification of the derived material parameters are basically the same. A description can be found in Section 5.3.6. The difference is that the adhesive layer is modelled with the ACZ approach using cohesive elements with a thickness of 0.15 mm and an in-plane edge length of 0.5 mm. The stiffnesses presented in Section 6.7.1 are used for the cohesive elements.

6.8.1 Surface pretreatment and fracture pattern

As mentioned above, the surfaces of the cured composite plates have to be pretreated prior to bonding.

The standard surface pretreatment process used at DLR for the bonding of composites with film adhesive is a plasma treatment under atmospheric pressure. For a detailed description, the author would like to refer to the PhD-thesis of Löbel [26], which was also written at DLR. In addition to a description of the state of the art, it also contains a parameter study on the settings of the plasma system. The parameters established by Löbel are used in

this work.

It can be said that the pretreatment of the 8552-IM7 plates could be performed without any problems. However, the plates made from M21-T700GC were clearly visibly bent with a curvature perpendicular to the fibre direction after the plasma treatment. The plates with a thickness between 1.5 mm and 1.6 mm show a permanent deflection of several millimetres in the middle of the plate. A workaround was the change from plasma treatment to the more conventional manual grinding as part of the pretreatment process, which is also described by Löbel [26].

This change made it necessary to evaluate the influence of the pretreatment process. To do so, for the DCB and ENF tests, three series each were manufactured: one with plasma pretreated 8552-IM7 adherends as well as one each with 8552-IM7 and M21-T700GC with manual grinding.

The fracture surfaces of a plasma treated and a grinded 8552-IM7 post-mortem opened specimen are shown in Fig. 6.14.

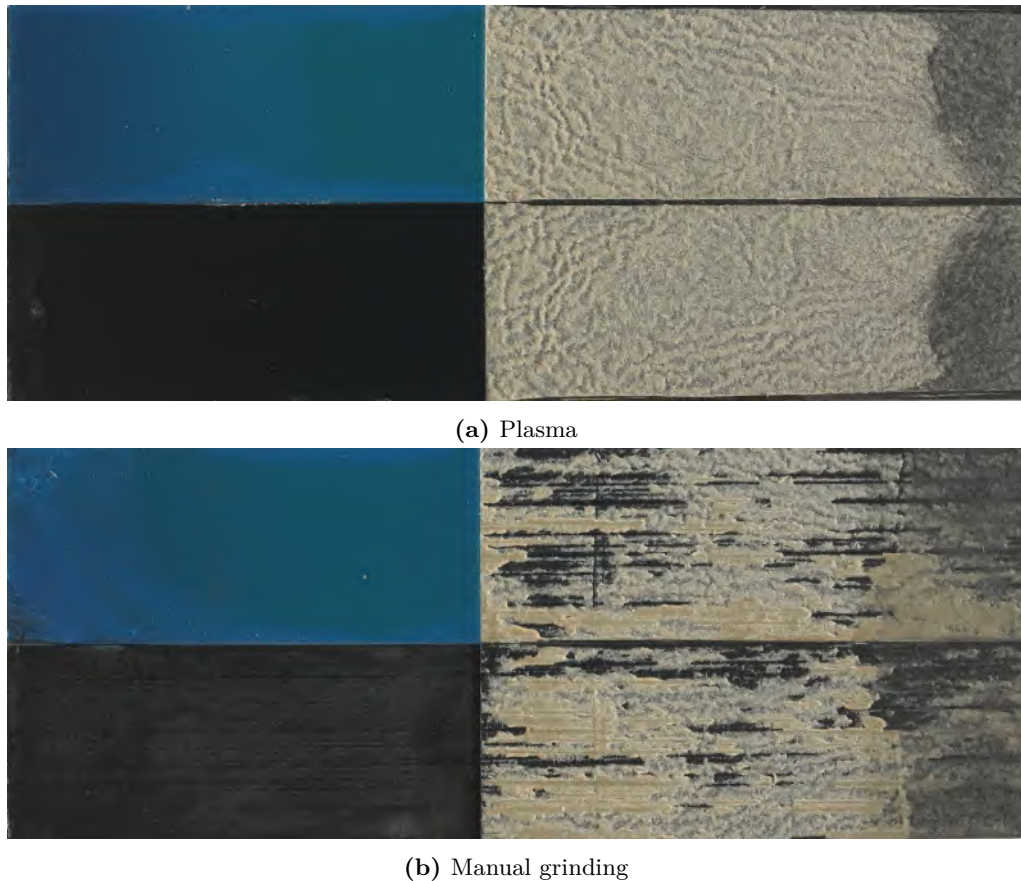


Figure 6.14: Fracture pattern of DCB tests with Hysol EA9695 and 8552-IM7 with different surface pretreatments

On the left-hand side of the specimens, the blue PTFE film for the initial precrack can be seen. The adhesive is visible on the right in yellow / beige colour, whereas it is covered by the blue PTFE film on the left-hand side. Regardless of the surface pretreatment, the adhesive is left on both adherends after the test. Therefore, the failure mode is mainly cohesive. However, depending on the surface pretreatment, the fracture surfaces display considerable differences.

It can be said that the fracture surface of the specimen pretreated with plasma is more homogenous compared to the manually grinded specimen. Except for the edges of the specimen, the adherends are stained with adhesive everywhere. Only the thickness of the remaining adhesive varies and leads to the impression of a scaly surface.

The fracture surface of the grinded specimen is much more inhomogenous. It has areas where the black CFRP adherend is clearly visible and none or only a thin layer of adhesive remains on the surface. In these areas, more adhesive is left on the opposite adherend's surface. In addition, it can be seen that the black areas are oriented with the fibre orientation. This indicates that the fibres were damaged by the grinding process and then broke out in the test. Therefore, the failure mode is partially thin-layered cohesive and partially light-fibre-tear.

The same findings hold true for the ENF specimen and images of the ENF fracture patterns can be found in Appendix G.

In subsequent tests, it was found that the heat input from the plasma torch was too high and that multiple treatments with gaps between the lines prevented the plates from warping. However, no second series of M21-T700GC with the modified plasma treatment was manufactured and tested. As will be presented in detail later, no great influence of the adherend material and the pretreatment process on the cERR has been found. However, the fracture surfaces of the plasma-treated specimens are clearly more homogeneous. Due to this, MMB tests are only performed with 8552-IM7 adherend material and plasma pretreatment.

6.8.2 Double cantilever beam tests for mode I parameters

The dimensions of the DCB specimens tested are shown in Tab. 6.3.

Table 6.3: Dimensions of DCB specimens for film adhesive characterisation

Parameter				Value	Unit
Length	l_{DCB}			250.0	mm
Width	w_{DCB}			25.0	mm
Total thickness	t_t	8552-IM7		3.25	mm
		M21-T700GC		3.35	mm
Bondline thickness	t_b			0.2	mm
Initial crack length	a_0			42	mm

It is apparent that the thickness varies slightly depending on the composite material

used. This is due to the different cured ply thicknesses of 8552-IM7 and M21-T700GC. The specimens were tested according to ASTM D5528. A natural initial crack was generated by a preloading of the specimens until a crack extension of 3 mm was reached. In this way, the initial crack length a_0 is extended from 39 mm to 42 mm. After the preloading, the specimens were unloaded and then the actual test was started with the new initial crack position marked. As recommended by the ASTM D5528 standard, the MBT data reduction method is used. It is described for the interlaminar tests in Section 5.5.3.

In Tab. 6.4, the determined G_{Ic} values are given.

Table 6.4: Mode I fracture toughness values G_{Ic} of Hysol EA9695 from DCB tests in N/mm

Adherend material	8552-IM7	8552-IM7	M21-T700GC
Surface pretreatment	Release film + plasma	Release film + grinding	Release film + grinding
n_{sp}	6	6	5
G_{Ic}	0.806 ± 0.045	0.697 ± 0.107	0.755 ± 0.023

The highest value is determined for specimens with 8552-IM7 and plasma surface pretreatment with $G_{Ic} = 0.806$ N/mm. The mode I cERRs of the grinded series are lower but differ only by approximately 0.05 N/mm between the two adherend materials. This leads to the conclusion that adherend materials have no significant influence on the G_{Ic} determination of the adhesive. The manually grinded series with 8552-IM7 is 13.5 % lower than the plasma series and the series with M21-T700GC adherends lies between the two 8552-IM7 series. For the further work, the value of the plasma pretreated series is chosen because of the more homogeneous fracture surface without fibre-tear shown in Fig. 6.14(a) above.

Fig. 6.15 shows the force-displacement curves of the specimens made from 8552-IM7 recorded during the experiments as well as the analytical solution and the numerically generated data. The experimental data of the experiments with M21-T700GC can be found in Appendix G. The experimental force-displacement data shows nearly linear behaviour up to the maximum force. After that, a stable propagation region with degressively decreasing force can be observed.

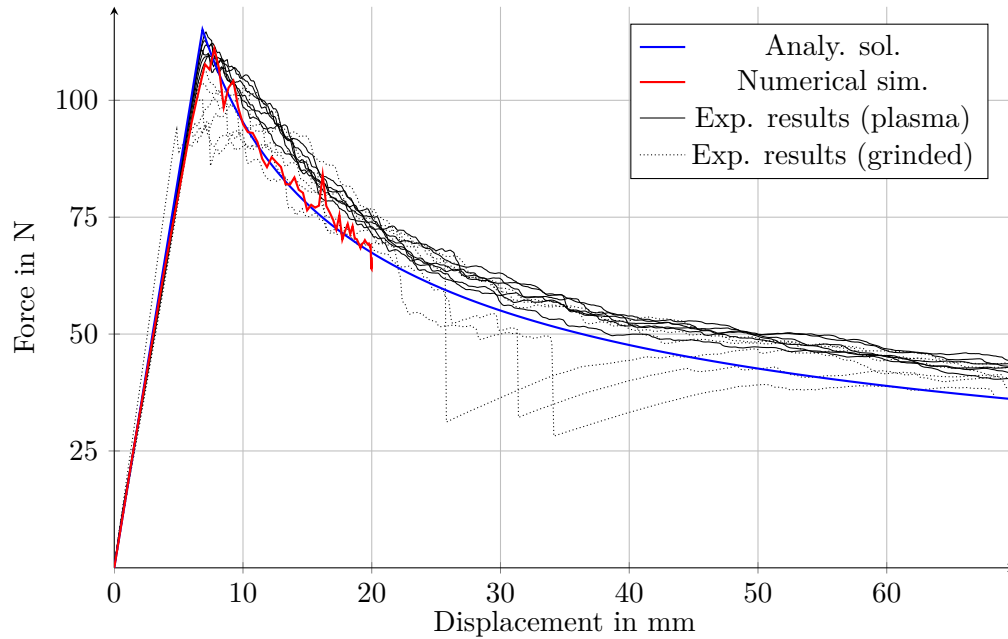


Figure 6.15: Experimentally, analytically and numerically determined load-displacement curves of a Hysol EA9695 film adhesive DCB test with 8552-IM7 adherend material

The forces of the plasma pretreated specimens are slightly higher than the ones from the grinded specimens. The maximum force of the plasma series is 111.84 ± 1.85 N, whereas the maximum force from the grinded series is 96.36 ± 12.13 N. This is also reflected in the G_{Ic} values. In addition, the grinded specimens show load drops of more than 50 N between 25 mm and 35 mm displacement. This corresponds to the inhomogenous fracture pattern.

It can be said that the analytical solution and numerical simulations agree well and can capture the experimental behaviour. The progression region is slightly lower in the analytical and numerical solution compared to the experiments. This could be attributed to the conservative MBT data reduction scheme. The maximum forces of analytical solution (115.14 N) and numerical simulation (116.10 N) lie closely together and are also in agreement with the maximum force of the experiments with plasma pretreatment. Hence, it can be concluded that the behaviour can be described well with the determined G_{Ic} value of 0.806 N/mm.

6.8.3 End notched flexure tests for mode II parameters

This section describes and discusses the results of the conducted ENF tests. The introduction of a natural precrack by preloading, like with the DCB specimens, is not possible because the crack growth in the ENF specimens is unstable once started. Accordingly, the ASTM D7905 standard recommends using a thin non-adhesive film with a maximum thickness of 0.013 mm and does not require a natural initial crack. The test is started from the artificial precrack introduced by the non-adhesive film. As only a PTFE film

with a thickness of 0.025 mm was available, the requirements of the standard could not be met. Thus, other measures to introduce a valid precrack in the specimens had to be found. The standards DIN EN 6034 and AITM 1-0006 recommend cutting ENF specimens from the tested DCB specimens. By doing so, the mode I crack grown during DCB testing can be used as a natural precrack for mode II testing. In the context of this work, both approaches were investigated.

For this reason, five series of ENF specimens were tested. Three series with mode I precrack under variation of the surface pretreatment as well as a variation of the adherend material are considered. For the artificial precrack starting from the PTFE film, the same three variations were planned. However, due to testing issues only the series 8552-IM7 with plasma pretreatment and the manually grinded M21-T700GC series could be evaluated. The dimensions of the specimens are summarised in Tab. 6.5.

Table 6.5: Dimensions of ENF specimens for film adhesive characterisation

Parameter		Value	Unit
Length	l_{ENF}	110.0	mm
Span length	L	100.0	mm
Width	w_{ENF}	25.0	mm
Total thickness	t_t	8552-IM7	3.25 mm
		M21-T700GC	3.35 mm
Bondline thickness	t_b	0.2	mm
Initial crack length	a_0	41	mm

It needs to be mentioned that the use of the DCB test specimens necessitated a change in the evaluation. Other than with the interlaminar tests, the data reduction was not performed with the CC method, but with the method described in DIN EN 6034 / AITM 1-0006, cf. Eq. 6.11. Due to the cutting from the DCB specimen, the ENF specimens were too short to measure the compliance with different crack lengths. As a result, the correction parameter m_{CC} could not be determined.

$$G_{IIc} = \frac{9Pa_0^2d}{2w(1/4)L^3 + 3a_0^3} \quad (6.11)$$

It is recommended to determine the load P by visual inspection. For this, the load at which first crack growth can be observed on the side of the test specimen is used. In part, however, the visual determination of crack initiation was ambiguous. For this reason, the maximum load was used. This is also mentioned as an option in the standards. In the cases of clearly visible crack initiation, the load at crack initiation is close to the maximum load.

The determined values of G_{IIc} are shown in Tab. 6.6.

Table 6.6: Mode II fracture toughness values G_{IIc} of Hysol EA9695 from ENF tests in N/mm

	Adherend material	8552-IM7	8552-IM7	M21-T700GC
	Surface pretreatment	Release film + plasma	Release film + grinding	Release film + grinding
Mode I precrack	n_{sp} G_{IIc}	6 4.035 ± 0.466	6 4.278 ± 0.369	5 3.704 ± 0.574
Artificial precrack	n_{sp} G_{IIc}	3 3.280 ± 1.536	- -	6 3.970 ± 0.210

The highest value of 4.278 N/mm is determined for the grinded series with mode I precrack and 8552-IM7 adherend material. The lowest value of 3.280 also results from a series with 8852-IM7 as adherend material but with plasma pretreatment and artificial precrack. Nevertheless, the standard deviation of this series is with 1.536 very high compared to the other series, because only three specimens could be evaluated.

The difference between natural mode I and artificial precrack is discussed using the example of the two grinded series with M21-T700GC adherends. The difference of the mean values with 3.704 N/mm for the mode I precrack and 3.970 N/mm for the artificial precrack is not very high. The influence of the nature of the prerack is therefore not assessed as decisive. When looking at the series with mode I precrack and 8552-IM7 adherends, it can be said that the influence of the surface pretreatment under mode II loading is also rather small with 4.035 N/mm to 4.278 N/mm.

Consequently, it was decided to use the $G_{IIc} = 4.035$ N/mm value from the series with mode I precrack, 8552-IM7 adherends and plasma surface pretreatment for the further course of this work. This is again justified by the fact that the plasma treated fracture surface is more homogenous. The nature of the precrack seems to not make a considerable difference and the corresponding series with artificial precrack only contains three valid specimens. It can also be concluded, that there is no major difference between the two adherend materials. In this way, it is also ensured that mode I and mode II parameters fit together.

Fig. 6.16 shows the recorded load-displacement curves from the 8552-IM7 experiments with mode I precrack. In addition, force-displacement curves from the analytical solution as well as from the numerical simulation of the test are included. The experimental load-displacement data of the M21-T700GC experiments can be found in Appendix G.

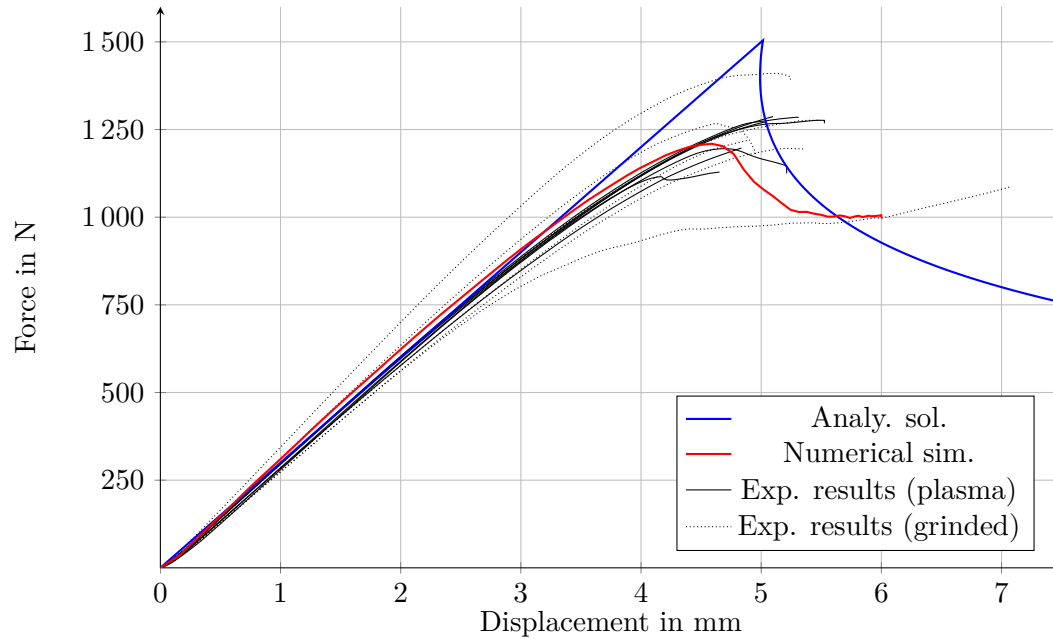


Figure 6.16: Experimentally, analytically and numerically determined load-displacement curves of a Hysol EA9695 film adhesive ENF test with 8552-IM7 adherend material

In general, it can be seen that the data from the grinded series has more scatter than from the one with plasma pretreatment. Although, the maximum forces measured for the series do not differ much with 1234.64 ± 56.87 N for the plasma series and 1242.81 ± 96.97 N for the grinded series. The initial stiffness is well represented by both the analytical solution and the numerical simulation. Moreover, the force-displacement curve of the experiments starts to become non-linear between 750 N and 1000 N. In contrast, the analytical solution is linear up to the maximum force and overshoots the experimentally determined maximum forces with 1504 N. This is different to the curve generated by the simulation since the numerical simulation is capable of modelling the non-linear behaviour as well as the maximum force. With 1207.46 N the calculated maximum force deviates by only -2.2% to the experiments. For this reason, the selected value for G_{IIc} is considered to be verified.

6.8.4 Mixed mode bending tests for mixed mode parameters

As the DCB and ENF tests did not reveal major influences of surface pretreatment and adherend material on the fracture toughness, the MMB tests are only performed with 8552-IM7 adherends and plasma surface pretreatment. The dimensions of the specimens are given in Tab. 6.7.

Table 6.7: Dimensions of MMB specimens for film adhesive characterisation

Parameter		Value	Unit
Length	l_{MMB}	137.0	mm
Width	w_{MMB}	25.0	mm
Total thickness	t_t	3.25	mm
Bondline thickness	t_b	0.2	mm
Initial crack length	a_0	50	mm

Two different mode ratios were tested, with the aspired ratios being $G_{II}/G_T = 0.2$ and $G_{II}/G_T = 0.6$. Measurements with an ATOS 3D scanner by GOM indicated that the targeted lever length c was well calibrated in the MMB apparatus, so that the mode ratio barely deviates with $G_{II}/G_T = 0.2052$ and $G_{II}/G_T = 0.629$. The exact values are used for the evaluation.

The resulting cERRs for the different modes are given in Tab. 6.8.

Table 6.8: Mixed-mode fracture toughness values of Hysol EA9695 from MMB tests in N/mm

a $G_{II}/G_T = 0.21$		b $G_{II}/G_T = 0.63$	
Adherend material	8552-IM7	Adherend material	8552-IM7
Surface	Release film	Surface	Release film
pretreatment	+ plasma	pretreatment	+ plasma
$n_{specimen}$	7	$n_{specimen}$	7
G_I	0.693 ± 0.026	G_I	0.527 ± 0.029
G_{II}	0.124 ± 0.007	G_{II}	0.894 ± 0.054
G_T	0.875 ± 0.003	G_T	1.421 ± 0.083
G_{II}/G_T	0.208 ± 0.000	G_{II}/G_T	0.629 ± 0.001

As expected, the total cERR G_T is with 1.421 ± 0.083 N/mm higher for specimens with the high mode II loading compared to the 0.875 ± 0.003 N/mm for the high mode I loading. This can be explained by the significantly higher G_{IIc} of the adhesive compared to G_{Ic} . The resulting values for G_T are used together with the pure mode I G_{Ic} from the DCB and the pure mode II G_{IIc} from the ENF tests to fit the BK-law. Thus, four support points are available for the curve fit. The fit is performed with a Python script and results in a mixed-mode parameter of $\eta_{BK} = 3.6$.

The load displacement curves recorded during experimental testing are shown in figures 6.17 and 6.18 for the different mode ratios.

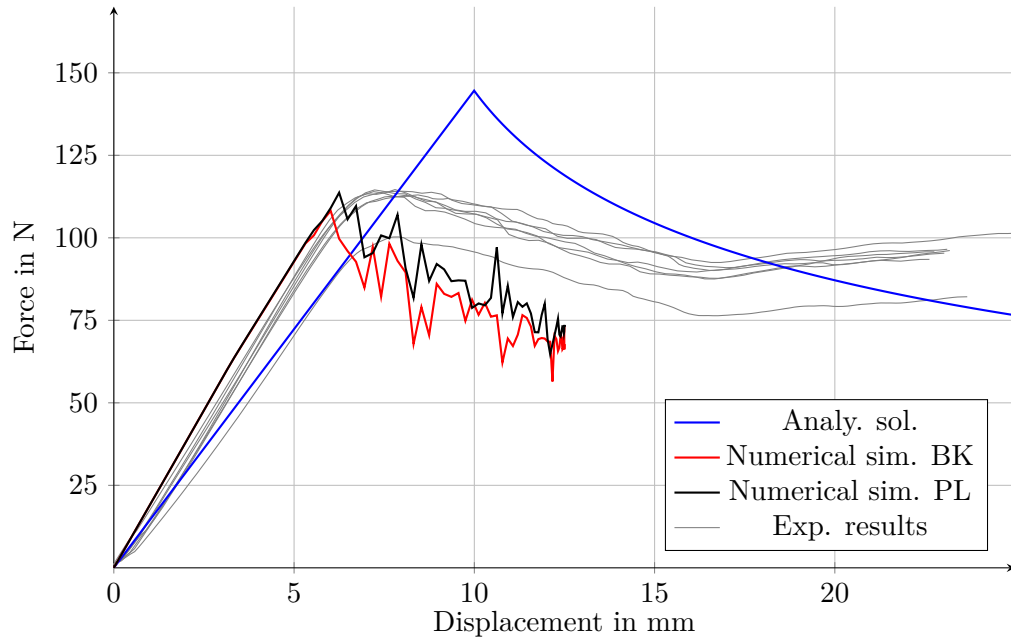


Figure 6.17: Experimentally, analytically and numerically determined load-displacement curves of a Hysol EA9695 film adhesive MMB test with $G_{II}/G_T = 0.21$ and 8552-IM7 adherend material

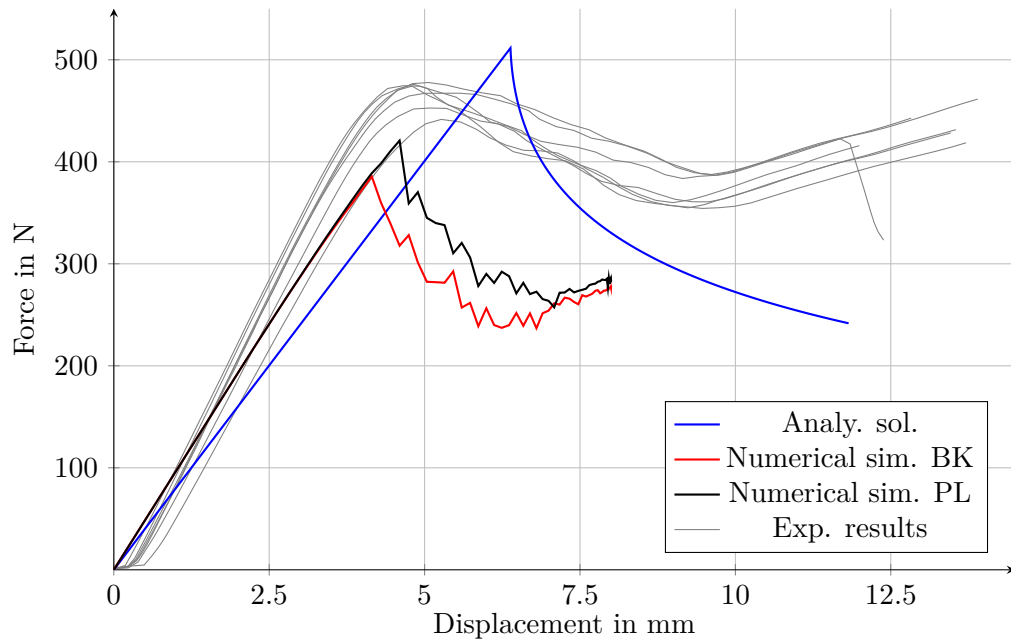


Figure 6.18: Experimentally, analytically and numerically determined load-displacement curves of a Hysol EA9695 film adhesive MMB test with $G_{II}/G_T = 0.63$ and 8552-IM7 adherend material

As for the DCB and ENF tests, in addition to the analytical solution, also data from two numerical simulations for each mode ratio is plotted. The simulations differ in terms of the crack propagation law. One simulation uses the BK-law with $\eta_{BK} = 3.6$ fitted from the MMB experiments and the other simulation uses the power law recommended in literature with $\alpha = 1.0$. A short discussion of the laws can be found in Section 6.4.4.

In general, the shape of the force-displacement curve is the same for both experiments. After a nearly linear increase of the force up to its maximum, a linear progression region is followed by another force increase. The second force increase happens when the propagating crack reaches the fulcrum of the MMB apparatus. The maximum force for $G_{II}/G_T = 0.63$ is with 466.77 ± 12.96 N significantly higher than for $G_{II}/G_T = 0.21$ with 112.01 ± 4.84 N. This is expected due to the higher G_T value at the mode ratio 0.63.

Unlike for the interlaminar experiments, the analytical solution is not able to predict the behaviour of the MMB tests as it is far off for both series in terms of stiffness, strength and propagation.

However, the simulations are able to reproduce the stiffness of the test series with $G_{II}/G_T = 0.21$ up to the maximum force. With a value of 113.70 N, the maximum force itself is well captured by the simulation with the power law. Yet, the simulation with the BK-law underestimates the maximum force with a value of 98.21 N. Moreover, the crack propagation phase is underestimated by both simulations. However, again the simulation with the power law shows higher forces and is therefore closer to the experiments.

The stiffness predicted by the simulations for the second series with $G_{II}/G_T = 0.63$ is significantly too low. When looking at the maximum force, the power law simulation is again closer to the experiments than the BK-law simulation. With 420.77 N for the one using the power law simulation and 385.63 N for the one using the BK-law, both simulations give lower maximum forces than the experimental value. For the crack propagation phase, the same picture emerges as for the other test series. Both simulations output forces that are too low, but the power law simulation is with significantly higher values closer to the experiment.

Basically, the same simulation models as for the interlaminar MMB tests are used. Other than for the interlaminar tests, they cannot model the behaviour of the experimental tests very accurately. In addition, the analytical solution is also not able to capture the experimental force-displacement behaviour. This leads to the conclusion that causal research should be carried out. After that, the experiments should be repeated, however, this is beyond the scope of this work.

For this reason, the power law recommended in literature with the standard value of $\alpha = 1$ is used for the remainder of the work as opposed to the BK-law with the parameter η_{BK} determined from possibly erroneous experiments.

Additional MMB tests carried out jointly with Fraunhofer IFAM confirmed the assumption that the power law with $\alpha = 1.0$ is a valid approximation of the mixed mode behaviour. A comparison of the results can be found in Appendix H. However, further experiments and detailed investigations are still necessary.

6.8.5 Calculation of fracture toughness for AACZ and XFEM approach

As described in Subchapter 6.4, in the AACZ and the XFEM approaches only the dissipation by separation of the fracture surfaces controls the damage of the cohesive zone. The dissipation due to plastic deformation is modelled with elastoplastic solid elements. However, the cERR values $G_{c,i}$ measured with the DCB, ENF, and MMB specimens contain the elastic, the hardening as well as the softening part, cf. Eq. 6.12. This is illustrated with a schematic traction-separation law in Fig. 6.19.

$$G_{c,i} = G_{el,i} + G_{hard,i} + G_{soft,i} \quad (6.12)$$

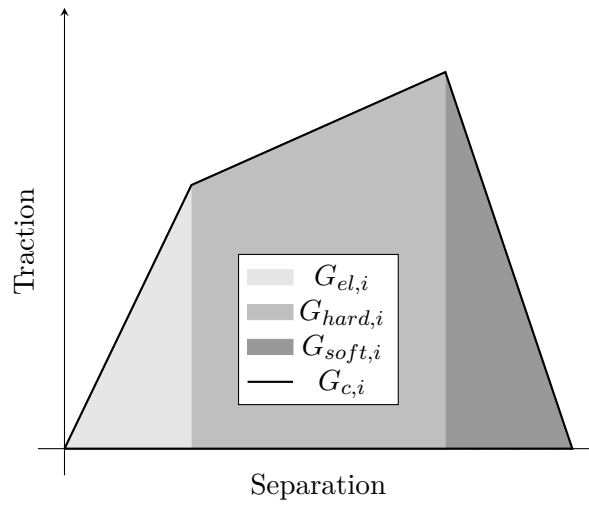


Figure 6.19: ERRs in traction-separation laws

To determine $G_{soft,i}$, $G_{el,i}$ and $G_{hard,i}$ have to be identified for mode I and mode II. With this information the remaining $G_{soft,i}$ for the CZM in the AACZ and XFEM approaches can be calculated. To do so, an approach described by Sachse [276] is adopted.

For mode II the shear-stress strain curves recorded from the TAST specimens are used as input. Due to the lack of test data in mode I, the simulation of the BJ specimen from Nagel and Klapp [273] presented in Section 6.6.2 is used to generate a calculated stress strain curve. The mode I curve is cut off at the first load drop and the mode II data is used as presented in Fig. 6.7(a). In a first step the strains are converted to separations by multiplying each value with the bondline thickness as described by Sachse [276]. Nevertheless, unlike described by Sachse, the area under the resulting traction-separation curve is numerically integrated using the Python module Numpy with a composite trapezoidal rule. In Sachse's PhD-thesis, this is done by calculating the area of a trapezoid by hand using the yield stress and strain as well as the strength and failure strain. The area determined in this way represents the sum of $G_{el,i}$ and $G_{hard,i}$ and should be more accurate than Sachse's estimation. This value is subtracted from the measured $G_{c,i}$ and the remainder represents the softening ERR G_{soft} .

$$G_{soft,i} = G_{c,i} - G_{el,i} - G_{hard,i} \quad (6.13)$$

The application of this approach results in $G_{soft,I} = 0.637$ N/mm and $G_{soft,II} = 1.664 \pm 0.173$ N/mm. In the Subchapter 6.9, these values are verified by means of comparative calculations using TAST specimens.

6.8.6 Summary of fracture mechanical properties

The material parameters determined and used for the CZM modelling in this work are summarised in Tab. 6.9. The cohesive stiffness for the AACZ approach is set to $K = 10^5$ N/mm³, which is the same value that has been used for interlaminar modelling. For the ACZ approach, the original stiffness is used.

Table 6.9: Parameters of Loctite EA 9695 050 NW AERO for CZM modelling

Property		
$K_I = K_{II} = K_{III}$	10^5	N/mm ³
G_{Ic}	0.806	N/mm
$G_{IIc} = G_{IIIc}$	4.035	N/mm
$G_{soft,I}$	0.637	N/mm
$G_{soft,II} = G_{soft,III}$	1.488	N/mm
T_I^0	51.94	MPa
$T_{II}^0 = T_{III}^0$	51.28	MPa
Damage Initiation Criterion	QUADS	
Damage Propagation Criterion	Power Law (PL)	
α_{PL}	1	

As a starting point, the experimentally determined failure stresses described in Section 6.6.2 are used as cohesive strengths. However, since these parameters are more numerical in nature, they will be investigated in the following section.

There is a publication by Floros et al. [277] in which the fracture mechanics values were determined for a different variant of the adhesive, called Loctite EA 9695 0.05 PSF K, with a different carrier fabric.

The G_{Ic} from Floros et al. is with 1.018 N/mm slightly higher than the values determined in this thesis. This can be explained by the use of the Simple Beam Theory (SBT) instead of MBT, which is used in this thesis. It needs to be mentioned that MBT is known to give more conservative values.

With 0.783 N/mm, the value for G_{IIc} is significantly lower than the value of 4.035 N/mm determined in this work. However, it is unusual that the mode II value is lower than

the mode I value. Furthermore, the value determined in the present work is within the expected range, as mode II values of similar magnitude have been published for similar adhesives such as FM73 [278]. Moreover, in MMB experiments with nearly the same mode ratios, similar values for G_T were measured as in this work. It is noteworthy that a cERR value that decreases again with a pure mode II load is also uncommon. In contrast to the study in this work, Floros et al. did not use UD ply lay-ups according to the standard, but used QI lay-ups instead. This could have led to laminate damage and, in turn, might have influenced the measured values.

6.9 Comparison of damage modelling approaches on the basis of TAST specimens

In this subchapter, the ACZ, AACZ, and XFEM modelling are tested in combination with the previously determined material parameters using the TAST specimen as an example. The influence of mesh size, cohesive strength, predicted crack path, and computational aspects are compared. Since the amount of hydrostatic stress in the TAST specimen is low and the two yield models, v.M. and exp.D.-P., provide very similar results in this case, cf. Section 6.7.4, the comparison of the yield models is carried out with different specimens in the next chapter. The simulation models are similar to the models described in Section 6.7.4 but with different element sizes. Furthermore, the baseline for the in-plane edge-length is 0.5 mm with one cohesive element in case of ACZ and two solid elements in case of AACZ and XFEM in through-thickness direction. If not otherwise stated, the simulations, except from the ones using XFEM, are carried out using Abaqus/Explicit. In addition, a comparison between Abaqus/Standard and Abaqus/Explicit results for ACZ and AACZ is given. As the simulation runtimes of the XFEM models are considerably high, the parametric studies are only performed for ACZ and AACZ. The results for the AACZ approach are then transferred to the XFEM approach because the approaches are quite similar except for the crack path definition.

6.9.1 Influence of cohesive strength

Since the cohesive strength has an influence on the predicted failure load, a study is performed to assess this influence for ACZ and AACZ. As the TAST specimen is mainly loaded in shear, this is done by varying the mode II cohesive strength T_{II}^0 only. The strength is varied between 25 MPa and 100 MPa and the results are shown in Fig. 6.20.

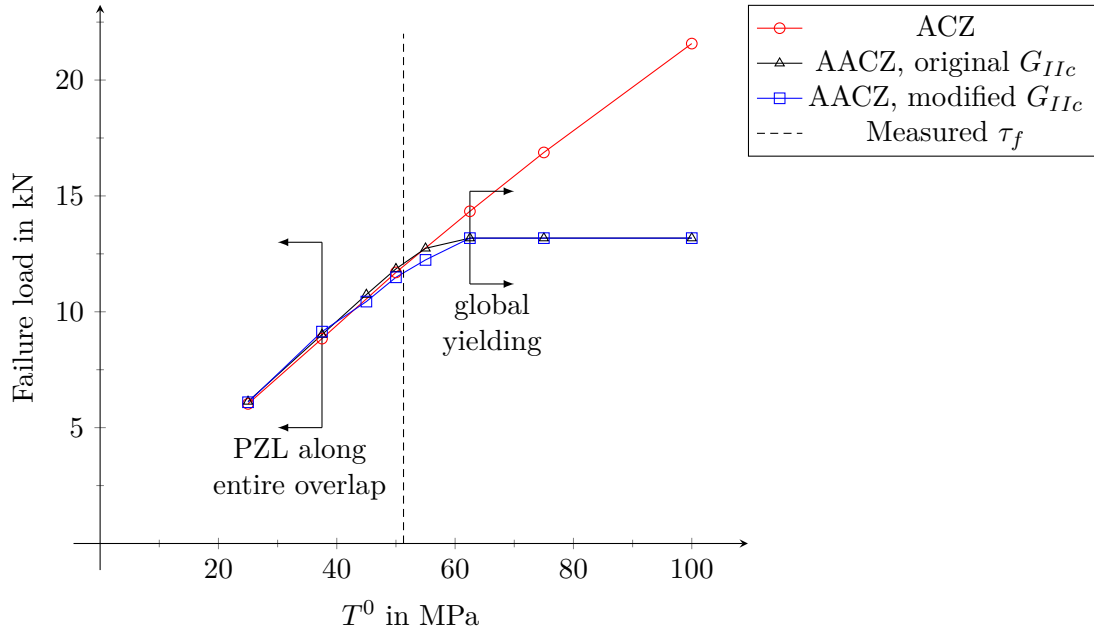


Figure 6.20: The effect of the CZM parameters on the predicted TAST failure load

The simulations with the ACZ approach show that the failure load is linearly dependent on the mode II cohesive strength, whereas for AACZ the failure load only increases until $T_s^0 = 65$ MPa. From 65 MPa on, the whole adhesive layer yields and cannot bear further loads before the cohesive surface is damaged.

In addition, for AACZ the influence of the cohesive strength T_s^0 for both measured G_{IIc} and the calculated softening ERR $G_{soft,II}$ is investigated. It is found that below 37.5 MPa the failure load is not sensitive to the ERR value. In this range of cohesive strength values, the damage initiation criterion is reached along the entire length of the adhesive layer before individual surfaces are completely detached. This release happens abruptly over the entire length of the adhesive layer. Therefore, the Process Zone Length (PZL) equals the overlap length.

With the cohesive strength set to the measured failure strength τ_f , a failure load of 11.693 kN, which is close to the results of the 2017 campaign with 11.993 ± 0.193 kN, is achieved. This value also lies between the region of global yielding and the region where the PZL has formed along the entire bond line. This underlines that the use of measured strength is a sound choice. Based on this investigation, it is decided to use the experimentally determined failure stresses for the CZM modelling.

6.9.2 Influence of mesh size

In order to investigate the influence of the mesh size, TAST simulations with ACZ and AACZ modelling were performed with meshes using elements with in-plane edge lengths between 0.125 mm and 1.0 mm. The ACZ models use one cohesive element in through-thickness direction and the AACZ models are discretised with the minimum possible number of two elements in through-thickness direction. It needs to be noted that the AACZ simulations are performed using G_{IIc} and not $G_{soft,II}$. However, as can be seen from Fig. 6.20 the difference in predicted strength between the two values is only small. For both types of modelling, the determined strengths vary only slightly, cf. Fig. 6.21.

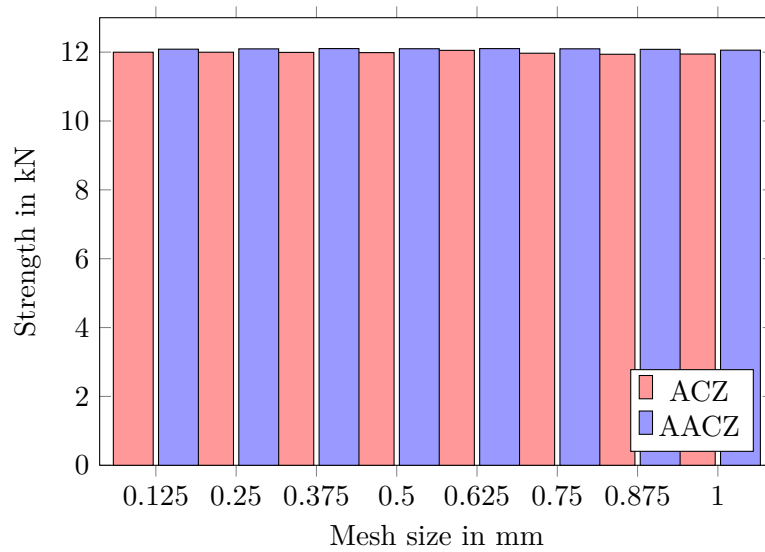


Figure 6.21: Mesh convergence of ACZ and AACZ approach predicting TAST strength

The highest ACZ strength is 12.052 kN and lowest one is 11.939 kN, whereas the corresponding values for AACZ are 12.103 kN and 12.057 kN.

In addition to the influence of the in-plane element size, for the AACZ approach, also the discretisation in through-thickness direction is investigated. This is done by using meshes with an element in-plane edge length of 0.25 mm and from two to six elements in thickness direction. The predicted strengths vary only between 12.076 kN and 12.095 kN.

In summary, it can be said that the influence of mesh size is negligible in this context. One cohesive element for ACZ or two solid elements for AACZ modelling are sufficient. Moreover, the investigation showed that the in-plane element edge length can be chosen according to the adherend mesh size.

6.9.3 Stiffness and strength comparison

The force-displacement plots in Fig. 6.22 show the results from the different modelling approaches. In addition, mean failure loads of the two experimental TAST campaigns from 2017 and 2021 are given.

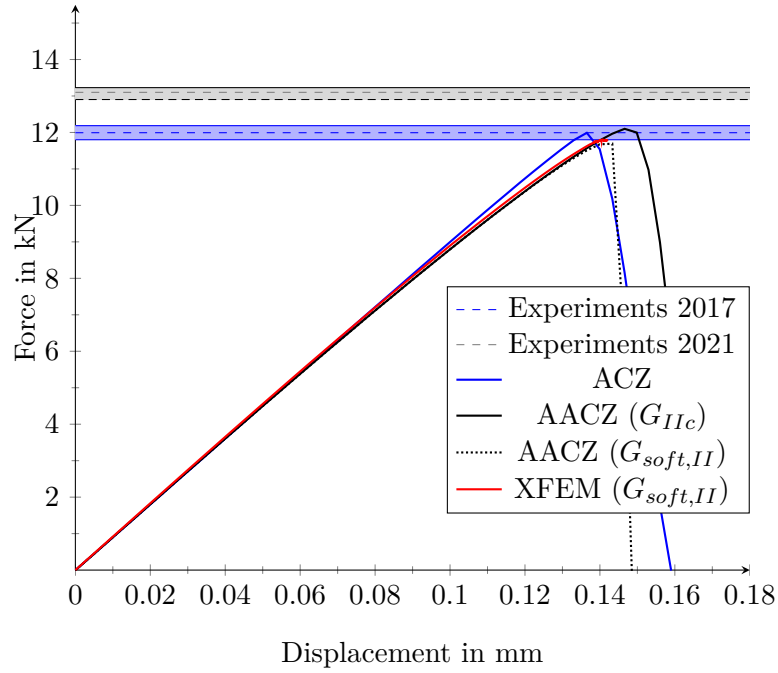


Figure 6.22: Load-displacement curves gained with different modelling approaches

It becomes apparent that the stiffnesses of all approaches agree up to 8 kN. Beyond this loading, the stiffnesses of AACZ and XFEM models are lower than the ACZ-predicted stiffness. This could be attributed to the plasticity models used by these approaches in conjunction with CZM. Consequently, the ACZ modelling gives the lowest displacement at failure

In Tab. 6.10 the failure loads of the simulations and experiments as well as the deviations between simulations and experiments are summarised.

Table 6.10: Comparison of failure loads of TAST specimens from experiments and simulations

	Failure load in kN	Difference to 2017 experiments in %	Difference to 2021 experiments in %
Experiments 2017	11.993 ± 0.193		
Experiments 2021	13.100 ± 0.133		
ACZ	11.990	-0.03	-8.47
AACZ G_{IIc}	12.100	+0.89	-7.63
AACZ $G_{soft,II}$	11.693	-2.50	-10.74
XFEM $G_{soft,II}$	11.794	-1.66	-9.97

Two simulations were performed with the AACZ modelling approach. One with the measured G_{IIc} and the other one with the $G_{soft,II}$ calculated in Section 6.8.5. Although the

difference between the ERRs is significant, the failure loads do not show a large difference. It is interesting to note that the simulations with AACZ and XFEM approaches, both with $G_{soft,II}$, result in nearly the same force-displacement curve and thus also almost identical failure loads.

Moreover, it needs to be mentioned that all calculated strength values lie in the range of scatter of the 2017 experiments. The largest difference between simulations and 2017 experiments is with -2.5% very small. As discussed in Section 6.6.1, the campaign from 2021 resulted in a mean failure load that was about 1 kN higher. Possible reasons for the difference are also discussed in Section 6.6.1. However, even for this campaign, the difference is in the range of 10 % and the simulations are always conservative.

Accordingly, it can be stated, that for the TAST specimens all three approaches produce useful results. If only a strength prediction is needed, even the simple ACZ approach is sufficient. However, the differences in stiffness at higher loads suggest that the AACZ and XFEM approaches are more accurate. These findings need to be further investigated with different types of specimens as well as with DIC-measured force-displacement curves during experiments.

6.9.4 Crack path

When modelling the adhesive layer with the ACZ and AACZ approaches, the crack path is not explicitly modelled for ACZ and defined a priori to be in the middle of the adhesive layer for AACZ. In the XFEM approach however, the crack path is part of the solution. In the experiments a Z-jump in the adhesive layer could be observed. This jump is also described with a schematic depiction by Öz and Özer [279]. Cracks start at both overlap ends near the continuous adherend. Then both cracks grow towards each other. In the middle of the overlap, the cracks unite by a jump to bridge the height difference. This behaviour could also be observed in the XFEM simulations, cf. Fig. 6.23. With these observations, it is underlined that the XFEM approach is able to accurately predict the crack path.

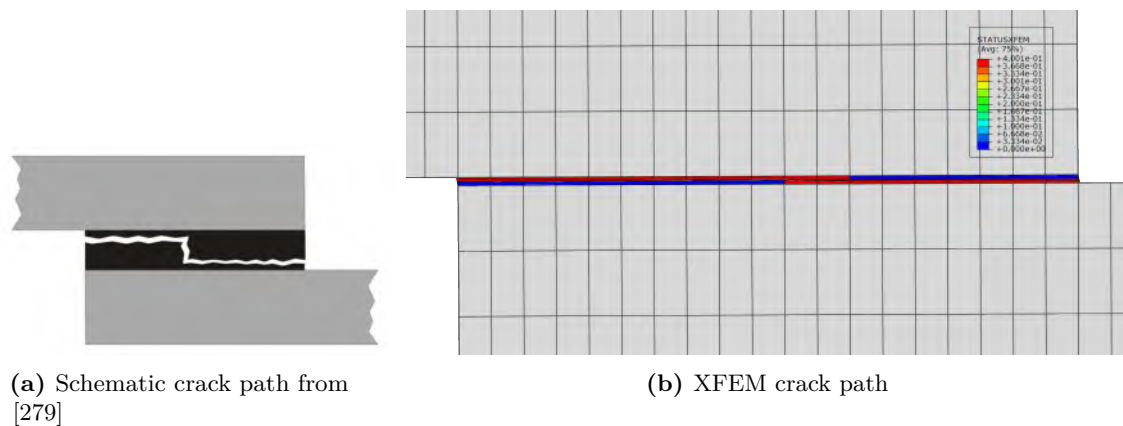


Figure 6.23: Schematic of experimentally observed and XFEM-predicted crack path

6.9.5 Computational aspects

This section discusses the computational aspects of the different approaches. It needs to be mentioned that XFEM is only available in Abaqus/Standard. This is a drawback since the holistic method is likely to require an explicit solver due to the large number of non-linearities. ACZ and AACZ, on the other hand, are available for both Abaqus/Standard and for Abaqus/Explicit. Nevertheless, a comparison of the computation times based on Abaqus/Standard will be carried out first to see if XFEM is competitive when using Abaqus/Standard.

With the example of the TAST model and same meshes for ACZ, AACZ and XFEM, calculations are performed using eight CPU cores on a workstation with an Intel® Xeon® E5-2670 v3 processor and 48 GB RAM. The simulations are terminated as soon as a load drop has occurred. From Tab. 6.11, it can be seen that the ACZ approach is with only 50 increments and an average time of 25.58 s per increments by far the most efficient approach.

Table 6.11: Comparison of computational expense of the modelling approaches on the basis of the TAST specimen

Modelling approach	Nr. of increments	Total CPU time in s	Average time per increment in s
ACZ	50	1,279	25.58
AACZ	570	30,631	53.74
XFEM	860	581,517	676.18

The AACZ approach needs more than ten times more increments until a load drop has occurred and the average time per increment is also more than double compared to ACZ. This is not surprising, as the solid elements for the adhesive layer in combination with the plasticity model make the model significantly more complex and require more computing time.

The XFEM approach, in contrast, requires ten times more computing time per increment compared to the AACZ approach. Moreover, 290 additional increments are needed until a load drop is reached. This results in a nearly 20 times higher total CPU time for XFEM compared to AACZ.

Since the accuracy, except for the crack path, is not significantly higher for the investigated TAST example, the XFEM approach is not further pursued for the holistic method.

As mentioned above, the ACZ and AACZ approaches are available both for implicit and explicit solvers. To ensure that the choice of solver does not have an influence on the result, the results from both solvers are compared. This is illustrated in Fig. 6.24 by using the load-displacement curves.

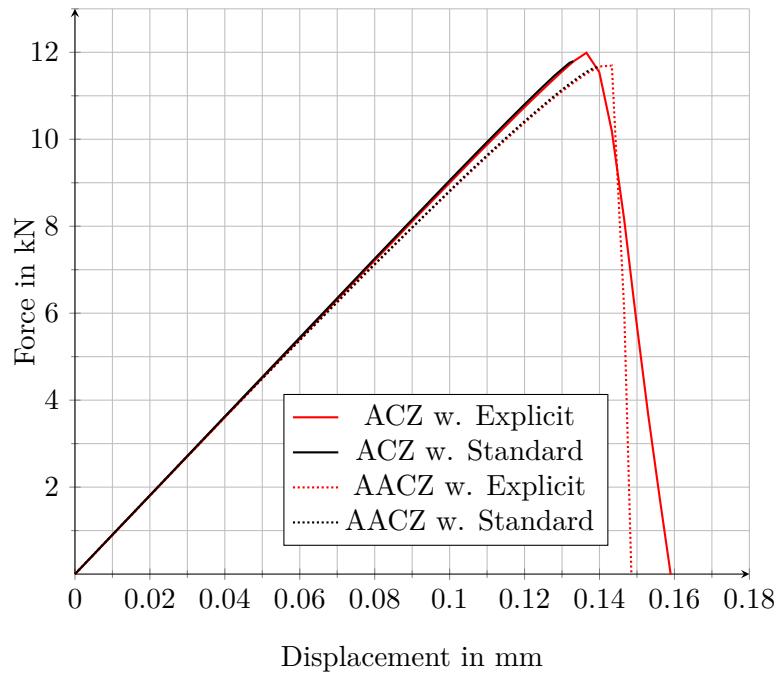


Figure 6.24: Influence of solver on load-displacement curves from ACZ and AACZ approach

It can be seen that the stiffnesses determined with Abaqus/Standard and Abaqus/Explicit agree. However, in contrast to the simulations with Abaqus/Explicit, the simulations with Abaqus/Standard are terminated at the first load drop and not when the specimens are completely unloaded, because the convergence after damage of the adhesive layer is slow. Nevertheless, the failure loads are considerably close to each other. The ACZ failure load determined with Abaqus/Standard is a bit lower than with Abaqus/Explicit. This may be due to the natural damping in Abaqus/Explicit.

In general, it can be stated that ACZ and AACZ provide comparable results regardless of the solver used.

6.10 Conclusions and recommendations for the holistic approach

In this chapter, three different modelling approaches for the adhesive layer were investigated. For this purpose, the needed elastoplastic as well as fracture mechanical parameters were identified. It could be shown that ACZ, AACZ, and XFEM in combination with the determined material parameters are able to predict the failure load of mainly shear loaded joints with high accuracy. In addition, it has been demonstrated that the results are nearly independent from discretisation. Due to the neglect of plasticity in the ACZ approach, in terms of stiffness the ACZ approach differs under high loadings from the AACZ and XFEM approaches. Although, XFEM is in contrast to the AACZ approach able to predict the crack path, XFEM is not recommended for the holistic model since it is only available for Abaqus/Standard and is very costly in terms of computational effort.

It needs to be noted that some questions remain open. ACZ and AACZ, the two approaches still under consideration do not provide significantly different results for the TAST example. However, the use of the AACZ approach for modelling the adhesive layer increases the computation time noticeably. Hence, it must be investigated on the basis of examples that are similar to the planned application whether this additional effort results in a significantly improved accuracy or not. For the AACZ approach, it was also not possible to finally specify with which plasticity model the approach should be combined. Both plasticity models, v.M. and exp.D.-P., could be verified under pure shear loading. Furthermore, differences between the two models for specimens with high hydrostatic stress are shown. Nevertheless, the difference should be further investigated on test specimens that are closer to the target application of the holistic method. Only in this way, it can be finally clarified whether the additional effort in characterisation for the exp.D.-P. model is worthwhile. In addition, the derivation of a softening ERR $G_{soft,i}$ for the AACZ approach from the cERR $G_{i,c}$ has been described. Testing both values using the TAST test specimens does also not provide a clear indication which of the two values should be used in the holistic method. This is also a point of investigation for additional studies.

For future work, a compromise between accuracy and computation time could be the implementation of a yield criterion sensitive to hydrostatic pressure into a user-defined material model for cohesive elements, as described by Jousset and Rachik [264].

Having completed the investigation of the modelling of the adhesive, including the determination of material parameters, all components for the holistic PDA approach are available. In the next chapter, all three components for the holistic PDA approach are put together to be validated using various SLS joint element specimens. In addition, remaining open questions about the modelling of the individual components are addressed.

CHAPTER 7

Validation of the holistic progressive damage model with experimental data

Can the holistic progressive damage analysis be validated with experimental data?

Chapters 4, 5, and 6 provide the individual components for the holistic model as well as the needed material data for the individual material models. In addition, verification and validation of the individual components of the holistic approach is performed in the corresponding chapters. However, a validation of the holistic model is still missing. Furthermore, there are still some open questions that could not be finally clarified at the level of the individual components. In this chapter, an experimental campaign is developed to validate the holistic model. After a recap of open questions regarding the modelling decisions, validation tests are selected. This is followed by a description of the experimental testing itself. After that a description of the numerical counterparts of the test specimens is also given. The chapter closes with results and a discussion as well as modelling recommendations for the final holistic approach.

7.1 Open questions regarding the holistic approach

Apart from the question of the actual validation, there are still some open questions from the previous chapters regarding the recommendation of a modelling strategy for the holistic model:

Regarding the adhesive modelling for the TAST specimen in Chapter 6, it can be said that the ACZ and the AACZ approach performed equally well in terms of accuracy. The TAST specimen is also not well suited to decide whether the v.M. plasticity model for the AACZ approach is sufficient or if the exp.D.-P. model considering the effect of hydrostatic stress on yielding is necessary. In addition, the difference between the results when using the measured cERR G_c versus the softening ERR G_{soft} calculated for AACZ is not major on the TAST example. These three items for the adhesive modelling shall be further investigated on specimens with mixed mode loading but with a cohesive failure mode.

The open questions regarding the composite modelling are whether solid or continuum shell elements should be used and if they can or should be combined with discrete delamination modelling using cohesive surfaces. These questions should be answered with specimens corresponding to the target application with an at least partial failure in the composite adherends.

7.2 Selection of validation tests

The SLS joint is a typical configuration of bonded joints. The TAST specimens in Chapter 6 are also a representation of a SLS joint but with thick aluminium adherends. However, common fibre composite structures have significantly lower thicknesses than the adherends of the TAST test specimens tested and analysed in the previous chapter. For composite SLS joints, although they are, as the name indicates, mainly loaded in shear, this leads to a mixed mode loading with shares of peel loading especially at the overlap edges of the joints. This can be explained by the secondary bending which occurs due to the thinner adherends.

This aspect makes SLS joints suitable to answer the open questions regarding the adhesive modelling mentioned in Section 7.1. To add, a variation of the overlap length leads to changed mixed mode ratios which also supports the validation.

To answer the questions regarding the composite modelling, the different validation test specimens should fail in different failure modes, cf. ASTM D 5573. In this way, besides the open questions regarding the composite modelling, it can be validated if different failure modes can be predicted by the same method using the same material parameters. This can be achieved by changing the layup. Especially the orientation of the ply adjacent to the adhesive layer is decisive for the failure mode, cf. Section 2.2.2.

During the processing of the work, the material M21-T700GC was discontinued by Hexcel in the considered cured ply thickness of 0.13 mm. Therefore, the validation tests are performed using 8552-IM7 only. However, both composite materials were successfully validated in Chapter 4 and this circumstance should not limit the quality of the validation of the holistic method.

7.3 Single lap shear joint elements

The following sections describe the validation based on the SLS joint elements starting with a description of the basic specimen and its variants. Then the manufacturing and experimental test is described followed by a description of the numerical modelling. At the end of the subchapter the experimental as well as the numerical results are presented and discussed.

7.3.1 Test specimen variants

The tests are performed following the standards ASTM D 5868 and DIN EN 1465. The standards mainly differ in terms of geometry, but the geometry is changed in this test campaign anyway. In Fig. 7.1, a sketch of the specimen with the main dimensions is shown.

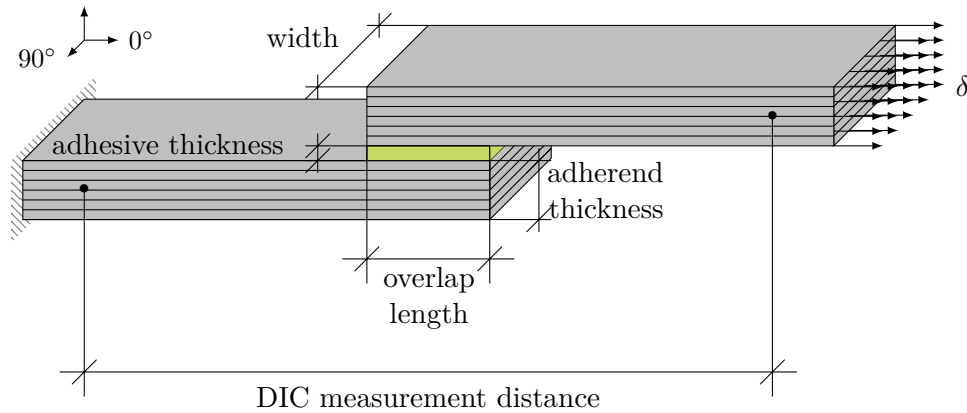


Figure 7.1: Sketch of SLS joint simulation model (not to scale)

In total, four different variants of SLS specimens are built and tested. Tab. 7.1 shows layups and nominal dimensions of the different series.

Table 7.1: Nominal geometry and layups of SLS joint element specimens

Series	Layup	Width in mm	Specimen thickness in mm	Adhesive thickness in mm	Overlap length in mm	Free length in mm
SLS-0-15	[0,45,90,-45]2s	25.0	2.0	0.15	15.0	175.0
SLS-0-25	[0,45,90,-45]2s	25.0	2.0	0.15	25.0	175.0
SLS-0-35	[0,45,90,-45]2s	25.0	2.0	0.15	35.0	175.0
SLS-45-12	[45,90,-45,0]2s	25.0	2.0	0.15	12.0	85.0

All series have QI layups with a nominal adherends thickness of 2.0 mm. This leads to 16 plies per adherend. In addition, the width of 25.0 mm is also the same for all specimens. Three series, referred to as SLS-0, have the same QI layup with 0°-plies adjacent to the adhesive layer. They differ in the overlap length with values of 15 mm, 25 mm, and 35 mm. The free length between the clamping in the testing machine is 175.0 mm for these specimens. According to the state of the art, all of these specimens should fail cohesively in the adhesive layer.

It needs to be mentioned that the fourth series has a changed layup. For this configuration, the 0°-ply is as far away as possible from the adhesive layer, so that a QI layup is still ensured. A 45°-ply is adjacent to the adhesive layer. For this reason, the series is called SLS-45. With 12.0 mm, the overlap length is as well as the 85.0 mm free length, the SLS-45 series is smaller than the SLS-0 series. Referring to the state of the art, the specimens in this series should, at least partly, show failure in the composite adherend.

7.3.2 Specimen manufacturing

The joints are manufactured as secondary bonded joints, cf. Section 2.1.4. At first, the composite plates for the adherends are manufactured separately. The plates are laid by hand, vacuum sealed, and cured in an autoclave with the curing cycle recommended by the manufacturer. After curing, the plates are demoulded and cut down to size. The bonding process is performed with composite adherend plates in a size to allow cutting six specimens from each. In this way, one bonding process is needed for each of the four series. To set and ensure the desired overlap length, the cured laminates are drilled to allow centring with alignment pins. Also, prior to bonding, the plates are cleaned with isopropyl and then treated with an atmospheric pressure plasma process which is described by Löbel [26] and also used for the fracture mechanics specimens in Section 6.8.1. After that, the film adhesive is applied. To ensure the defined geometry, metal cover sheets are used. The cover sheets are also prepared for alignment pins and have slotted holes on one side to compensate for the different thermal expansion coefficients of metal and composite. Areas with holes for the alignment pins are later not part of the individual specimens. The adhesive curing is done in an autoclave process applying vacuum and temperature for the times prescribed by the adhesive manufacturer.

7.3.3 Experimental testing

The tests were carried out in a Zwick servomechanical testing machine (Zwick 1476) equipped with a 250 kN load cell. To ensure a non-eccentric load introduction of the otherwise eccentric specimens, the hydraulic specimen grips are positioned with an offset in y-direction to each other. In addition, a small end stop is bonded to the grips to ensure a correct alignment in the x-z-plane. Testing is performed at an ambient temperature of $23 \pm 2^\circ\text{C}$. The specimens are loaded with a constant crosshead speed of 1.0 mm/min until a load drop of 75 % has occurred. During testing of one specimen of each series, GOM's 12 M ARAMIS system was used as a DIC system to be able to measure the displacement respective strain of the specimen between the grips without the influence of the testing machines stiffness. The distance between the DIC measurement points is 50 mm for the SLS-45 series and 100 mm for the SLS-0 series regardless of the overlap length. The position of the DIC measurement points is shown in Fig. 7.1.

7.3.4 Numerical modelling

The full three-dimensional numerical models are generated using an Abaqus Python model generator and are solved with Abaqus/Explicit. Preliminary simulation runs with Abaqus/Standard showed that it was not possible to achieve convergence for all models, due to the several sources of non-linearity including plasticity and damage of both composite adherends and adhesive. The specimens are modelled without the clamping areas, so that the length of the numerical model corresponds to the free length shown in Tab. 7.1. As illustrated in the sketch in Fig. 7.1, all degrees of freedom are locked on one side of the specimen and on the opposite side, only the translatory degrees in y- and z-direction are locked. At this end, a displacement is applied in x-direction with a smooth step to prevent oscillations in the model. The mean velocity of the load application is 100 mm/s and mass scaling is applied with a fixed factor of 10. The influence of loading speed and mass

scaling was tested in preliminary simulations and is negligible. No distinct mesh studies are performed and the findings in the previous chapters are used for the mesh size.

The composite adherends of the specimens are modelled according to the findings in Chapter 4 with a LWT approach and the material model developed in this thesis. Moreover, pseudoplasticity is considered. The adherends of the SLS-0 series are discretised with reduced integrated 8 node linear brick elements (C3D8R) with an in-plane edge-length of 0.625 mm and one element per layer in the thickness direction. Delaminations are not discretely modelled, but the effect of the damage is captured by the 3D failure model. This is the baseline composite modelling in this work.

The SLS-45-12 specimen is discretised with the same mesh density but the modelling approach and therefore the element choice is varied. In total, four different approaches are considered. In the first variation, the adherends are modelled like the specimens of the SLS-0 series with C3D8R solid elements only. In a second variant, the element type is changed to SC8R continuum shell elements, while the third and fourth variants combine the two element types with cohesive surfaces for discrete delamination modelling. In this way, the composite modelling approaches remaining after the investigations in chapters 4 and 5 are validated with the target application.

For the composite adherends made from 8552-IM7, the material data summarised in tables E.1 and E.2 in Appendix E are used.

The adhesive in the SLS-45-12 specimen is modelled using the baseline ACZ approach with an in-plane element edge length of 0.625 mm to match the adherend's mesh. It is noteworthy that the specimens of the SLS-0 series are also modelled with the baseline modelling approach but also with the AACZ approach using linear incompatible mode solid elements (C3D8I). The adhesive layer is discretised with two elements in through-thickness direction and the same in-plane element edge length of 0.625 mm. In addition, for the AACZ modelling, the plasticity model is varied between v.M. and exp.D.-P.. This results in three different modelling approaches for the adhesive layer with the same goal as for the composite modelling: To evaluate the remaining modelling approaches with the target application.

The material data for the adhesive is taken from Chapter 6, cf. subchapters 6.7 and 6.8. As baseline for the AACZ approach, the calculated ERR G_{soft} is used. However, additional simulations with AACZ exp.D.-P. modelling are performed using the original G_c to assess the influence of the correction.

It needs to be mentioned that the majority of the simulations in this thesis are carried out with Abaqus version 2020. When using the AACZ technique to model the adhesive layer in SLS joint specimens with Abaqus 2020, an unusual behaviour of the solid elements and cohesive surfaces in the adhesive layer was observed. This also affects the determined failure load. Switching to Abaqus version 2018 results in a behaviour of the adhesive layer being assessed as normal. Due to this reason, the AACZ simulations are performed with Abaqus version 2018. A more detailed description of this observation can be found in Appendix J.

7.3.5 Results and discussion

This section describes the results from the SLS-0 and SLS-45 experimental testing and numerical simulation. The results from the SLS-0 campaign and the SLS-45 campaign are presented and discussed in sequence. Starting with the fracture patterns, the strength results are presented and finally the load-displacement curves are evaluated to assess the stiffness and the behaviour close to failure. The section also includes an evaluation of the results regarding the items under investigations for the holistic model.

Single lap shear joints with 0°-interface ply

Fig. 7.2 illustrates the fracture pattern of an SLS-0-25 specimen and the damage at maximum force F_{max} in the simulation for the ACZ and AACZ exp.D.-P. approaches as an example.

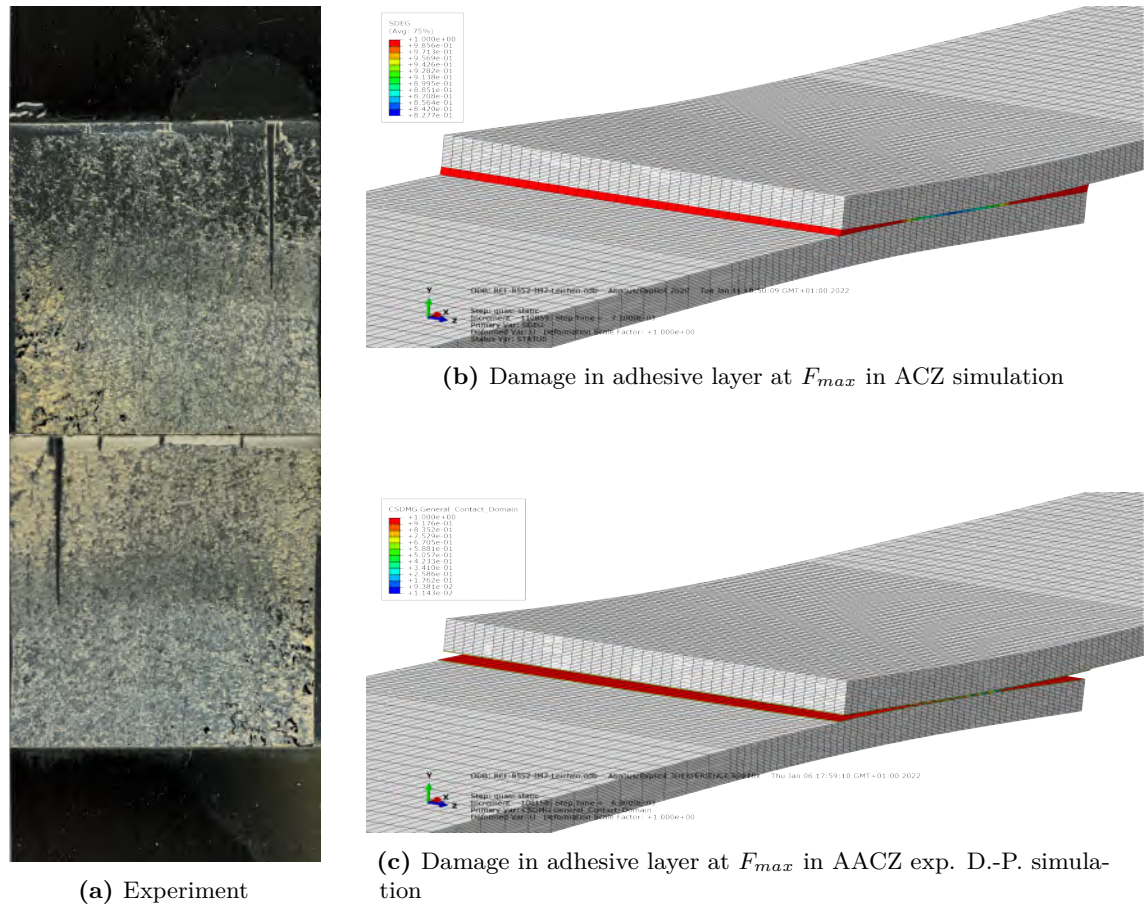


Figure 7.2: Experimentally and numerically observed damage patterns for SLS-0-25

As expected for the layup, cohesive failure with adhesive left on both adherends is observed. This failure behaviour is representative for all SLS-0 specimens regardless of the

overlap length. The fracture patterns of all specimens can be found in Fig. I.1 in Appendix I.

The simulations also only predict damage in the adhesive layer regardless of the modelling approaches. To support this, the material stressing efforts in the adherends calculated by the user-defined material model using Cuntze's FMC are summarised in Tab. 7.2.

Table 7.2: Cuntze failure mode material stressing effort for SLS-0

Specimen	FF1	FF2	IFF1	IFF2	IFF3
SLS-0-15	0.60	0.27	0.58	0.41	0.44
SLS-0-25	0.60	0.29	0.58	0.24	0.42
SLS-0-35	0.67	0.33	0.70	0.33	0.47

It can be seen that for SLS-0-15, SLS-0-25, and SLS-0-35 all material stressing efforts are considerably below 1.0, which means that no damage occurs in the adherends. The highest effort is calculated for FF1 with 0.60 for SLS-0-15 and SLS-0-25, and 0.67 for SLS-0-35. In general, the stressing efforts of SLS-0-15 and SLS-0-25 are comparable, but slightly higher for SLS-0-35.

To provide an overview, the experimentally as well as the numerically determined strengths are shown in the bar chart in Fig. 7.3. All strength values including deviations between the simulations and the experiments can be found in Tab. I.1 in Appendix I. For the experiments, it can be observed that the failure load increases with increasing overlap length. The experimental mean failure loads are 10.573 ± 0.326 kN for the SLS-0-15, 14.355 ± 1.503 kN for the SLS-0-25 and 19.581 ± 0.730 kN for the SLS-0-35 specimens. Furthermore, the mean shear stress decreases with increasing overlap length, from 28.2 MPa to 22.4 MPa. It must be noted, that the first specimen in each series was removed from the evaluation. These specimens were located at the edge of the bonded panel, and all showed a significantly lower failure load than the other specimens of the series. This indicates a process problem at the edge area of the panel. It should also be noted that the SLS-0-25 series consists of only three valid test specimens. This explains the increased standard deviation compared to the other two series.

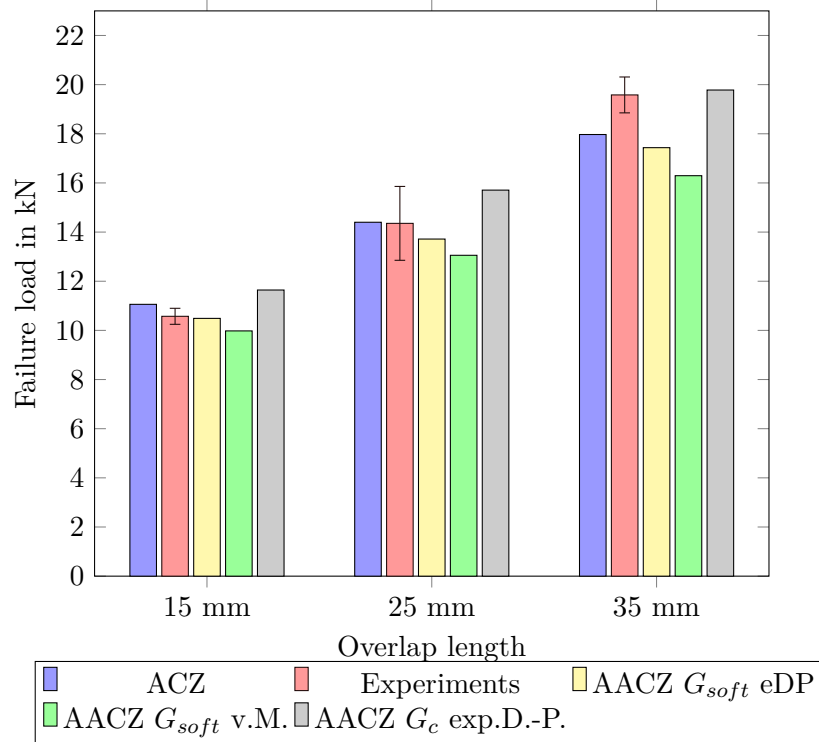


Figure 7.3: Comparison of experiments and simulations of SLS-0 tests

It is noteworthy that the accuracy of the simulations depends on the approach and material parameters used for the adhesive layer. In general, it can be said that SLS-0-15 and SLS-0-25 can be predicted well and that the difference between experiment and simulation is the largest for the series SLS-0-35. For this series, the failure load is underestimated by up to -17% except for one modelling approach.

Going into more detail, it can be seen that ACZ, and AACZ exp.D.-P. using G_{soft} as ERR have a comparable accuracy. Simulations with the ACZ approach result in deviations to the experimental mean failure load between $+8\%$ and -5% . For the latter approach the deviations to the different experiments are between -1% and -11% . Although the deviations are comparable in amount, it can be said that the AACZ exp.D.-P. approach performs better because the results are always conservative.

Moreover, even though the differences in the TAST test specimen were not significant, a clear answer can now be found for the question of whether exp.D.-P. or v.M. and whether G_c or G_{soft} should be used. With deviations between -6% and -17% , the simulation with v.M. is significantly more conservative than with exp.D.-P.. Therefore, it cannot be recommended. The use of G_c instead of G_{soft} on the other hand results in considerably higher failure loads than the simulations using G_{soft} with deviations between $+1\%$ and $+11\%$. Although, the magnitude of deviation is the same when using G_{soft} , the results for G_c are not conservative. Therefore, the use of G_{soft} is recommended.

In Fig. 7.4 the force-displacement curve of the SLS-0-15 specimen recorded during experimental testing with the DIC system as well as the curves from the different simulations

are shown.

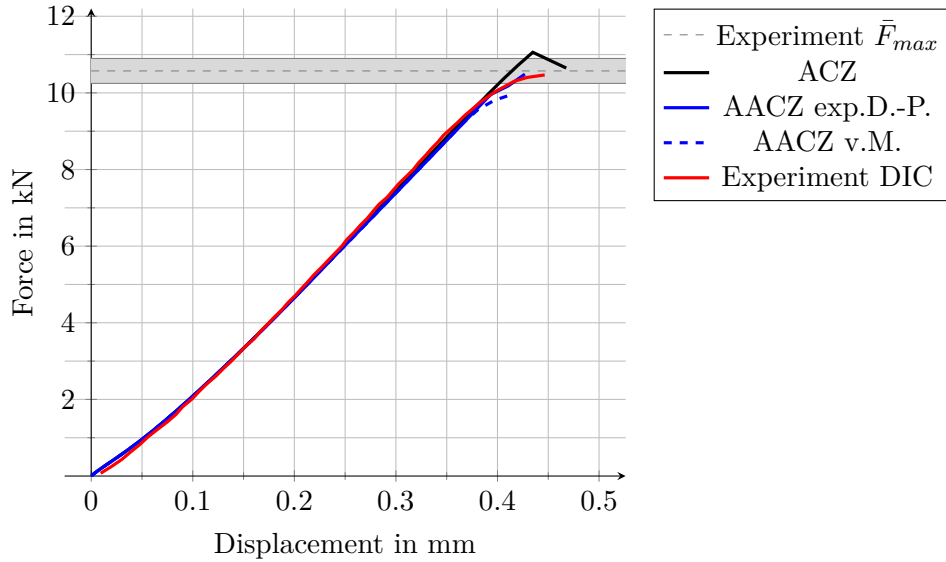


Figure 7.4: Force-displacement curves of SLS-0-15 joint coupon

It can be observed that all simulations show the same stiffness up to 9.5 kN. In this region, they also agree with the DIC-measured stiffness. Nonetheless, the simulations using the AACZ modelling technique show a more non-linear behaviour prior to failure than the one using ACZ modelling. In addition, AACZ modelling in combination with exp.D.-P. agrees with the DIC curve up to failure but bears a little higher maximum load. The load increase above the experimental failure load is accompanied by a large increase in displacement of 0.05 mm up to failure in simulation. Also, the behaviour of the simulation using AACZ with v.M. shows comparable non-linear behaviour prior to failure but at lower loading levels.

As can be seen from Fig. 7.5 for SLS-0-25, the stiffnesses of all simulations agree up to 12.5 kN. Beyond this loading, the strongly non-linear behaviour of all three simulations is comparable but starts at different load levels. This is in line with the different failure loads determined with the simulations. The specimen measured with the DIC system is slightly stiffer than the simulations and the difference in stiffness becomes larger with increasing load. Therefore, it is not only an offset in load level. This difference may be attributed to scatter as only one specimen of each series was measured with DIC.

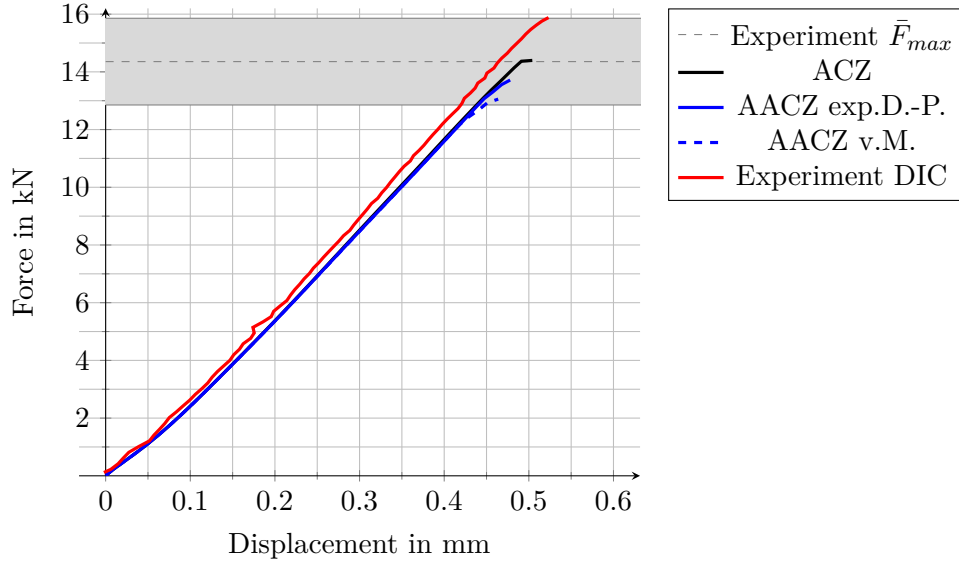


Figure 7.5: Force-displacement curves of SLS-0-25 joint coupon

In Fig. 7.6, the experimentally and numerically determined force-displacement curves of the SLS-0-35 specimen are shown.

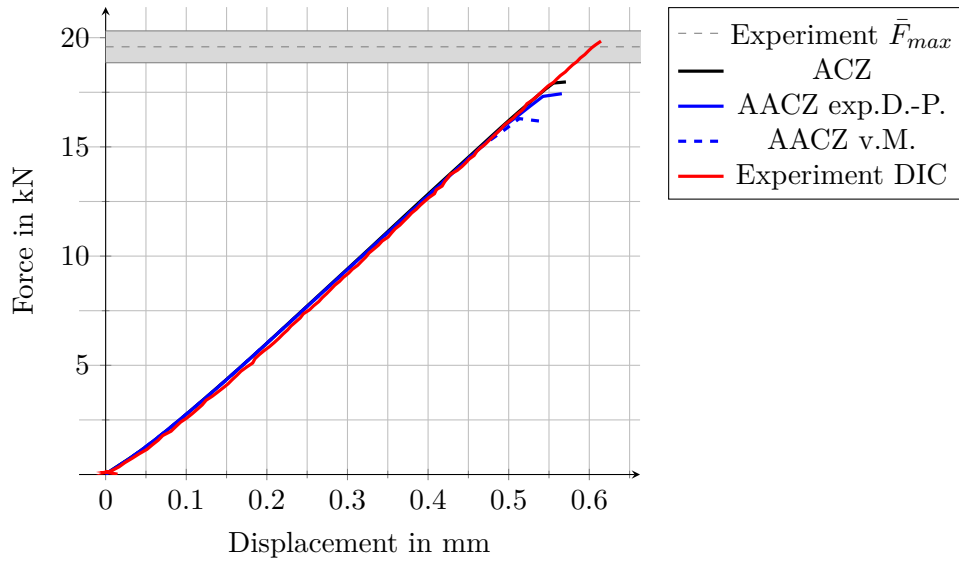


Figure 7.6: Force-displacement curves of SLS-0-35 joint coupon

Like for the SLS-0-25 specimen, the simulations agree up to a certain loading, in this case 16.0 kN. After that loading, the first simulations show strong non-linear behaviour followed by total failure of the specimen. The other two simulations show a comparable behaviour but at higher load levels. Different to the previous SLS-0-25 specimen and like in the first case with the SLS-0-15 specimen, in the present case, the stiffnesses of experiment

and simulation agree well.

Qualitative comparison of DIC-measured and FEM-calculated strain fields

With the example of the SLS-0-25 specimen, a qualitative comparison of ε_{xy} strain fields measured during the experiments with DIC and strain fields determined with the PDA approach is performed. Two different DIC measurement systems were used in parallel during the experimental tests. The first system is an off-the-shelf ARAMIS 12M from GOM and it is used for a more global view on the specimen. This system is also used to generate data for the previously discussed force-displacement comparison.

However, with the resolution of the ARAMIS 12M, it is not possible to determine the strains in the bondline or layer wise strains in the adherends. For this reason, the second system uses a consumer digital single-lens mirrorless camera combined with a macro lens capable of a 5-times magnification. With this system, which was also used for the TAST DIC measurements, a local strain field covering half of the overlap length is captured. The following figures comparing the DIC strain field with the contour plots of FEM have matching limits of their spectra.

The loading for the first two comparisons, global and local, is with 13.7 kN close to total failure of the specimen. In Fig. 7.7, the global strain field is shown.

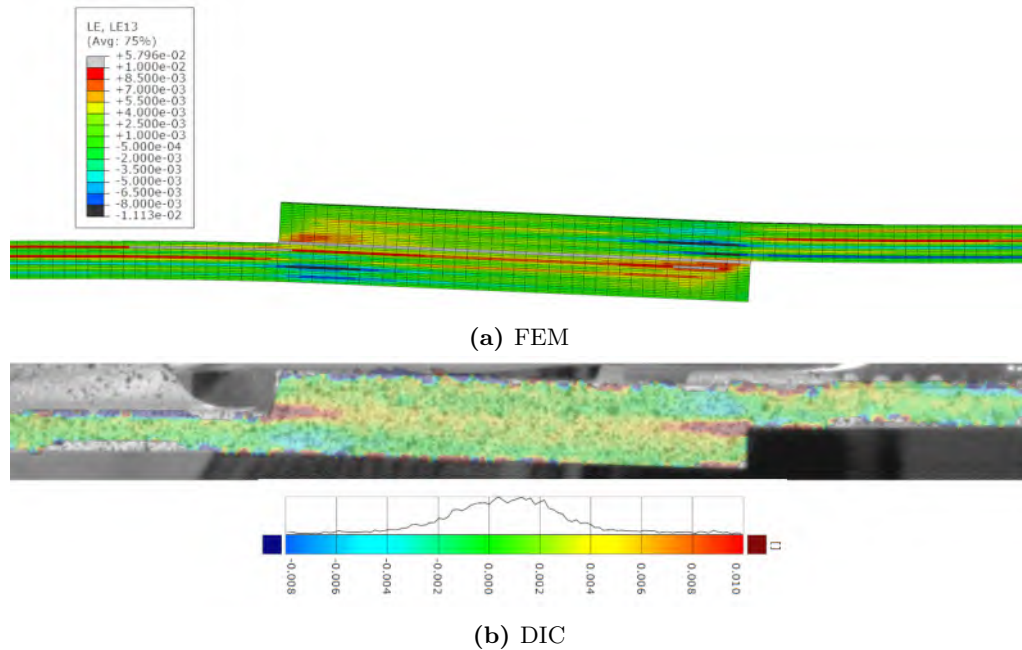


Figure 7.7: Global ε_{xy} strain field of SLS-0-25 at 13.7 kN

The shear strains shown in the figure are between -0.008 and 0.01 . As discussed, the resolution is too small for the thin adhesive as well as ply thickness to measure strains in

the bondline or to obtain layerwise information in the adherends. However, a qualitatively good agreement between FEM and DIC can be observed. For the red-coloured regions of high positive values of ε_{xy} at the adherend ends as well as the blue areas in the continuous adherend at the same x-position, negative values can be found both in the FEM and in the DIC data.

Fig. 7.8 shows the local DIC measurement with higher resolution as well as the corresponding FEM contour plot.

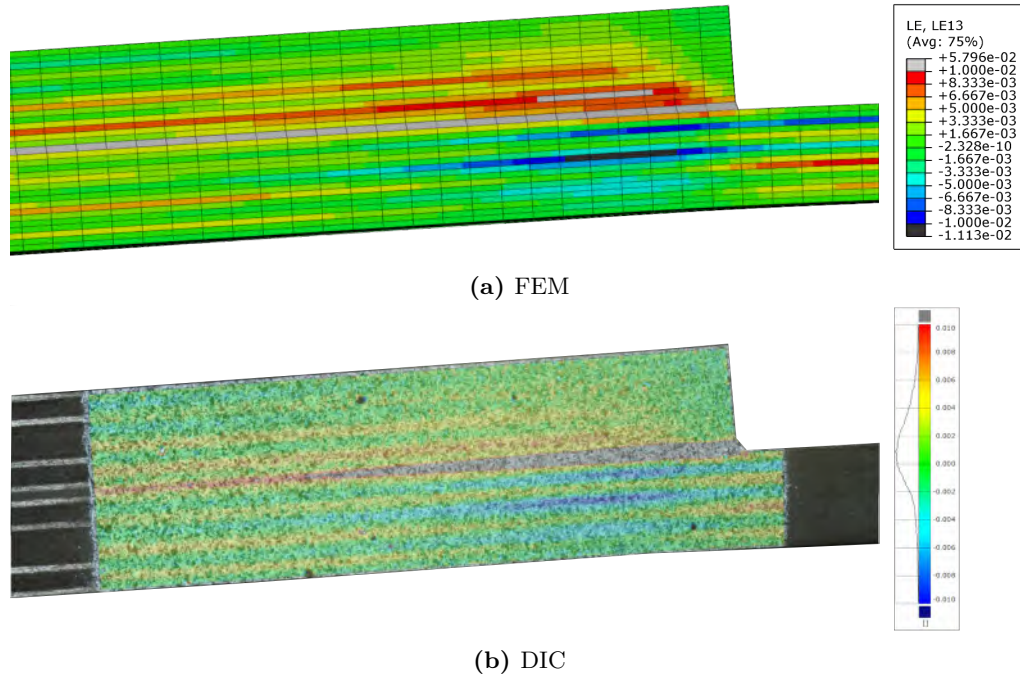


Figure 7.8: Local ε_{xy} strain field in the adherend of SLS-0-25 at 13.7 kN

With -0.01 to 0.01 , the limits of the spectrum are chosen in a way that the strains in the plies can be evaluated. With the higher resolution of the custom set-up, discrete strains in each ply can be seen. At the left edge of the DIC image, in the area without speckle pattern, the significantly brighter 0° -plies can be seen.

Overall, a fairly good agreement between DIC and FEM can be observed. In the top adherend, both strain fields show a high positive strain region near the bondline at the overlap edge. At the same x-position in the continuous bottom adherend, high negative shear strains can be observed. The differently elongated plies of different fibre orientation can also be found in both images.

In order to evaluate the strain field in the adhesive, a third comparison is made. Shear strain fields in a different interval than previously determined with ACZ, AACZ, and DIC are shown Fig. 7.9.

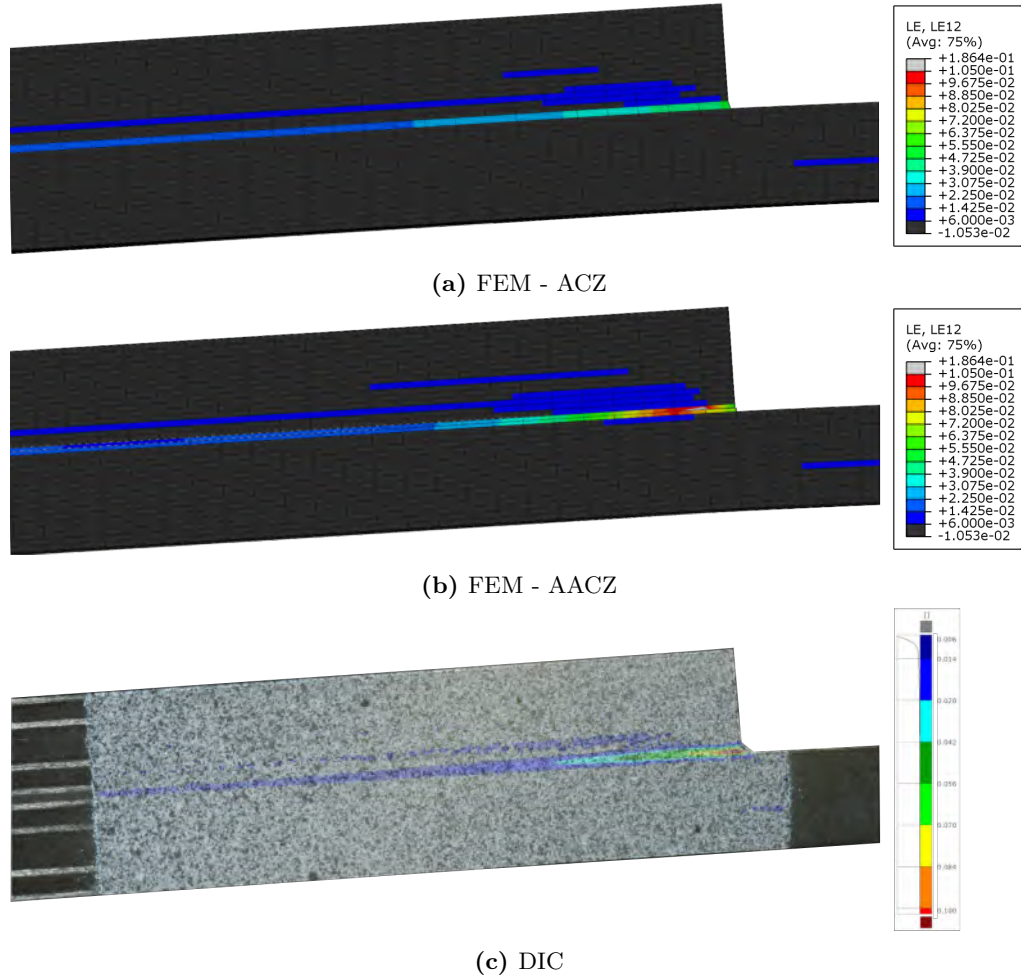


Figure 7.9: Local ε_{xy} strain field in the adhesive of SLS-0-25 at 11.8 kN

The loading for this comparison is reduced to 11.8 kN, because at higher loads cracks start to grow to a significant extent. Furthermore, the spectrum is chosen to show shear strains between $\varepsilon_{xy} = 0.01$ and $\varepsilon_{xy} = 0.1$. As expected and seen in the previous figures, strains in the adherends are nearly everywhere below this lower limit.

In general, there is again a good agreement between DIC and FEM. Nevertheless, it can be seen that the area of highly-strained adhesive in the simulations is slightly larger than in the DIC measurement. The strain peak at the overlap edge in the bondline can be seen in the DIC measurement and in the AACZ-based simulation. However, this strain peak is shifted to the left in the AACZ simulation since crack growth has already begun and unloaded the first row of adhesive elements. In addition, the shear strain at the overlap edge in the ACZ simulation is lower than in the AACZ simulation and in the DIC measurement. This is an expected result, since no plasticity is considered in the ACZ approach, which leads to smaller strains at the same stress level. This comparison can therefore be used to illustrate the effect of this simplification.

Single lap shear joints with 45°-interface ply

After analysing the results for the SLS-0 specimens with 0°-plies adjacent to the adhesive, the focus is now on the SLS-45 specimens. Fig. 7.10 shows post-mortem pictures of a representative experimentally tested specimen as well as the damage patterns of the simulation. The simulation shown in Fig. 7.10 uses the modelling approach which combines continuum shell elements for the intralaminar behaviour with cohesive surfaces for the interlaminar behaviour. The fracture patterns of all specimens can be found in Fig. I.2 in Appendix I.

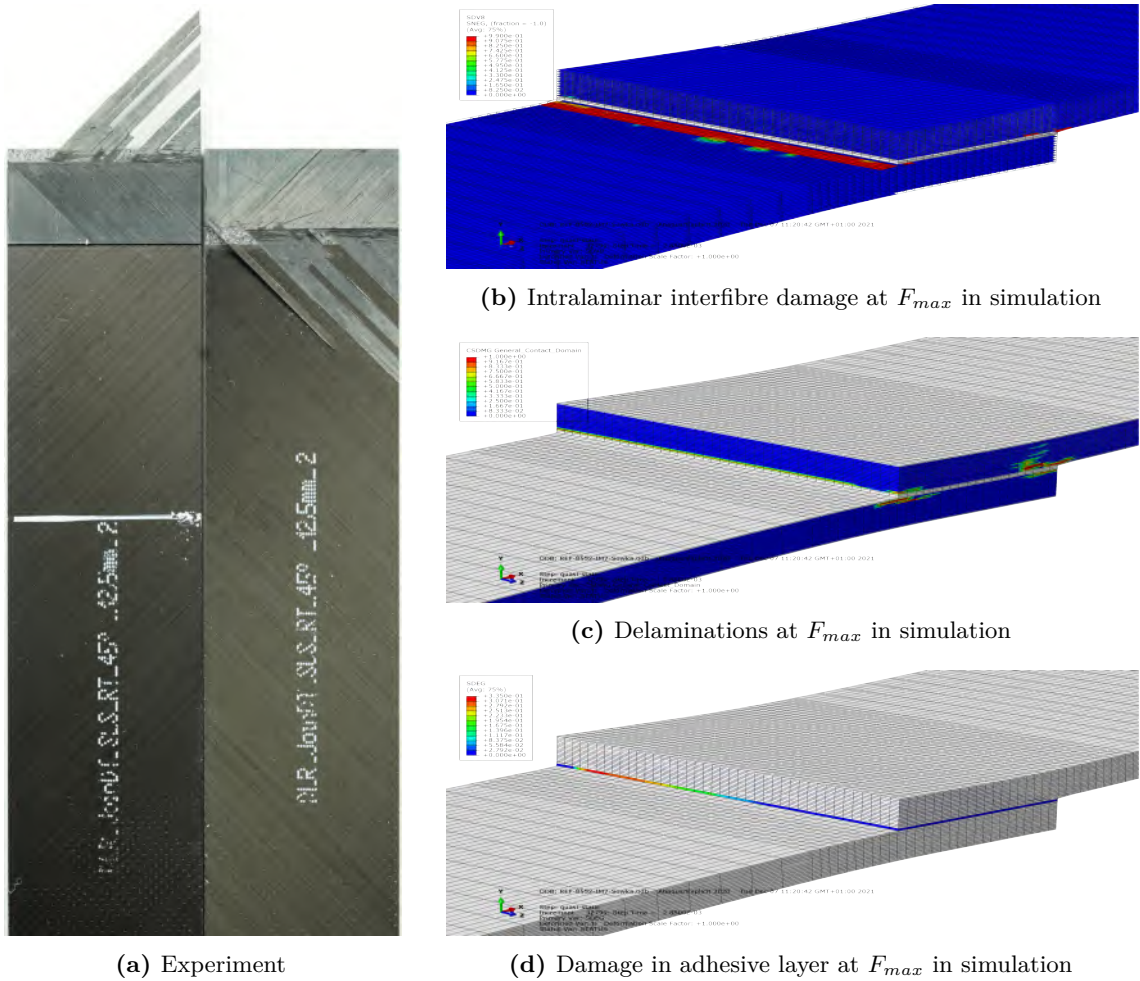


Figure 7.10: Experimentally and numerically (ACZ) observed damage patterns for SLS-45-12

In the experiment, cf. Fig 7.10(a), a combination of cohesive and laminate failure is observed. The 45°-plies adjacent to the adhesive layer failed due to intralaminar interfibre damage. In addition, a large triangular shaped part of the 45°-ply has delaminated. Look-

ing from the adhesive layer, the second and third plies orientated with 90° and -45° are also damaged.

Furthermore, looking at the simulation results in Fig. 7.10(b) at F_{max} , it can be seen that at both overlap ends, the 45° -plies adjacent to the adhesive show IFF damage. However, the inclination of the damage in accordance with the ply orientation could not be observed. Delaminations are predicted between first and second ply as well as between second and third ply, cf. Fig. 7.10(c). Furthermore, some local damage in the adhesive is calculated, but the elements are not fully damaged with a maximum value of 0.34 for the damage variable. To summarise, all relevant failure modes from the experiment can be seen in the simulation, but the damage patterns themselves are slightly different. This is shown in Fig. 7.10(d).

The failure loads from the experimental tests as well as from the different simulations are shown in bar plots in Fig. 7.11.

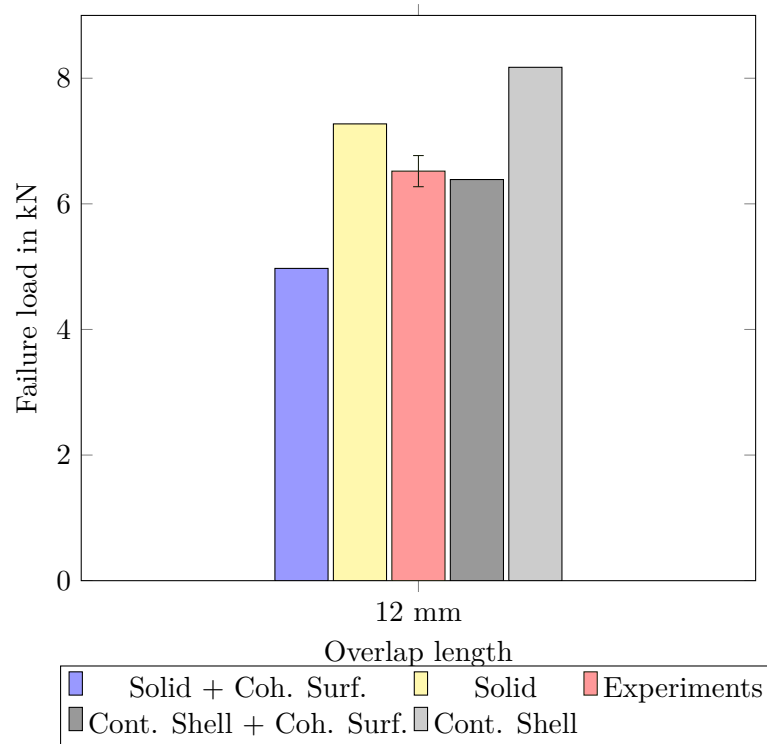


Figure 7.11: Comparison of experiments and simulations of SLS-45 tests

The experimental failure mean load from the five specimens is 6.521 ± 0.248 kN. An overview of the corresponding values from the different simulations with deviations to the experiments can be found in Tab. I.2 in Appendix I.

The simulation using solid elements only for the composite parts overpredicts the experiments by +12 %, whereas the simulation using only continuum shell elements overpredicts the failure load by far with +25 %. When combining the continuum shell elements with

cohesive surfaces to model delaminations, the experimental failure load is well captured with -2% . On the contrary, the simulation with solid elements combined with cohesive surfaces is with -24% compared to the experiment far too conservative.

The evaluation of the different modelling techniques with respect to their deviation from the experimental failure load is consistent with the observations of the OHT specimens in Section 4.7.1. Yet, the difference is that the use of cohesive surfaces on the OHT specimens resulted in nearly the same failure load regardless of whether solid or continuum shell elements were used, cf. Subchapter 5.6. In the present case, the combination of continuum shell elements with cohesive surfaces results in a very good accuracy, whereas the combination with solid elements yields a far too low failure load and cannot be recommended.

The force-displacement curve from the experiment is shown together with the curves from the different simulations in Fig. 7.12.

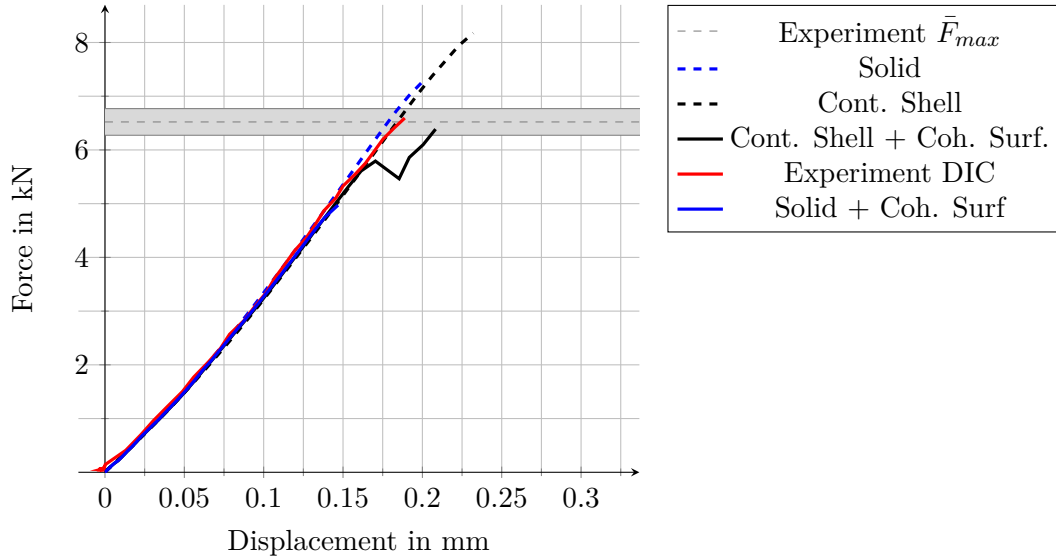


Figure 7.12: Force-displacement curves of SLS-45 joint coupon

Like for the simulations of the SLS-0-15 and the SLS-0-35 specimens, the stiffness between simulation and experiment agrees well.

As previously discussed, the simulations with solid and continuum shell elements without cohesive surfaces result in higher failure loads than observed in the experiments. However, the curve shape is comparable to the experiment. A similar curve shape without significant non-linearities prior to total failure results from the simulation which combines solid elements with cohesive surfaces but with a significantly too low failure load. It is noteworthy that the simulation which uses a combination of continuum shell elements with cohesive surfaces has a different load-displacement behaviour prior to total failure. It shows a load drop at 5.75 kN and 0.17 mm displacement. After that load decrease, the force increases again with a slope, comparable with the one prior to the decrease, up to a failure load

close to the experimental mean value. However, this curve shape with the significant load drop is not observed in experiments.

7.4 Conclusions and guideline to compile a problem-specific holistic approach

The preceding sections show that the holistic model could be validated in combination with material parameters using SLS joint element tests. In general, it can be said that the findings from the previous chapters 4, 5, and 6 for the individual components hold true when applied in the holistic method. Regardless of the varying individual components of the simulation models, the stiffnesses of the specimens are well modelled. However, there are differences in the predicted failure loads.

Two approaches performed well in modelling the adhesive: the ACZ modelling approach as well as the AACZ technique combined with the exp.D.-P. plasticity model and G_{soft} as ERR. It could be observed, that the AACZ technique in combination with exp.D.-P. is significantly more accurate than if it was combined with v.M. as plasticity model. This makes the extra effort in characterisation worthwhile. When using the original G_c instead of G_{soft} the strength is overpredicted and not conservative. Thus, also in this case, the additional step to determine G_{soft} should be taken.

Regarding the composite adherend modelling, there are also two modelling techniques with good performance in terms of accuracy: the sole usage of solid elements with the three-dimensional failure model and the combination of continuum shell elements considering only in-plane damage with cohesive surfaces for delamination modelling. The other two techniques, namely the combination of solid elements with cohesive surfaces as well as the sole usage of continuum shell elements are significantly less accurate.

With respect to Working hypothesis III, the computational costs of the different techniques are evaluated. Tab. 7.3 shows a comparison of increments and total CPU time needed until F_{max} is reached. In addition, the average time per increment is given. The simulations have been performed on a workstation with an Intel® Xeon® E5-2670 v3 processor and 48 GB RAM using eight CPU cores.

Table 7.3: Comparison of computational expense of the modelling approaches on the basis of the SLS-0-25 and SLS-45-12 specimens using Abaqus/Explicit

Specimen	Modelling approach	No. of increments	Total CPU time in s	Average time per increment in s
SLS-0-25	ACZ	131,445	13,674	0.104
SLS-0-25	AACZ eDP	128,614	13,861	0.108
SLS-45-12	Solid	60,405	2,453	0.041
SLS-45-12	Cont. Shell + Coh. Surf.	33,493	4,982	0.149

Therefore, it can be stated that the difference between the ACZ and the AACZ technique

is not large. Attributed to the fact that the major computational expense goes into the simulation of the behaviour of the composite adherends, the differences between ACZ and AACZ do not come into effect like they did for the TAST specimen, cf. Section 6.9.5. The use of continuum shell elements with cohesive surfaces is about two times more expensive in terms of increments and total CPU time needed. In addition, the average time needed to calculate an increment is increased by a factor of more than three.

With this additional information, it can be concluded that various holistic modelling approaches can be compiled, depending on the specific application. As can be seen from the analysis of computational expense of the different approaches, a trade-off between accuracy and cost in terms of characterisation and computational effort is useful. To provide a guideline to the reader a decision tree, with the help of which the modelling strategy for the composite adherends can be selected in dependence of the application, is shown in Fig. 7.13. Decision-making parameters are the need for definite information on delamination areas and whether significant plasticity is expected. Similar to the first decision tree, one is also provided to decide the modelling strategy for the adhesive layer, cf. Fig. 7.14. In this case, the decision depends on whether the strain field must be accurately represented or the effect of occurring damage is sufficient, whether significant plasticity is expected, and whether significant hydrostatic stress is likely.

Two edge cases can be taken from the decision trees for adhesive and adherend modelling: On the one hand, an efficient but less accurate, and on the other hand, a slower but more accurate approach. The efficient approach uses only solid elements for the adherends and

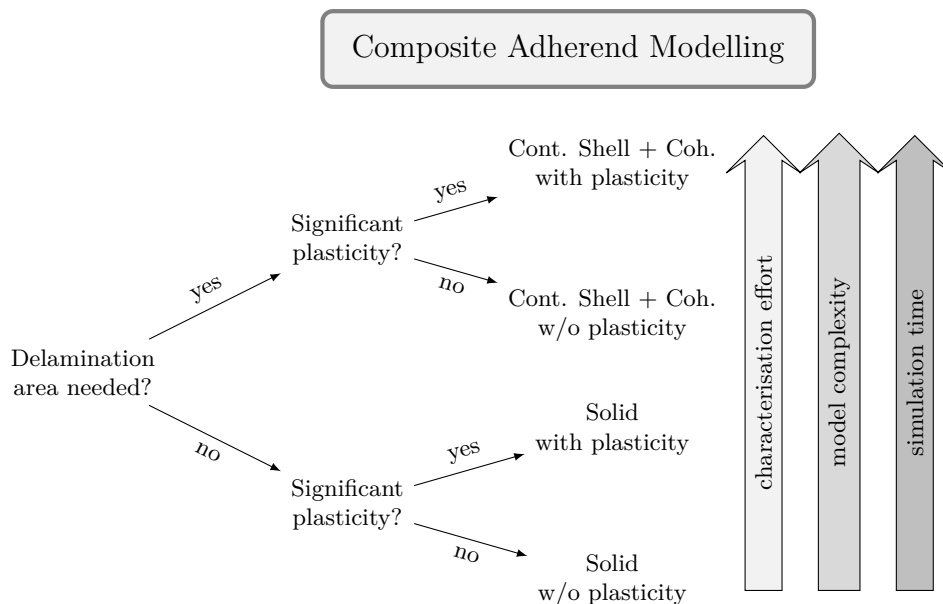


Figure 7.13: Decision support for composite adherend modelling strategy

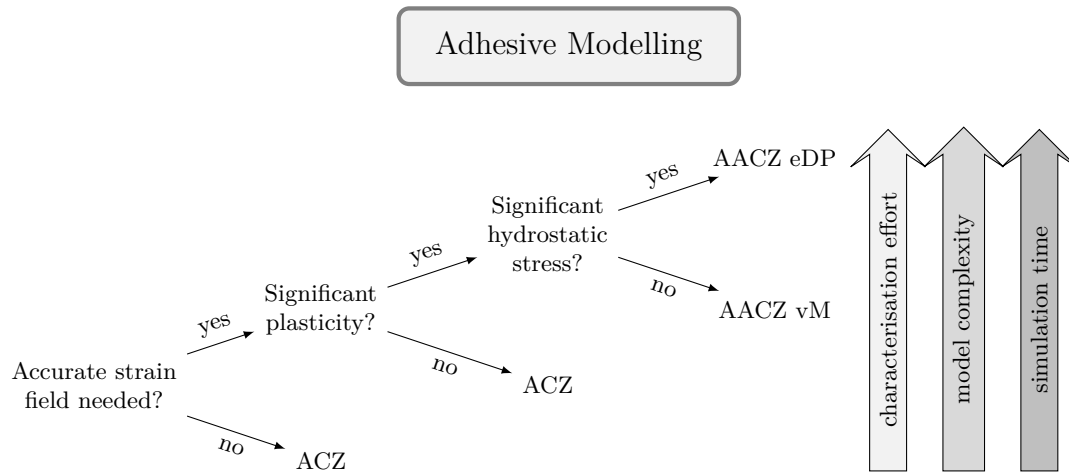


Figure 7.14: Decision support for adhesive modelling strategy

neglects intralaminar plasticity of the composite adherends. This composite modelling is combined with the ACZ technique for the adhesive layer. This efficient holistic approach is significantly faster and, in addition, needs less effort in characterisation as the characterisation of the hydrostatic pressure-sensitive yielding of the adhesive as well as the characterisation of fibre composite plasticity can be omitted.

By contrast, the accurate holistic approach models the adherends with continuum shell elements and cohesive surfaces. The adhesive is modelled using the AACZ technique with the exp.D.-P. plasticity model. The resulting holistic model is more accurate than the efficient model as it provides additional information regarding delaminated areas as well as plastic deformation of the adhesive and the composite adherends. However, it needs to be mentioned that any combination of the modeling strategy shown in the decision trees is possible and, depending on the application, reasonable.

The open questions left at the beginning of the chapter have thus been clarified and the holistic PDA approach has been validated in different compilations. To demonstrate the potential of the validated holistic PDA approach as a tool in the design of aircraft structures, it will be applied to a design issue of a bonded longitudinal joint of a fibre composite fuselage in the next chapter.

CHAPTER 8

Design of a bonded longitudinal fuselage joint using the holistic PDA approach

How could the design process of a bonded longitudinal fuselage joint using the holistic PDA approach look like?

This chapter introduces the application example for the proposed holistic PDA to answer design and certification issues with virtual tests. Starting with a brief introduction on virtual testing of aircraft structures, the MFFD, which serves as a reference structure, is introduced. Loads on the longitudinal fuselage joint under investigation are briefly introduced as well as the design variants to be studied. The chapter concludes with the problem statement considered in detail in this work: The positioning accuracy of the two fuselage half-shells and its effect on the mechanical performance of the joints.

Parts of this chapter were published in [7]. In the publication, however, the considered materials are different. While in the present work bonded joints with thermoset-based fibre composite adherends are analysed, in the published study, fusion bonded or welded joints in thermoplastic-based fibre composite adherends were investigated.

8.1 Virtual testing of aircraft structures

The first applications of today's FEM took place in the aerospace industry in the 1950s. Turner et al.'s [280], published in 1956, in which an aircraft wing structure was analysed, is considered as a starting point of current FEM.

In the past, the use of FEA in commercial aircraft design and certification was limited to linear analysis for initial sizing and later for more detailed simulations for certification. Due to conservatism, both in methods and material properties this approach demonstrated and ensured an adequate strength of aircraft structures. In the more recent past, advanced non-linear analysis methods considering plasticity, failure, and damage allowed for actual strength and failure mode predictions. With the increase in available computing power and further development of methods, there is potential for virtual testing to mitigate risks associated with physical testing or to replace it, at least in part [281].

First applications in this field have already been published: Ostergaard et al. [281] show the virtual test of the Airbus A380 wing and point to the EU Seventh Framework Programme (FP7) project Maaximus. This is a major project with Airbus and Dassault Systemes SIMULIA involved making progress towards advanced virtual testing meth-

ods. In addition, some recent publications deal with the development of virtual testing methods. For instance, Lopes et al. [282] propose a roadmap for multiscale virtual testing to efficiently design fibre composite structures. Gigliotti and Pinho [283] have also published a paper on virtual testing of large fibre composite structures. Concepts for a hybrid simulation-physical test pyramid for fibre composites were developed by Tijs et al. [284]. Focusing more on larger structures, Gorskii et al. [285] show virtual test rigs for static strength, and fatigue, as well as bird- and hailstrike investigations of aircraft structures. All these works have also led to a certification memorandum from EASA that addresses requirements for modelling and simulation in the context of certification [19].

In parallel, the design of aircraft has moved from metallic to fibre composite structures with thermoset matrix materials [286]. This development continues in the change from mechanical fasteners towards adhesive bonding as joining technology. Adhesive bonding enables changed and more efficient production processes [287] which will be discussed in more detail later.

Although some work on virtual testing has been pointed out, there is still little work that addresses how to incorporate virtual testing methods into the design and certification process. The vast majority of publications focus on the development of the numerical methods themselves and on their validation with standard test specimens, as can be seen, for example, in the reviews [122] and [288].

For this reason, this study focuses on answering design and certification issues using virtual testing. Illustrated with the example of an adhesive bonded longitudinal fuselage joint, in this chapter a design and certification process assisted by virtual testing using progressive damage analyses is proposed.

A brief overview of the certification requirements and design methodologies for composite bonded joints has already been given in Section 2.1.5. Therefore, the next subchapter introduces the application example with a design issue to be answered. After that, the development of the simulation models for virtual testing with two preliminary studies is described. The work closes with results and conclusions from the virtual test bed as well as a short outlook with a proposed strategy for reduced experimental testing.

8.2 Application example: longitudinal fuselage joints

This subchapter introduces the longitudinal fuselage joint as an application example for the design with the proposed holistic progressive damage model. As reference structure, the MFFD, which is briefly introduced in the following section, is adopted. It was originally developed for thermoplastic composite materials and fusion bonded joints. Nonetheless, the material choice is altered to the material under consideration in this work: The M21-T700GC thermoset composite material and the Hysol EA9695 film adhesive for the bonds. After the general description of the reference structure, the loads on the longitudinal joint are briefly introduced as well as the design variants to be investigated. This section concludes with the problem statement, which is considered in detail in this work: The positioning

accuracy of the two fuselage half-shells and its effect on the mechanical performance of the joints.

8.2.1 Longitudinal joint of multifunctional fuselage demonstrator

Although the material of the MFFD is altered from thermoplastic to thermoset for purpose of consistency in this work, the motivation for the MFFD based on the thermoplastic material choice is briefly discussed below.

The aviation sector is estimated to be responsible for 2-3 % of global CO₂ emissions with an expected doubling of emissions by 2050 [289]. As flying brings economic benefits and connectivity, ways must be found to reduce emissions. Mass reduction is one of the approaches since a mass reduction of 100 kg is estimated to save 600,000 litres of fuel in an aircraft life [290].

This is already done by the aircraft manufacturers by replacing metallic alloys with fibre composite materials. Most advanced fibre composite aircraft structures are made from continuous carbon or glass fibres with a thermoset polymer matrix material. These materials are well developed, have competitive prices, mature manufacturing processes, and well-established supply chains. Though, they are manufactured in a long and labour-intensive manufacturing process and have only limited recycling possibilities. Due to this, high-performance thermoplastic matrix materials are considered as an alternative. Thermoplastics can be processed by heating above their glass transition temperature and do not crosslink or cure like thermoset materials [291].

However, one of the main advantages of thermoplastics is that they can be heated and cooled down multiple times without loss of mechanical properties and therefore they can be welded or fusion bonded [292, 293].

It is noteworthy that there are already some certified and flying components made of thermoplastic composites [294]. However, a complete aircraft fuselage made of this class of material does not yet exist. For this reason, the MFFD made from thermoplastic composite material was conceived for research and technology development [287]. The possibility of fusion bonding and a dustless joining process is important for the concept. Unlike before, where holes had to be drilled and mechanical fasteners had to be installed to join the parts, with fusion bonding, electrical systems can be installed prior to assembling the aircraft structures because no conductive carbon fibre chips are produced [287]. This allows for large pre-equipped sub-assemblies with a high cost-saving potential.

This enables the concept of a lower and upper fuselage half shell with a high-level pre-installation of systems prior to the final assembly line. The MFFD features the asymmetrical single-aisle fuselage of the Airbus A321 and is built from four main modules: The upper and lower shells as well as a floor and a crown module with the main systems. The dimensions of the demonstrator are 8,000 mm in length and a varying radius between 2,000 m and 2,500 mm [291].

The ideas of a changed manufacturing process are not only valid for a thermoplastic fusion bonded fuselage, but also hold true for thermoset adhesively bonded variants. An adhesively bonded longitudinal joint between the lower and upper shell of the fuselage is

the object of investigation in this work. More details of the MFFD and the manufacturing concept are published in [291] and [287] and an illustration of a pre-equipped fuselage section with adhesive joints can be seen in Fig. 8.1.

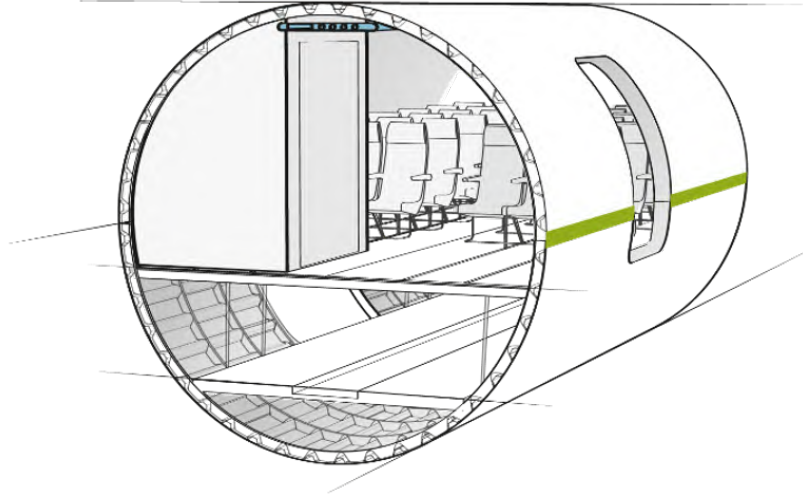


Figure 8.1: Illustration of pre-equipped fuselage section with adhesive joints (green)

8.2.2 Loads on the longitudinal joint

The main loads on aircraft fuselages are manoeuvring and gust, internal cabin pressure, landing procedure and, ground handling [295]. However, the primary loading for the fuselage skin and thus, for the longitudinal joint, is hoop stress caused by the difference between the atmospheric and cabin pressure [296]. These hoop stresses, resulting in a tensile loading of the longitudinal joint in circumferential direction, are used for the joint design.

In this context, the decisive factor for sizing is the maximum pressure difference between internal and external pressure. Typically, the aircraft's internal pressure is 0.075 MPa, which corresponds to an altitude of 8,000 ft, whereas the average maximum altitude of commercial aircraft is 45,000 ft, which corresponds to an air pressure of 0.015 MPa. This results in a pressure difference of 0.06 MPa [296]. According to CS 25, this maximum expected load is referred to as the DLL. If not further specified, a safety factor sf of 1.5 has to be considered for the structure, resulting in the DUL. For pressurised components of aircraft operating up to an altitude of 45,000 ft, an additional sf of 1.33 shall be applied:

$$DUL = DLL \cdot sf = DLL \cdot 1.5 \cdot 1.3 = 2.0 \cdot DLL \quad (8.1)$$

The hoop stress σ_h can be calculated from the pressure p , the radius of the fuselage r ,

and the skin thickness t with:

$$\sigma_h = p \cdot \frac{r}{t} \quad (8.2)$$

With a skin thickness of 1.572 mm, the equation above results in a hoop stress of $\sigma_z = 95.4$ MPa. Niu [295] states that, depending on the aircraft type, the hoop stress varies between 80 MPa and 110 MPa.

A more advanced analytical solution for the hoop stress considering circumferential and axial stiffening elements is proposed by Flügge [297]. However, the simple approximation is sufficient for this consideration.

8.2.3 Design variants to be investigated

Three different design variants are investigated in this study. The Configuration A1, cf. Fig. 8.2, is a simple single overlap joint. The fibre composite fuselage skin consists of two sublaminates, each of which has the layup $[45^\circ, -45^\circ, 0^\circ, 90^\circ, -45^\circ, 45^\circ]$. The initial overlap length of the adhesive bond is 30 mm.

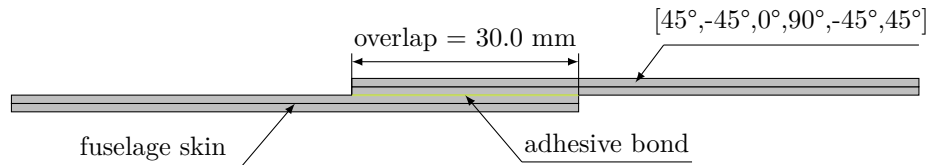


Figure 8.2: Configuration A1

The second variant under investigation is Configuration A2. Again, the fuselage skin is made from two sublaminates, but in A2, the joint is formed as an stepped lap joint with two steps. Each step has a length of 30 mm.

Like Configuration A2, the third variant A3 is a stepped joint. The difference is a thicker fuselage skin. In the A3 variant, the skin consists of three sublaminates and the joint is formed by three steps with a 30 mm length each.

The configurations A2 and A3 are illustrated in figures 8.3 and 8.4. Common to all configurations is that by using the sublaminates, the adhesively bonded interface has a 45° fibre orientation.



Figure 8.3: Configuration A2



Figure 8.4: Configuration A3

8.2.4 Positioning accuracy of the fuselage halves

As described in the section on the MFFD, cf. Section 8.2.1, the pre-equipped fuselage half-shells shall be joined by adhesive bonding with a target overlap length of 30 mm. One of the major challenges during joining is the positioning of the components, which

are quite large with 8,000 mm in length and 4,000 mm in diameter. Moreover, due to the pre-equipment, they are also considerably heavy and sensitive. The positioning accuracy in circumferential direction that can be tolerated in the design is therefore a decisive parameter for the complexity of the joining process. A larger tolerance range for the overlap length simplifies and speeds up the joining process, thus saving costs. As an example, Fig. 8.5 shows the Configuration A2 with the defined step length of 30 mm, but with an overlap of only 15 mm and a gap of 15 mm.

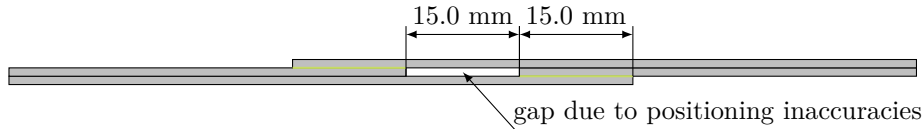


Figure 8.5: Configuration A2 with 15 mm gap

The PDA-based design process proposed in this work is used to determine the strength and failure mode of the different configurations with varying gap lengths. It is expected that the strength of all variants is far higher than the desired strength. Hence, the focus is on the desired failure mode. In this way, the largest allowable tolerance will be determined without physical testing.

8.3 Simulation model for virtual testing

This subchapter briefly describes the requirements for the simulation models, simplifications, loads and boundary conditions, the material modelling as well as element size considerations. The simulations in this study are performed using Abaqus/Explicit. More details on the simulation hardware and runtimes are given in Subchapter 8.4.

8.3.1 Requirements

To be able to predict the strength and failure behaviour of the different design variants with different gap lengths, the relevant failure mechanisms must be captured by the simulation method used. This includes the behaviour of the fibre composite adherends up to total failure as well as damage of the adhesive bond itself. The material model used for the composite adherends should include failure criteria as well as damage progression models for fibre and matrix failure. Furthermore, the latter should be captured in-plane as well as out-of-plane (delamination failure). Whether modelling the pseudoplasticity of the composite adherends is necessary or not is also investigated in this study.

In addition, to be able to use simulations for certification purposes in the future, the requirements stated in the EASA certification memorandum regarding modelling and simulation in the context of certification of CS-25 aircraft [19] have to be fulfilled. It needs to be mentioned that the requirements are not fully met in this study as this work is intended to be a proposal for a way in which simulations can be used in the context of future design and certification activities.

8.3.2 Modelling simplifications

The design of aircraft longitudinal fuselage joints is mostly based on the results of static and dynamic tests of uniaxially loaded flat specimens [296]. With regard to the actual conditions, not only the real (much larger) dimensions and the surrounding connections to other structural components are neglected, but also the influence of the curved fuselage structure. The fact that these simplifications are justified is shown by their application in practice over many years with sufficiently good results to consider them within a design. However, uncertainties are absorbed by large safety factors [298].

At this point, at least the effect of curvature should be briefly explained in some detail. So far, only a few investigations on overlap joints of curved structures can be found in the relevant literature. One example is given by Parida and Pradhan [299]. Among other things, the influence of a variable radius of curvature on the strength of a composite lap joint is investigated. The ERR is used as an indicator of crack growth and delamination processes. Parida and Pradhan's findings are that failure processes are always multiaxial and that flat lap joints (infinite radius of curvature) generally have a higher resistance to crack growth than curved ones. Comparable statements are also made by Liu et al. [298]. In their study, the joint strength of curved structures is analysed using CZM. Liu et al. state that the effect of moderate curvatures on the maximum bearable load of a joint is negligible. More specifically, they show that, as the radius of curvature decreases, the peel stresses at the overlap ends change from tensile to compressive. Liu et al. recommend neglecting curvature in the joint design if the radius of curvature is greater than 2,000 mm, otherwise the curvature should be considered. This recommendation results from a variation of radii of curvature with a step size of 1,000 mm. It needs to be mentioned that the radius of the MFFD considered in this work is 1,950.5 mm on average. As this is close to the limit established by Liu et al., the recommendation of a flat modelling approach is used.

As described before, in this study, only tensile loads on the joint due to cabin pressure are considered. By neglecting the loads in the longitudinal direction of the fuselage, the problem can be modelled in 2D by using the plane strain assumption [249]. This state can be used if displacements in a three-dimensional component occur only in two spatial directions or if forces acting in one plane do not cause displacements perpendicular to this plane. This is the case, for example, with planar components, if the expansion in the depth direction is considerably greater than in the other directions. Thus, the modelling of a cross-section (2D) is sufficient and displacements in depth direction may be neglected. However, the single plies of the composite adherends shall be modelled for the PDA. This is, at least for the $\pm 45^\circ$ -plies, not possible in Abaqus using plane strain elements, because the fibre orientation would have to be rotated out of the shell plane and, therefore, a full three-dimensional model is necessary. In order to save computational effort a model with small expansion in the longitudinal direction of the fuselage is used in this study. Using advanced coupling constraints, which will be explained in detail in the next section, by complete elimination of finite width effects a plane strain state is generated in the model. In this way, size and calculation times of the models can be significantly reduced.

8.3.3 Loads and boundary conditions

This section describes the loads and boundary conditions of the simulation models which are used to eliminate finite width effects. They are illustrated using the example of Configuration A1, cf. Fig. 8.6.

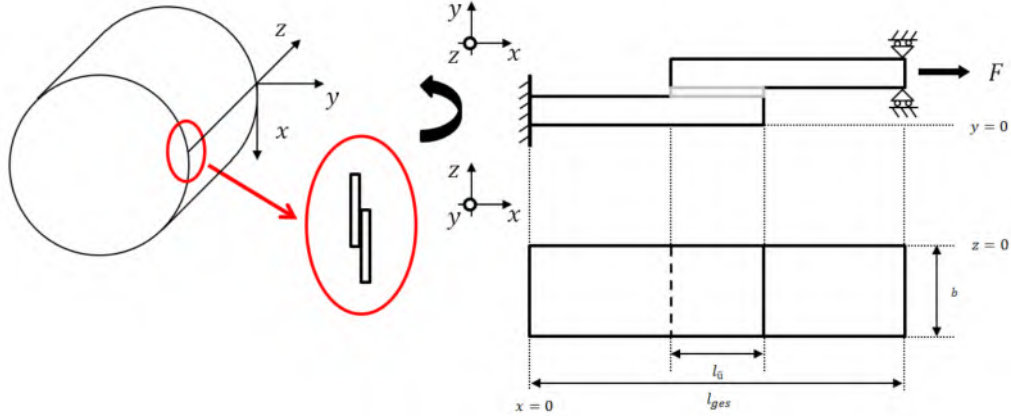


Figure 8.6: Coordinate system used for the aircraft fuselage as well as geometry, boundary conditions and coordinate system of the simulation model

First, the conditions at the two edges in circumferential x -direction are described. The left side of the model ($x = 0$) is fully constrained ($u_x = u_y = u_z = u_{rx} = u_{ry} = u_{rz} = 0$), whereas, on the opposite side ($x = l$), a load is applied as a displacement. In addition, at this edge ($x = l$), the displacements in the y - and z -directions are suppressed ($u_y = u_z = 0$).

Like described in Section 8.3.2, a stress state like in the middle of an infinitely wide structure must be achieved in the simulation model. This requires special boundary conditions, which rely on coupling of displacements. A simple coupling only of the free edges of the model ($z = 0$ and $z = b$) is only sufficient if parts with isotropic materials or composites with longitudinal and/or transverse fibre orientations are coupled. However, if the parts also contain layers with off-axis fibre orientations, like $\pm 45^\circ$, simple coupling results in edge effects [300]. This is the case in the present application example. Therefore, more advanced coupling conditions have to be used. This is done by adopting the coupling conditions described by Al-Ramanhi et al. [300]. In the following, a brief overview of the advanced coupling conditions is given.

The first coupling involves nodes on the free edges of the model ($z = 0$ and $z = b$). The z -displacements of nodes that have the same x -coordinate and are consequently on a vertical line are coupled. This is illustrated in Fig. 8.7. The coupling is applied along the length of the model on every set of nodes sharing the same x -coordinate, but on both edges ($z = 0$ and $z = b$) separately. In this way, all nodes on these vertical lines have the same

displacement u_z :

$$u_{z-coupled}^m = (x_m, Y, 0); u_{z-coupled}^m = (x_m, Y, b) \quad (8.3)$$



Figure 8.7: Front view for coupling of displacement u_z applied on the nodes with the same x -coordinate belonging to the vertical lines on the edge adopted from [300].

The index m describes the variable x -position, Y includes all nodes of a vertical line, and 0 or b indicate the position of the edge (z -position). The second coupling runs through the width of model and couples the x - and y -displacements of nodes, which lie on a line in depth direction, cf. Fig. 8.8. It needs to be noted that every node in the model is affected by this coupling. In contrast to the first condition, the lines of the coupled nodes are not only on one variable coordinate, but on two. Ergo, a second position index n has to be introduced:

$$u_{z-coupled}^{m,n} = (x_m, y_n, Z); u_{y-coupled}^{m,n} = (x_m, Y_n, Z) \quad (8.4)$$

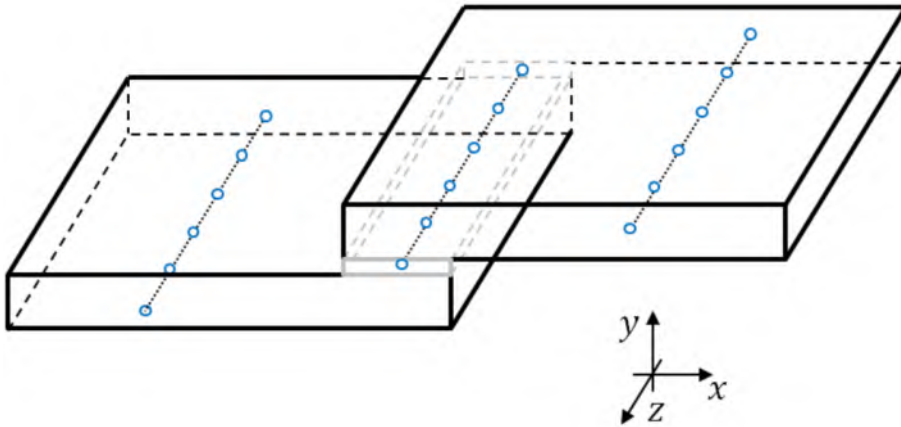


Figure 8.8: Coupling of u_x and u_y on nodes belonging to lines through the width of the joint adopted from [300]

By introducing these coupling conditions, edge effects are not completely eliminated,

but strongly reduced. This allows reducing the width of the model to a minimum without noticeably changing the result. A width study to prove this and to find a width for the virtual testing of the different joint configurations is presented in Subchapter 8.4.

8.3.4 Selection of holistic modelling approach

As described in Section 8.2.4, the desired information in the present application case is, beside the strength, in particular the occurring failure mode. The fast modelling approach has less accuracy in terms of strength. However, it is shown in Chapter 7 that a precise failure mode prediction is not only possible with the accurate but also with the fast modelling approach, and in this case, strength is secondary. For this reason, the fast modelling approach is utilised to save computational effort.

This means, that for adherend modelling, the user-defined material model developed in Chapter 4 is used in combination with reduced integrated solid elements (C3D8R) and the material properties determined in chapters 4 and 5. Yet, delaminations are not explicitly modelled. A summary of the composite material parameters can be found in Tab. 4.7. As recommended in Chapter 4, the necessity for modelling pseudoplasticity is investigated for the present application in the following subchapter.

According to the fast modelling approach described in Chapter 7, the adhesive is modelled using the ACZ approach, and thus, by cohesive elements (COH3D8) only. The material properties used for the adhesive are summarised in Section 6.7.1 and Tab. 6.9.

For the choice of discretisation, the findings in chapters 4 and 6 are used, resulting in an in-plane element edge length of 0.85 mm.

8.4 Preliminary studies for modelling

In this subchapter, two preliminary studies are conducted to determine the final modelling for the main study to find the maximum tolerable gap of the adhesive joints. Firstly, the model width of the 2.5D model is investigated and secondly, the need to consider pseudoplasticity is studied.

8.4.1 Investigation of the required model width

Configuration A1 with the nominal overlap length of 30 mm is taken as an example for the width study. For this purpose, four models were set up and simulated, differing only in width. The width varies from one element to three and five, up to a maximum of ten elements. For this variation, the element size is kept the same, so that the absolute width of the model varies from 0.83 mm to 8.3 mm. The results in the form of a stress-strain diagram are shown in Fig. 8.9.

It can be seen that the model with one element width results in the lowest stiffness, which is significantly lower than the stiffness of the remaining models. This is attributed to the fact that the coupling conditions at the two free sides of the model are applied on the same element. Additionally, the predicted strength is also the lowest of the four models. It is noteworthy that the difference in stiffness and strength between the models decreases with increasing model width. The strength predicted with the three-element model is at 410.4 MPa 4.9 % lower than the strength of the ten-element model at 431.5 MPa. The

five-element model gives a strength of 417.0 MPa, which is only 3.4 % lower than the widest model.

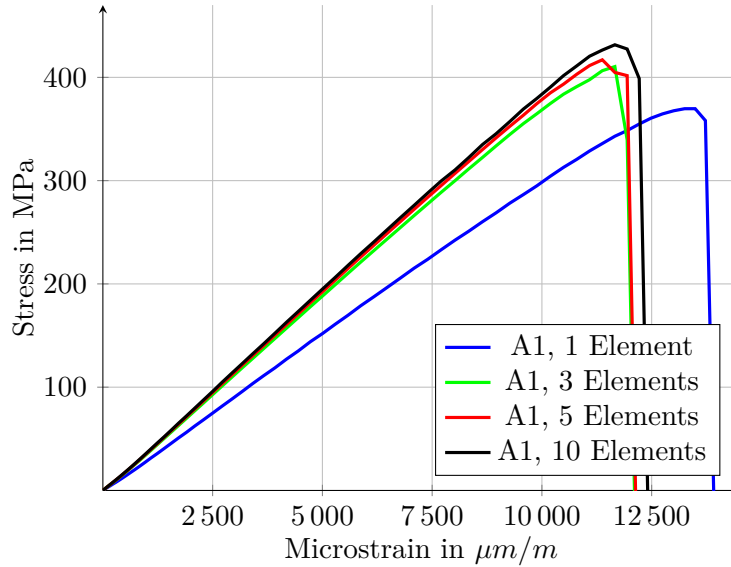


Figure 8.9: Stress-strain curves from configuration A1 with different model widths

In Tab. 8.1 the wall clock time of the simulations using one CPU core on a workstation with an Intel® Xeon® E5-2670 v3 processor and 48 GB RAM is given.

Table 8.1: Wall clock time for the different model widths

Model width	Wall clock time in s
1 element	2,901
3 elements	7,536
5 elements	12,467
10 elements	47,934

Considering the simulation runtimes, the model with five elements is chosen as a compromise between runtime and accuracy. It is not substantially less accurate in terms of stiffness and is slightly conservative in terms of strength, but with 12,467 s to 47,934 s wall clock time, it requires almost only a third of the runtime of the ten elements model.

8.4.2 Influence of pseudoplasticity of composite adherends

As described earlier in this work, the consideration of pseudoplasticity is optional in the material model for the fibre composite. To study the influence of plasticity, simulations of the configurations A2 and A3 are performed without a gap. The configurations are chosen because of the high material stressing in these configurations due to reduced eccentricity compared to Configuration A1 and consequently, a potentially high plasticity. The results

in terms of stress-strain plots are shown in figures 8.10 and 8.11. In general, the same findings are found for configurations A2 and A3.

The simulation of A2 with linear-elastic behaviour of the adherends up to initial damage results in a strength of 496.7 MPa at 13,445 microstrain, while the simulation considering plasticity predicts a strength of 506.6 MPa at 13,677 microstrain. Thus, the strength when plasticity is neglected is 10 MPa lower. The same difference in terms of strength is observed for the Configuration A3 with 491.7 MPa at 12,789 microstrain in case of the elastic modelling up to failure and 500.8 MPa at 13,593 microstrain for the elastoplastic modelling. As can be seen from the values, the failure strain is also slightly lower for the elastic modelling.

In terms of stiffness, it can be said that without plasticity both joints, A2 and A3, are slightly stiffer between 7,500 and 12,500 microstrain.

Nevertheless, a more significant deviation can be observed in the region of maximum stress. The models using elastoplastic adherend modelling show a sharp load drop, whereas the elastic modelling results in a behaviour which shows some retained load carrying capabilities after the maximum loading and prior to the final load drop. However, the damage pattern observed in the simulation is the same regardless of the adherend modelling.

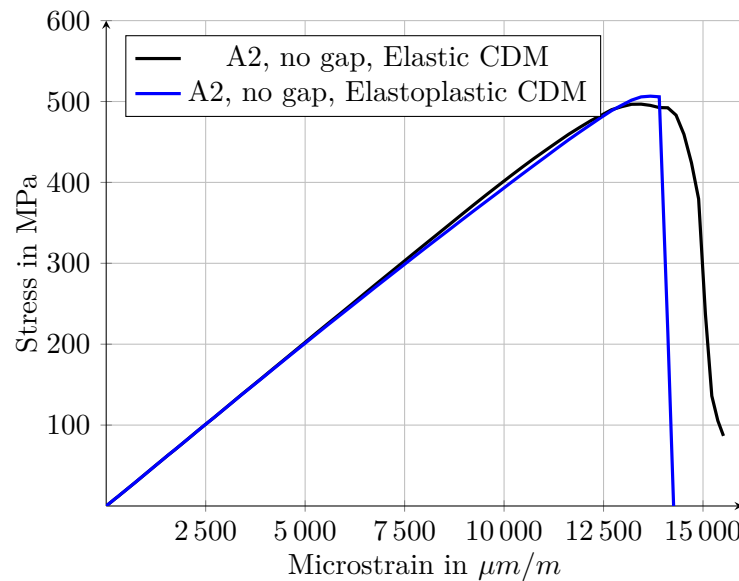


Figure 8.10: Influence of pseudoplasticity of composite adherends - stress-strain curves from Configuration A2 without a gap

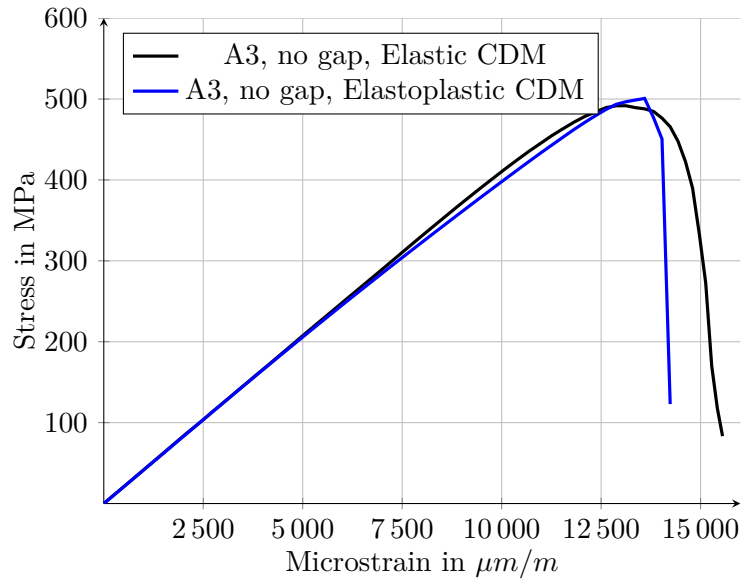


Figure 8.11: Influence of pseudoplasticity of composite adherends - stress-strain curves from Configuration A3 without a gap

Based on the above results, it has been decided to perform all further analyses with elastoplastic modelling. This is justified by the slight differences in the structural response described above. Nevertheless, the decision is influenced by the fact that both an elastoplastic material model and the material parameters for M21-T700GC are available. As the deviations are only marginal, this application case is considered a good example for an application specific modelling. Yet, the optional pseudoplasticity could be omitted in this case to save computation time. The wall clock times needed for the analysis of the A2 models are given in Tab. 8.2. It can be seen that the computation time is reduced to 70 % of the elastoplastic model when neglecting plasticity.

Table 8.2: Wall clock time in dependency of plasticity modelling (Configuration A2)

Plasticity	Wall clock time in s
Yes	24,580
No	17,054

8.5 Results from virtual test bed and discussion

This subchapter covers the results from the virtual test bed with focus on strength and failure behaviour of the different design variants. A design guideline for positioning accuracy is derived and an outlook regarding a proposed strategy for reduced experimental testing is given.

8.5.1 Strength and failure behaviour of the design variants

In figures 8.12, 8.13, and 8.14 the stress-strain curves from the simulations of the configurations A1, A2 and A3 are shown.

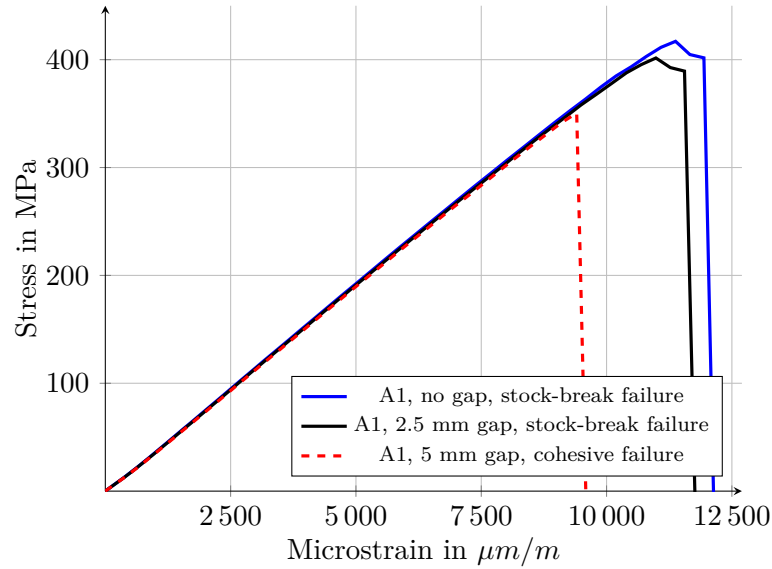


Figure 8.12: Stress-strain curves from Configuration A1 with different gap lengths

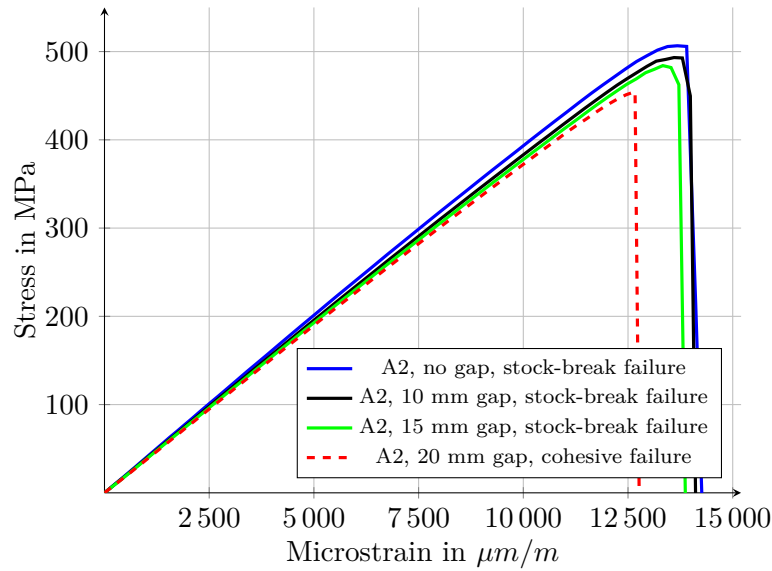


Figure 8.13: Stress-strain curves from Configuration A2 with different gap lengths

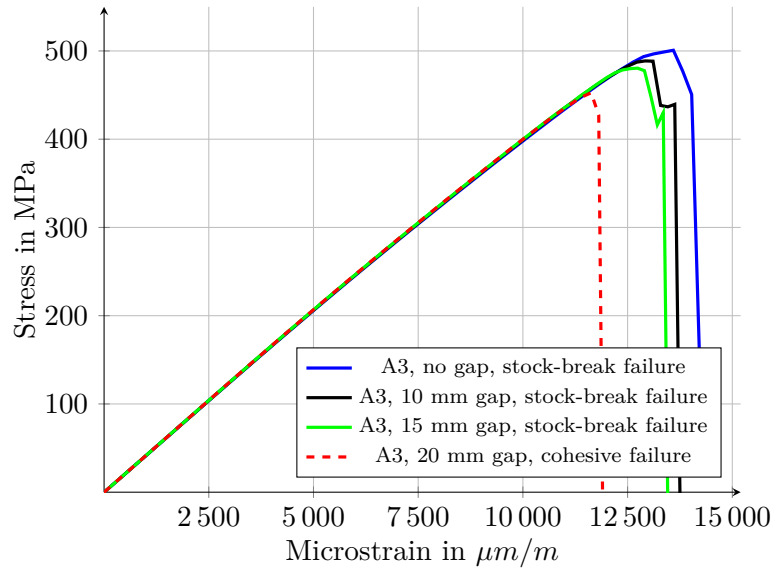


Figure 8.14: Stress-strain curves from Configuration A3 with different gap lengths

All configurations are simulated with the initial overlap length of 30 mm. These results are marked as ‘no gap’. In addition, models with gap length of 10 mm, 15 mm and 20 mm are simulated for all three variants. These result in remaining adhesive bond lengths of 20 mm, 15 mm and 10 mm. In general, the stiffness of the variants A1, A2 and A3 as well as strength and failure strain are very similar. The non-linearity at high loading increases from Configuration A1 through to Configuration A3, while the strength level of Configuration A1 is slightly lower than the strength of A2 and A3. The strength of A1 without gap is lower at 417.0 MPa, compared to 506.6 MPa for configuration A2 and 500.1 MPa for Configuration A3. This is attributed to the reduced secondary bending of the stepped joints and to the doubled or tripled bonding area for the configurations A1 and A2.

When the overlap length is reduced, configurations A2 and A3, on the one hand, behave almost the same. Configuration A1, on the other hand, shows a significantly different behaviour.

The reduction of the overlap length to 25 mm in Configuration A1 leads to a change in failure mode and therefore to a significant strength decrease. For this reason no simulations with further reduced overlap length were performed for Configuration A1. However, a simulation with a shorter gap or positioning inaccuracy of 2.5 mm is performed. This variant leads to a significantly lower decrease in failure load and strain compared to the previously mentioned variant with 5 mm gap and the failure mode is still stock-break.

For the other two variants, however, the extension of the gap length from no gap at all up to 15 mm only has a minor impact on strength and failure strain. A gap length of 20 mm, on the other hand, which is represented with dashed curves in the above diagrams, leads to a considerable reduction in strength. Accordingly, with 454.6 MPa for A2 and 452.6 MPa for A3, the strengths of both configurations are significantly reduced again to nearly the

same load level.

It must be noted that all variants withstand significantly more than the DUL of 90 - 120 MPa described in Section 8.2.2 on loads for all considered gap lengths. Nevertheless, beside the pure load capacity, as stated before, there is also a requirement for the failure mode. Therefore, the failure mode is considered in more detail in the following.

Configuration A2 is taken as an example to compare the failure modes between the models with 15 mm and 20 mm gap length. Thus, between the models where there is a significant drop in load. Though, up to 15 mm gap length, the joints fail near the adhesive bond, the final failure is caused by breakage in the composite adherend modelled with the intralaminar damage model from Chapter 4. This can be seen in Fig. 8.15(a).

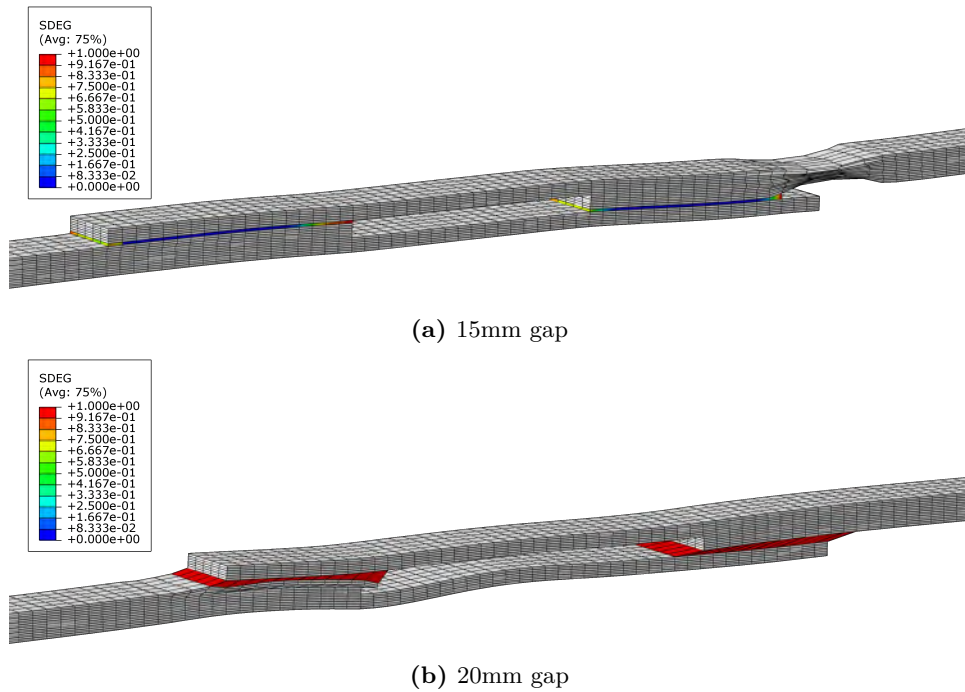


Figure 8.15: Configuration A2: change in failure mode from a 15 mm gap (stock-break failure) to a 20 mm gap (cohesive failure)

It can be noted that the damage variable SDEG, which stands for stiffness degradation of the cohesive elements representing the adhesive, reaches the value 1.0 only at the free edges of the adhesive layer. However, the right adherend is already completely damaged, which can be seen from the severe necking. This is not a typical behaviour of brittle composites and must therefore be explained. The damage mainly occurs in the form of IFF, as only a total of two plies have a fibre orientation in load direction. Since elements are only deleted, when the damage in fibre direction d_{11} reaches 1.0, the fully damaged elements transverse to the fibre are highly distorted.

With a 20 mm gap length, the composite adherends remain nearly intact, but the adhesive

bond itself, modelled with the ACZ approach introduced in Chapter 6, fails, cf. Fig. 8.15(b). Moreover, some elements of the left adherend below the adhesive layer are damaged and highly distorted. Nevertheless, at this point, the adhesive layers are already completely damaged ($SDEG = 1.0$). This change in failure mode between 15 mm and 20 mm gap length can be observed in configurations A2 and A3. For the Configuration A1 the change in failure mode already occurs between 2.5 mm and 5 mm positioning inaccuracy. The observed failure modes are also indicated in the legend of the stress-strain plots in figures 8.12 to 8.14.

8.5.2 Design guideline for positioning accuracy

A design guideline with regard to positioning accuracy can now be derived from the virtual test bed results. First, it can be stated that all three investigated configurations meet the requirements in their initial definition. Regarding the specification of the required positioning accuracy, a distinction must be made between Configuration A1 and configurations A2 and A3.

For the configurations A2 and A3, it can be confirmed, that if a nominal overlap length of 30 mm is designed, the strength is sufficient even with an inaccurate positioning of 20 mm. However, then, with the remaining joint length of only 10 mm of the initial 30 mm, the failure mode changes from stock-break to cohesive or debonding failure. When considering the previously introduced design methodology from Davis and Bond [30] as well as Hart-Smith [27], this is not tolerable. It must therefore be ensured during manufacturing that an overlap length of at least 15 mm from the initial overlap of 30 mm is adhesively bonded to ensure the desired failure mode.

Furthermore, it can be said that the failure mode of Configuration A1 already changes with an overlap reduction of 5 mm. A simulation with 2.5 mm overlap reduction or gap represents a sufficient strength and stock-break failure. This shows that the positioning accuracy for the configuration must be very high, or, in other words, that this configuration cannot be recommended for a cost-effective production.

8.5.3 Outlook: proposed strategy for reduced experimental testing

Using the example of the longitudinal fuselage joint, a strategy for reducing physical testing can be derived. To allow for the largest possible tolerance in the overlap at which the joint still fails in the desired failure mode, an extensive experimental test campaign with varying gap lengths has so far been necessary. With the capabilities of the newly-developed holistic PDA approach, the gap length at which the failure mode changes can be found by virtual testing. It is then only necessary to experimentally validate the region in which the change of failure mode occurs. This is illustrated in Fig. 8.16. This significantly reduces the amount of expensive physical testing. Of course, this requires additional validation of the holistic PDA approach. Furthermore, as described in Section 2.1.3, it is required by EASA [19], to not only perform a Uncertainty Quantification (UQ) for experimental tests, but also for virtual tests.

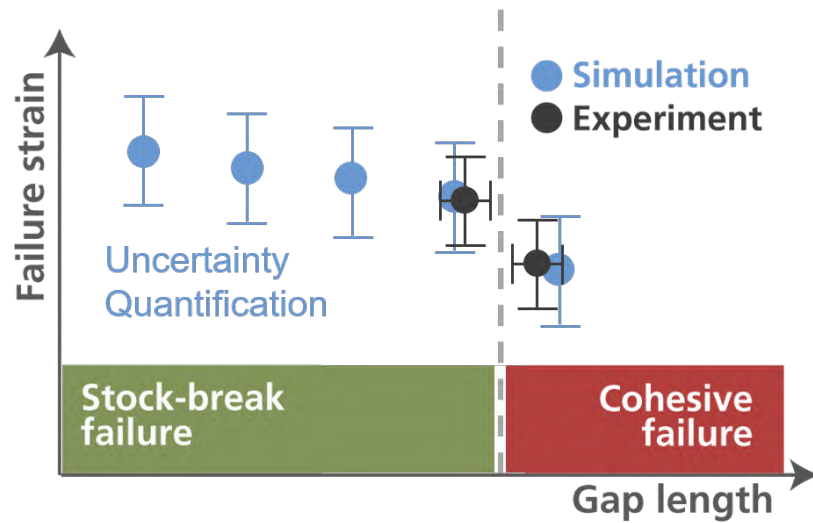


Figure 8.16: Illustration of the proposed strategy to reduce physical testing

8.6 Conclusion: decisive change in failure mode

This chapter showed the potential of virtual testing in the design and certification of bonded joints using FEM-based PDA. The design of a bonded longitudinal joint in an aircraft fuselage made from fibre composite material serves as an example to showcase the proposed method.

Taking advantage of the plane strain condition and limiting the main load case to the one resulting from cabin pressure, virtual structural tests can be realised with manageable computation times. This does not only allow to determine the behaviour of different design variants, but also to numerically investigate further parameters such as the influence of the overlap length on the failure behaviour. Designers thus gain not only a tool to validate designs, but also get a deeper understanding of the effective mechanisms in the joint. To join the two half-shells of the example into a fuselage section, two large components must be aligned very precisely. The required positioning accuracy and the resulting overlap length of the bond significantly influence the assembly effort and consequently the production costs. Based on the nominal overlap length, the proposed method is used to find the minimum possible length at which the failure mode does not change for different joint configurations. By doing so, it is ensured that the failure in case of an overload does not occur in the bond itself but remains limited to the surrounding structure. Once this overlap length is determined, it is sufficient to verify this one configuration with physical tests. In this way, in future a large share of physical tests can be replaced by virtual ones.

However, as described in detail in Section 2.1.3, there is still a lot of work to do regarding the fulfilment of the M&S requirements from the authorities. The purpose of this chapter was to provide a practical example of a way in which the holistic PDA approach for bonded

joints can be used in design and certification in the future.

After applying the validated holistic PDA approach to derive a design guideline for a representative aircraft structure in this chapter, the next chapter draws conclusions from the results of the present thesis and discusses the hypotheses established in Chapter 3. Finally, an outlook is given with regard to possible future applications and extensions of the developed approach.

CHAPTER 9

Conclusions and outlook

The design of bonded joints is a complex task, as there are other requirements to be met besides pure strength, such as a desired failure mode outside of the bond itself, cf. Chapter 2. In addition, it must be noted that the occurring damage depends on many design parameters. This prevents easy prediction of strength and failure mode. Hence, experimental testing is state-of-the-art. As the experimental determination of the required information is time-consuming and expensive as well as limiting the scope of the variants that can be investigated, there is a need for a numerical method to investigate bonded joints in composite structures for design and certification. There are a few studies that deal with the numerical determination of the failure behaviour of the entire bonded joint, but they all have specific shortcomings. This raises the main question of this thesis:

Can Finite Element-based progressive damage analyses be used to show compliance with design and certification requirements of bonded joints in fibre composite aircraft structures?

To pave the way towards a simulation-driven design of bonded joints, in this thesis a holistic PDA approach was developed, the needed material parameters were experimentally determined and its application to a design issue regarding a longitudinal aircraft fuselage joint was investigated. The question above will be answered in the following conclusion along one research hypothesis as well as three working hypotheses postulated in Chapter 3 to focus the research in this thesis:

Conclusions

Working hypothesis I: *Using a combination of selected mesoscale models for the intra- and interlaminar as well as the mechanical behaviour of the adhesive, each taking into account the progressive damage up to total failure, is a suitable approach to compile a holistic tool for analysing the strength and failure behaviour in the design process of fibre composite bonded joints.*

Modelling on the mesoscale without direct coupling of the individual model components was chosen as compromise between numerical effort and possibility to capture the different damage phenomena within a holistic model.

In the chapters 4, 5 and 6 mesoscale models to be used in the holistic tool were selected. Each chapter describes the selection of models addressing individual components of the entire bonded joint with its damage phenomena. This is accompanied in each case by an

experimental determination of the material parameters needed, by a verification of the approaches and by a validation. In this way, mesoscale models for the intra- and interlaminar behaviour of the composite adherends as well as for the adhesive were developed.

In Chapter 7, it could be shown, that the holistic approach established in this way, is able to predict the stiffness, the strength as well as the failure modes of different bonded specimens. It should be emphasised that it was also possible to predict different failure modes without calibrating the model to the application.

With these results, it can be stated that mesoscale modelling can be used without direct coupling of the individual model to predict strength and failure mode of bonded joints.

However, it could be shown that the interlaminar behaviour does not necessarily have to be explicitly modelled. The three-dimensional failure criterion from Cuntze, in combination with solid elements, also gives sufficiently accurate results without distinct interlaminar modelling. Cuntze's FMC takes interlaminar stresses into account, therefore also interlaminar or out-of-plane failure is represented. Thus, explicit modelling of the interlaminar material behaviour is not necessarily required and the hypothesis above could be modified in this way.

Working hypothesis II: The individual components of the holistic model, which have been verified and validated with high accuracy at the individual level, also show high accuracy for the entire composite bond in the holistic PDA approach.

When modelling at the mesoscale, there are different modelling approaches for both the composite and the adhesive that can be incorporated into the holistic model. A number of promising approaches were identified for each component. These individual model components have been validated in the corresponding chapters 4, 5 and 6. In this process, some favoured approaches were revealed, which were then used at the holistic level.

As a next step, in Chapter 7, the selected individual approaches were combined and used to predict the mechanical behaviour of bonded SLS coupons for validation. With the different approaches available at the individual level, several holistic models were derived.

In general, holistic models created from individual model components which performed well at the individual level resulted in good accuracy at the holistic level. This verifies the above working hypothesis.

However, it needs to be mentioned that this is not true for one case. The combination of solid elements with cohesive surfaces as a composite modelling approach achieved similar results in terms of stiffness and strength as the combination of cohesive surfaces with continuum shell elements for OHT specimens. Nevertheless, the predicted delamination areas are different. In contrast, when applied to SLS joints, the two approaches differed strongly from each other, and the solid element-based modelling had to be considered unsuitable for this usecase.

Working hypothesis III: The application-specific selection of the different model components in terms of accuracy, computational costs, and effort for parameter identification results in a capable but pragmatic tool.

As already mentioned, there are different approaches for the individual components to

be modelled. They differ in terms of accuracy but also with regard to effort for parameter identification and computation costs during simulation. Working hypothesis III states that a selection of these approaches for the holistic model, not only with accuracy but also with efficiency in mind, results in a pragmatic but still capable tool.

At the individual level, for example, it could be shown that the FMC by Cuntze is at least as accurate as Puck's APSC but needs less simulation runtime.

At the holistic level, the combined model can be assembled in a way that results in a considerably accurate model. On the one hand, the use of continuum shell elements in combination with cohesive surfaces for the composite and the AACZ approach with the exp.D.-P. yield criterion leads to a holistic model that can discretely capture delaminations in the composite and hydrostatic, stress-state dependent plastic yielding of the adhesive. On the other hand, it could be shown that modelling of plasticity is not absolutely necessary for the thin film adhesive under consideration. The simple ACZ approach leads to sufficiently good predictions, and as already mentioned, modelling based solely on solid elements may also be sufficient for the composite adherends.

Furthermore, it could be shown that the holistic approach described first, referred to as accurate model, gives additional and more accurate information, but needs significantly more computation time. The second holistic model, referred to as fast approach, is still reasonably accurate, but does not provide information regarding delamination areas and plastic yielding of the adhesive. However, the adhesive must not be characterised for a plasticity model, the generation of the simulation model is more straightforward, and the computation times are significantly shorter.

Therefore, the latter holistic model is still capable but more pragmatic. Accordingly, the Working hypothesis III can be considered proven. This leads to the main research hypothesis:

Research hypothesis: A validated PDA approach taking into account all relevant occurring damage phenomena combined with carefully determined mechanical parameters enables the derivation of design guidelines for bonded joints in composite structures while reducing experimental tests to an absolute minimum.

To show the implementation of the holistic PDA approach in the design process, the fast approach developed in Chapter 7 is applied to the design of a bonded longitudinal joint in an aircraft fuselage in Chapter 8. Using the holistic PDA approach, the necessary positioning accuracy of the two fuselage half-shells to be bonded has been investigated. For this purpose, a simplified simulation model using the plane strain state of the joint was developed, which allows studying many different variants due to reasonable computation times.

As shown in Chapter 2, not only the strength but also the failure behaviour is decisive in the design of bonded joints. With the developed holistic approach, it could be shown that all investigated configurations bear more than the required strength regardless of the overlap lengths. However, it could also be revealed that above a certain positioning inaccuracy and thus reduced overlap length, the failure mode changes from the desired stock-break failure to an undesired cohesive failure. Furthermore, this change of failure

mode is highly dependent on whether it is a simple overlap or a stepped joint. With the information gained using the holistic PDA, a design or manufacturing guideline can be established that takes this decisive failure mode change into account. To substantiate this design guideline, only configurations near the point of failure mode change need to be physically tested. Without the developed holistic PDA, the point at which the failure mode changes, would first have to be found through an extensive physical test campaign. In this way, a design guideline could be derived for the example application and physical testing may be reduced to a minimum. This shows that the above working hypothesis could be verified using the example of the longitudinal fuselage joint.

In summary, the question raised initially can be answered by stating that FEM-based PDA can be used in a simulation-driven design and certification process for bonded joints in composite aircraft structures to develop designs and reduce the physical testing to substantiate them. Thus, the possibilities shown in this thesis can help to facilitate the application of bonded joints in aircraft structures.

The holistic PDA approach developed and validated in this work provides an excellent basis to extend it in the future in order to answer further questions in the context of bonded joint design. Nevertheless, it should be noted that there are still many requirements to be met by M&S in the context of certification for implementation in industry, cf. Chapter 2. This leads to the outlook of the work.

Outlook

The outlook is divided into two parts. First, open questions are mentioned that could not be conclusively clarified within the scope of this work:

1. For explicit modelling of delaminations by CZM, the results depend on the type of intralaminar modelling, i.e. whether continuum shell or volume elements are used. This is investigated in some detail in Section 5.6.2. Using the example of an OHT test specimen, it could be shown that the delamination areas differ depending on the intralaminar modelling. However, the comparison with the ultrasonic data from the test is not as conclusive as to allow a quantitative assessment. Hence, further investigations, for example with different specimen types and improved ultrasonic testing technology, are needed to provide a conclusive explanation for the different behaviour.
2. In the characterisation tests for the interlaminar behaviour, cf. Subchapter 5.5, it was found that the delamination behaviour depends on the ply orientation adjacent to the interface. When applying the interface-orientation-dependent values determined in this work to OHT test specimens, no clear trend towards more accurate results could be established. This needs to be further investigated using more OHT variants and additional specimen types.

3. Additional characterisation tests for the considered film adhesive under tensile and combined tensile-shear loading should be carried out and accompanied with DIC measurements, as strain data are needed for verification of the adhesive modelling as well as for calibration of the mode I cERR for the AACZ approach. In this work, cf. Section 6.6.2, the information required from these tests is taken from literature with limited measurement data scope.
4. The mixed-mode characterisation of the adhesive in Section 6.8.4 should be investigated and repeated if necessary. Unlike the interlaminar MMB tests, the MMB tests for adhesive characterisation could not be successfully simulated with the derived values. With the test standard being based on linear elastic fracture mechanics, this may be attributed to the ductile behaviour of the adhesive compared to the more brittle behaviour of the composite material. In this context, it would be beneficial to compare the application of the test and evaluation methods as well as the results of the fracture mechanical characterisation for the two applications, adhesive and interlaminar characterisation, in more detail.

Second, to give an outlook for future applications for which the developed holistic PDA approach represents the necessary basis, a number of features to be implemented in subsequent studies is mentioned below. These additional features are also illustrated in Fig. 9.1.

1. In this work, a direct coupling of the various mesoscale models was omitted and fairly accurate results were achieved with this simplification. Nevertheless, it should be checked in the future whether an information exchange between the models through direct coupling significantly improves the accuracy.
2. The possibility to include multifunctional elements in the joint, such as a hybrid bondline or surface toughening, for disbond arresting [26], strength improvement [34] or sensing [301] should be implemented. As explained in Section 2.1.4 such features, especially DAFs, are necessary for certification of primary bonded joints.
3. To use the holistic PDA approach to design for damage tolerance, the possibility of importing pre-damages from impact and fatigue simulations or experiments should be provided in order to be able to assess the residual strength of the damaged joint. In addition, an assessment of strength with a pre-defined maximum disbond is necessary for certification and can also be performed using the holistic PDA approach.
4. The approach in the present work can be used to investigate the influence of advanced laminate designs, like the double-double concept from Tsai [302], on the strength and failure behaviour of the bonded joint.

5. Further adhesives should be characterised for the method to be able to investigate structures with other adhesive materials using the holistic approach. In particular, paste adhesives with thicker adhesive layers could lead to a more pronounced advantage of the AACZ approach.
6. To pave the way for more M&S in certification, as outlined in Section 2.1.3, there are still some points to be addressed. In addition to an extensive validation, UQ should be carried out for the determined material parameters and the results achieved using the PDA approach. Furthermore, processes that ensure the credibility of the PDA simulations have to be implemented.

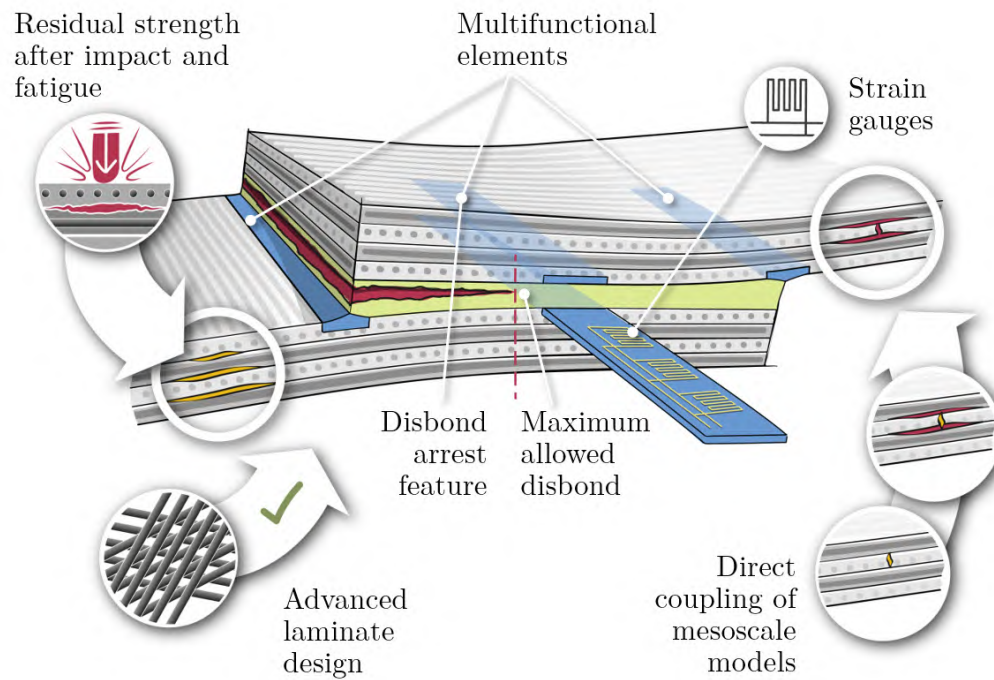


Figure 9.1: Graphical overview of future enhancements and applications

Bibliography

1. MARKATOS, D., K. TSERPEIS, E. RAU, S. MARKUS, B. EHRHART, and S. PANTELAKIS: ‘The effects of manufacturing-induced and in-service related bonding quality reduction on the mode-I fracture toughness of composite bonded joints for aeronautical use’. *Composites Part B: Engineering* (2013), vol. 45(1): pp. 556–564 (cit. on p. 1).
2. THRALL JR, E. W.: ‘Primary adhesively bonded structure technology (PABST)’. *Journal of Aircraft* (1977), vol. 14(6): pp. 588–594 (cit. on p. 1).
3. MARA, V., R. HAGHANI, and M. AL-EMRANI: ‘Improving the performance of bolted joints in composite structures using metal inserts’. *Journal of Composite Materials* (2016), vol. 50(21): pp. 3001–3018 (cit. on p. 1).
4. FUERTES, T. A. S., T. KRUSE, T. KÖWIEN, and M. GEISTBECK: ‘Bonding of CFRP primary aerospace structures - discussion of the certification boundary conditions and related technology fields addressing the needs for development’. *Composite Interfaces* (2015), vol. 22(8): pp. 795–808 (cit. on p. 2).
5. VÖLKERINK, O., J. KOSMANN, M. J. SCHOLLERER, D. HOLZHÜTER, and C. HÜHNE: ‘Strength prediction of adhesively bonded single lap joints with the eXtended Finite Element Method’. *The Journal of Adhesion* (2019), vol.: pp. 1–21 (cit. on pp. 4, 141).
6. VÖLKERINK, O., E. PETERSEN, J. KOORD, and C. HÜHNE: ‘A pragmatic approach for a 3D material model considering elasto-plastic behaviour, damage initiation by Puck or Cuntze and progressive failure of fibre-reinforced plastics’. *Computers & Structures* (2020), vol. 236: p. 106280 (cit. on pp. 4, 41, 102, 106).
7. VÖLKERINK, O. and C. HÜHNE: ‘Virtual testing for design and certification of (fusion) bonded longitudinal joints in a fibre composite fuselage: A proposal using FEM-based progressive damage analysis’. *Composites Part C: Open Access* (2022), vol.: p. 100236 (cit. on pp. 4, 201).
8. VÖLKERINK, O., J. KOORD, E. PETERSEN, and C. HÜHNE: ‘Holistic determination of physical fracture toughness values and numerical parameters for delamination analysis considering multidirectional-interfaces’. *Composites Part C: Open Access* (2022), vol.: p. 100277 (cit. on pp. 4, 95).
9. EASA: *AMC 20-29 Composite Aircraft Structure*. 2010 (cit. on pp. 6, 8, 14, 15).
10. FAA: *AC 20-107B, Composite Aircraft Structure*. 2009 (cit. on pp. 6, 15).

11. ASHFORTH, C. and L. ILCEWICZ: 'Certification of Bonded Aircraft Structure and Repairs'. *NATO Science and Technology Organization STO-MP-AVT-266* (2018), vol. (cit. on pp. 6, 8).
12. WAITE, S.: 'Certification and airworthiness of polymer composite aircraft'. *Polymer Composites in the Aerospace Industry*. Elsevier, 2020: pp. 593–645 (cit. on pp. 6, 15).
13. FEDERAL AVIATION ADMINISTRATION: *Damage tolerance assessment handbook, volume I: Introduction fracture mechanics fatigue crack propagation*. Tech. rep. DOT/FAA/CT-93/69, I. FAA Technical Center Atlantic Airport, 1993 (cit. on pp. 6, 7).
14. MILITARY SPECIFICATION: *MIL-A-83444*. 1974 (cit. on p. 7).
15. DILGER, R., H. HICKETHIER, and M. D. GREENHALGH: 'Eurofighter a safe life aircraft in the age of damage tolerance'. *International Journal of Fatigue* (2009), vol. 31(6): pp. 1017–1023 (cit. on p. 7).
16. ESP, B.: *Practical analysis of aircraft composites*. Grand Oak Publishing USA, 2017 (cit. on pp. 7, 24).
17. DE FLORIO, F.: *Airworthiness: An introduction to aircraft certification and operations*. Butterworth-Heinemann, 2016 (cit. on p. 7).
18. SCHOEPPNER, G. A. and M. S. TILLMAN: 'Composite structures durability design and substantiation'. *Long-Term Durability of Polymeric Matrix Composites*. Springer, 2012: pp. 427–481 (cit. on p. 9).
19. EASA: *Modelling & Simulation – CS-25 Structural Certification Specifications EASA Proposed CM No.: CM-S-014 Issue 01*. 2020 (cit. on pp. 9, 10, 202, 206, 217).
20. ASME: *Standard for Verification and Validation in Computational Solid Mechanics V & V 10 - 2019*. 2020 (cit. on pp. 10, 11).
21. SAFARIAN, P.: 'Finite Element Modeling and Analysis Validation'. *Femap Symposium 2015*. FAA. Seattle, 2015 (cit. on pp. 11, 12).
22. COMPUTATIONAL FLUID DYNAMICS COMMITTEE: *Guide for the Verification and Validation of Computational Fluid Dynamics Simulations (AIAA G-077-1998(2002))*. Tech. rep. American Institute of Aeronautics and Astronautics, 2002 (cit. on p. 11).
23. OBERKAMPF, W. L., T. G. TRUCANO, and C. HIRSCH: 'Verification, validation, and predictive capability in computational engineering and physics'. *Appl. Mech. Rev.* (2004), vol. 57(5): pp. 345–384 (cit. on p. 12).
24. MAHDI, S.: 'Bondline analysis and Bonded Repairs'. *CACRC Meeting/Workshop for Composite DT & Maintenance, Tokyo*. 2009 (cit. on p. 14).
25. ADAMS, R. and B. DRINKWATER: 'Nondestructive testing of adhesively-bonded joints'. *NDT & E International* (1997), vol. 30(2): pp. 93–98 (cit. on p. 14).
26. LÖBEL, T.: 'The Hybrid Bondline: A Novel Disbond-Stopping Design for Adhesively Bonded Composite Joints'. PhD thesis. Technische Universität Braunschweig, 2016 (cit. on pp. 15, 17, 141, 160, 161, 184, 225).

27. HART-SMITH, L.: 'The Bonded Lap-Shear Coupon—Useful for Quality Assurance But Dangerously Misleading for Design Data, 38th Int'. *Symp. And Exhib., Anaheim, CA, May*. 1993 (cit. on pp. 15, 217).
28. *ASTM D5573-99: Standard Practice for Classifying Failure Modes in Fiber-Reinforced-Plastic (FRP) Joints*. West Conshohocken, PA: ASTM, 1999 (cit. on pp. 15, 16).
29. ASHCROFT, I., M. A. WAHAB, A. CROCOMBE, D. HUGHES, and S. SHAW: 'The effect of environment on the fatigue of bonded composite joints. Part 1: testing and fractography'. *Composites Part A: Applied Science and Manufacturing* (2001), vol. 32(1): pp. 45–58 (cit. on p. 16).
30. DAVIS, M. and D. BOND: 'Certification of adhesive bonds for construction and repair'. *Proceedings of the 4th Joint DoD/FAA/NASA Conference on Aging Aircraft*. 2000: pp. 15–18 (cit. on pp. 16, 217).
31. DE GOEIJ, W., M. VAN TOOREN, and A. BEUKERS: 'Composite adhesive joints under cyclic loading'. *Materials & Design* (1999), vol. 20(5): pp. 213–221 (cit. on pp. 17, 262).
32. KHAN, M. A.: 'Development of Rules for the Design of Adhesively Bonded Fibre-Reinforced Plastic Composite Joints in Aerospace Applications'. PhD thesis. University of Surrey (United Kingdom), 2018 (cit. on pp. 17, 262).
33. SCHOLLERER, M. J., J. KOSMANN, O. VÖLKERINK, D. HOLZHÜTER, and C. HÜHNE: 'Surface toughening—a concept to decrease stress peaks in bonded joints'. *The Journal of Adhesion* (2019), vol. 95(5-7): pp. 495–514 (cit. on p. 17).
34. SCHOLLERER, M. J., J. KOSMANN, D. HOLZHÜTER, C. BELLO-LARROCHE, and C. HÜHNE: 'Surface toughening—An industrial approach to increase the robustness of pure adhesive joints with film adhesives'. *Proceedings of the Institution of Mechanical Engineers, Part G: Journal of Aerospace Engineering* (2020), vol. 234(13): pp. 1980–1987 (cit. on pp. 17, 225).
35. SACHSE, R., A. PICKETT, W. ADEBAHR, M. KLEIN, M. KÄSS, and P. MIDDENDORF: 'Experimental investigation of mechanical fasteners regarding their influence on crack growth in adhesively bonded CFRP-joints subjected to fatigue loading'. *20th International Conference on Composite Materials Copenhagen, 19-24th July 2015*. 2015 (cit. on p. 17).
36. SACHSE, R., A. PICKETT, M. KÄSS, and P. MIDDENDORF: 'Numerical Simulation of Fatigue Crack Growth in the Adhesive Bondline of Hybrid CFRP Joints'. *V ECCOMAS Thematic Conference on the Mechanical Response of Composites COMPOSITES 2015*. Ed. by HALLETT, S. and J. REMMERS. 2015 (cit. on p. 17).
37. KIM, H. and K. KEDWARD: *Stress Analysis of In-Plane, Shear-Loaded, Adhesively Bonded Composite Joints and Assemblies*. Tech. rep. DOT/FAA/AR-01/7. University of California Santa Barbara, 2001 (cit. on p. 18).
38. HART-SMITH, L. J.: 'Adhesively Bonded Joints in Aircraft Structures'. *Handbook of Adhesion Technology*. Ed. by SILVA, L. F. M. da, A. ÖCHSNER, and R. D. ADAMS. Cham: Springer International Publishing, 2018: pp. 1235–1284 (cit. on p. 19).

39. KASSAPOGLOU, C., K. RANGELOV, and S. RANGELOV: 'Repair of composites: design choices leading to lower life-cycle cost'. *Applied Composite Materials* (2017), vol. 24(4): pp. 945–963 (cit. on p. 19).
40. ARCHER, E. and A. MCILHAGGER: 'Repair of damaged aerospace composite structures'. *Polymer composites in the aerospace industry*. Elsevier, 2020: pp. 441–459 (cit. on p. 19).
41. PURIMPAT, S., R. JÉRÔME, and A. SHAHRAM: 'Effect of fiber angle orientation on a laminated composite single-lap adhesive joint'. *Advanced Composite Materials* (2013), vol. 22(3): pp. 139–149 (cit. on p. 19).
42. KUPSKI, J., S. T. de FREITAS, D. ZAROUCAS, P. CAMANHO, and R. BENEDICTUS: 'Composite layup effect on the failure mechanism of single lap bonded joints'. *Composite Structures* (2019), vol. 217: pp. 14–26 (cit. on pp. 20, 23).
43. POTTER, K., F. GUILD, H. HARVEY, M. WISNOM, and R. ADAMS: 'Understanding and control of adhesive crack propagation in bonded joints between carbon fibre composite adherends I. Experimental'. *International Journal of Adhesion and Adhesives* (2001), vol. 21(6): pp. 435–443 (cit. on pp. 20, 21, 23).
44. KRUEGER, R., M. K. CVITKOVICH, T. K. O'BRIEN, and P. J. MINGUET: 'Testing and analysis of composite skin/stringer debonding under multi-axial loading'. *Journal of Composite Materials* (2000), vol. 34(15): pp. 1263–1300 (cit. on pp. 21–23).
45. KUMAR, S. B., I. SRIDHAR, S. SIVASHANKER, S. OSIYEMI, and A. BAG: 'Tensile failure of adhesively bonded CFRP composite scarf joints'. *Materials Science and Engineering: B* (2006), vol. 132(1-2): pp. 113–120 (cit. on p. 22).
46. BANE, M. and L. F. da SILVA: 'Adhesively bonded joints in composite materials: an overview'. *Proceedings of the Institution of Mechanical Engineers, Part L: Journal of Materials: Design and Applications* (2009), vol. 223(1): pp. 1–18 (cit. on pp. 24–26).
47. HE, X.: 'A review of finite element analysis of adhesively bonded joints'. *International Journal of Adhesion and Adhesives* (2011), vol. 31(4): pp. 248–264 (cit. on pp. 24, 142).
48. BUDHE, S., M. BANE, S. DE BARROS, and L. DA SILVA: 'An updated review of adhesively bonded joints in composite materials'. *International Journal of Adhesion and Adhesives* (2017), vol. 72: pp. 30–42 (cit. on pp. 24, 26).
49. VOLKERSEN, O.: 'Die Nietkraftverteilung in zugbeanspruchten Nietverbindungen mit konstanten Laschenquerschnitten'. *Luftfahrtforschung* (1938), vol. 15(1/2): pp. 41–47 (cit. on p. 24).
50. GOLAND, M. and E. REISSNER: 'The stresses in cemented joints'. *Journal of Applied Mechanics* (1944), vol. 11(1): A17–A27 (cit. on p. 24).
51. HART-SMITH, L.: *Adhesive-bonded double lap joints*. Technical Report NASA CR-112235. Hampton, Virginia: Langley Research Center, 1973 (cit. on p. 24).
52. OJALVO, I. and H. EIDINOFF: 'Bond thickness effects upon stresses in single-lap adhesive joints'. *AIAA Journal* (1978), vol. 16(3): pp. 204–211 (cit. on p. 24).

53. TSAI, M., D. OPLINGER, and J. MORTON: 'Improved theoretical solutions for adhesive lap joints'. *International Journal of Solids and Structures* (1998), vol. 35(12): pp. 1163–1185 (cit. on p. 24).
54. WAH, T.: 'Stress distribution in a bonded anisotropic lap joint'. *Journal of Engineering Materials and Technology* (1973), vol. (cit. on p. 24).
55. YANG, C. and S.-S. PANG: 'Stress-strain analysis of single-lap composite joints under tension'. *Journal of Engineering Materials and Technology* (1996), vol. (cit. on p. 24).
56. ALLMAN, D.: 'A theory for elastic stresses in adhesive bonded lap joints'. *The Quarterly Journal of Mechanics and Applied Mathematics* (1977), vol. 30(4): pp. 415–436 (cit. on p. 24).
57. RENTON, J. and J. VINSON: 'On the behavior of bonded joints in composite material structures'. *Engineering Fracture Mechanics* (1975), vol. 7(1): pp. 41–60 (cit. on p. 24).
58. BIGWOOD, D. and A. CROCOMBE: 'Non-linear adhesive bonded joint design analyses'. *International Journal of Adhesion and Adhesives* (1990), vol. 10(1): pp. 31–41 (cit. on p. 24).
59. WANG, R., J. CUI, A. SINCLAIR, and J. SPELT: 'Strength of adhesive joints with adherend yielding: I. analytical model'. *The Journal of Adhesion* (2003), vol. 79(1): pp. 23–48 (cit. on p. 24).
60. ADAMS, R. and V. MALLICK: 'A method for the stress analysis of lap joints'. *The Journal of Adhesion* (1992), vol. 38(3-4): pp. 199–217 (cit. on p. 24).
61. SILVA, L. F. da, P. J. das NEVES, R. ADAMS, and J. SPELT: 'Analytical models of adhesively bonded joints—Part I: Literature survey'. *International Journal of Adhesion and Adhesives* (2009), vol. 29(3): pp. 319–330 (cit. on pp. 25, 142).
62. SILVA, L. F. da, P. J. das NEVES, R. ADAMS, A. WANG, and J. SPELT: 'Analytical models of adhesively bonded joints—Part II: Comparative study'. *International Journal of Adhesion and Adhesives* (2009), vol. 29(3): pp. 331–341 (cit. on pp. 25, 142).
63. SCHAEFER, J., B. WERNER, and I. DANIEL: 'Strain-rate-dependent failure of a toughened matrix composite'. *Experimental Mechanics* (2014), vol. 54(6): pp. 1111–1120 (cit. on p. 25).
64. HAWARD, R. N.: *The physics of glassy polymers*. Applied Science Publ., 1973 (cit. on p. 25).
65. WANG, C. H. and P. CHALKLEY: 'Plastic yielding of a film adhesive under multiaxial stresses'. *International Journal of Adhesion and Adhesives* (2000), vol. 20(2): pp. 155–164 (cit. on pp. 25, 154).
66. TOWSE, A., K. POTTER, M. WISNOM, and R. ADAMS: 'The sensitivity of a Weibull failure criterion to singularity strength and local geometry variations'. *International Journal of Adhesion and Adhesives* (1999), vol. 19(1): pp. 71–82 (cit. on p. 25).

67. KRUEGER, R.: 'Virtual crack closure technique: History, approach, and applications'. *Applied Mechanics Reviews* (2004), vol. 57(2): pp. 109–143 (cit. on pp. 26, 100, 142).
68. TURON, A., P. P. CAMANHO, J. COSTA, and C. DÁVILA: 'A damage model for the simulation of delamination in advanced composites under variable-mode loading'. *Mechanics of Materials* (2006), vol. 38(11): pp. 1072–1089 (cit. on pp. 26, 103).
69. YANG, Q., M. THOULESS, and S. WARD: 'Elastic–plastic mode-II fracture of adhesive joints'. *International Journal of Solids and Structures* (2001), vol. 38(18): pp. 3251–3262 (cit. on p. 26).
70. SONG, S. H., G. H. PAULINO, and W. G. BUTTLAR: 'A bilinear cohesive zone model tailored for fracture of asphalt concrete considering viscoelastic bulk material'. *Engineering Fracture Mechanics* (2006), vol. 73(18): pp. 2829–2848 (cit. on p. 26).
71. KAFKALIDIS, M. and M. THOULESS: 'The effects of geometry and material properties on the fracture of single lap-shear joints'. *International Journal of Solids and Structures* (2002), vol. 39(17): pp. 4367–4383 (cit. on p. 26).
72. KIM, M., D. ELDER, C. WANG, and S. FEIH: 'Interaction of laminate damage and adhesive disbonding in composite scarf joints subjected to combined in-plane loading and impact'. *Composite Structures* (2012), vol. 94(3): pp. 945–953 (cit. on pp. 26, 27).
73. SHANG, X., E. MARQUES, R. CARBAS, A. BARBOSA, D. JIANG, L. da SILVA, D. CHEN, and S. JU: 'Fracture mechanism of adhesive single-lap joints with composite adherends under quasi-static tension'. *Composite Structures* (2020), vol.: p. 112639 (cit. on p. 27).
74. CAMPILHO, R. D., M. DE MOURA, and J. DOMINGUES: 'Modelling single and double-lap repairs on composite materials'. *Composites Science and Technology* (2005), vol. 65(13): pp. 1948–1958 (cit. on p. 27).
75. LEONE, F. A., C. G. DÁVILA, and D. GIROLAMO: 'Progressive damage analysis as a design tool for composite bonded joints'. *Composites Part B: Engineering* (2015), vol. 77: pp. 474–483 (cit. on pp. 27–30, 35).
76. TAOTAO, Z., L. WENBO, X. WEI, and Y. YING: 'Numerical simulation of single-lap adhesive joint of composite laminates'. *Journal of Reinforced Plastics and Composites* (2018), vol. 37(8): pp. 520–532 (cit. on pp. 27–29).
77. SUN, L., C. LI, Y. TIE, Y. HOU, and Y. DUAN: 'Experimental and numerical investigations of adhesively bonded CFRP single-lap joints subjected to tensile loads'. *International Journal of Adhesion and Adhesives* (2019), vol. 95: p. 102402 (cit. on pp. 27–29).
78. GOH, J.: 'Damage tolerance of flush repairs of dissimilar composite material systems'. PhD thesis. RMIT University, 2015 (cit. on pp. 27–29).
79. LIU, B., N. GAO, B. TANG, Y. GAO, P. JIN, Z. LU, and Z. FU: 'Progressive damage behaviors of the stepped-lap composite joints under bending load'. *Journal of Composite Materials* (2019), vol.: p. 0021998319889119 (cit. on pp. 27–29).

80. REINOSO, J., G. CATALANOTTI, A. BLÁZQUEZ, P. AREIAS, P. CAMANHO, and F. PARÍS: 'A consistent anisotropic damage model for laminated fiber-reinforced composites using the 3D-version of the Puck failure criterion'. *International Journal of Solids and Structures* (2017), vol. 126: pp. 37–53 (cit. on pp. 29, 50, 52, 56).
81. VASIUKOV, D., S. PANIER, and A. HACHEMI: 'Non-linear material modeling of fiber-reinforced polymers based on coupled viscoelasticity–viscoplasticity with anisotropic continuous damage mechanics'. *Composite Structures* (2015), vol. 132: pp. 527–535 (cit. on pp. 29, 50).
82. LAPCZYK, I. and J. A. HURTADO: 'Progressive damage modeling in fiber-reinforced materials'. *Composites Part A: Applied Science and Manufacturing* (2007), vol. 38(11): pp. 2333–2341 (cit. on pp. 29, 50, 57, 62).
83. CUNTZE, R.: 'The predictive capability of failure mode concept-based strength conditions for laminates composed of unidirectional laminae under static triaxial stress states'. *Journal of Composite Materials* (Sept. 2012), vol. 46(19-20): pp. 2563–2594 (cit. on pp. 29, 50, 55, 77).
84. DEUSCHLE, M. H. and B.-H. KRÖPLIN: 'Finite element implementation of Puck's failure theory for fibre-reinforced composites under three-dimensional stress'. *Journal of Composite Materials* (2012), vol. 46(19-20): pp. 2485–2513 (cit. on pp. 29, 55).
85. KADDOUR, A. and M. HINTON: 'Maturity of 3D failure criteria for fibre-reinforced composites: Comparison between theories and experiments: Part B of WWFE-II'. *Journal of Composite Materials* (2013), vol. 47(6-7): pp. 925–966 (cit. on pp. 29, 50, 55).
86. SHI, Y., T. SWAIT, and C. SOUTIS: 'Modelling damage evolution in composite laminates subjected to low velocity impact'. *Composite Structures* (2012), vol. 94(9): pp. 2902–2913 (cit. on p. 29).
87. WANG, J., P. CALLUS, and M. BANNISTER: 'Experimental and numerical investigation of the tension and compression strength of un-notched and notched quasi-isotropic laminates'. *Composite Structures* (2004), vol. 64(3): pp. 297–306 (cit. on pp. 30, 47).
88. VAN PAEPEGEM, W., I. DE BAERE, and J. DEGRIECK: 'Modelling the nonlinear shear stress–strain response of glass fibre-reinforced composites. Part I: Experimental results'. *Composites Science and Technology* (2006), vol. 66(10): pp. 1455–1464 (cit. on pp. 30, 47).
89. LAFARIE-FRENOT, M. and F. TOUCHARD: 'Comparative in-plane shear behaviour of long-carbon-fibre composites with thermoset or thermoplastic matrix'. *Composites Science and Technology* (1994), vol. 52(3): pp. 417–425 (cit. on pp. 30, 47, 48, 68, 69).
90. VOGLER, T. and S. KYRIAKIDES: 'Inelastic behavior of an AS4/PEEK composite under combined transverse compression and shear. Part I: Experiments'. *International Journal of Plasticity* (1999), vol. 15(8): pp. 783–806 (cit. on pp. 30, 47, 48).

91. JOHNSON, W. S. and P. MANGALGIRI: 'Investigation of fiber bridging in double cantilever beam specimens'. *Journal of Composites, Technology and Research* (1987), vol. 9(1): pp. 10–13 (cit. on p. 30).
92. ANDERSONS, J. and M. KÖNIG: 'Dependence of fracture toughness of composite laminates on interface ply orientations and delamination growth direction'. *Composites Science and Technology* (2004), vol. 64(13-14): pp. 2139–2152 (cit. on pp. 30, 98).
93. JOUSSET, P. and M. RACHIK: 'Comparison and evaluation of two types of cohesive zone models for the finite element analysis of fracture propagation in industrial bonded structures'. *Engineering Fracture Mechanics* (2014), vol. 132: pp. 48–69 (cit. on pp. 30, 148).
94. PARDOEN, T., T. FERRACIN, C. LANDIS, and F. DELANNAY: 'Constraint effects in adhesive joint fracture'. *Journal of the Mechanics and Physics of Solids* (2005), vol. 53(9): pp. 1951–1983 (cit. on pp. 30, 143).
95. LLORCA, J., C. GONZÁLEZ, J. M. MOLINA-ALDAREGUÍA, J. SEGURADO, R. SELTZER, F. SKET, M. RODRÍGUEZ, S. SÁDABA, R. MUÑOZ, and L. P. CANAL: 'Multiscale modeling of composite materials: a roadmap towards virtual testing'. *Advanced Materials* (2011), vol. 23(44): pp. 5130–5147 (cit. on p. 31).
96. RÄDEL, M., C. WILLBERG, and D. KRAUSE: 'Peridynamic analysis of fibre-matrix debond and matrix failure mechanisms in composites under transverse tensile load by an energy-based damage criterion'. *Composites Part B: Engineering* (2019), vol. 158: pp. 18–27 (cit. on pp. 35, 42, 43).
97. QUINTANAS-COROMINAS, A., A. TURON, J. REINOSO, E. CASONI, M. PAGGI, and J. MAYUGO: 'A phase field approach enhanced with a cohesive zone model for modeling delamination induced by matrix cracking'. *Computer Methods in Applied Mechanics and Engineering* (2020), vol. 358: p. 112618 (cit. on p. 36).
98. OKEREKE, M. I.: 'Prediction of finite deformation of thermoplastic matrix composites'. PhD thesis. Oxford University, 2009 (cit. on p. 42).
99. DEUSCHLE, H. M.: '3D failure analysis of UD fibre reinforced composites: Puck's theory within FEA'. PhD thesis. 2010 (cit. on pp. 42, 44–47, 58, 59).
100. GAMSTEDT, E. and B. SJÖGREN: 'Micromechanisms in tension-compression fatigue of composite laminates containing transverse plies'. *Composites Science and Technology* (1999), vol. 59(2): pp. 167–178 (cit. on p. 43).
101. D'OTTAVIO, M.: 'Advanced Hierarchical Models of Multilayered Plates and Shells Including Mechanical and electrical Interfaces'. PhD thesis. Uni Stuttgart, 2007 (cit. on p. 43).
102. ALTENBACH, H., J. ALTENBACH, and W. KISSING: *Mechanics of composite structural elements*. 2nd Edition. Springer, 2018 (cit. on pp. 43, 44).
103. WASHIZU, K.: *Variational Methods in Elasticity and Plasticity*. Elsevier Science & Technology, 1982 (cit. on p. 43).

104. LOVE, A. E. H.: 'The small free vibrations and deformation of a thin elastic shell'. *Philosophical Transactions of the Royal Society of London.(A.)* (1888), vol. (179): pp. 491–546 (cit. on p. 44).
105. MINDLIN, R. D.: 'Influence of rotatory inertia and shear on flexural motions of isotropic, elastic plates'. *Journal of Applied Mechanics* (1951), vol. (cit. on p. 44).
106. REISSNER, E.: 'The effect of transverse shear deformation on the bending of elastic plates'. *Journal of Applied Mechanics* (1945), vol. (cit. on pp. 44, 46).
107. GHUGAL, Y. and R. SHIMPI: 'A review of refined shear deformation theories of isotropic and anisotropic laminated plates'. *Journal of Reinforced Plastics and Composites* (2002), vol. 21(9): pp. 775–813 (cit. on p. 44).
108. DASSAULT SYSTEMES SIMULIA CORP.: *Abaqus 2020 Analysis User's Manual*. 2020 (cit. on pp. 44, 45).
109. CARRERA, E.: 'CZ requirements—models for the two dimensional analysis of multi-layered structures'. *Composite Structures* (1997), vol. 37(3-4): pp. 373–383 (cit. on pp. 44, 45).
110. NOOR, A. K. and W. S. BURTON: 'Assessment of computational models for multi-layered composite shells'. *Applied Mechanics Reviews* (1990), vol. (cit. on p. 44).
111. REDDY, J. and D. ROBBINS JR: 'Theories and computational models for composite laminates'. *Applied Mechanics Reviews* (1994), vol. (cit. on p. 44).
112. CARRERA, E.: 'An assessment of mixed and classical theories on global and local response of multilayered orthotropic plates'. *Composite Structures* (2000), vol. 50(2): pp. 183–198 (cit. on p. 44).
113. LO, K., R. CHRISTENSEN, and E. WU: 'Stress solution determination for high order plate theory'. *International Journal of Solids and Structures* (1978), vol. 14(8): pp. 655–662 (cit. on p. 44).
114. WHITNEY, J.: 'The effect of transverse shear deformation on the bending of laminated plates'. *Journal of Composite Materials* (1969), vol. 3(3): pp. 534–547 (cit. on p. 44).
115. NASDALA, L.: *FEM-Formelsammlung Statik und Dynamik: Hintergrundinformationen, Tipps und Tricks*. Springer-Verlag, 2015 (cit. on pp. 44, 45).
116. PAGANO, N. J.: 'Exact solutions for rectangular bidirectional composites and sandwich plates'. *Journal of Composite Materials* (1970), vol. 4(1): pp. 20–34 (cit. on p. 45).
117. PUCK, A.: *Festigkeitsanalyse von Faser-Matrix-Laminaten—Modelle für die Praxis (Carl Hanser Verlag München Wien, 1996)*. (Cit. on p. 48).
118. SCHÜRMANN, H.: *Konstruieren mit Faser-Kunststoff-Verbunden*. Springer, 2005 (cit. on p. 48).
119. PETERSEN, E., R. CUNTZE, and C. HÜHNE: 'Experimental determination of material parameters in Cuntzes Failure-Mode-Concept-based UD strength failure conditions'. *Composites Science and Technology* (Oct. 2016), vol. 134: pp. 12–25 (cit. on pp. 49, 55, 64, 69, 76, 77, 105, 106).

120. SCHUECKER, C. and H. PETTERMANN: 'Fiber reinforced laminates: Progressive damage modeling based on failure mechanisms'. *Archives of Computational Methods in Engineering* (2008), vol. 15(2): pp. 163–184 (cit. on p. 49).
121. CHEN, J., E. MOROZOV, and K. SHANKAR: 'A combined elastoplastic damage model for progressive failure analysis of composite materials and structures'. *Composite Structures* (2012), vol. 94(12): pp. 3478–3489 (cit. on pp. 49–51, 54, 56, 57, 63, 64).
122. LIU, P. and J. ZHENG: 'Recent developments on damage modeling and finite element analysis for composite laminates: A review'. *Materials & Design* (2010), vol. 31(8): pp. 3825–3834 (cit. on pp. 49, 202).
123. MCCARTHY, C. T., M. A. MCCARTHY, and V. LAWLOR: 'Progressive damage analysis of multi-bolt composite joints with variable bolt-hole clearances'. *Composites Part B: Engineering* (2005), vol. 36(4): pp. 290–305 (cit. on p. 49).
124. CAMANHO, P. and F. MATTHEWS: 'A Progressive Damage Model for Mechanically Fastened Joints in Composite Laminates'. *Journal of Composite Materials* (1999), vol. 33(24): pp. 2248–2280 (cit. on p. 49).
125. TSERPES, K., G. LABEAS, P. PAPANIKOS, and T. KERMANIDIS: 'Strength prediction of bolted joints in graphite/epoxy composite laminates'. *Composites Part B: Engineering* (2002), vol. 7(33): pp. 521–529 (cit. on p. 49).
126. HASHIN, Z.: 'Failure criteria for unidirectional fiber composites'. *Journal of Applied Mechanics* (1980), vol. 47(2): pp. 329–334 (cit. on pp. 50, 55).
127. HÜHNE, C., A.-K. ZERBST, G. KUHLMANN, C. STEENBOCK, and R. ROLFES: 'Progressive damage analysis of composite bolted joints with liquid shim layers using constant and continuous degradation models'. *Composite Structures* (2010), vol. 92(2): pp. 189–200 (cit. on p. 50).
128. TAN, S. C.: 'A progressive failure model for composite laminates containing openings'. *Journal of Composite Materials* (1991), vol. 25(5): pp. 556–577 (cit. on pp. 50, 56).
129. MAIMÍ, P., P. P. CAMANHO, J. MAYUGO, and C. DÁVILA: 'A continuum damage model for composite laminates: Part I - Constitutive model'. *Mechanics of Materials* (2007), vol. 39(10): pp. 897–908 (cit. on pp. 50, 56).
130. PUCK, A. and H. SCHÜRMANN: 'Failure analysis of FRP laminates by means of physically based phenomenological models'. *Composites Science and Technology* (2002), vol. 62(12-13): pp. 1633–1662 (cit. on pp. 50, 58, 77).
131. TSAI, S. W. and E. M. WU: 'A general theory of strength for anisotropic materials'. *Journal of Composite Materials* (1971), vol. 5(1): pp. 58–80 (cit. on p. 50).
132. DAVILA, C. G., P. P. CAMANHO, and C. A. ROSE: 'Failure criteria for FRP laminates'. *Journal of Composite materials* (2005), vol. 39(4): pp. 323–345 (cit. on pp. 50, 75).
133. LÜDERS, C., D. KRAUSE, and J. KREIKEMEIER: 'Fatigue damage model for fibre-reinforced polymers at different temperatures considering stress ratio effects'. *Journal of Composite Materials* (2018), vol. 52(29): pp. 4023–4050 (cit. on p. 50).

134. DONADON, M., L. IANNUCCI, B. G. FALZON, J. HODGKINSON, and S. F. de ALMEIDA: 'A progressive failure model for composite laminates subjected to low velocity impact damage'. *Computers & Structures* (2008), vol. 86(11-12): pp. 1232–1252 (cit. on p. 50).
135. ERNST, G., M. VOGLER, C. HÜHNE, and R. ROLFES: 'Multiscale progressive failure analysis of textile composites'. *Composites Science and Technology* (2010), vol. 70(1): pp. 61–72 (cit. on p. 50).
136. VOGLER, M., R. ROLFES, and P. CAMANHO: 'Modeling the inelastic deformation and fracture of polymer composites—Part I: plasticity model'. *Mechanics of Materials* (2013), vol. 59: pp. 50–64 (cit. on p. 50).
137. SUN, C. and J. CHEN: 'A simple flow rule for characterizing nonlinear behavior of fiber composites'. *Journal of Composite Materials* (1989), vol. 23(10): pp. 1009–1020 (cit. on pp. 50, 53, 54, 60, 62, 69–71).
138. DIN, I. U., P. HAO, G. FRANZ, and S. PANIER: 'Elastoplastic CDM model based on Puck's theory for the prediction of mechanical behavior of Fiber Reinforced Polymer (FRP) composites'. *Composite Structures* (2018), vol. 201: pp. 291–302 (cit. on pp. 50, 51, 54, 56, 60, 62, 91).
139. KACHANOV, L.: *Introduction to continuum damage mechanics*. Vol. 10. Springer Science & Business Media, 2013 (cit. on pp. 51, 52).
140. MATZENMILLER, A., J. LUBLINER, and R. TAYLOR: 'A constitutive model for anisotropic damage in fiber-composites'. *Mechanics of Materials* (1995), vol. 20(2): pp. 125–152 (cit. on p. 52).
141. WEEKS, C. and C. SUN: 'Modeling non-linear rate-dependent behavior in fiber-reinforced composites'. *Composites Science and Technology* (1998), vol. 58(3-4): pp. 603–611 (cit. on pp. 53, 54).
142. SOUZA NETO, E. de, D. PERIC, and D. OWEN: *Computational Methods for Plasticity: Theory and Applications*. John Wiley & Sons, 2009 (cit. on pp. 54, 59, 60).
143. SUN, C. and K. YOON: 'Characterization of elastic-plastic behavior of AS4/PEEK thermoplastic composite for temperature variation'. *Journal of Composite Materials* (1991), vol. 25(10): pp. 1297–1313 (cit. on pp. 54, 64).
144. DEUSCHLE, H. M. and A. PUCK: 'Application of the Puck failure theory for fibre-reinforced composites under three-dimensional stress: Comparison with experimental results'. *Journal of Composite Materials* (2013), vol. 47(6-7): pp. 827–846 (cit. on p. 55).
145. CUNTZE, R.: 'Efficient 3D and 2D failure conditions for UD laminae and their application within the verification of the laminate design'. *Composites Science and Technology* (2006), vol. 66(7-8): pp. 1081–1096 (cit. on pp. 55, 91).
146. CUNTZE, R. and A. FREUND: 'The predictive capability of failure mode concept-based strength criteria for multidirectional laminates'. *Composite Science and Technology* (2004), vol.: pp. 429–489 (cit. on p. 55).

147. ROHWER, K.: 'Predicting fiber composite damage and failure'. *Journal of Composite Materials* (2015), vol. 49(21): pp. 2673–2683 (cit. on p. 56).
148. JIRÁSEK, M.: 'Nonlocal damage mechanics'. *Revue européenne de génie civil* (2007), vol. 11(7-8): pp. 993–1021 (cit. on p. 57).
149. JIRÁSEK, M.: 'Mathematical analysis of strain localization'. *Revue européenne de génie civil* (2007), vol. 11(7-8): pp. 977–991 (cit. on p. 57).
150. BAŽANT, Z. P. and B. H. OH: 'Crack band theory for fracture of concrete'. *Matériaux et construction* (1983), vol. 16(3): pp. 155–177 (cit. on pp. 57, 63, 82, 84).
151. 'Guideline VDI 2014 Part 3: Development of Fibre Reinforced Plastics Components, Analysis'. *Aircraft Engineering and Aerospace Technology* (2007), vol. 79(1) (cit. on p. 58).
152. MEIER, F., C. SCHWARZ, and E. WERNER: 'Numerical calculation of the tangent stiffness matrix in materials modeling'. *PAMM* (2014), vol. 14(1): pp. 425–426 (cit. on p. 62).
153. DUVAUT, G. and J. L. LIONS: *Inequalities in mechanics and physics*. Springer, 1976 (cit. on p. 62).
154. MAIMÍ, P., P. P. CAMANHO, J. MAYUGO, and C. DÁVILA: 'A continuum damage model for composite laminates: Part II - Computational implementation and validation'. *Mechanics of Materials* (2007), vol. 39(10): pp. 909–919 (cit. on p. 63).
155. KAWAI, M., Y. MASUKO, Y. KAWASE, and R. NEGISHI: 'Micromechanical analysis of the off-axis rate-dependent inelastic behavior of unidirectional AS4/PEEK at high temperature'. *International Journal of Mechanical Sciences* (2001), vol. 43(9): pp. 2069–2090 (cit. on p. 64).
156. SUN, C. and Y. RUI: 'Orthotropic elasto-plastic behavior of AS4/PEEK thermoplastic composite in compression'. *Mechanics of Materials* (1990), vol. 10(1-2): pp. 117–125 (cit. on p. 64).
157. CARLILE, D. R., D. C. LEACH, D. R. MOORE, and N. ZAHLAN: 'Mechanical properties of the carbon fiber/PEEK composite APC-2/AS-4 for structural applications'. *Advances in thermoplastic matrix composite materials*. ASTM International, 1989 (cit. on p. 64).
158. OMAIREY, S. L., P. D. DUNNING, and S. SRIRAMULA: 'Development of an ABAQUS plugin tool for periodic RVE homogenisation'. *Engineering with Computers* (2018), vol.: pp. 1–11 (cit. on p. 64).
159. MOLL, J.: 'Erarbeitung einer Modellierungsstrategie für die progressive Schädigungsanalyse von Open Hole Tension Prüfkörpern aus faserverstärktem Kunststoff unter Berücksichtigung intralaminarer Plastizität'. unpublished. Diplomarbeit. TU Dresden, 2021 (cit. on pp. 69, 70, 76, 77).
160. WINN, V. M. and S. SRIDHARAN: 'An investigation into the accuracy of a one-parameter nonlinear model for unidirectional composites'. *Journal of Composite Materials* (2001), vol. 35(16): pp. 1491–1507 (cit. on pp. 69, 73).

161. SUN, C. and S. BERRETH: 'A new end tab design for off-axis tension test of composite materials'. *Journal of Composite Materials* (1988), vol. 22(8): pp. 766–779 (cit. on p. 70).
162. XIAO, Y., M. KAWAI, and H. HATTA: 'An integrated method for off-axis tension and compression testing of unidirectional composites'. *Journal of Composite Materials* (2011), vol. 45(6): pp. 657–669 (cit. on p. 70).
163. SUN, C. and I. CHUNG: 'An oblique end-tab design for testing off-axis composite specimens'. *Composites* (1993), vol. 24(8): pp. 619–623 (cit. on p. 70).
164. PARVIZI, A., K. GARRETT, and J. BAILEY: 'Constrained cracking in glass fibre-reinforced epoxy cross-ply laminates'. *Journal of Materials Science* (1978), vol. 13(1): pp. 195–201 (cit. on pp. 75, 265).
165. CAMANHO, P. P., C. G. DÁVILA, S. T. PINHO, L. IANNUCCI, and P. ROBINSON: 'Prediction of in situ strengths and matrix cracking in composites under transverse tension and in-plane shear'. *Composites Part A: Applied Science and Manufacturing* (2006), vol. 37(2): pp. 165–176 (cit. on pp. 75, 265).
166. CHANG, F.-K. and M.-H. CHEN: 'The in situ ply shear strength distributions in graphite/epoxy laminated composites'. *Journal of Composite Materials* (1987), vol. 21(8): pp. 708–733 (cit. on p. 75).
167. FLAGGS, D. L. and M. H. KURAL: 'Experimental determination of the in situ transverse lamina strength in graphite/epoxy laminates'. *Journal of Composite Materials* (1982), vol. 16(2): pp. 103–116 (cit. on p. 75).
168. PINHO, S. T., C. G. DÁVILA, P. P. CAMANHO, L. IANNUCCI, and P. ROBINSON: *Failure Models and Criteria for FRP Under-In-Plane or Three-Dimensional Stress States Including Shear Non-Linearity*. Tech. rep. TM-2005-213530. NASA, 2005 (cit. on p. 75).
169. PINHO, S., R. DARVIZEH, P. ROBINSON, C. SCHUECKER, and P. CAMANHO: 'Material and structural response of polymer-matrix fibre-reinforced composites'. *Journal of Composite Materials* (2012), vol. 46(19-20): pp. 2313–2341 (cit. on p. 75).
170. PINHO, S., G. VYAS, and P. ROBINSON: 'Response and damage propagation of polymer-matrix fibre-reinforced composites: Predictions for WWFE-III Part A'. *Journal of Composite Materials* (2013), vol. 47(20-21): pp. 2595–2612 (cit. on p. 75).
171. DVORAK, G. J. and N. LAWS: 'Analysis of progressive matrix cracking in composite laminates II. First ply failure'. *Journal of Composite Materials* (1987), vol. 21(4): pp. 309–329 (cit. on pp. 75, 265).
172. HAHN, H. T. and S. W. TSAI: 'Nonlinear elastic behavior of unidirectional composite laminae'. *Journal of Composite Materials* (1973), vol. 7(1): pp. 102–118 (cit. on p. 75).
173. CAMANHO, P. P. and M. LAMBERT: 'A design methodology for mechanically fastened joints in laminated composite materials'. *Composites Science and Technology* (2006), vol. 66(15): pp. 3004–3020 (cit. on pp. 75, 270).

174. PUCK, A., J. KOPP, and M. KNOPS: 'Guidelines for the determination of the parameters in Puck's action plane strength criterion'. *Composites Science and Technology* (2002), vol. 62(3): pp. 371–378 (cit. on p. 77).
175. FURTADO, C., A. ARTEIRO, P. LINDE, B. WARDLE, and P. CAMANHO: 'Is there a ply thickness effect on the mode I intralaminar fracture toughness of composite laminates?' *Theoretical and Applied Fracture Mechanics* (2020), vol. 107: p. 102473 (cit. on pp. 78, 79, 131).
176. CZABAJ, M. W. and J. G. RATCLIFFE: 'Comparison of intralaminar and interlaminar mode I fracture toughnesses of a unidirectional IM7/8552 carbon/epoxy composite'. *Composites Science and Technology* (2013), vol. 89: pp. 15–23 (cit. on p. 79).
177. *AITM 1-0007: Determination of plain, open hole and filled hole tensile strength*. AITM, 2016 (cit. on p. 81).
178. COELHO, A. M. G., J. T. MOTTRAM, and K. A. HARRIES: 'Finite element guidelines for simulation of fibre-tension dominated failures in composite materials validated by case studies'. *Composite Structures* (2015), vol. 126: pp. 299–313 (cit. on p. 82).
179. BARBERO, E. J. and M. SHAHBAZI: 'Determination of material properties for ANSYS progressive damage analysis of laminated composites'. *Composite Structures* (2017), vol. 176: pp. 768–779 (cit. on p. 84).
180. OLIVER, J.: 'A consistent characteristic length for smeared cracking models'. *International Journal for Numerical Methods in Engineering* (1989), vol. 28(2): pp. 461–474 (cit. on p. 84).
181. WIEGAND, J., N. PETRINIC, and B. ELLIOTT: 'An algorithm for determination of the fracture angle for the three-dimensional Puck matrix failure criterion for UD composites'. *Composites Science and Technology* (2008), vol. 68(12): pp. 2511–2517 (cit. on p. 90).
182. SCHIRMAIER, F., J. WEILAND, L. KÄRGER, and F. HENNING: 'A new efficient and reliable algorithm to determine the fracture angle for Puck's 3D matrix failure criterion for UD composites'. *Composites Science and Technology* (2014), vol. 100: pp. 19–25 (cit. on p. 90).
183. WISNOM, M.: 'The role of delamination in failure of fibre-reinforced composites'. *Philosophical Transactions of the Royal Society A: Mathematical, Physical and Engineering Sciences* (2012), vol. 370(1965): pp. 1850–1870 (cit. on pp. 95, 131).
184. GRIFFITH, A. A.: 'The phenomena of rupture and flow in solids'. *Philosophical Transactions of the Royal Society of London* (1920), vol. A 221(-): pp. 163–198 (cit. on p. 96).
185. ASTM: *Standard Test Method for Mode I Interlaminar Fracture Toughness of Unidirectional Fiber-Reinforced Polymer Matrix Composites*. 2001 (cit. on p. 96).
186. PEREIRA, A. and A. B. MORAIS: 'Mode I interlaminar fracture of carbon/epoxy multidirectional laminates'. *Composites Science and Technology* (2004), vol. 64(-): pp. 2267–2270 (cit. on pp. 96, 98).

187. ASTM: *Test Method for Determination of the Mode II Interlaminar Fracture Toughness of Unidirectional Fiber-Reinforced Polymer Matrix Composites*. West Conshohocken, PA, 2014 (cit. on p. 96).
188. WANG, W.-X., M. NAKATA, Y. TAKAO, and T. MATSUBARA: 'Experimental investigation on test methods for mode II interlaminar fracture testing of carbon fiber reinforced composites'. *Composites Part A: Applied Science and Manufacturing* (2009), vol. 40(9): pp. 1447–1455 (cit. on p. 97).
189. SCHUECKER, C. and B. D. DAVIDSON: 'Evaluation of the accuracy of the four-point bend end-notched flexure test for mode II delamination toughness determination'. *Composites Science and Technology* (2000), vol. 60(11): pp. 2137–2146 (cit. on p. 97).
190. BENZEGGAGH, M. L. and M. KENANE: 'Measurement of mixed-mode delamination fracture toughness of unidirectional glass/epoxy composites with mixed-mode bending apparatus'. *Composites Science and Technology* (1996), vol. 56(4): pp. 439–449 (cit. on pp. 97, 103).
191. CREWS, J. H. and J. R. REEDER: *A mixed-mode bending apparatus for delamination testing*. National Aeronautics and Space Administration, Langley Research Center, 1988 (cit. on p. 97).
192. JOHNSON, W. S. and P. D. MANGALGIRI: *Investigation of Fiber Bridging in Double Cantilever Beam Specimens: National Aeronautics and Space Administration Hampton VA Langley Research Center*. 1986 (cit. on p. 97).
193. SUO, Z., G. BAO, and B. FAN: 'Delamination R-curve phenomena due to damage'. *Journal of the Mechanics and Physics of Solids* (1992), vol. 40(1): pp. 1–16 (cit. on p. 97).
194. PEREIRA, A. B., A. B. D. MORAIS, M. D. MOURA, and A. G. MAGALHÃES: 'Mode I interlaminar fracture of woven glass/epoxy multidirectional laminates'. *Composites Part A: Applied Science and Manufacturing* (2005), vol. 36(8): pp. 1119–1127 (cit. on p. 98).
195. PEREIRA, A. B., A. B. D. MORAIS, A. T. MARQUES, and P. T. D. CASTRO: 'Mode II interlaminar fracture of carbon/epoxy multidirectional laminates'. *Composites Science and Technology* (2004), vol. 64(10-11): pp. 1653–1659 (cit. on pp. 98, 99).
196. BIENIAŚ, J., K. DADEJ, and B. SUROWSKA: 'Interlaminar fracture toughness of glass and carbon reinforced multidirectional fiber metal laminates'. *Engineering Fracture Mechanics* (2017), vol. 175: pp. 127–145 (cit. on p. 98).
197. ANDERSONS, J. and M. KÖNIG: 'Dependence of fracture toughness of composite laminates on interface ply orientations and delamination growth direction'. *Composites Science and Technology* (2004), vol. 64(13-14): pp. 2139–2152 (cit. on pp. 98, 99).
198. BLONDEAU, C., G. PAPPAS, and J. BOTSIS: 'Influence of ply-angle on fracture in antisymmetric interfaces of CFRP laminates'. *Composite Structures* (2019), vol. 216: pp. 464–476 (cit. on p. 98).

199. GONG, Y., X. CHEN, W. LI, L. ZHAO, J. TAO, J. ZHANG, and N. HU: 'Delamination in carbon fiber epoxy DCB laminates with different stacking sequences: R-curve behavior and bridging traction-separation relation'. *Composite Structures* (2021), vol. 262: p. 113605 (cit. on p. 98).
200. GREENHALGH, E. S.: *Failure analysis and fractography of polymer composites*. Woodhead Publishing in materials. Cambridge: Woodhead Pub., 2009 (cit. on p. 98).
201. MORAIS, A. B. D. and A. B. PEREIRA: 'Mixed mode I+II interlaminar fracture of glass/epoxy multidirectional laminates – Part 1: Analysis'. *Composites Science and Technology* (2006), vol. 66(13): pp. 1889–1895 (cit. on pp. 99, 108).
202. PEREIRA, A. B. and A. B. D. MORAIS: 'Mixed mode I+II interlaminar fracture of glass/epoxy multidirectional laminates – Part 2: Experiments'. *Composites Science and Technology* (2006), vol. 66(13): pp. 1896–1902 (cit. on pp. 99, 108).
203. BENNATI, S., M. COLLELUORI, D. CORIGLIANO, and P. S. VALVO: 'An enhanced beam-theory model of the asymmetric double cantilever beam (ADCB) test for composite laminates'. *Composites Science and Technology* (2009), vol. 69(11-12): pp. 1735–1745 (cit. on p. 99).
204. BENNATI, S., P. FISICARO, and P. S. VALVO: 'An enhanced beam-theory model of the mixed-mode bending (MMB) test—Part II: Applications and results'. *Meccanica* (2013), vol. 48(2): pp. 465–484 (cit. on p. 99).
205. DAVIDSON, B., R. KRÜGER, M. KÖNIG, and B. D. DAVIDSON: 'Effect of Stacking Sequence on Energy Release Rate Distribution in Multidirectional DCB and ENF Specimens - Effect of stacking sequence on energy release rate distributions in multidirectional dcb and enf specimens'. *Engineering Fracture Mechanics* (1996), vol. 55(4): pp. 557–569 (cit. on p. 99).
206. PROMBUT, P., L. MICHEL, F. LACHAUD, and J. BARRAU: 'Delamination of multidirectional composite laminates at 0/Theta ply interfaces'. *Engineering Fracture Mechanics* (2006), vol. 73(-): pp. 2427–2442 (cit. on pp. 99, 108, 109).
207. TAO, J., C. SUN, J. TAO, and C. T. SUN: 'Influence of Ply Orientation on Delamination in Composite Laminates'. *Journal of Composite Materials* (1998 // 2016), vol. 32(21): pp. 1933–1948 (cit. on pp. 99, 109).
208. CHOI, N., A. KINLOCH, and J. WILLIAMS: 'Delamination of Multidirectional Carbon-Fiber / Epoxy Composites under Mode I, Mode II and Mixed-Mode I-II Loading'. *Journal of Composite Materials* (1999), vol. (-): pp. 73–101 (cit. on pp. 99, 109).
209. DE MORAIS, A. and M. F. DE MOURA: 'Evaluation of initiation criteria used in interlaminar fracture tests'. *Engineering Fracture Mechanics* (2006), vol. 73(16): pp. 2264–2276 (cit. on p. 99).
210. CAMANHO, P. P., C. G. DAVILA, and M. DE MOURA: 'Numerical simulation of mixed-mode progressive delamination in composite materials'. *Journal of Composite Materials* (2003), vol. 37(16): pp. 1415–1438 (cit. on pp. 100, 102, 103).

211. HEIDARI-RARANI, M. and M. SAYEDAIN: 'Finite element modeling strategies for 2D and 3D delamination propagation in composite DCB specimens using VCCT, CZM and XFEM approaches'. *Theoretical and Applied Fracture Mechanics* (2019), vol. 103: p. 102246 (cit. on p. 100).
212. DÁVILA, C. G., C. A. ROSE, and P. P. CAMANHO: 'A procedure for superposing linear cohesive laws to represent multiple damage mechanisms in the fracture of composites'. *International Journal of Fracture* (2009), vol. 158(2): pp. 211–223 (cit. on pp. 100, 103, 104).
213. TURON, A., C. G. DAVILA, P. P. CAMANHO, and J. COSTA: 'An engineering solution for mesh size effects in the simulation of delamination using cohesive zone models'. *Engineering Fracture Mechanics* (2007), vol. 74(10): pp. 1665–1682 (cit. on pp. 100–102).
214. LU, X., M. RIDHA, B. CHEN, V. TAN, and T. TAY: 'On cohesive element parameters and delamination modelling'. *Engineering Fracture Mechanics* (2019), vol. 206: pp. 278–296 (cit. on p. 100).
215. HARPER, P. W. and S. R. HALLETT: 'Cohesive zone length in numerical simulations of composite delamination'. *Engineering Fracture Mechanics* (2008), vol. 75(16): pp. 4774–4792 (cit. on pp. 101, 102, 107, 115).
216. HILLERBORG, A., M. MODÉER, and P.-E. PETERSSON: 'Analysis of crack formation and crack growth in concrete by means of fracture mechanics and finite elements'. *Cement and Concrete Research* (1976), vol. 6(6): pp. 773–781 (cit. on p. 101).
217. YANG, Q. and B. COX: 'Cohesive models for damage evolution in laminated composites'. *International Journal of Fracture* (2005), vol. 133(2): pp. 107–137 (cit. on p. 101).
218. PETERSEN, E., E. KAPPEL, J. KOORD, O. VÖLKERINK, and C. HÜHNE: 'Determination of stresses, strains and failure types in multidirectional laminates under pure bending'. *Journal of Composite Materials* (2020), vol.: p. 0021998320932301 (cit. on p. 102).
219. CUI, W., M. WISNOM, and M. JONES: 'A comparison of failure criteria to predict delamination of unidirectional glass/epoxy specimens waisted through the thickness'. *Composites* (1992), vol. 23(3): pp. 158–166 (cit. on p. 102).
220. CAMANHO, P. P. and C. G. DÁVILA: *Mixed-mode decohesion finite elements for the simulation of delamination in composite materials*. Tech. rep. TM-2002-211737. NASA, 2002 (cit. on p. 102).
221. DE MOURA, M. and J. GONÇALVES: 'Cohesive zone model for high-cycle fatigue of adhesively bonded joints under mode I loading'. *International Journal of Solids and Structures* (2014), vol. 51(5): pp. 1123–1131 (cit. on p. 102).
222. WU, E. M. and R. REUTER JR: *Crack extension in fiberglass reinforced plastics*. Tech. rep. Illinois University at Urbana Department of Theoretical and Applied Mechanics, 1965 (cit. on p. 103).

223. GUTKIN, R., M. LAFFAN, S. PINHO, P. ROBINSON, and P. CURTIS: 'Modelling the R-curve effect and its specimen-dependence'. *International Journal of Solids and Structures* (2011), vol. 48(11-12): pp. 1767–1777 (cit. on pp. 104, 270).
224. AIROLDI, A. and C. G. DÁVILA: 'Identification of material parameters for modelling delamination in the presence of fibre bridging'. *Composite Structures* (2012), vol. 94(11): pp. 3240–3249 (cit. on p. 104).
225. DAVILA, C. G., F. A. LEONE, K. SONG, J. G. RATCLIFFE, and C. A. ROSE: 'Material Characterization for the Analysis of Skin/Stiffener Separation'. *32nd American Society for Composites (ASC) Technical Conference*. 2017 (cit. on p. 104).
226. RANZ, D., J. CUARTERO, L. CASTEJÓN, R. MIRALBES, and D. VALLADARES: 'Enhanced cohesive zone model to predict delamination behavior of carbon/epoxy laminated curved beams'. *Mechanics of Advanced Materials and Structures* (2020), vol.: pp. 1–11 (cit. on p. 104).
227. MORAIS, A. D.: 'Beam analysis of the double cantilever beam specimen with fibre bridging'. *Journal of Composite Materials* (2015), vol. 49(14): pp. 1681–1688 (cit. on p. 104).
228. ZHAO, L., Y. GONG, J. ZHANG, Y. CHEN, and B. FEI: 'Simulation of delamination growth in multidirectional laminates under mode I and mixed mode I/II loadings using cohesive elements'. *Composite Structures* (2014), vol. 116: pp. 509–522 (cit. on p. 104).
229. URCELAY OCA, I.: 'Experimental determination of fracture toughness for delamination analysis in structural components'. MA thesis. TU Delft, 2020 (cit. on pp. 104, 119).
230. RAIMONDO, A., I. URCELAY OCA, and C. BISAGNI: 'Influence of interface ply orientation on delamination growth in composite laminates'. *Journal of Composite Materials* (2021), vol.: p. 00219983211031636 (cit. on p. 104).
231. DARICIK, F.: 'Mesh size sensitivity analysis for interlaminar fracture of the fiber-reinforced laminated composites'. *Journal of Engineered Fibers and Fabrics* (2019), vol. 14: p. 1558925019883460 (cit. on p. 105).
232. SEBAEY, T., N. BLANCO, C. LOPES, and J. COSTA: 'Numerical investigation to prevent crack jumping in Double Cantilever Beam tests of multidirectional composite laminates'. *Composites Science and Technology* (2011), vol. 71(13): pp. 1587–1592 (cit. on p. 106).
233. MORAIS, A. de and A. PEREIRA: 'Interlaminar fracture of multidirectional glass/epoxy laminates under mixed-mode I+ II loading'. *Mechanics of Composite Materials* (2007), vol. 43(3): pp. 233–244 (cit. on p. 108).
234. ROBINSON, P. and D. SONG: 'A Modified DCB Specimen for Mode I Testing of Multidirectional Laminates'. *Journal of Composite Materials* (1992), vol. 26(11): pp. 1554–1578 (cit. on p. 109).

235. PETERSEN, E.: ‘Auslegung des Metalllagenauslaufs bei lokaler Stahlhybridisierung von Kohlenstofffaser-Kunststoff-Laminaten’. PhD thesis. Technische Universität Braunschweig, 2019 (cit. on pp. 117, 124, 129).
236. GARULLI, T., A. CATAPANO, D. FANTERIA, J. JUMEL, and E. MARTIN: ‘Design and finite element assessment of fully uncoupled multi-directional layups for delamination tests’. *Journal of Composite Materials* (2020), vol. 54(6): pp. 773–790 (cit. on p. 125).
237. RODRÍGUEZ, R. Q., W. P. de PAIVA, P. SOLLERO, M. R. B. RODRIGUES, and É. L. de ALBUQUERQUE: ‘Failure criteria for adhesively bonded joints’. *International Journal of Adhesion and Adhesives* (2012), vol. 37: pp. 26–36 (cit. on p. 142).
238. JIA, Z. M., G. Q. YUAN, and D. HUI: ‘Research Progress on Finite Element Analysis Methods for Bonded Joints at Different Strain Rates’. *Advanced Materials Research* (2014), vol. 1049: pp. 892–900 (cit. on p. 142).
239. ÖZER, H. and Ö. ÖZ: ‘The use of the exponential Drucker-Prager material model for defining the failure loads of the mono and bi-adhesive joints’. *International Journal of Adhesion and Adhesives* (2017), vol. (cit. on pp. 142, 147, 148).
240. TOMBLIN, J., K. STROLE, G. DODOSH, and L. ILCEWICZ: *Assessment of industry practices for aircraft bonded joints and structures*. Tech. rep. DOT/FAA/AR-05/13. Washington: Federal Aviation Administration, 2005 (cit. on p. 142).
241. PASCOE, J., R. ALDERLIESTEN, and R. BENEDICTUS: ‘Methods for the prediction of fatigue delamination growth in composites and adhesive bonds—a critical review’. *Engineering Fracture Mechanics* (2013), vol. 112: pp. 72–96 (cit. on p. 142).
242. BLACKMAN, B.: ‘The use of a cohesive zone model to study the fracture of fibre composites and adhesively-bonded joints’. *International Journal of Fracture* (2003), vol. 119(1): pp. 25–46 (cit. on p. 142).
243. CAMPILHO, R., M. BANEJA, J. NETO, and L. da SILVA: ‘Modelling adhesive joints with cohesive zone models: effect of the cohesive law shape of the adhesive layer’. *International Journal of Adhesion and Adhesives* (July 2013), vol. 44: pp. 48–56 (cit. on pp. 142, 143).
244. NETO, J., R. D. CAMPILHO, and L. DA SILVA: ‘Parametric study of adhesive joints with composites’. *International Journal of Adhesion and Adhesives* (2012), vol. 37: pp. 96–101 (cit. on p. 143).
245. LILJEDAHL, C., A. CROCOMBE, M. WAHAB, and I. ASHCROFT: ‘Damage modelling of adhesively bonded joints’. *International Journal of Fracture* (2006), vol. 141(1-2): pp. 147–161 (cit. on p. 144).
246. MARTINY, P., F. LANI, A. KINLOCH, and T. PARDOEN: ‘Numerical analysis of the energy contributions in peel tests: A steady-state multilevel finite element approach’. *International Journal of Adhesion and Adhesives* (2008), vol. 28(4-5): pp. 222–236 (cit. on p. 144).

247. PIRONDI, A.: 'Failure prediction of T-peel adhesive joints by different cohesive laws and modelling approaches'. *Frattura ed Integrità Strutturale* (2009), vol. 3(10): pp. 21–28 (cit. on pp. 144, 145).
248. MARTINY, P.: 'The failure of metal-to-metal adhesive joints: numerical modelling, energy contributions and constraint effects'. PhD thesis. UCL-Université Catholique de Louvain, 2012 (cit. on p. 144).
249. SILVA, L. F. M. da and R. D. S. G. CAMPILHO: *Advances in Numerical Modeling of Adhesive Joints*. Springer Berlin Heidelberg, Oct. 15, 2011. 151 pp. (cit. on pp. 145, 207).
250. BELYTSCHKO, T. and T. BLACK: 'Elastic crack growth in finite elements with minimal remeshing'. *International Journal for Numerical Methods in Engineering* (1999), vol. 45(5): pp. 601–620 (cit. on p. 145).
251. BELYTSCHKO, T., N. MOËS, S. USUI, and C. PARIMI: 'Arbitrary discontinuities in finite elements'. *International Journal for Numerical Methods in Engineering* (2001), vol. 50(4): pp. 993–1013 (cit. on p. 146).
252. CAMPILHO, R. D., M. D. BANEÁ, A. M. PINTO, L. F. da SILVA, and A. DE JESUS: 'Strength prediction of single-and double-lap joints by standard and extended finite element modelling'. *International Journal of Adhesion and Adhesives* (2011), vol. 31(5): pp. 363–372 (cit. on p. 146).
253. MUBASHAR, A., I. ASHCROFT, and A. CROCOMBE: 'Modelling damage and failure in adhesive joints using a combined XFEM-cohesive element methodology'. *The Journal of Adhesion* (2014), vol. 90(8): pp. 682–697 (cit. on p. 146).
254. XARÁ, J. and R. CAMPILHO: 'Strength estimation of hybrid single-L bonded joints by the eXtended Finite Element Method'. *Composite Structures* (2018), vol. 183: pp. 397–406 (cit. on pp. 146, 147).
255. ROCHA, R. and R. CAMPILHO: 'Evaluation of different modelling conditions in the cohesive zone analysis of single-lap bonded joints'. *The Journal of Adhesion* (2018), vol. 94(7): pp. 562–582 (cit. on p. 147).
256. DEAN, G., B. E. READ, and B. DUNCAN: *An evaluation of yield criteria for adhesives for finite element analysis*. NPL Report CMMT(A)117. Queens Road, Teddington, Middlesex TW11 0LW: Centre for Materials Measurement & Technology - National Physical Laboratory, 1999 (cit. on pp. 147, 148).
257. MISES, R. v.: 'Mechanik der festen Körper im plastisch-deformablen Zustand'. *Nachrichten von der Gesellschaft der Wissenschaften zu Göttingen, Mathematisch-Physikalische Klasse* (1913), vol. 1913: pp. 582–592 (cit. on p. 147).
258. DRUCKER, D. C. and W. PRAGER: 'Soil mechanics and plastic analysis or limit design'. *Quarterly of Applied Mathematics* (1952), vol. 10(2): pp. 157–165 (cit. on p. 148).

259. DEAN, G., L. CROCKER, B. READ, and L. WRIGHT: 'Prediction of deformation and failure of rubber-toughened adhesive joints'. *International Journal of Adhesion and Adhesives* (2004), vol. 24(4): pp. 295–306 (cit. on p. 148).
260. GARCÍA, J., A. CHIMINELLI, B. GARCÍA, M. LIZARANZU, and M. JIMÉNEZ: 'Characterization and material model definition of toughened adhesives for finite element analysis'. *International Journal of Adhesion and Adhesives* (2011), vol. 31(4): pp. 182–192 (cit. on p. 148).
261. JEANDRAU, J.-P., C. PEYRAC, F. LEFEBVRE, J. RENARD, V. GANTCHENKO, B. PATAMAPROHM, and C. GUINAULT: 'Fatigue behaviour of adhesive joints'. *Procedia Engineering* (2015), vol. 133: pp. 508–517 (cit. on p. 148).
262. QUAN, H. and R. ALDERLIESTEN: 'On the effect of plastic model on simulation of adhesive bonded joints with FM94'. *International Journal of Adhesion and Adhesives* (2021), vol.: p. 102916 (cit. on p. 148).
263. MAHNKEN, R. and M. SCHLIMMER: 'Simulation of strength difference in elastoplasticity for adhesive materials'. *International Journal for Numerical Methods in Engineering* (2005), vol. 63(10): pp. 1461–1477 (cit. on pp. 148, 149).
264. JOUSSET, P. and M. RACHIK: 'Elasto-Plastic Constitutive Model for Finite Element Simulation of structural Adhesives'. *SIMULIA Customer Conference* (2009), vol. (cit. on pp. 148, 149, 180).
265. BURBULLA, F.: 'Kontinuumsmechanische und bruchmechanische Modelle für Werkstoffverbunde'. PhD thesis. Universität Kassel, 2015 (cit. on p. 149).
266. ALFONSO, L., C. BADULESCU, and N. CARRERE: 'Use of the modified Arcan fixture to study the strength of bonded assemblies for automotive applications'. *International Journal of Adhesion and Adhesives* (2018), vol. 80: pp. 104–114 (cit. on p. 149).
267. SCHOLLERER, M. J., J. KOSMANN, T. LÖBEL, D. HOLZHÜTER, and C. HÜHNE: 'A new joining-device for manufacturing tubular butt joints with higher curing temperatures of film adhesives'. *Applied Adhesion Science* (Sept. 2017), vol. 5(1): p. 15 (cit. on p. 149).
268. KOSMANN, J., O. KLAPP, D. HOLZHÜTER, M. J. SCHOLLERER, A. FIEDLER, C. NAGEL, and C. HÜHNE: 'Measurement of epoxy film adhesive properties in torsion and tension using tubular butt joints'. *International Journal of Adhesion and Adhesives* (2018), vol. (cit. on pp. 149, 151).
269. ASTM D5656-10(2017): *Standard test method for thick-adherend metal lap-shear joints for determination of the stress-strain behavior of adhesives in shear by tension loading*. West Conshohocken, PA: ASTM, 2017 (cit. on p. 149).
270. HENKEL CORPORATION AEROSPACE: *LOCTITE EA 9695 AERO Epoxy Film Adhesive*. Technical Process Bulletin. 2013 (cit. on p. 150).
271. SILVA, L. F. da and M. J. C. LOPES: 'Joint strength optimization by the mixed-adhesive technique'. *International Journal of Adhesion and Adhesives* (2009), vol. 29(5): pp. 509–514 (cit. on p. 152).

272. DA SILVA, L. F., T. RODRIGUES, M. FIGUEIREDO, M. DE MOURA, and J. CHOUSAL: 'Effect of adhesive type and thickness on the lap shear strength'. *The Journal of Adhesion* (2006), vol. 82(11): pp. 1091–1115 (cit. on p. 152).
273. NAGEL, C. and O. KLAPP: 'Yield and Fracture of Bonded Joints using Hot-Curing Epoxy Film Adhesive - Multiaxial Tests and Theoretical Analysis'. *International Symposium on Sustainable Aviation 2018*. July 2018 (cit. on pp. 153, 156, 171).
274. JOUAN, A. and A. CONSTANTINESCU: 'A critical comparison of shear tests for adhesive joints'. *International Journal of Adhesion and Adhesives* (2018), vol. 84: pp. 63–79 (cit. on p. 159).
275. KLIMMECK, F.: 'Charakterisierung der kritischen Energiefreisetzungsrate eines Filmklebstoffs für Luftfahrtanwendungen unter Mode-I, Mode-II sowie Mixed-Mode Belastung'. MA thesis. Leibniz Universität Hannover, June 2021 (cit. on p. 160).
276. SACHSE, R.: 'Untersuchungen zur Auslegung von schadenstoleranten Klebeverbindungen durch mechanische Riss-Stopper-Elemente'. PhD thesis. Uni Stuttgart, 2020 (cit. on p. 171).
277. FLOROS, I., K. TSERPEIS, and T. LÖBEL: 'Mode-I, mode-II and mixed-mode I+ II fracture behavior of composite bonded joints: Experimental characterization and numerical simulation'. *Composites Part B: Engineering* (2015), vol. 78: pp. 459–468 (cit. on p. 172).
278. DUTTON, S., D. KELLY, and A. BAKER: *Composite materials for aircraft structures*. American Institute of Aeronautics and Astronautics, 2004 (cit. on p. 173).
279. ÖZ, Ö. and H. ÖZER: 'An experimental investigation on the failure loads of the mono and bi-adhesive joints'. *Journal of Adhesion Science and Technology* (2017), vol. 31(19-20): pp. 2251–2270 (cit. on p. 177).
280. TURNER, M. J., R. W. CLOUGH, H. C. MARTIN, and L. TOPP: 'Stiffness and deflection analysis of complex structures'. *Journal of the Aeronautical Sciences* (1956), vol. 23(9): pp. 805–823 (cit. on p. 201).
281. OSTERGAARD, M. G., A. R. IBBOTSON, O. LE ROUX, and A. M. PRIOR: 'Virtual testing of aircraft structures'. *CEAS Aeronautical Journal* (2011), vol. 1(1-4): p. 83 (cit. on p. 201).
282. LOPES, C., C. GONZÁLEZ, O. FALCÓ, F. NAYA, J. LLORCA, and B. TIJS: 'Multiscale virtual testing: the roadmap to efficient design of composites for damage resistance and tolerance'. *CEAS Aeronautical Journal* (2016), vol. 7(4): pp. 607–619 (cit. on p. 202).
283. GIGLIOTTI, L. and S. T. PINHO: 'Virtual testing of large composite structures: a multiple length/time-scale framework'. *Journal of Multiscale Modelling* (2015), vol. 6(03): p. 1550008 (cit. on p. 202).

284. TIJS, B., C. LOPES, A. TURON, C. BISAGNI, J. WALESON, J. van INGEN, and S. VELDMAN: 'Virtual testing of thermoplastic composites: towards a hybrid simulation-physical testing pyramid'. *ECCM18-18th European Conference on Composite Materials, Athens, Greece*. 2018 (cit. on p. 202).
285. GORSKII, Y. A., P. GAVRILOV, and A. BOROVKOV: 'Virtual proving ground for aircraft structures'. *IOP Conference Series: Materials Science and Engineering*. Vol. 986. 1. IOP Publishing. 2020: p. 012020 (cit. on p. 202).
286. SOUTIS, C.: 'Aerospace engineering requirements in building with composites'. *Polymer Composites in the Aerospace Industry*. Elsevier, 2020: pp. 3–22 (cit. on p. 202).
287. VELDMAN, S., P. KORTBEEK, P. WÖLCKEN, R. HERRMANN, J. KOS, and I. F. VILLEGAS: 'Development of a multifunctional fuselage demonstrator'. *Proceedings of the Aerospace Europe Conference*. 2020: pp. 25–28 (cit. on pp. 202–204).
288. GUO, Q., W. YAO, W. LI, and N. GUPTA: 'Constitutive models for the structural analysis of composite materials for the finite element analysis: A review of recent practices'. *Composite Structures* (2021), vol. 260: p. 113267 (cit. on p. 202).
289. RANASINGHE, K., K. GUAN, A. GARDI, and R. SABATINI: 'Review of advanced low-emission technologies for sustainable aviation'. *Energy* (2019), vol. 188: p. 115945 (cit. on p. 203).
290. BEUKERS, A. and E. van HINTE: *Designing Lightness*. 2020 (cit. on p. 203).
291. OMAIREY, S. L., S. SAMPETHAI, L. HANS, C. WORRALL, S. LEWIS, D. NEGRO, T. SATTAR, E. FERRERA, E. BLANCO, J. WIGHTON, et al.: 'Development of innovative automated solutions for the assembly of multifunctional thermoplastic composite fuselage'. *The International Journal of Advanced Manufacturing Technology* (2021), vol. 117(5): pp. 1721–1738 (cit. on pp. 203, 204).
292. AGEORGES, C., L. YE, and M. HOU: 'Advances in fusion bonding techniques for joining thermoplastic matrix composites: a review'. *Composites Part A: Applied Science and Manufacturing* (2001), vol. 32(6): pp. 839–857 (cit. on p. 203).
293. YOUSEFFPOUR, A., M. HOJJATI, and J.-P. IMMARIGEON: 'Fusion bonding/welding of thermoplastic composites'. *Journal of Thermoplastic Composite Materials* (2004), vol. 17(4): pp. 303–341 (cit. on p. 203).
294. VAN INGEN, J. W., A. BUITENHUIS, M. van WIJNGAARDEN, and F. SIMMONS: 'Development of the Gulfstream G650 induction welded thermoplastic elevators and rudder'. *Proceedings of the international SAMPE symposium and exhibition, Seattle, WA, USA*. 2010 (cit. on p. 203).
295. NIU, C.: *Airframe stress analysis and sizing*. AD Adaso/Adastr Engineering LLC, 1997 (cit. on pp. 204, 205).
296. SKORUPA, A. and M. SKORUPA: *Riveted lap joints in aircraft fuselage: design, analysis and properties*. Vol. 189. Springer Science & Business Media, 2012 (cit. on pp. 204, 207).

297. FLUGGE, W.: *Stress problems in pressurized cabins*. Tech. rep. TN 6212. NASA, 1952 (cit. on p. 205).
298. LIU, Y., S. LEMANSKI, and X. ZHANG: ‘Parametric study of size, curvature and free edge effects on the predicted strength of bonded composite joints’. *Composite Structures* (2018), vol. 202: pp. 364–373 (cit. on p. 207).
299. PARIDA, S. and A. PRADHAN: ‘Influence of curvature geometry of laminated FRP composite panels on delamination damage in adhesively bonded lap shear joints’. *International Journal of Adhesion and Adhesives* (2014), vol. 54: pp. 57–66 (cit. on p. 207).
300. AL-RAMAHI, N. J., R. JOFFE, and J. VARNA: ‘Investigation of end and edge effects on results of numerical simulation of single lap adhesive joint with non-linear materials’. *International Journal of Adhesion and Adhesives* (2018), vol. 87: pp. 191–204 (cit. on pp. 208, 209).
301. HEIDE, C. von der, J. STEINMETZ, M. J. SCHOLLERER, C. HÜHNE, M. SINAPIUS, and A. DIETZEL: ‘Smart Inlays for Simultaneous Crack Sensing and Arrest in Multifunctional Bondlines of Composites’. *Sensors* (2021), vol. 21(11): p. 3852 (cit. on p. 225).
302. TSAI, S. W.: ‘Double–Double: New Family of Composite Laminates’. *AIAA Journal* (2021), vol. 59(11): pp. 4293–4305 (cit. on p. 225).
303. WANG, Y., D. CHEN, N. LI, H. YUAN, Z. ZHU, Y. LI, and Z. HUANG: ‘A micromechanics based elasto-plastic damage model for unidirectional composites under off-axis tensile loads’. *Scientific Reports* (2020), vol. 10(1): pp. 1–17 (cit. on p. 269).
304. KUHN, P., M. PLOECKL, and H. KOERBER: ‘Experimental investigation of the failure envelope of unidirectional carbon-epoxy composite under high strain rate transverse and off-axis tensile loading’. *EPJ Web of Conferences*. Vol. 94. EDP Sciences. 2015: p. 01040 (cit. on p. 269).
305. NING, Z. H., G. L. HUO, R. H. LIU, W. L. WU, and J. M. XIE: ‘Progressive Failure Analysis of Laminates with Embedded Wrinkle Defects Based on an Elastoplastic Damage Model’. *Materials* (2020), vol. 13(10): p. 2422 (cit. on p. 269).
306. WANTHAL, S., J. SCHAEFER, B. JUSTUSSON, I. HYDER, S. ENGELSTAD, and C. ROSE: ‘Verification and validation process for progressive damage and failure analysis methods in the NASA Advanced Composites Consortium’. *American Society for Composites (ASC) Technical Conference*. NF1676L-26362. 2017 (cit. on p. 270).
307. MARLETT, K., Y. NG, and J. TOMBLIN: ‘Hexcel 8552 IM7 unidirectional prepreg 190 gsm & 35% RC qualification material property data report’. *National Center for Advanced Materials Performance, Wichita, Kansas. Test Report CAM-RP-2009-015, Rev. A* (2011), vol.: pp. 1–238 (cit. on pp. 270, 271).
308. FURTADO, C., G. CATALANOTTI, A. ARTEIRO, P. GRAY, B. WARDLE, and P. CAMANHO: ‘Simulation of failure in laminated polymer composites: Building-block validation’. *Composite Structures* (2019), vol. 226: p. 111168 (cit. on p. 270).

- 309. CATALANOTTI, G., J. XAVIER, and P. CAMANHO: ‘Measurement of the compressive crack resistance curve of composites using the size effect law’. *Composites Part A: Applied Science and Manufacturing* (2014), vol. 56: pp. 300–307 (cit. on p. 270).
- 310. DÁVILA, C. G.: *From SN to the Paris law with a new mixed-mode cohesive fatigue model*. National Aeronautics and Space Administration, Langley Research Center, 2018 (cit. on p. 270).
- 311. JOSEPH, A. P., A. M. WAAS, W. JI, E. J. PINEDA, S. L. LIGUORE, and S. P. WANTHAL: ‘Progressive damage and failure prediction of open hole tension and open hole compression specimens’. *56th AIAA/ASCE/AHS/ASC Structures, Structural Dynamics, and Materials Conference*. 2015: p. 0466 (cit. on p. 271).

List of figures

2.1	Building block approach [18]	9
2.2	Validation metrics for strains [21]	12
2.3	Possible relationships of the validation domain to the application domain [23]	12
2.4	Definition of a bonded joint adopted from [24]	14
2.5	Sketches illustrating failure modes [28]	16
2.6	Parameters of influence on static failure of composite adhesive joints, figure based on tables from [31] and [32], cf. A.1	17
2.7	Examples of single lap joints in aircraft structures [37]	18
2.8	Generic bonded wing spar construction with double lap joint [37]	18
2.9	Cessna Citation III bonded frame/longeron intersection [38]	19
2.10	Examples of stepped and scarf repair in aircraft structures	19
2.11	Fracture surfaces of single lap joints with different layups [42]	20
2.12	Schematic representation of double-lap joint made with UD laminate. [43]	21
2.13	Influence of fillet on failure behaviour [43]	21
2.14	Skin-stringer bond line specimen with crack locations [44]	22
2.15	Skin-stringer bondline specimen: Typical damage patterns in corners 1 and 4 [44]	22
2.16	Skin-stringer bondline specimen: Typical damage patterns in corners 2 and 3 [44]	23
3.1	Damage phenomena in the FRP adherends and in the adhesive layer (f. l. t. r.: crack in bondline, delamination, IFF, FF)	34
3.2	Graphical outline of work breakdown with chapter assignments	39
4.1	Scales of a UD fibre reinforced composite: (a) The micro-, (b) the meso-, and (c) the macroscale. [99]	42
4.2	Transverse matrix cracks on microscale: Comparison of experimental investigation from Gamstedt and Sjögren [100] with peridynamic simulation from Rädcl et al. [96]	43
4.3	Pagano's analytical solution: Geometry, stacking sequence, load and displacement boundary conditions of the reference laminate plate. [99]	46
4.4	Observed failure modes for transversely-isotropic materials according to Cuntze. [119]	49
4.5	Stress-strain curve showing individual components of the proposed material model	51
4.6	Algorithm flow chart of UMAT subroutine	61

4.7	Single element model with periodic boundary conditions with loading in 12-direction	65
4.8	Load-displacement curves under uniaxial tensile-compressive cycling load in fibre direction	65
4.9	Stress-strain curve of a cubic model subjected to transverse tension loading and discretised with different meshes	66
4.10	Stress-strain curve of a cubic model subjected to cyclic in-plane shear loading	67
4.11	Fracture stress τ_{12} vs. stress $-p_{hyd}(= \sigma_{11} = \sigma_{22} = \sigma_{33})$ following WWFE-II Test Case 2	67
4.12	Finite element model of AS4/PEEK $[\pm 45^\circ]_{2s}$ tensile test with periodic boundary conditions	68
4.13	Experimentally [89] and numerically determined stress-strain curves of an AS4/PEEK $[\pm 45^\circ]_{2s}$ tensile test	69
4.14	Geometry of off-axis tension test specimens with oblique tabs adopted from [159]	70
4.15	Goodness of fit for different values of a_{66}	72
4.16	Experimental and numerical results of UD composites made from M21-T700GC under off-axial tensile loads ($a_{66} = 0.8$, $\alpha = 0.218$, $\beta = 336.4$) . . .	73
4.17	Comparison of experimentally and numerically determined stress-strain curves of a M21-T700GC $[\pm 45]_{2s}$ tensile test with different a -values	74
4.18	Cuntze $\sigma_2 - \tau_{21}$ -fracture curve (left) and $\sigma_2 - \sigma_3$ -fracture curve (right) adopted from [159]	76
4.19	Puck $\sigma_2 - \tau_{21}$ -fracture curve adopted from [159]	77
4.20	Sketch of model geometry and boundary conditions	82
4.21	Comparison of fibre damage path d_f in OHT QI-II simulation models with structured and unstructured meshes	83
4.22	Mesh convergence of M21-T700GC 25/50/25 laminate (QI-II)	83
4.23	Comparison of experiments and simulations of M21-T700GC OHT tests . .	85
4.24	Comparison of stress-strain data of OHT simulations with and without plasticity with experimental data (M21-T700GC, QI-II, 25/50/25)	86
4.25	Comparison of experimental fracture pattern with numerical damage due to IFF	87
4.26	Comparison of strength prediction between Cuntze's FMC and Puck's APSC	89
4.27	Comparison of stress-strain data from OHT simulations with Cuntze's FMC and Puck's APSC (M21-T700GC, QI-II, 25/50/25)	90
4.28	Comparison of solid and continuum shell based modelling at the example of open hole tension test (QI-II)	92
4.29	Comparison of stress-strain data of OHT simulations with UMAT (dynamic implicit solver) and VUMAT (explicit solver) (M21-T700GC, QI-II, 25/50/25)	93
5.1	Fracture modes under peel and shear loading in and normal to the plane of crack propagation	96
5.2	Schematic illustration of fibre bridging in the DCB test	97
5.3	Trilinear traction-separation-law obtained by superposing two bilinear laws	103

5.4	DCB model for mode I parameter calibration	105
5.5	ENF model for mode II parameter calibration	106
5.6	MMB model for mixed-mode parameter calibration	106
5.7	DCB specimen inside fixture according to ASTM D5528	110
5.8	ENF specimen inside 3-point bend setup according to ASTM D7905	110
5.9	MMB specimen inside fixture according to ASTM D6671	111
5.10	Experimentally, analytically and numerically determined load-displacement curves of DCB test	114
5.11	Resistance curves of DCB tests with different interfaces (MBT)	115
5.12	Fracture surfaces of DCB specimens [235]	117
5.13	Crack paths in DCB specimens	118
5.14	Comparison of crack front shape from ultrasonic C-scan inspection and simulation results of DCB specimens	120
5.15	Experimentally, analytically and numerically determined load-displacement curves of ENF tests	123
5.16	Fracture surfaces of ENF specimens [235]	124
5.17	ENF crack front shapes observed in numerical simulations	125
5.18	Fracture toughness vs. mode mixture curves	126
5.19	Experimentally, analytically and numerically determined load-displacement curves of MMB tests	128
5.20	Fracture surfaces of MMB specimens [235]	129
5.21	Comparison of modelling approaches with the example of QI-II OHT tests	132
5.22	Comparison of solid and continuum shell based modelling with the example of QI-III OHT tests	133
5.23	Comparison of predicted delaminations areas between individual plies	134
5.24	Comparison of predicted delaminations areas with experimental results	135
5.25	Comparison of standard and orientation specific ERRs with continuum shell + cohesive surface based modelling with the example of QI-II OHT tests	136
5.26	Comparison of standard and orientation specific ERRs with continuum shell + cohesive surface based modelling with the example of QI-III OHT tests	137
6.1	Illustration of ACZ (a), AACZ (b) and XFEM-based (c) CZM techniques	144
6.2	Sketch of a TAST specimen	150
6.3	DIC setup for thick adherend shear tests	151
6.4	Failure surface of the specimen with $t_b = 0.21$ mm	151
6.5	Force-displacement data from TAST experiments	152
6.6	Sketches of BJ and 20° IBJ specimen	153
6.7	Hardening curve derived from TAST shear stress-strain data	155
6.8	Yield data expressed in hydrostatic p and deviatoric q stresses	155
6.9	3D FE-model of half TAST specimen using x-z symmetry plane and tied contact between adhesive and adherends	157
6.10	TAST strain comparison at 1.5 kN	157
6.11	TAST strain comparison at 6.0 kN	158
6.12	TAST strain comparison at 10.0 kN	158

6.13	Force-displacement data from BJ simulations	159
6.14	Fracture pattern of DCB tests with Hysol EA9695 and 8552-IM7 with different surface pretreatments	161
6.15	Experimentally, analytically and numerically determined load-displacement curves of a Hysol EA9695 film adhesive DCB test with 8552-IM7 adherend material	164
6.16	Experimentally, analytically and numerically determined load-displacement curves of a Hysol EA9695 film adhesive ENF test with 8552-IM7 adherend material	167
6.17	Experimentally, analytically and numerically determined load-displacement curves of a Hysol EA9695 film adhesive MMB test with $G_{II}/G_T = 0.21$ and 8552-IM7 adherend material	169
6.18	Experimentally, analytically and numerically determined load-displacement curves of a Hysol EA9695 film adhesive MMB test with $G_{II}/G_T = 0.63$ and 8552-IM7 adherend material	169
6.19	ERRs in traction-separation laws	171
6.20	The effect of the CZM parameters on the predicted TAST failure load . . .	174
6.21	Mesh convergence of ACZ and AACZ approach predicting TAST strength .	175
6.22	Load-displacement curves gained with different modelling approaches . . .	176
6.23	Schematic of experimentally observed and XFEM-predicted crack path . . .	177
6.24	Influence of solver on load-displacement curves from ACZ and AACZ approach	179
7.1	Sketch of SLS joint simulation model (not to scale)	183
7.2	Experimentally and numerically observed damage patterns for SLS-0-25 . .	186
7.3	Comparison of experiments and simulations of SLS-0 tests	188
7.4	Force-displacement curves of SLS-0-15 joint coupon	189
7.5	Force-displacement curves of SLS-0-25 joint coupon	190
7.6	Force-displacement curves of SLS-0-35 joint coupon	190
7.7	Global ε_{xy} strain field of SLS-0-25 at 13.7 kN	191
7.8	Local ε_{xy} strain field in the adherend of SLS-0-25 at 13.7 kN	192
7.9	Local ε_{xy} strain field in the adhesive of SLS-0-25 at 11.8 kN	193
7.10	Experimentally and numerically (ACZ) observed damage patterns for SLS-45-12	194
7.11	Comparison of experiments and simulations of SLS-45 tests	195
7.12	Force-displacement curves of SLS-45 joint coupon	196
7.13	Decision support for composite adherend modelling strategy	198
7.14	Decision support for adhesive modelling strategy	199
8.1	Illustration of pre-equipped fuselage section with adhesive joints (green) . .	204
8.2	Configuration A1	205
8.3	Configuration A2	205
8.4	Configuration A3	205
8.5	Configuration A2 with 15 mm gap	206

8.6	Coordinate system used for the aircraft fuselage as well as geometry, boundary conditions and coordinate system of the simulation model	208
8.7	Front view for coupling of displacement u_z applied on the nodes with the same x -coordinate belonging to the vertical lines on the edge adopted from [300].	209
8.8	Coupling of u_x and u_y on nodes belonging to lines through the width of the joint adopted from [300]	209
8.9	Stress-strain curves from configuration A1 with different model widths . . .	211
8.10	Influence of pseudoplasticity of composite adherends - stress-strain curves from Configuration A2 without a gap	212
8.11	Influence of pseudoplasticity of composite adherends - stress-strain curves from Configuration A3 without a gap	213
8.12	Stress-strain curves from Configuration A1 with different gap lengths	214
8.13	Stress-strain curves from Configuration A2 with different gap lengths	214
8.14	Stress-strain curves from Configuration A3 with different gap lengths	215
8.15	Configuration A2: change in failure mode from a 15 mm gap (stock-break failure) to a 20 mm gap (cohesive failure)	216
8.16	Illustration of the proposed strategy to reduce physical testing	218
9.1	Graphical overview of future enhancements and applications	226
D.1	Comparison of single element tests of UMAT and VUMAT with M21-T700GC268	
E.1	Experimental [303] and numerical results of UD composites made from 8552-IM7 under off-axial tensile loads	269
F.1	Mesh convergence of 8552-IM7 25/50/25 laminate with unstructured mesh .	272
F.2	Comparison of experiments and simulations of 8552-IM7 OHT tests	273
F.3	Comparison of stress-strain data of OHT simulations with and without plasticity (50/40/10, 8552-IM7)	273
F.4	Comparison of stress-strain data of OHT simulations with and without plasticity (25/50/25, 8552-IM7)	274
F.5	Comparison of stress-strain data of OHT simulations with and without plasticity (10/80/10, 8552-IM7)	274
F.6	Force-displacement data from open hole tension simulation compared with experimental failure loads (8552-IM7, 50/40/10)	275
G.1	Fracture pattern of ENF tests with Hysol EA9695 with different surface pretreatments	277
G.2	Experimentally determined load-displacement curves of a Hysol EA9695 film adhesive DCB test with M21-T700GC adherend material	278
G.3	Experimentally determined load-displacement curves of a Hysol EA9695 film adhesive ENF test with M21-T700GC adherend material	278
H.1	Fracture toughness of EA9695 in dependence of mode mixture	280

I.1	Cohesive fracture patterns of SLS-0 specimens	282
I.2	Fracture patterns of SLS-45 specimens	283
J.1	Comparison of SLS-0-25 AACZ CSDMG results with different versions of Abaqus	285
J.2	Force-displacement curves of SLS-0-25 joint coupon determined with different Abaqus version	286

List of tables

2.1	EASA certification specifications	6
2.2	Comparison of publications considering intra-, interlaminar and adhesive damage	28
2.3	Quality of the numerical predictions in the identified publications	29
4.1	FEAs of Pagano reference with different approaches, element types and through-thickness discretisations, R denotes to reduced integration, * to a quadratic ansatz. The Pagano analytical reference for the vertical displacement $u_z(a/2; b/2; -t/2)$ is 22.27 mm. [99]	47
4.2	Assignment of failure modes to damage variables	56
4.3	Angles of most direct impact on the stiffness components	59
4.4	Material properties and model parameters for AS4/PEEK	64
4.5	Comparison of UD and in-situ strengths of M21-T700GC	75
4.6	Parameters for Cuntze's FMC and Puck's APSC	78
4.7	Material properties and model parameters for M21/T700GC	80
4.8	Geometries of the M21-T700GC OHT configurations	80
4.9	List of M21-T700GC OHT configurations and experimental results	81
4.10	Comparison of computational expense of proposed material model with different failure criteria on the basis of OHT specimens with different layups	91
5.1	Laminate layups for multidirectional interface testing	108
5.2	Summary of calibrated mode I parameters	113
5.3	Cuntze failure mode material stressing effort (DCB)	119
5.4	Crack front shape: Distances of the right and left edges to the most advanced point of the crack front	121
5.5	ERR components and mode mixture for different interfaces (DCB)	121
5.6	Summary of calibrated mode II parameters	122
5.7	Cuntze failure mode material stressing effort (ENF)	124
5.8	Highest (h) and in the middle (m) measured ERR components and mode mixture for different interfaces (ENF)	125
5.9	Cuntze failure mode material stressing effort (MMB)	129
5.10	Summary of calibrated M21-T700GC CZM parameters for different interfaces	130
5.11	Comparison of failure loads of OHT specimens with different modelling approaches from experiment and simulation	134
6.1	TASJ, BJ and IBJ yield and failure stresses from [273]	153

6.2	Fitted exp D.-P. parameters for LOCTITE EA 9695 050 NW AERO epoxy film adhesive	156
6.3	Dimensions of DCB specimens for film adhesive characterisation	162
6.4	Mode I fracture toughness values G_{Ic} of Hysol EA9695 from DCB tests in N/mm	163
6.5	Dimensions of ENF specimens for film adhesive characterisation	165
6.6	Mode II fracture toughness values G_{IIc} of Hysol EA9695 from ENF tests in N/mm	166
6.7	Dimensions of MMB specimens for film adhesive characterisation	168
6.8	Mixed-mode fracture toughness values of Hysol EA9695 from MMB tests in N/mm	168
6.9	Parameters of Loctite EA 9695 050 NW AERO for CZM modelling	172
6.10	Comparison of failure loads of TAST specimens from experiments and simulations	176
6.11	Comparison of computational expense of the modelling approaches on the basis of the TAST specimen	178
7.1	Nominal geometry and layups of SLS joint element specimens	183
7.2	Cuntze failure mode material stressing effort for SLS-0	187
7.3	Comparison of computational expense of the modelling approaches on the basis of the SLS-0-25 and SLS-45-12 specimens using Abaqus/Explicit	197
8.1	Wall clock time for the different model widths	211
8.2	Wall clock time in dependency of plasticity modelling (Configuration A2)	213
A.1	Parameters of influence on static failure of composite adhesive joints originally from [31] and modified from [32]	262
B.1	In-plane elastic properties of M21/T700GC	263
B.2	In-plane strength properties of M21/T700GC	264
E.1	Intralaminar material properties and model parameters for 8552-IM7 with references	270
E.2	Interlaminar material properties and model parameters for 8552-IM7 with references	270
F.1	Geometry of the 8552-IM7 OHT configurations	271
F.2	List of 8552-IM7 OHT configurations and experimental results	271
I.1	Comparison of failure loads of single lap shear coupons with 0°-interface layer from experiment and simulation	283
I.2	Comparison of failure loads of single lap shear coupons with 45°-interface layer from experiment and simulation	284

A Parameters of influence on static failure of composite adhesive joints

Table A.1: Parameters of influence on static failure of composite adhesive joints originally from [31] and modified from [32]

	Influence of:		Influence on static failure:
Adhesive properties	Ductile/ Brittle Adhesives		For a brittle adhesive, static fracture strength under mode I loading is typically 20% lower than under mixed mode (I-II) loading. The same effect does not exist for ductile adhesive.
	Toughened/ Non-Toughened Adhesives		In general, toughening of an adhesive improves its static strength whilst increasing fracture energy.
Adhered Configuration	Adherend Stiffness		The rigidity of the adherend influences the stress distribution along the bondline. The influence of the stiffness can be described by using the ratio: $\frac{E_{Adherend}}{E_{Adhesive}}$. Higher values of this ratio mean lower crack resistance.
	Adherend Thickness		The thickness influences stress distribution, and, for some joint geometries such as SLS joints, the amount of eccentricity and peel stresses along the overlap.
	Fracture Surface		For 0° surface ply, fibre pull-out can be found. For specimens with 45° surface ply, the crack can extend along the ply interface and further into the substrate.
Joint geometry	Bondline Thickness		Increasing the bondline thickness will increase the fracture resistance until a certain ‘optimum’ thickness is reached.
	Joint Width		With increasing joint width, the effect of edge interaction on the stress distribution towards the middle of the joint will reduce.
	Overlap Length		Joint strength increases with increasing overlap length until the adherends become the critical point of failure.
Geometry	Overlap Shape		Square End: The stress peak is highest due to the sudden stiffness jump. Taper: The stress peak is reduced relative to the square end overlap due to the more gradual introduction of the stress peak. Inverse Taper: The thick fillet results in a plane strain stress condition, causing the fracture resistance to be lower.
	Fillet		A small fillet can reduce the peel stress peak near the overlap end due to a more gradual introduction of the shear stress.
Interface	Adhesive/ Cohesive Failure		The ultimate static strength is always greater for a cohesive failure compared to an adhesive failure. This depends strongly on the quality of pre-treatments.
Loading Parameters	Loading rate		In general, the fracture resistance is lower for higher strain rates.

B Stiffness and strength data of M21-T700GC

Table B.1: In-plane elastic properties of M21/T700GC

			Batch 1	Batch 2	Mean
E_{11}^t	Mean	MPa	125489	122296	124121
	Stddev.	MPa	2710	2993	2831
	C.o.V.	%	2.16	2.45	2.28
	n	-	4	3	7
E_{11}^c	Mean	MPa	102800	106108	103401
	Stddev.	MPa	360	343	357
	C.o.V.	%	0.35	0.32	0.35
	n	-	9	2	11
E_{22}^t	Mean	MPa	8330	8593	8382
	Stddev.	MPa	81	182	106
	C.o.V.	%	0.98	2.11	1.27
	n	-	6	2	8
E_{22}^c	Mean	MPa	8260	8595	8316
	Stddev.	MPa	152	31	132
	C.o.V.	%	1.84	0.36	1.59
	n	-	10	2	12
ν_{12}	Mean	MPa	0.294	0.285	0.291
	Stddev.	MPa	0.012	0.008	0.011
	C.o.V.	%	4.19	2.97	3.67
	n	-	6	3	9
G_{12}	Mean	MPa	4355	4306	4341
	Stddev.	MPa	87	127	98
	C.o.V.	%	2.01	2.94	2.27
	n	-	5	2	7

Table B.2: In-plane strength properties of M21/T700GC

			Batch 1	Batch 2	Mean
R_{\parallel}^t	Mean	MPa	2232	2200	2214
	Stddev.	MPa	116	135	127
	C.o.V.	%	5.19	6.12	5.72
	n	-	4	5	9
R_{\parallel}^c	Mean	MPa	1537	1442	1521
	Stddev.	MPa	77	177	94
	C.o.V.	%	5.03	12.31	6.16
	n	-	10	2	12
R_{\perp}^t	Mean	MPa	71	86	78
	Stddev.	MPa	3	1	-
	C.o.V.	%	4.75	1.31	-
	n	-	6	5	(-)
R_{\perp}^c	Mean	MPa	202	231	207
	Stddev.	MPa	10	1	9
	C.o.V.	%	3.06	0.45	4.11
	n	-	10	2	12
$R_{\perp\parallel}$	Mean	MPa	78	75	77
	Stddev.	MPa	3	0.47	2
	C.o.V.	%	3.85	0.63	2.80
	n	-	4	2	6

C Analytical determination of in-situ strengths

Parvizi et al. [164] observed that the transverse tensile strength as well as the shear strength of plies differ from the strengths measured from UD laminates depending on whether the plies are embedded in a multidirectional laminate or not. These so called in-situ strengths depend in the thickness and orientation of the plies. The in-situ strength increases with decreasing ply thickness and differ depending on the constraining effects of the surrounding plies which in turn depends on the fibre orientation.

These in-situ strength can be incorporated in PDA by replacing the strength values measured in UD laminates with their in-situ counterparts.

Camanho et al. [165] developed the most predominant theory which analytically predicts the in-situ strengths. It is based on a analysis of cracks in thick, than as well as embedded plies in the course of Dvorak and Laws [171]. The analytical solution of Camanho et al. [165] is based on the cERR and takes into account the thickness as well as the position of the ply in a laminate. The in-situ strength of an embedded ply is higher than the in-situ strength of an outer ply because the former ply is constrained from both sides whereas the latter only from one side. Furthermore, a thin embedded ply has a higher strength than a thick embedded ply as within thinner plies there is less space for unobstructed crack growth. In Camanho's model there is a solutions for both thin and thick plies and the transition between the two solutions is at the intersection of both theories. This means that the in-situ strength from thick ply theory is a lower bound for embedded plies.

The theory uses the Hahn-Tsai fit of the in-plane shear stress-strain curve to include the shear non-lineatiy with an analytical solution:

$$\gamma_{12} = \frac{1}{G_{12}}\tau_{12} + \beta_{HT}\tau_{12}^3 \quad (C.1)$$

With β_{HT} fitted from experimental data, the in-situ in-plane shear strength can be calculated with:

$$R_{\perp||,is} = \sqrt{\frac{\sqrt{1 + \beta_{HT}\Phi G_{12}^2} - 1}{3\beta_{HT}G_{12}}} \quad (C.2)$$

where Φ is

$$\Phi = \begin{cases} 12 \frac{R_{\perp\parallel}}{G_{12}} + 18\beta_{HT} R_{\perp\parallel}^4 & \text{for thick (embedded) ply} \\ \frac{48G_{IIc}}{\pi t} & \text{for thin (embedded) ply} \\ \frac{24G_{IIc}}{\pi t} & \text{for an outer ply} \end{cases} \quad (\text{C.3})$$

The in-situ transverse tensile strength is given by:

$$R_{\perp,\text{is}}^t = \begin{cases} 1.12\sqrt{2}R_{\perp}^t & \text{for thick (embedded) ply} \\ \sqrt{\frac{8G_{Ic}}{\pi t\Lambda_{22}^0}} & \text{for thin (embedded) ply} \\ 1.79\sqrt{\frac{G_{Ic}}{\pi t\Lambda_{22}^0}} & \text{for an outer ply} \end{cases} \quad (\text{C.4})$$

with

$$\Lambda_{22}^0 = 2 \left(\frac{1}{E_{22}} - \frac{\mu_{21}^2}{E_{11}} \right) \quad (\text{C.5})$$

The solutions for the thin embedded as well as for the outer ply are used in this work.

D Single element tests of intralaminar material model

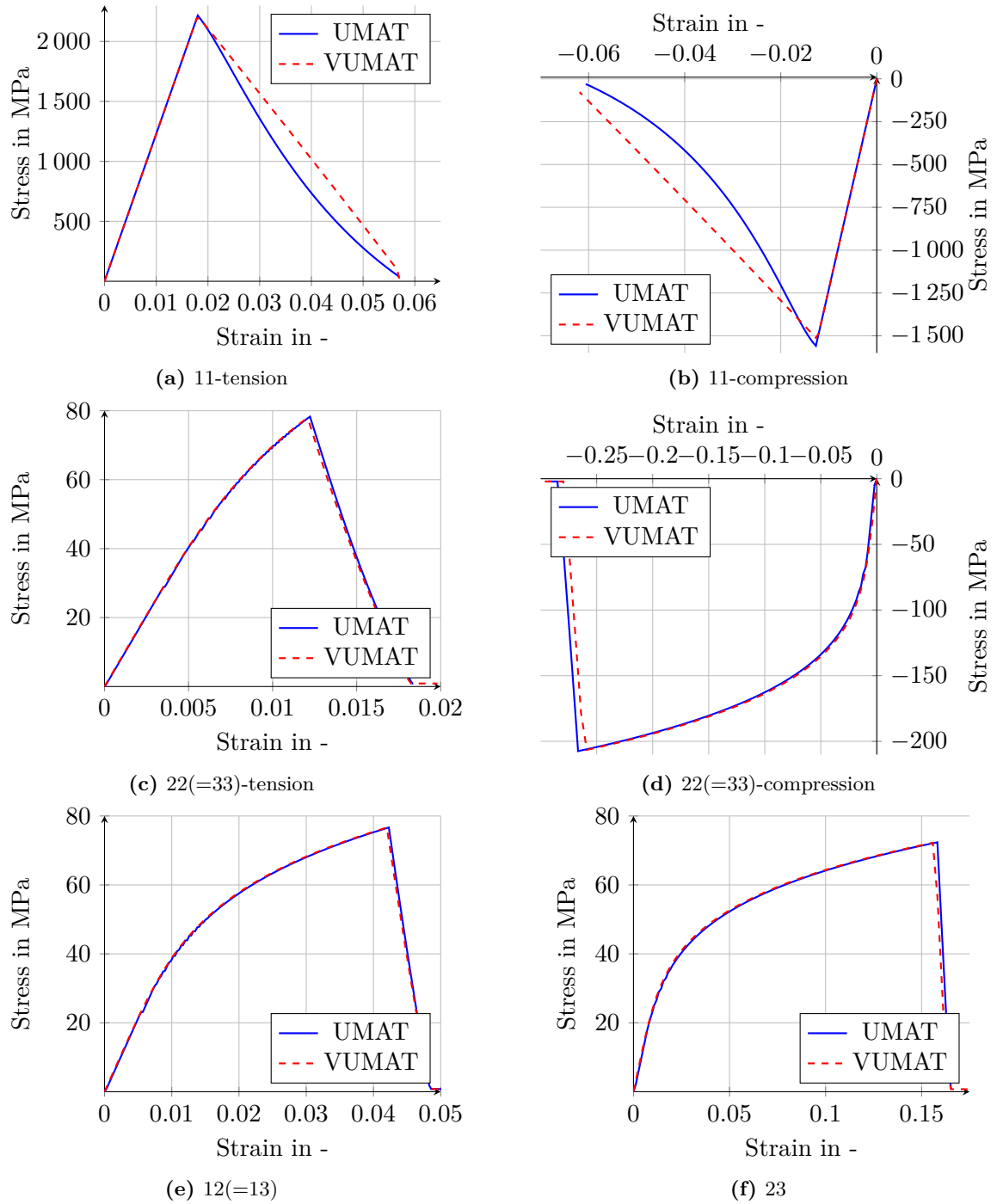


Figure D.1: Comparison of single element tests of UMAT and VUMAT with M21-T700GC

E Material data for 8552-IM7

Off-axis tension tests

Off-axis tensile test data for 8552-IM7 taken from Wang et al. [303] originally from Kuhn et al. [304] are used to fit the parameters of the plasticity model from Sun and Chen. The parameter a_{66} is predefined to the value 2.6 taken from Ning et al. [305]. With the procedure described in section 4.5.2 the remaining to values are determined to $\alpha = 0.252$ and $\beta = 950.1$. In Fig. E.1 the experimental as well as the numerical results with the fitted parameters are shown.

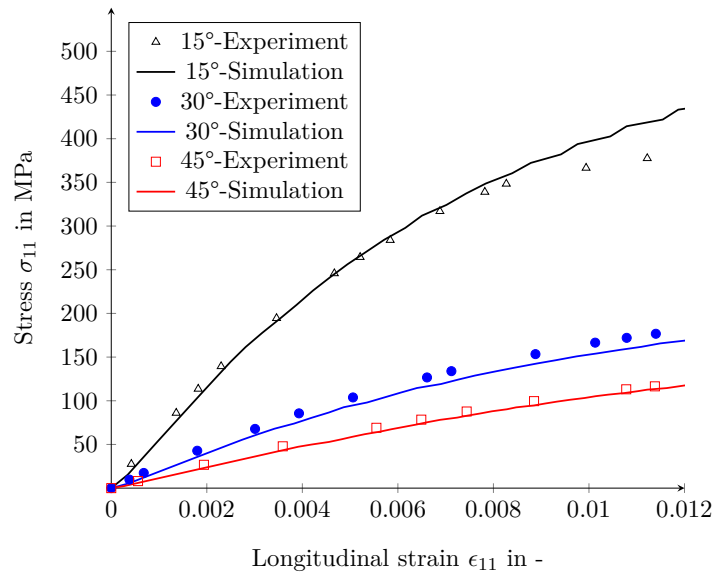


Figure E.1: Experimental [303] and numerical results of UD composites made from 8552-IM7 under off-axial tensile loads

Intralaminar material data of 8552-IM7

In Tab. E.1 the material properties of the Hexcel 8552-IM7 material are summarised. Most of the material properties are from literature. In this case a reference is given. The strength $R_{||}^c$ was tested by University of Stuttgart in the course of a joint project. Parameters for the plasticity model were derived from the above introduced off-axis tension tests.

Table E.1: Intralaminar material properties and model parameters for 8552-IM7 with references

Elasticity	E_{11} 171.4 GPa [173]	$E_{22} = E_{33}$ 9.1 GPa [173]	$G_{12} = G_{13}$ 4.5 GPa [223]	G_{23} 3.0 GPa [306]	$\nu_{12} = \nu_{13}$ 0.32 [306]	ν_{23} 0.45 [306]
Plasticity	a 2.6	α 0.252	β 950.1			
Strength	R_{\parallel}^t 2500.4 MPa [307]	R_{\parallel}^c 1200.1 MPa [173]	R_{\perp}^t 50.8 MPa	R_{\perp}^c 253.0 MPa [308]	$R_{\perp\parallel}$ 91.1 MPa [307]	
Fracture Toughness	G_{ft} 133.3 N/mm [308]	G_{fc} 61.0 N/mm [309]	$G_{mt} = G_{mc}$ 0.24 N/mm [310]	G_s 0.74 N/mm [310]		

Interlaminar material data of 8552-IM7

In Tab. E.2 the interlaminar material parameters for 8552-IM7 are summarised. The data is taken from literature. The references are given in the table.

Table E.2: Interlaminar material properties and model parameters for 8552-IM7 with references

Property	Ref.	Value	Unit
$K_I = K_{II} = K_{III}$		10^5	N/mm ³
G_{Ic}	[310]	0.24	N/mm
$G_{IIc} = G_{IIIc}$	[310]	0.74	N/mm
T_n^0	[308]	62.3*	MPa
$T_s^0 = T_t^0$	[308]	92.3	MPa
Damage Initiation Criterion		QUADS	
Damage Propagation Criterion	[306]	BK-law	
η_{BK}	[306]	2.07	

* Reduced to 15 MPa with approach described in section 5.3.2 to account for element size.

F Validation of 8552-IM7 intralaminar modelling with OHT tests

The material parameters presented in Appendix E are validated together with the modelling approaches from Chapter 4 using OHT tests.

Experimental data of open hole tension specimens made from 8552-IM7 from literature

Experimental data from OHT tests with three different layups can be found in [307]. The same specimen configurations are also tested and used for validation for example in [311]. All specimens have the same geometry but different layups. The geometry is given in Tab. F.1. The different layups as well as the resulting strengths are presented in Tab. F.2.

Table F.1: Geometry of the 8552-IM7 OHT configurations

Width	Free length	Ply thickness	Hole diameter
mm	mm	mm	mm
38.1	177.8	0.183	6.35

Table F.2: List of 8552-IM7 OHT configurations and experimental results

Laminate	Lay-up	NIAR [307]	Joseph et al. [311]	
		Peak Stress MPa	Peak Stress MPa	Modulus GPa
50/40/10	[0/45/0/90/0/-45/0/45/0/-45] _s	594.0 ± 34.1	628.1 ± 21.4	90.3 ± 4.3
25/50/25	[45/0/-45/90] _{2s}	406.8 ± 11.3	432.8 ± 12.4	57.2 ± 6.6
10/80/10	[45/-45/0/45/-45/90/45/-45/45/-45] _s	301.0 ± 12.3	315.9 ± 3.9	37.2 ± 2.8

Mesh sensitivity study

The critical mesh sizes to prevent for local snap backs are calculated with Eq. 4.55 for the different loadings. The smallest element size is calculated for compression loading perpendicular to the fibre with 0.17 mm. Since this loading is not relevant in OHT tests, the next larger element size of 0.64 mm under shear loading is adopted.

With this information, as for the M21-T700GC, a mesh sensitivity study is performed using the OHT test with the 25/50/25 QI laminate. As can be seen from Fig. F.1 there is no clear trend for mesh sizes between 0.40 and 1.45 mm in-plane mesh size. Together with the mesh size calculated with Eq. 4.55 it is decided to use 0.625 mm in the further course of the thesis.

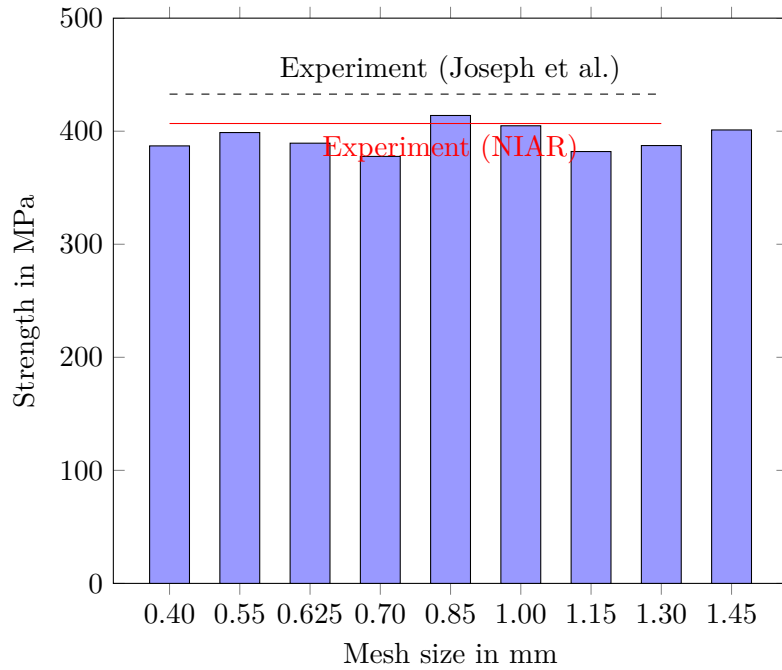


Figure F.1: Mesh convergence of 8552-IM7 25/50/25 laminate with unstructured mesh

Simulation results of open hole tension tests

Fig. F.2 shows the strength results of the experiments from two studies as well as the numerical results. Each specimen configuration is simulated using the normal UD strength as well as the in-situ strength. It can be seen that the simulations using in-situ strength show better agreement with the experimental results. Another finding is that the influence of the in-situ strength increases with increasing amount of off-axis plies. This can be attributed to the fact that the in-situ strength only affects the matrix dominated strength values.

In the figures F.6, F.4 and F.5 the force-displacement data of the simulations with and without plasticity are shown. The stiffness is barely affected, but the simulations without plasticity modelling give significantly lower strength values. It can be seen that in all cases the simulations which model plasticity are in better agreement with the experimental strength results.

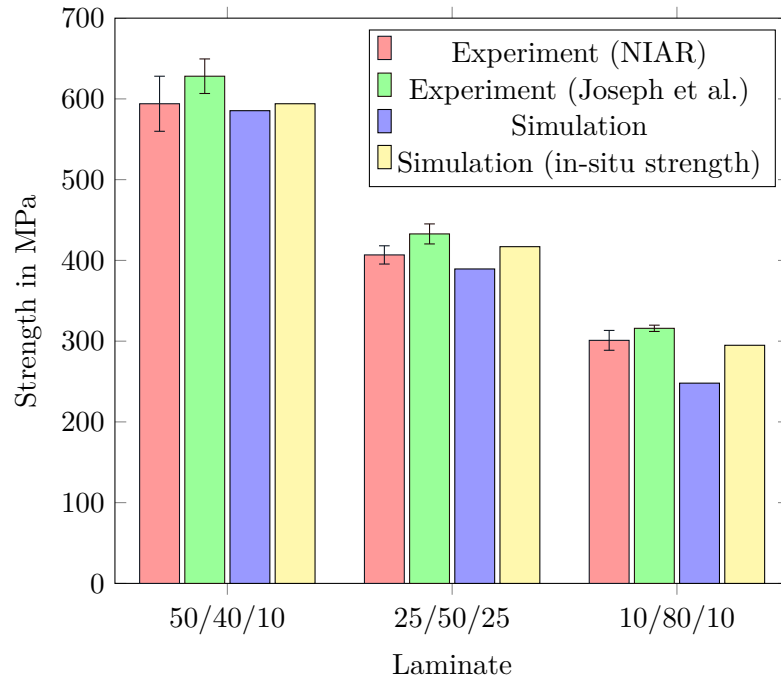


Figure F.2: Comparison of experiments and simulations of 8552-IM7 OHT tests

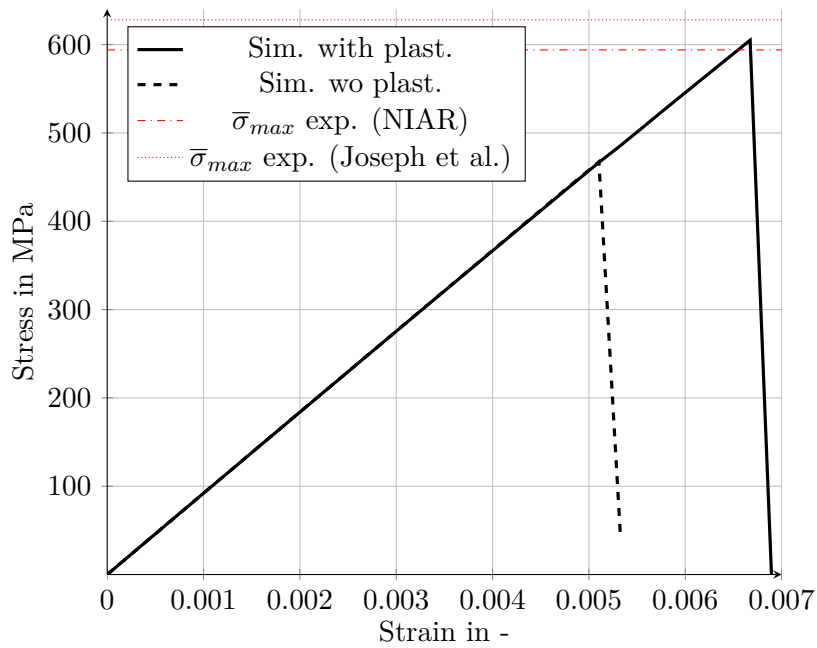


Figure F.3: Comparison of stress-strain data of OHT simulations with and without plasticity (50/40/10, 8552-IM7)

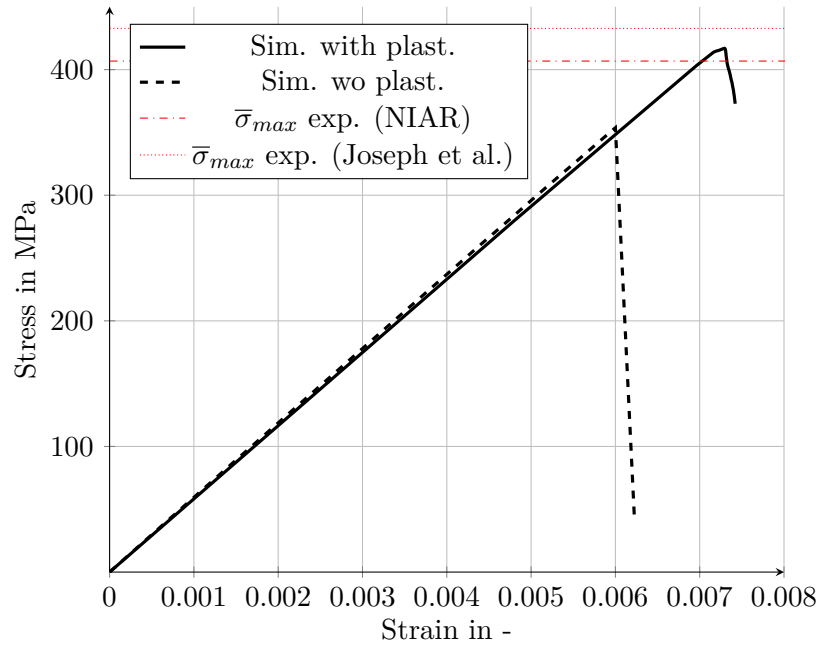


Figure F.4: Comparison of stress-strain data of OHT simulations with and without plasticity (25/50/25, 8552-IM7)

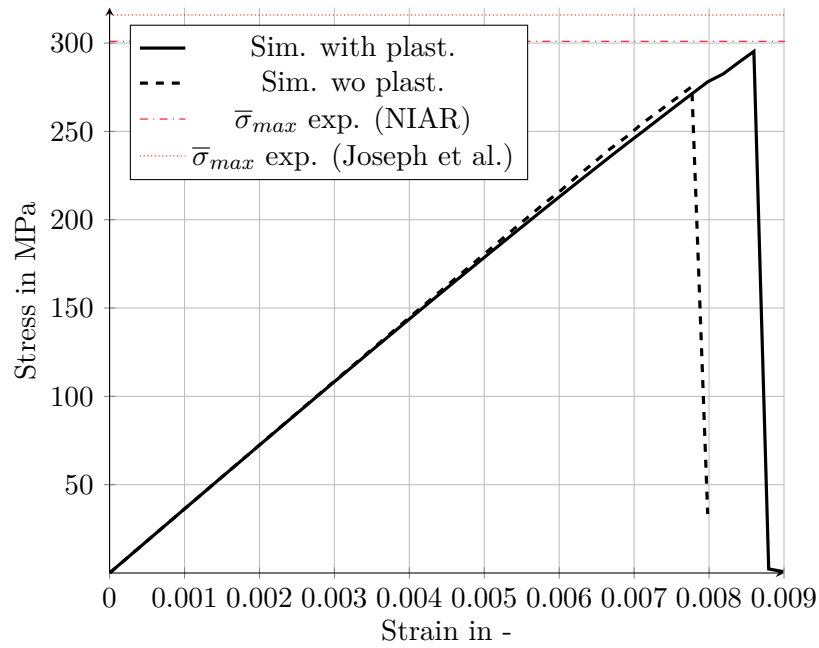


Figure F.5: Comparison of stress-strain data of OHT simulations with and without plasticity (10/80/10, 8552-IM7)

Shell vs. solid element based modelling

The plots in Fig. F.6 show the force-displacement data of the 50/40/10 OHT specimen gained with different modelling approaches. Like for the M21-T700GC study in Section 4.7.1, it can be seen that the solid element-based modelling results in a strength which agrees well with the experiments. The continuum shell element-based modelling as well as the solid element-based modelling only with in-plane damage results in nearly the same strength which is higher the upper bound of the experimental values. However, the behaviour close to total failure is different between the latter two modelling approaches.

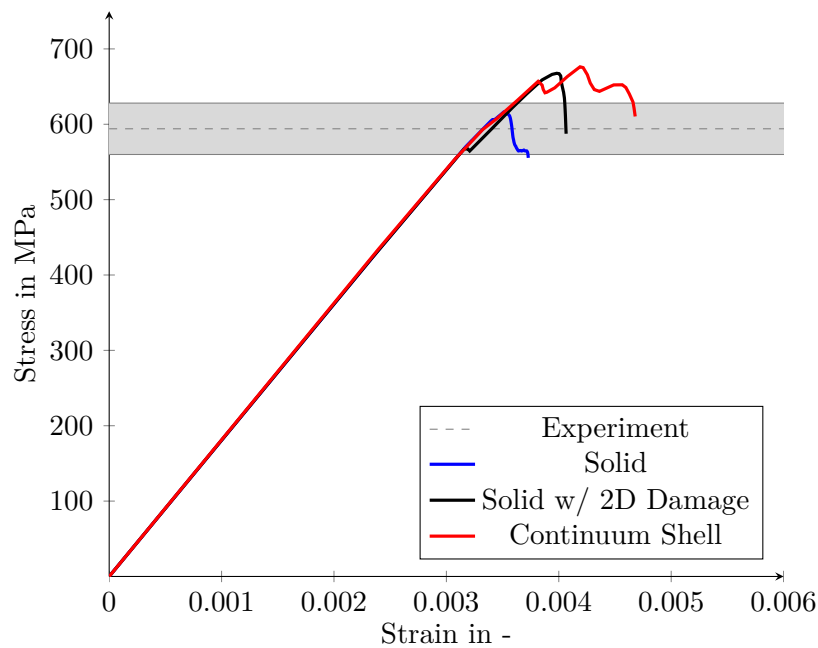
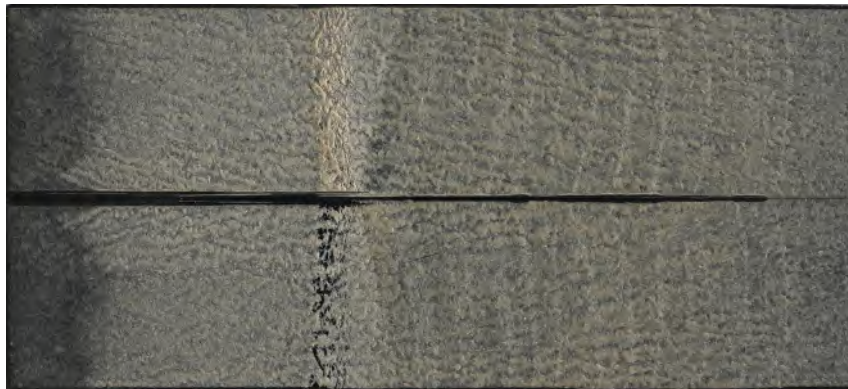


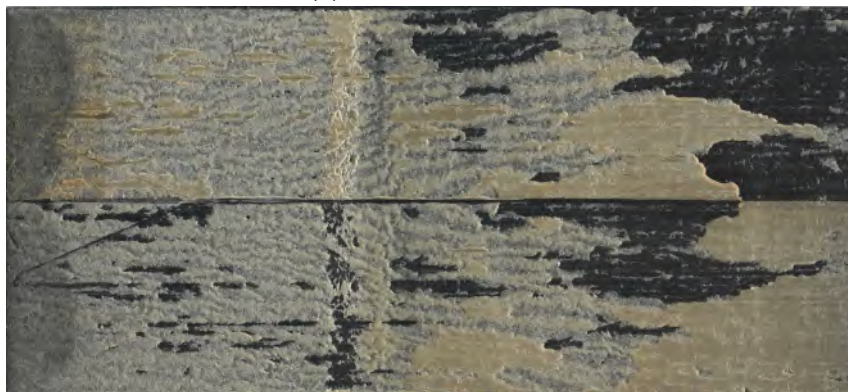
Figure F.6: Force-displacement data from open hole tension simulation compared with experimental failure loads (8552-IM7, 50/40/10)

G Experimental results of Hysol EA9695 DCB and ENF tests

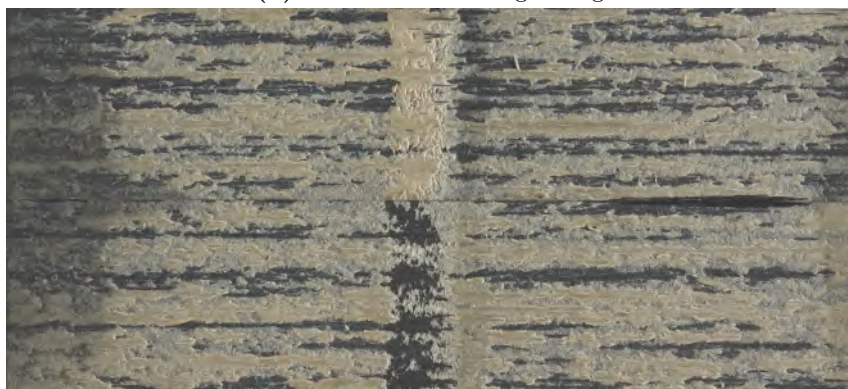
ENF fracture patterns



(a) 8552-IM7 - plasma



(b) 8552-IM7 - manual grinding



(c) M21-T700GC - manual grinding

Figure G.1: Fracture pattern of ENF tests with Hysol EA9695 with different surface pretreatments

Force-displacement curves of tests with M21-T700GC adherends

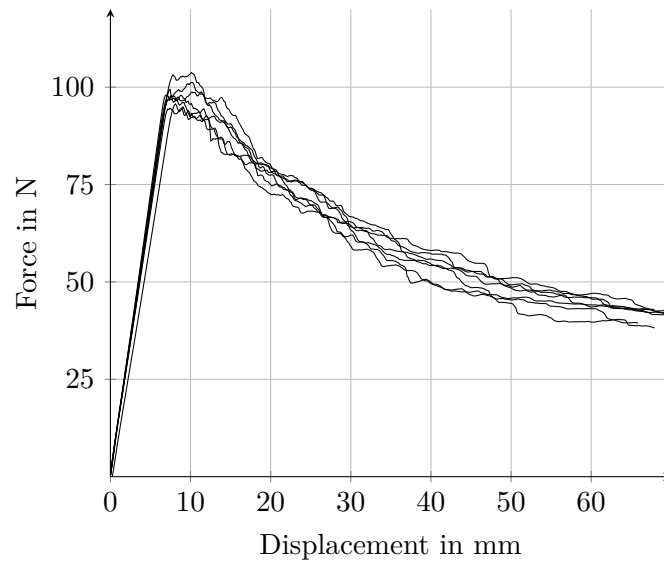


Figure G.2: Experimentally determined load-displacement curves of a Hysol EA9695 film adhesive DCB test with M21-T700GC adherend material

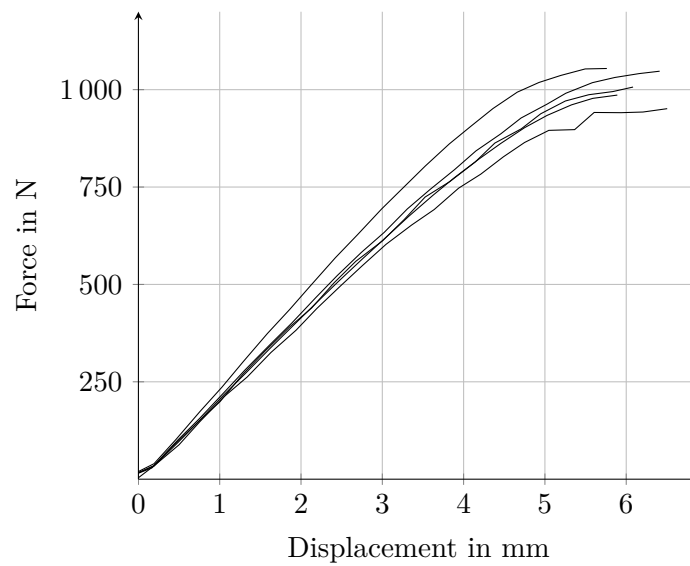


Figure G.3: Experimentally determined load-displacement curves of a Hysol EA9695 film adhesive ENF test with M21-T700GC adherend material

H Additional MMB tests with Hysol EA9695

Due to doubts regarding the original MMB results, cf. Section 6.8.4, additional MMB tests were carried out at Fraunhofer IFAM using test specimens manufactured at DLR. A total of four test specimens were tested and evaluated using the same methods: one test specimen with a target mode ratio of 0.2 and three test specimens with a target mode ratio of 0.6. The results are shown together with the original results in Fig. H.1. It needs to be mentioned that the actual mode ratio, which is not exactly equal to the target values, is plotted in the figure.

The test at a target mode ratio of 0.2 gives a very comparable result of 0.857 kN/mm to the mean value of the original series of 0.875 kN/mm.

However, there is a slight deviation for a mode ratio of 0.6. The three newly conducted tests show a slightly higher result of 1.556 kN/mm compared to 1.421 kN/mm.

As a result, the BK fit no longer yields an exponent of $\eta = 3.6$, but only of $\eta = 2.8$. The new results are also closer to the power law with an exponent of $\alpha = 1$. Thus, the new results confirm the assumption made in Section 6.8.4.

However, the results are not significantly different. For this reason, further tests should be carried out with additional mode ratios and, if necessary, other types of tests should be used to further investigate the behaviour under mixed fracture modes.

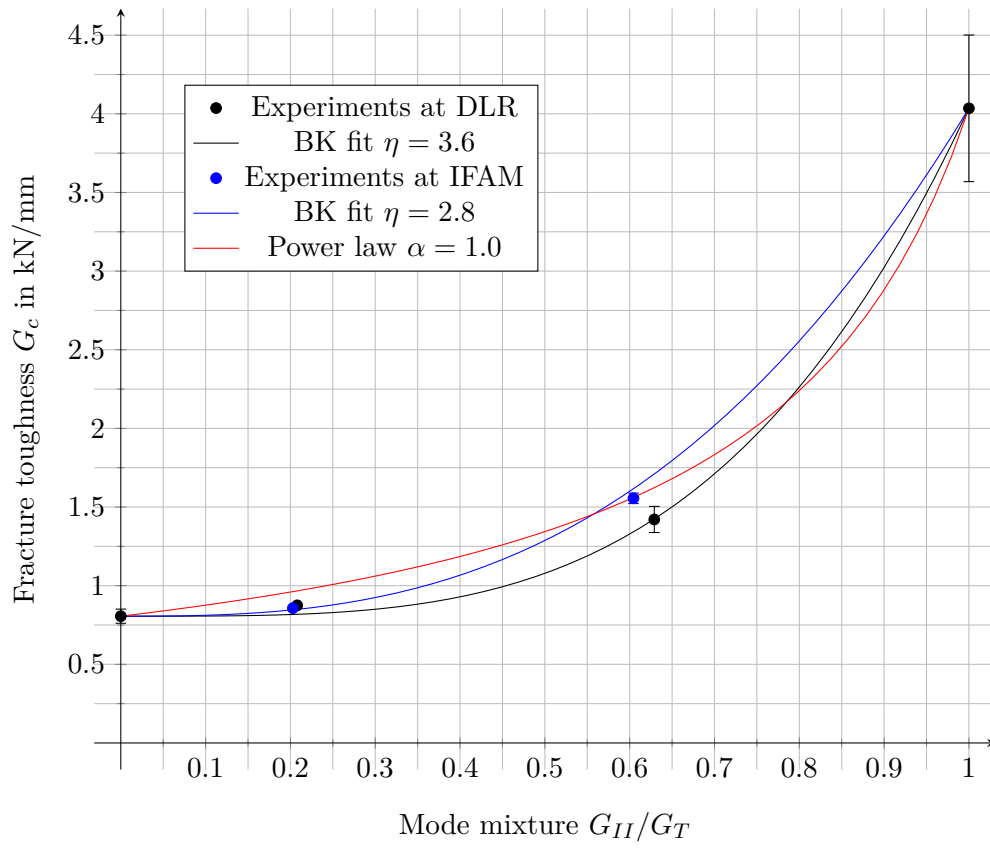


Figure H.1: Fracture toughness of EA9695 in dependence of mode mixture

I Results of fibre composite single lap shear joint tests

Fracture patterns



(a) SLS-0-15

(b) SLS-0-25

(c) SLS-0-35

Figure I.1: Cohesive fracture patterns of SLS-0 specimens

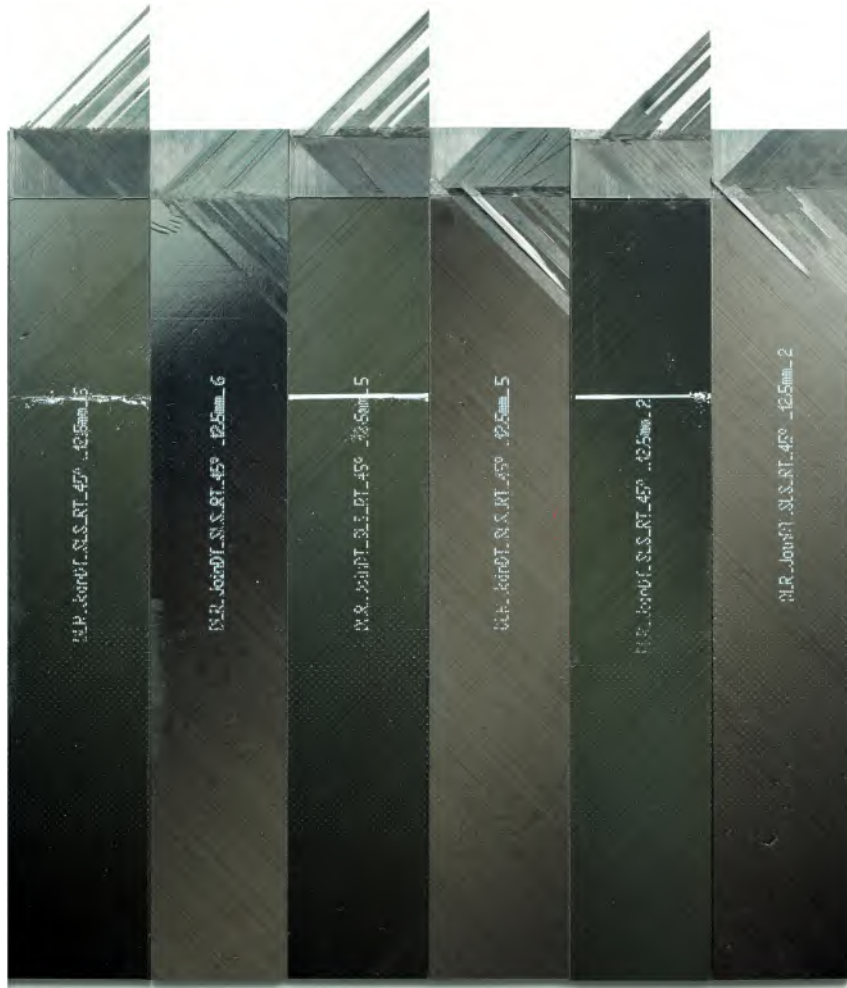


Figure I.2: Fracture patterns of SLS-45 specimens

Strength results

Table I.1: Comparison of failure loads of single lap shear coupons with 0°-interface layer from experiment and simulation

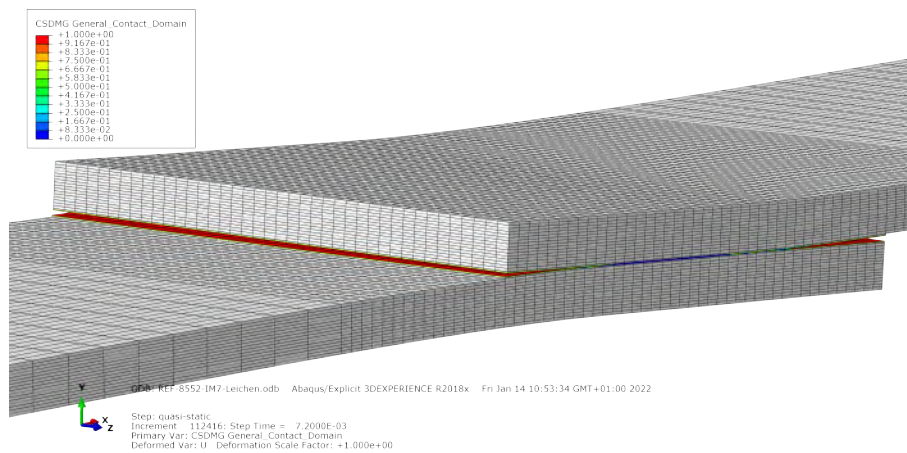
	SLS-0-15		SLS-0-25		SLS-0-35	
	F_{max} in kN	Diff. to Exp. in %	F_{max} in kN	Diff. to Exp. in %	F_{max} in kN	Diff. to Exp. in %
Experiment	10.573 ± 0.326		14.355 ± 1.503		19.581 ± 0.730	
n_{sp}	5		3		5	
ACZ	11.060	+4.6	14.397	+0.0	17.970	-8.2
AACZ eDP G_{soft}	10.489	-0.8	13.716	-4.4	17.435	-11.0
AACZ vM G_{soft}	9.979	-5.6	13.056	-9.1	16.295	-16.8
AACZ eDP G_c	11.643	+10.1	15.708	+9.4	19.780	+1.0

Table I.2: Comparison of failure loads of single lap shear coupons with 45°-interface layer from experiment and simulation

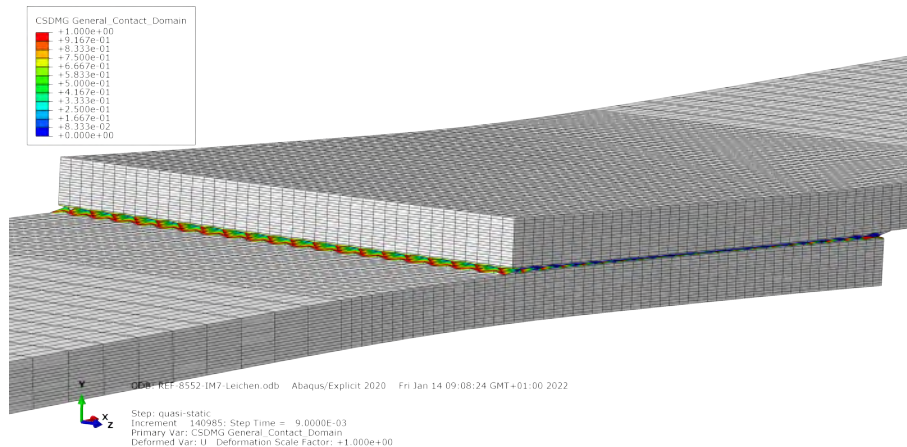
	SLS-45-12	
	F_{max} in kN	Diff. to Exp. in %
Experiment	6.521 ± 0.248	
n_{sp}	6	
Solid	7.273	+13.1
Solid + Coh. Surf.	4.972	−23.8
Cont. Shell + Coh. Surf.	6.387	−2.1
Cont. Shell	8.174	+25.3

J Observations regarding the use of different Abaqus versions

The majority of the simulations in this thesis were carried out with Abaqus version 2020. Using the AACZ technique to model the adhesive layer in single lap shear joint test specimens, with Abaqus 2020 an unusual behaviour of the solid elements and cohesive surfaces in the adhesive layer was observed. Switching to the Abaqus version 2018 results in a behaviour of the adhesive layer being assessed as normal. The behaviour of both Abaqus versions is shown in Fig. J.1 in terms of a deformation plot showing the damage variable *CSDMG* of the cohesive surface in the adhesive layer.



(a) Abaqus Version 2018



(b) Abaqus Version 2020

Figure J.1: Comparison of SLS-0-25 AACZ CSDMG results with different versions of Abaqus

In addition to the visibly incorrect behaviour of the adhesive layer, the failure load is also significantly increased when Abaqus 2020 is used. This is shown in the force-displacement plot in Fig. J.2 with force-displacement data from both simulations as well as the experimental results.

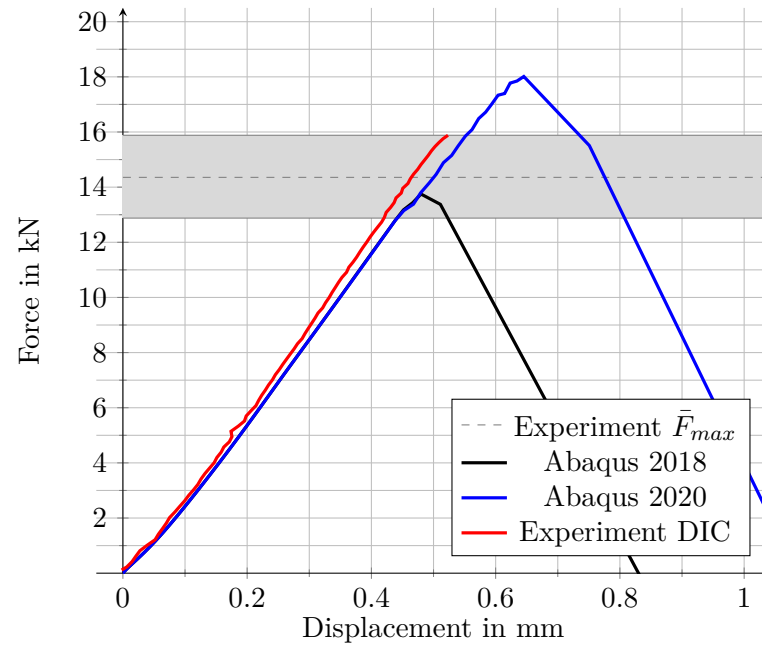


Figure J.2: Force-displacement curves of SLS-0-25 joint coupon determined with different Abaqus version

Own publications

Journal publications

1. **Völkerink**, O., J. KOORD, E. PETERSEN, and C. HÜHNE: ‘Holistic determination of physical fracture toughness values and numerical parameters for delamination analysis considering multidirectional-interfaces’. *Composites Part C: Open Access* (2022), vol.: p. 100277.
2. HEIDE, C. von der, J. STEINMETZ, O. **Völkerink**, P. MAKIELA, C. HÜHNE, M. SINAPIUS, and A. DIETZEL: ‘Polyetherimide-Reinforced Smart Inlays for Bondline Surveillance in Composites’. *Polymers* (2022), vol. 14(18).
3. KOORD, J., J.-L. STÜVEN, O. **Völkerink**, E. PETERSEN, and C. HÜHNE: ‘Investigation of exact analytical solutions for composite laminates under pin-bearing loading’. *Composite Structures* (2022), vol. 292: p. 115605.
4. **Völkerink**, O. and C. HÜHNE: ‘Virtual testing for design and certification of (fusion) bonded longitudinal joints in a fibre composite fuselage: A proposal using FEM-based progressive damage analysis’. *Composites Part C: Open Access* (2022), vol.: p. 100236.
5. STEINMETZ, J., T. LÖBEL, O. **Völkerink**, C. HÜHNE, M. SINAPIUS, C. von der HEIDE, and A. DIETZEL: ‘The Working Principles of a Multifunctional Bondline with Disbond Stopping and Health Monitoring Features for Composite Structures’. *Journal of Composites Science* (2021), vol. 5(2): p. 51.
6. **Völkerink**, O., E. PETERSEN, J. KOORD, and C. HÜHNE: ‘A pragmatic approach for a 3D material model considering elasto-plastic behaviour, damage initiation by Puck or Cuntze and progressive failure of fibre-reinforced plastics’. *Computers & Structures* (2020), vol. 236: p. 106280.
7. PETERSEN, E., E. KAPPEL, J. KOORD, O. **Völkerink**, and C. HÜHNE: ‘Determination of stresses, strains and failure types in multidirectional laminates under pure bending’. *Journal of Composite Materials* (2020), vol.: p. 0021998320932301.
8. PETERSEN, E., J. KOORD, O. **Völkerink**, D. STEFANIAK, and C. HÜHNE: ‘Experimental and numerical investigation of the transition zone of locally steel-reinforced joining areas under combined tension–bending loading’. *Journal of Composite Materials* (2020), vol. 54(17): pp. 2339–2352.
9. KOORD, J., J.-L. STÜVEN, E. PETERSEN, O. **Völkerink**, and C. HÜHNE: ‘Investigation of Exact Analytical Solutions for Circular Notched Composite Laminates under Tensile Loading’. *Composite Structures* (2020), vol.: p. 112180.

10. KOSMANN, J., O. **Völkerink**, M. J. SCHOLLERER, D. HOLZHÜTER, and C. HÜHNE: 'Digital image correlation strain measurement of thick adherend shear test specimen joined with an epoxy film adhesive'. *International Journal of Adhesion and Adhesives* (2019), vol. 90: pp. 32–37.
11. SCHOLLERER, M. J., J. KOSMANN, O. **Völkerink**, D. HOLZHÜTER, and C. HÜHNE: 'Surface toughening—a concept to decrease stress peaks in bonded joints'. *The Journal of Adhesion* (2019), vol. 95(5-7): pp. 495–514.
12. **Völkerink, O.**, J. KOSMANN, M. J. SCHOLLERER, D. HOLZHÜTER, and C. HÜHNE: 'Strength prediction of adhesively bonded single lap joints with the eXtended Finite Element Method'. *The Journal of Adhesion* (2019), vol.: pp. 1–21.

Conference contributions

1. **Völkerink, O.** and C. HÜHNE: 'Virtuelles Testen für Design und Zertifizierung von geklebten Längsnähten in FVK- Flugzeugrümpfen'. *NAFEMS DACH Regionalkonferenz 2022. Konferenz für Berechnung & Simulation im Engineering*. Bamberg, Germany, 2022.
2. **Völkerink, O.**, E. PETERSEN, and C. HÜHNE: 'A 3D Continuum Damage Model for Tough Fibre Reinforced Polymer Composites Using Cuntze's Failure Mode Concept'. *VI International Conference on Computational Modeling of Fracture and Failure of Materials and Structures*. Braunschweig, Germany, 2019.
3. **Völkerink, O.**, J. KOSMANN, M. J. SCHOLLERER, D. HOLZHÜTER, and C. HÜHNE: 'Strength prediction of adhesively bonded single lap joints with the eXtended Finite Element Method'. *12th European Adhesion Conference and 4th Luso-Brazilian conference on Adhesion and Adhesives*. Lisbon, Portugal, 2018.
4. HOLZHÜTER, D., J. KOSMANN, O. **Völkerink**, M. J. SCHOLLERER, and C. HÜHNE: 'Comparison of Stepped and Straight Design of Bonded Scarf Joints.' *12th European Adhesion Conference and 4th Luso-Brazilian conference on Adhesion and Adhesives*. Lisbon, Portugal, 2018.
5. KOSMANN, J., O. **Völkerink**, M. J. SCHOLLERER, D. HOLZHÜTER, and C. HÜHNE: 'Digital image correlation strain measurement of thick adherend shear test specimen joined with an epoxy film adhesive'. *12th European Adhesion Conference and 4th Luso-Brazilian conference on Adhesion and Adhesives*. Lisbon, Portugal, 2018.
6. SCHOLLERER, M. J., J. KOSMANN, O. **Völkerink**, D. HOLZHÜTER, and C. HÜHNE: 'Surface Toughening - A Concept to Decrease Stress Peaks in Bonded Joints'. *12th European Adhesion Conference and 4th Luso-Brazilian conference on Adhesion and Adhesives*. Lisbon, Portugal, 2018.